12-2009

Theoretical Study of Localized Surface Plasmons of Metal Nanoparticles, Clusters and Embedded Metal Nanoparticles in Matrices

Masoud Shabani Nezhad Navrood
Western Michigan University, shabani.msd@gmail.com

THEORETICAL STUDY OF LOCALIZED SURFACE PLASMONS OF METAL NANOPARTICLES, CLUSTERS AND EMBEDDED METAL NANOPARTICLES IN MATRICES

by

Masoud Shabani Nezhad Navrood

A dissertation submitted to the Graduate College
in partial fulfillment of the requirements
for the degree of Doctor of Philosophy
Physics
Western Michigan University
December 2019

Doctoral Committee:

Ramakrishna Guda, Ph.D., Chair
Asghar Kayani, Ph.D.
Alvin Rosenthal, Ph.D.
Yirong Mo, Ph.D.

ACKNOWLEDGMENTS

Firstly, I would like to express my sincere gratitude to my dissertation advisor Dr. Ramakrishna Guda who accept me in his research group. I express my thankfulness to him for all of his continuous support of my Ph.D. study and related research, for his patience, motivation, and immense knowledge. His guidance helped me in all the time of research and writing of this dissertation. Without Dr. Guda's help and suggestions this work would not have been completed.

I would like to thank the rest of my dissertation committee members, Dr. Asghar Kayani, Dr. Alvin Rosenthal, and Dr. Yirong Mo, for their insightful comments and encouragement, but also for the hard questions during the dissertation proposal presentation which incented me to widen my research from various perspectives, and their availability when I needed their help and advice.

My sincere thanks also go to Dr. Ajay Gupta and Dr. Fahad Saeed who kindly provided me access to Parallel Computing and Data Science Laboratory. I also would like to thank my friends Dr. Muaaz Gul Awan and Miss Rajani Pingili, and staff in the Information Technology Services of the Computer Science Department who kindly help me whenever I need their help.

Thanks and appreciations are expressed to Dr. Amala Dass, Dr. Dongil Lee, Dr. Asghar Kayani, and their group members for their collaborations and the scientific discussions.

I want to express my thanks to the Physics Department of Western Michigan University for financial support and to all faculty and staff of the Physics Department for their help and support during my years at Western Michigan University. I also want to express my special thanks to Prof. Kirk Korista who has been always supportive and helpful.

Last but not least, I would like to express my sincere gratitude to my parents, my brothers, and sisters for supporting me spiritually throughout my Ph.D. in the USA.

Masoud Shabani Nezhad Navrood

THEORETICAL STUDY OF LOCALIZED SURFACE PLASMONS OF METAL NANOPARTICLES, CLUSTERS AND EMBEDDED METAL NANOPARTICLES IN MATRICES

Masoud Shabani Nezhad Navrood, Ph.D.

Western Michigan University, 2019

Localized surface plasmons resonances (LSPRs) in metallic nanoparticles (NPs) arise from the interactions between incident light and conduction electrons and have attracted enormous research interest in recent years both for their fundamental nature as well as applications in inter-disciplinary areas of sciences such as biological imaging, plasmonic photo-thermal therapy, photovoltaics, and plasmonic sensors. LSPRs are strongly localized and depend on the shape, size, the composition of the NPs, the polarization direction of the incident light, refractive index (RI) of the surrounding medium as well as on the chemical environment that surrounded NPs. Although significant research has progressed both theoretically and experimentally, several questions need to be answered, including regarding the quantum size effects and the effect of the surface passivating layer on the LSPR. The research work carried out in this study is to understand the plasmonic properties of metal nanoparticles in different environments.

Firstly, we introduced a package written in MATLAB to describe discrete dipole approximation (DDA) method for computing optical properties of arbitrary-shaped NPs. This is the first package written in MATLAB language that implicates Biconjugate Gradient and one-dimensional Fast Fourier Transform techniques to reduce the computational cost of the DDA calculation significantly. This study also represents an algorithm to run the DDA in graphics processing units, which reduces the computational time by almost one order of magnitude. One aspect of LSPR that did not attract much research attention is for plasmons of small plasmonic NPs in size range from 2 to 10 nm. In this study, we investigated the influence of the size, RI of

the medium, and chemical ligand effect on the plasmonic properties of the spherical quantum-sized silver NPs using both quantum and classical models. Also, ligand and size effect on the electron-phonon (e-p) relaxation dynamics of the thiolate-protected gold (Au) clusters was unraveled. From the studies, it was shown that aromatic passivating ligands deaccelerate e-p relaxation dynamics of the Au clusters more in comparison to an aliphatic ligand.

Binding molecules on the surface of the NPs change the RI of the surrounding medium that results in shifting LSPR wavelength. This plasmonic shift can be used to detect biological molecules. In this study, we explore the LSPR sensitivity of six different hollow-Au nanoshells (sphere, disk, rod, ellipsoid, rectangular block, and prism). The results show that the shell thickness affects the LSPR sensitivity. Also, the study demonstrates that the LSPR sensitivity of the rod shape and rectangular block nanoshells are higher than other structures. In an effort to understand the plasmonic properties of embedded metal nanoparticles, LSPR properties of Au, Ag, and Cu NPs in silica matrix are studied using the DDA. The results show that rod-shaped NPs have higher extinction and produce stronger field enhancement in comparison to the spherical ones. The study also demonstrates that embedded Ag NPs have stronger plasmonic properties than Au and Cu NPs.

TABLE OF CONTENTS

LIST OF TABLES

LIST OF FIGURES

CHAPTER 1

INTRODUCTION

1.1. Introduction

The resonant interaction of the light beam with the free electrons of the noble metals led to the emerging of a fast-developing research field named plasmonics [1–3]. One of the oldest observations of the light-metal interaction dates back to Roman times in the Lycurgus cup [4]. Due to the presence of the nanoparticles with size up to 100 nm (silver 66.2%, gold 31.2%, and copper 2.6%), which dispersed in the cup [5], it appears green and purple-red when illuminated from inside and outside, respectively (see Figure 1.1). The green color is attributed to scattering of the light by silver nanoparticles dispersed in the cup, whereas purple-red colors are mainly due to absorption of the incident light by gold nanoparticles (see Figure 1.1) [5].

Figure 1.1. Lycurgus cup (left) appears green when illuminated from outside and (right) purple-red when shinned from inside. The images are kindly provided by the British Museum, ref [6].

The polarizability of the free electron cloud in the noble metals leads to efficient interaction of the incident light with particles that are much smaller than the incoming wavelength [1–3]. This phenomenon provides the opportunity to manipulate and control light on the nanometer scale [1–3] and opens up a new window for a variety of the applications in nanophotonic such as solar cells [7, 8], biological imaging [9–14], plasmonic photo-thermal therapy [15–20], photovoltaics [7], molecular diagnostics [21–26], plasmonic sensors [21–40], surface-enhanced Raman spectroscopy [41–47], metal-enhanced luminescence [48] and plasmonic rulers [49].

There are two types of plasmonic interaction: (1) interaction of the incident light with a dielectric-metal interface [1, 3, 50, 51], and (2) coupling of the electromagnetic wave with metallic nanoparticles [1, 3, 50]. In resonance condition, the coupling of the light with the first configuration (see Figure 1.2) creates the excited collective oscillations of free electrons, which propagates at the interface of the metal-dielectric and called surface plasmon resonance (SPR) [1, 3, 50, 51]. On the other hand, the resonance interaction of the incident electromagnetic wave with the free electron cloud of the metallic nanoparticles leads to collective oscillation of the free electrons in the close vicinity of the nanoparticle (refer to Figure 1.4) [1, 3, 50]. This phenomenon which produces an enhanced electric field by several orders magnitude of the incident light field around the nanoparticle (see Figure 1.5) is highly localized and called localized surface plasmon resonance (LSPR) [1, 3, 50].

In this chapter, I begin with a discussion about the fundamentals of the surface plasmon polaritons and localized surface plasmons, and then briefly discuss some interesting applications of the LSPRs property of the plasmonic nanoparticles. The chapter continues by stating the goals and questions of the research and ends with presenting our contributions and introducing the structure of the dissertation.

1.2. Surface Plasmon Polaritons and Localized Surface Plasmons

Free electrons in metals oscillate rapidly around positive ions with plasma frequency. This collective longitudinal oscillation of free electrons is quantized with the quantum of oscillation called plasmon [1, 3, 50, 51]. Plasmons play important roles in determining the optical properties of metals. Light with frequencies below than plasma frequency will be screened and reflected by free electrons oscillation in metals, while the light with frequencies above plasma frequencies is

transmitted through metals. The transmission is due to the fact that the oscillation of the electrons is not fast enough to screen the incident field [52].

When a beam of light travels through a dielectric medium and reaches the surface of the metal it can couple with oscillation of the delocalized electrons at the interface of the metal and dielectric. This coupling creates an electromagnetic wave at the boundary of two medium, called surface plasmon polaritons (SPPs) [1, 3, 50, 51]. SPPs includes charge motion in the metal (surface plasmon) and EM wave in the dielectric medium (polariton) [1, 3, 50, 51]. This surface wave propagates along with the interface, while decays exponentially in the directions perpendicular to the boundary of the two mediums (see Figure 1.2) [1, 3, 50, 51]. It should be noted that as SPPs propagate along with the interface loses its energy due to absorption by the metal and scattering into other directions [1, 3, 50, 51]. As shown in Figure 1.2 the characteristic distances of the surface plasmon are 1) decay length of the evanescent field in the dielectric, 2) decay length of the evanescent field in the metal and 3) propagation length in the interface of the dielectric and metal that are represented as δ_1 , δ_2 and δ_{spp} in Figure 1.2, respectively.

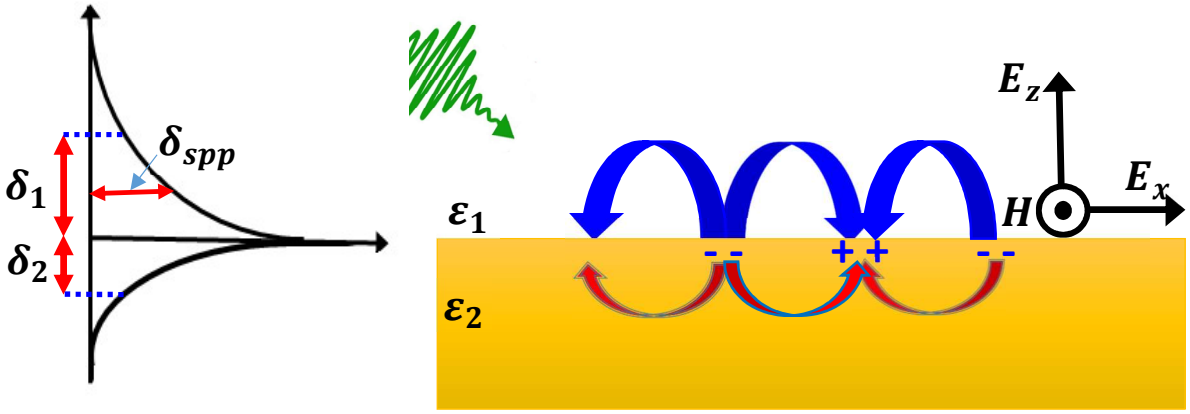

Figure 1.2. Exciting surface plasmon polaritons at the boundary of the metal and dielectric medium. Adapted by permission form Springer Nature, Nature, ref [53], 2003.

At the interface of the two mediums, the six components of the electromagnetic wave can be decomposed into two independent sets: transverse electric (TE) and transverse magnetic (TM). The SPPs normally can be excited by a p-polarized wave (TM mode) where the electric field has a component in the direction of the propagation [50]. If we consider the interface of the two medium at the x-y plane, three components of TM mode of the SPP wave which is propagating in

the x-direction and decaying in the z-direction can be expressed as following in the dielectric medium (Z > 0) [1, 3, 50]

$$H_{y_1} = A_1 \exp(ik_{x_1}X)\, e^{-k_{z_1}Z} \quad (1.1.a)$$

$$E_{x_1} = iA_1 \frac{k_{z_1}}{\omega\varepsilon_0\varepsilon_1} \exp(ik_{x_1}X)\, e^{-k_{z_1}Z} \quad (1.1.b)$$

$$E_{z_1} = -A_1 \frac{k_{x_1}}{\omega\varepsilon_0\varepsilon_1} \exp(ik_{x_1}X)\, e^{-k_{z_1}Z} \quad (1.1.c)$$

And in the metal (Z < 0) [1, 3, 50]

$$H_{y_2} = A_2 \exp(ik_{x_2}X)\, e^{k_{z_2}Z} \quad (1.2.a)$$

$$E_{x_2} = -iA_2 \frac{k_{z_2}}{\omega\varepsilon_0\varepsilon_2} \exp(ik_{x_2}X)\, e^{k_{z_2}Z} \quad (1.2.b)$$

$$E_{z_2} = -A_2 \frac{k_{x_2}}{\omega\varepsilon_0\varepsilon_2} \exp(ik_{x_2}X)\, e^{k_{z_2}Z} \quad (1.2.c)$$

Since the charge density is zero ($\rho = 0$), by applying the Maxwell equation ($\nabla . D = \rho$) in the above equations we have

$$ik_{x_1}E_{x_1} - k_{z_1}E_{z_1} = 0 \quad (1.3.a)$$

$$ik_{x_2}E_{x_2} + k_{z_2}E_{z_2} = 0 \quad (1.3.b)$$

By applying the boundary conditions [54, 55] ($E_{1t} = E_{2t}$, $H_{1t} = H_{2t}$, $D_{1n} = D_{2n}$) the surface plasmon polaritons dispersion relation can be expressed as [1, 3, 50, 51]

$$k_{spp} = \frac{\omega}{c}\sqrt{\frac{\varepsilon_1\varepsilon_2}{\varepsilon_1 + \varepsilon_2}} \quad (1.4)$$

where ω, c, ε_1 and ε_2 are the frequency and speed of the incident light in vacuum, dielectric function of the dielectric medium, and dielectric function of the metal, respectively. As mentioned already, the surface waves lose their energy while propagating in the interface. Thus, the real and imaginary part of the surface plasmon wavevector can be expressed as below [1, 3, 50, 51, 54]:

$$\mathrm{Re}\left(k_{spp}\right) = \frac{\omega}{c}\sqrt{\frac{\varepsilon_2 \mathrm{Re}(\varepsilon_1)}{\varepsilon_2 + \mathrm{Re}(\varepsilon_1)}} \tag{1.5.a}$$

$$\mathrm{Im}\left(k_{spp}\right) = \frac{\omega}{c}\sqrt{\frac{\varepsilon_2 \mathrm{Re}(\varepsilon_1)}{\varepsilon_2 + \mathrm{Re}(\varepsilon_1)}}\left[\frac{\varepsilon_2}{2\mathrm{Re}(\varepsilon_1)\left(\varepsilon_2 + \mathrm{Re}(\varepsilon_m)\right)}\right]\mathrm{Im}(\varepsilon_m) \tag{1.5.b}$$

where Re and Im denote the real and imaginary part, respectively. Also, the normal component of the wavevector of the SPP can be expressed as [1, 3, 50, 51, 54]

$$k_{z_i} = \frac{\omega}{c}\left(\frac{\varepsilon_i^2}{\varepsilon_1 + \varepsilon_2}\right)^{\frac{1}{2}} \tag{1.6}$$

where i = 1, 2 and represents the *i*-th medium.

If the incident light activates resonant oscillation of the conduction electrons in the metal, the surface plasmon resonance (SPR) occurs and gives rise strongly enhanced surface fields [1, 3, 50, 51]. To excite the surface plasmon in a resonant manner by the light beam, the momentum must be conserved at the interface of the two mediums [1, 3, 50, 51]. However, the wavevector of impinging light is smaller than the wavevector of the SPP in the metal and there is phase mismatch ($\sim\Delta k$) between the propagating light line and SPP [1, 3, 50, 51]. Hence, the SPPs cannot be excited resonantly by the direct shining of the light to the interface of the dielectric medium and the metal.

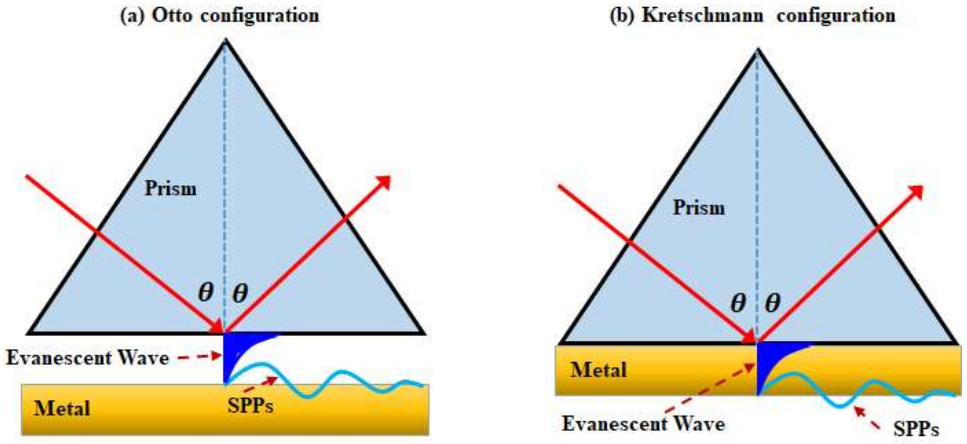

- **Figure 1.3.** Schematic of (a) Otto and (b) Kretschmann configuration to excite the surface plasmon resonances at the interface of the metal and dielectric medium. To excite surface plasmon resonances using Kretschmann configuration, the thickness of the metal layer must be smaller than the skin depth of the evanescent wave. Fig. (a) is adapted by permission form Springer Nature, Zeitschrift für Physik A Hadrons and Nuclei, ref [56], 1968.

To overcome the momentum mismatch problem and excite surface plasmons, the wavevector of the incident light can be increased using adaptive optics [57, 58]. Figure 1.3 shows the two examples of the configurations that have been proposed by Otto and Kretschmann to overcome the momentum mismatch problem [57, 58]. The total internal reflection of the incident light creates evanescent waves at the boundary of the two mediums (see Figure 1.3) that have higher wavevector in comparison to air and can be used to excite SPPs [57, 58].

If the dimension of the metal-dielectric interface is much smaller than the δ_{spp} a special kind of surface plasmon will be formed, called localized surface plasmon. In contrast to SPP, localized surface plasmons (SPP of the very small metallic nanoparticles (NPs)) are highly localized, non-propagative, and free from losses related to the retardation of large metallic surface (see Figure 1.4 and 1.5) [1, 3, 50, 59]. Due to the non-propagative property of surface plasmons of metal NPs, localized surface plasmon resonances (LSPRs) can be excited by direct illumination of the light without applying phase matching techniques at the boundary of the metal and surrounding medium [1, 50]. Thus, they are not characterized by a wavevector k_{spp}.

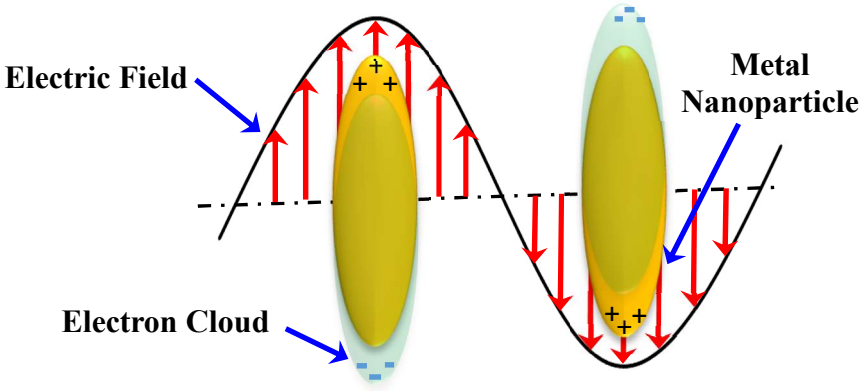

Figure 1.4. Schematic of excitation of localized surface plasmon resonances (LSPRs) of plasmonic nanoparticles by illuminating light to them.

Figure 1.5 shows electric field enhancement around a 40 nm spherical gold NP in the vacuum. As shown, due to LSPR a strong electric field has been produced at the surface of the NP (4.5 stronger than the incident field) that is decaying very fast by increasing distance from its surface. This optical phenomenon strongly depends on the shape, type, size, composition of the

nanoparticles, the polarization direction of the incident light as well as on the chemical environment that surrounded them [60–65].

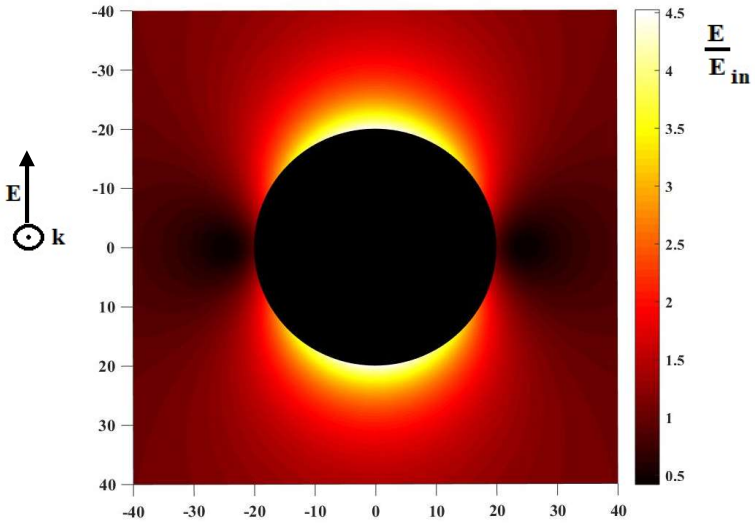

Figure 1.5. Strong localized electric field around a 40 nm spherical gold nanoparticle that is produced due to LSPR by direct illumination of the laser light to the nanoparticle.

In this dissertation, we focus on the LSPRs of the plasmonic nanoparticles. LSPRs attracted enormous research interest in recent years due to their profound applications in inter-disciplinary areas of sciences [7, 9–47, 49, 66]. In the next section of this chapter some of the applications of the LSPRs have been provided.

1.3. Some Applications of LSPRs

1.3.1. Plasmonic Photothermal Therapy (PPTT)

In the past few decades photothermal therapy (PTT) has been used to destroy cancer cells to some degree [15–20]. As minimally invasive therapy, the photothermal treatment strategy uses absorbing light dye molecules to absorb electromagnetic energy and convert it into enough heat to destroy cancer cells with minimum side effects [15–20]. However, because of the low absorption efficiency of natural tissue absorbents and conventional dye molecules, PTT has not been widely used for cancer therapy [15–20]. Recently plasmonic nanoparticles have attracted new interest to PTT [15–20]. Among these NPs, gold NPs in comparison to other plasmonic NPs attracted significant research attention as a potential candidate for photothermal therapy [15–20] due to their

unique properties such as non-toxicity, biocompatibility, inertness, and high scattering and absorption [27, 67, 68]. At LSPR frequency the light absorption and scattering of the Au NPs are much stronger than any organic dye molecule [14]. The absorbed light can be transferred from the NPs to the surrounding medium through three processes: (1) electron-electron scattering (occurring in order of 100 fs), (2) electron-phonon interaction (in order of ps) and (3) phonon-phonon relaxation (in order of 10 ps-100 ps) [14]. If the NPs are located in the close vicinity of the cancer cells, the transferred heat from NPs can destroy the malignant cells by increasing the temperature of the targeted region [11, 12, 15–20, 69, 70]. This photothermal therapy, which is induced by plasmonic gold nanoparticles, is called plasmonic photothermal therapy (PPTT) [11, 12, 15–20, 69, 70].

Lin and coworkers, for the first time, reported the destruction of over 90% of cancer cells using the illumination of a nanosecond visible laser light to the spherical Au nanoparticles, which were located in the close vicinity of the malicious cells [71]. Visible range PPTT of the cancer cells by shining the laser light to the Au nanospheres has also been studied by other groups [11, 70]. However, solid spherical Au nanoparticles practical applications in vivo are limited due to the fact that the light penetration in tissue is negligible at their corresponding LSPR frequencies (visible range).

The LSPR of the plasmonic NPs can be tuned from visible to the near-infrared (NIR) region by varying size, shape and refractive index (RI) of the medium [60–65]. Interestingly, in the NIR region, the biological tissue is transparent, and light penetration is optimum due to the minimum absorption of the hemoglobin and water molecules in tissues in this electromagnetic window [47]. Thus, plasmonic nanoparticles such as gold nanoshell [20] and gold nanorods [12] with LSPR in the NIR region received considerable attention in PPTT. As an example, in 2003 Hirsch et al. using gold nanoshells destroyed breast cancer tumors after exposure to NIR light at an intensity of 35 W/cm^2 for 7 minutes [20].

1.3.2. Biological Imaging

As mentioned already, plasmonic nanoparticles strongly scatter the incident light at their LSPRs frequencies due to resonant excitation of their free conduction electrons. The amount of scattering depends on the size of the nanoparticles and increases by expanding their dimensions

[9]. This optical property of the plasmonic NPs provides the opportunity to use them for making high-resolution optical images and labeling biological systems [9–14]. A simple optical microscope equipped with a dark-field condenser can be applied for imaging NPs in a dark medium by capturing the strong scattered light correspond to their LSPRs. Figure 1.6a and 1.6c show molecular imaging of the healthy cells which have been produced by capturing the scattered light of the randomly dispersed gold nanospheres and nanorods, respectively [12].

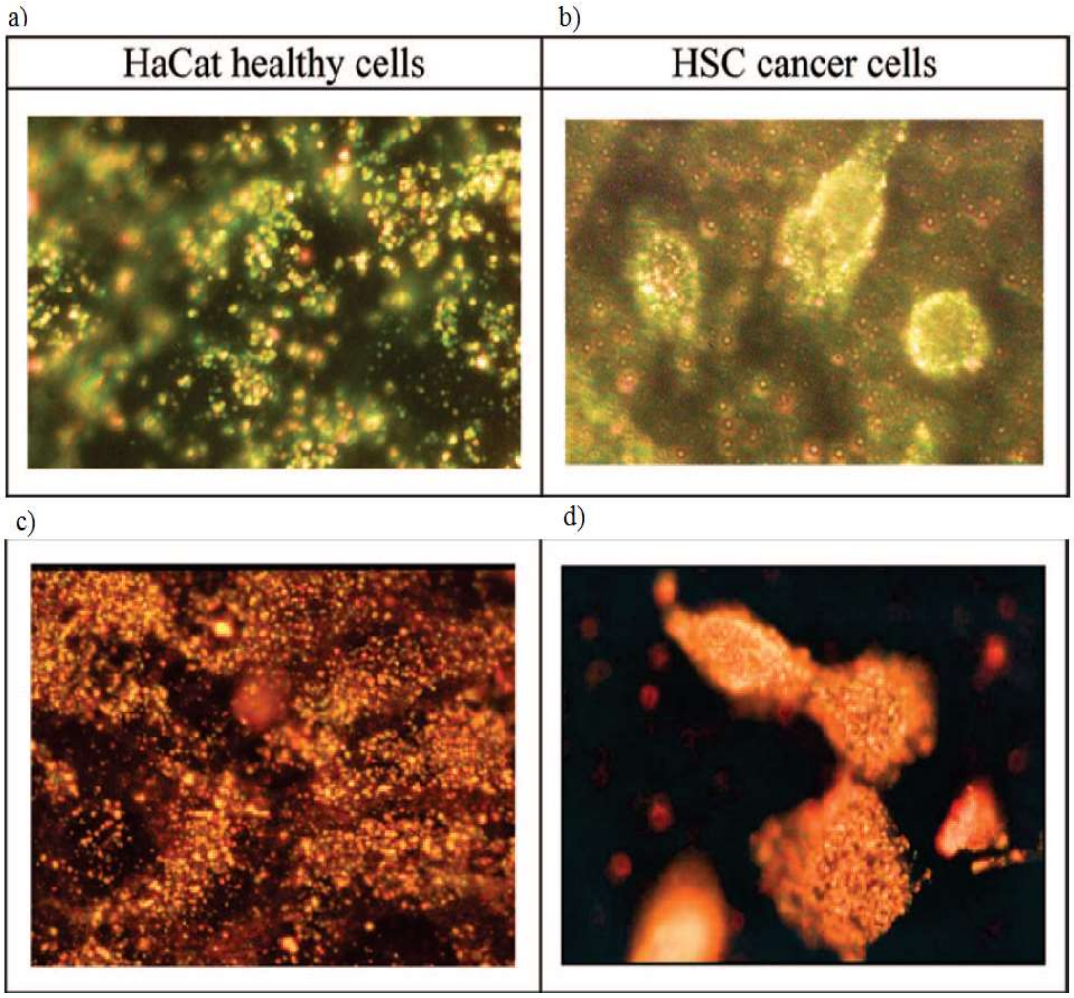

Figure 1.6. (a) Optical image of the biological cells by spherical gold NPs randomly dispersed on the tissue. (b) Optical image of the cancer cells targeted by anti-EGFR conjugated by spherical gold NPs. (c) Optical image of the biological cells by gold nanorods randomly dispersed on the tissue. (d) Optical image of the cancer cells targeted by anti-EGFR conjugated by gold nanorods. Reprinted by permission from ref. [12].

In addition, dark-field microscopy technique can be very effectively utilized for molecular imaging of biomolecules by conjugating the gold nanoparticles with specific targeting molecules [19]. As an example, to target specifically the cancer cells, El-Sayed and his group targeted cancer biomarkers epidermal growth factor receptor (EGFR) which highly present in cancer cells [12]. By conjugating Au nanoparticles with anti-EGFR, they bounded the NPs to the surface of the malignant cells and constructed their image by collecting the scattered light from the Au NPs in the dark medium [12]. Figure 1.6b and 1.6d show image of the cancer cells produced by the use of the gold nanospheres and gold nanorods, respectively. As shown, owing to high penetration of NIR frequencies at living tissues the gold nanorods provide a high-resolution image of the cancer cells in comparison to the Au nanospheres [12].

1.3.3. Plasmon – Fluorescence Enhancement

As demonstrated in Figure 1.7 (Jablonski diagram), the electrons of the fluorophore molecules transfer to the excited state by absorbing high energy photons and then move back from the excited state to the ground one through phonon-phonon collision (non-radiative decay) and emitting a low energy photon (radiative decay) [72]. The fluorescence or emitted light of the fluorophore molecules has been applied for the detection of biological and chemical species [72]. However, due to the low signal-to-noise ratio in this technique, the detection of desired species using the typical fluorescence methods is difficult [48].

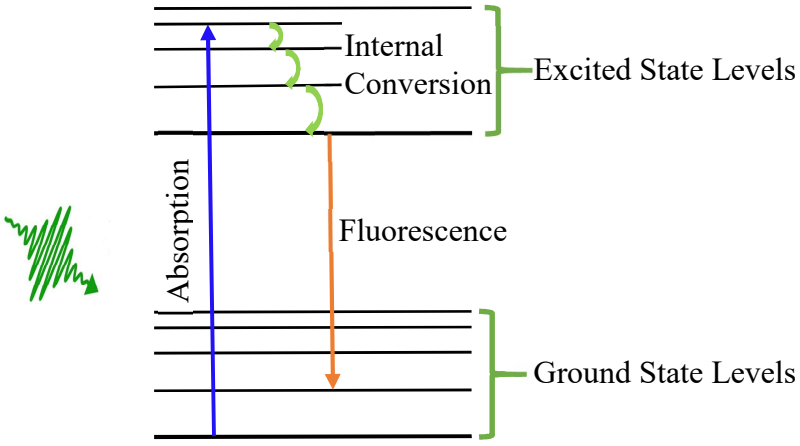

Figure 1.7. The excited electron will relax through two processes: phonon-phonon relaxation, and emitting a photon with the wavelength higher than the incident one (Jablonski diagram).

LSPRs properties of the plasmonic NPs offer an effective way to increase the efficiency of the fluorescence technique by introducing two enhancement mechanisms: excitation enhancement, and emission enhancement [73]. LSPR frequency of the isotropic plasmonic nanoparticles such as solid spherical nanoparticles or spherical nanoshells, which just have one resonance plasmon frequency, can be adjusted either to excitation or emission frequency of the fluorophore molecule to increase the fluorescence efficiency (see Figure 1.8a). More interestingly, anisotropic plasmonic NPs such as nanorods, which have two LSPRs peaks, simultaneously could enhance excitation wavelength and emission band of the fluorophores by matching them to the transversal and longitudinal LSPRs frequencies of the NPs, respectively (see Figure 1.8b) [74].

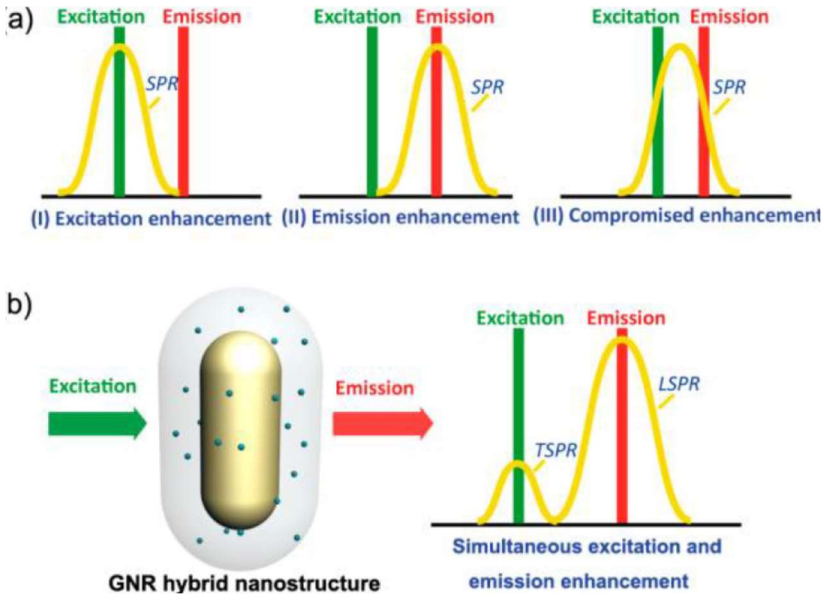

Figure 1.8. Schematic of fluorescence enhancement by LSPR of the plasmonic NPs. a) excitation enhancement (Left), emission enhancement (Middle) and compromised enhancement (Right) with the use of a single LSPR plasmonic NP. b) Simultaneous extinction and emission enhancement by a double LSPR metal NP. Reprinted by permission from ref [74].

Figure 1.9 shows an example of the fluorescence enhancement of fluorophore molecules using three different hybrid nanostructures [74]. The structures were composed of an Au core and fluorophore-embedded silica shell. The first sample (GNR1) is made of Au nanorod- silica shell with the length and diameter of the core, and thickness of the silica shell of 100 ± 4 nm, 44 ± 2 nm and 23 ± 1 nm, respectively. The second sample (GNS1) is a spherical core-shell (Au-silica) with

a core diameter of 69 ± 5 nm and a shell thickness of 23 ± 1 nm. The third composite is an Au nanorod- silica shell that the length and diameter of the core, and thickness of the silica shell are 43 ± 2 nm, 11 ± 3 nm and 22 ± 2 nm, respectively. Emission from the same number of the Oxazine-725 molecules (1000) from each sample has been obtained. As demonstrated in Figure 1.9, GNR1 significantly enhanced the fluorescence intensity of the fluorophore molecules in comparison to other samples. This result can be explained by the fact that transitional and longitudinal plasmon peaks of this sample (532nm and 693nm, consequently) are matched with the excitation wavelength (532nm) and emission band (with FWHM from 660nm to 702nm) of the Oxazine-725, respectively, that leads to simultaneous excitation and emission enhancement. However, the LSPR peak of the GNS1 (554 nm) is matched with the excitation wavelength of the fluorophore that enhances only the excitation. It should be noted that LSPRs frequencies of the GNR2 are matched neither with the excitation wavelength nor with the emission band of Oxazine-725 that results in less fluorescence enhancement in comparison to other samples [74].

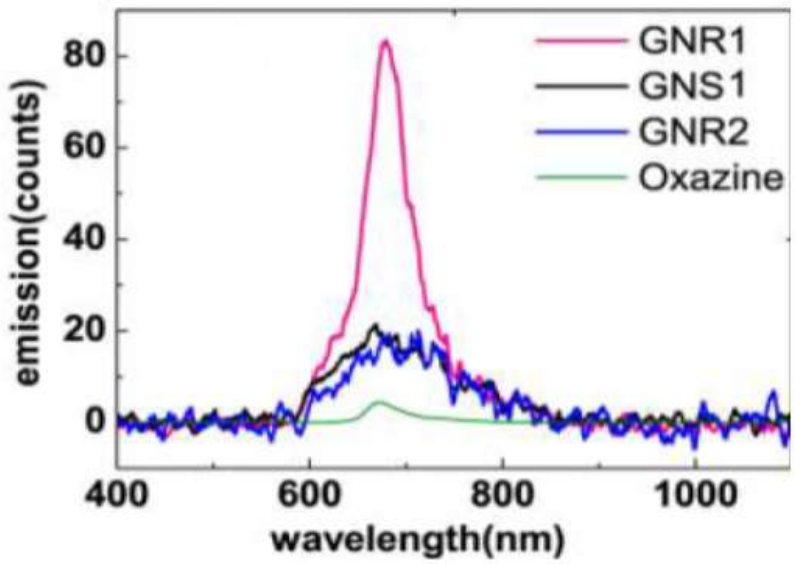

Figure 1.9. Fluorescence emission spectra of GNR1, GNS1, and GNR2. The peak fluorescence intensities from GNR1, GNS1, and GNR2 have been enhanced by the factors of 20.8, 5.3, and 4.5, respectively. Reprinted by permission from ref [74].

1.4. Goals of the Research

In this dissertation we aim to achieve the following goals:

a. Provide a comprehensive explanation for all steps of the discrete dipole approximation along with accelerative techniques such as Fast Fourier Transform (FFT) and Biconjugate Gradient (BCG). We also developed a MATLAB package to compute the optical properties of different kinds of nanostructures.
b. Explore the optical properties of the quantum-sized nanoparticle.
c. Study chemical ligand and size effect on the electron relaxation dynamics of the small-sized gold nanoparticles.
d. Introduce hollow-nanoshell structures to study size, shape, shell thickness and aspect ratio effects on the localized surface plasmon sensitivity of the gold nanoshells. Our goal is to obtain structures with high LSPR sensitivity.
e. Investigate optical properties of the different kind plasmonic nanoparticles which are embedded in a silica matrix. In addition, our goal is to explore the electric field enhancement of the different embedded structures.

1.5. Research Questions

In this dissertation we address the following questions:

a. How reducing the size of the NPs will change the optical properties of the plasmonic nanoparticles?
b. How will different chemical ligands affect electron relaxation process in small-sized heated plasmonic nanoparticles?
c. How can LSPR sensitivity of the hollow-Au nanoshells be adjusted by changing size, shape and shell thickness to obtain a structure with higher sensitivity?
d. How optical properties, such as absorption and electric field enhancement, in embedded plasmonic nanostructures depend on the type, size, shape, and the number of the embed nanoparticles?

1.6. Contributions

The main contributions of this dissertation are as follows:

a) In chapter II, we discuss the electromagnetic methods that have been used in this dissertation to simulate the optical properties of the studied plasmonic nanoparticles. In the first section, the modified dielectric permittivity of the small-sized bare and ligand-conjugated metallic nanoparticles have been discussed. In the second section, we review some electromagnetic methods such as Mie theory and Multilayered Mie theory as exact electromagnetic methods to calculate the optical properties of the solid spherical and multilayered spherical nanoparticles, respectively. In the last section of this chapter we review all steps of this DDA along with the accelerative methods. We also introduce a MATLAB package to calculate the optical properties of arbitrary shaped plasmonic NPs using DDA. One dimensional FFT and BCG have been applied in this proposed package to reduce the computational time and memory in the DDA method. To further accelerate the computational procedure, we applied the graphics processing unit (GPU) algorithm, which is provided in MATLAB software, to our problem. Using GPU, the computation cost decreased by almost one order of magnitude when compared to CPU. In the end, we calculated the optical properties of the plasmonic NPs such as extinction, absorption and scattering efficiencies, electric field enhancement around the NPs and creation of the hot spots in dimeric structures using this package.

b) In chapter III, we studied the plasmonic properties of the spherical Ag NPs in the size range of 3 to 20 nm. We used both quantum and classical modeling to understand the importance of invoking quantum regime to accurately describe Ag NPs properties in this size regime. As a case study, using standard Mie theory we monitored the LSPR peak shift and electric field enhancement as a function of the size of the metallic particle and the refractive index of the surrounding medium. Also, optical properties of Ag nanoparticles conjugated with a chemical ligand using multi-layered Mie theory were studied and interesting trends were observed.

c) In chapter IV, we explored the influence of passivating ligand on electron-phonon relaxation dynamics of the smallest sized gold clusters using ultrafast transient absorption spectroscopy. To study size and ligand effect, we explored electron

dynamics in seven different samples: Au_{279} passivated with 4-tert-butylbenzene thiol (TBBT), Au_{329} passivated with phenylethane thiol (SC_2Ph), Au_{329} and $Au_{\sim1400}$ and $Au_{\sim2000}$ conjugated with hexane thiol (SC_6), and 13 nm Au stabilized in citrate solution. The study has revealed interesting aspects of the role of ligand on electron-phonon relaxation dynamics wherein the aromatic passivating ligands, SC_2Ph and TBBT, have shown smaller power dependency and higher plasmonic bleach while the cluster with aliphatic passivating ligands has behaved similarly to regular plasmonic gold nanoparticles. Also, we modeled the effect of the ligand on the plasmonic properties of the investigated samples by calculating the free electron density correction factor of each sample using the three-layered Mie theory. The results show that SC_6 interacts least with core-gold while TBBT and SC_2Ph have a greater effect on the surface electronic conductivity that is attributed to π-interaction of the ligand with gold.

d) In chapter V, we investigated the localized surface plasmon resonance sensitivity of the hollow gold nanoshells using multi-layered Mie theory and discrete dipole approximation. In this research, the influence of shape, size, shell thickness and aspect ratio on the plasmon sensitivity of the hollow gold nanoshells are addressed. Different shapes of hollow-Au nanoshells are studied that include: sphere, disk, triangular prism, rod, ellipsoid, and rectangular block. Our results show that the rectangular block and rod-shaped Au nanoshells have maximum LSPR sensitivity when compared to other shaped Au nanoshells.

e) In chapter VI, the plasmonic properties of metallic NPs embedded in silica matrix were investigated using the DDA method. The optical properties of the spherical and rod shape Au, Ag, and Cu NPs were simulated. The influence of size and interparticle distance on the plasmonic spectra and field enhancement of the embedded NPs are studied in monomeric and dimeric structures, respectively. In dimeric structures, the electric field evolution versus distance from the center of the matrix was calculated. The study has revealed that rod-shaped NPs have higher field enhancement at the surface of the matrix when compared to the spherical case. Also, Ag NPs have shown higher extinction, greater scattering quantum yield, and stronger field enhancement in comparison to the Au and Cu. As a case of study, we also explored the effect of the

number of NPs on the aforementioned optical properties, and interesting results were observed.

It is worth mentioning that this research work has resulted in the following published and unpublished journal publications:

1. Masoud Shabaninezhad, Abubkr Abuhagr, Naga Arjun Sakthivel, Chanaka Kumara, Amal Dass, Kyuju Kwak, Kyunglim Pyo, Dongil Lee and Guda Ramakrishna. "Ultrafast Electron Dynamics in Thiolate-Protected Plasmonic Gold Clusters: Size and Ligand Effect". (Published: J. Phys. Chem. C 2019, 123, 13344−13353; DOI: 10.1021/acs.jpcc.9b01739).
2. Masoud Shabaninezhad, and Guda Ramakrishna. "Theoretical investigation of size, shape, and aspect ratio effect on the LSPR sensitivity of hollow-gold nanoshells". (Published: J. Chem. Phys. 150, 144116 (2019); DOI: /10.1063/1.5090885).
3. Shahid Iqbal, Masoud Shabaninezhad, Mohammad Hatshan, Prashanta M. Niraula, Abubaker Abuhagr, Hasna Alali, Ramakrishna Guda, and Asghar Kayani. "Ion-implanted silver nanoparticles for metal-enhanced fluorescence". (Published: AIP Advances 8, 095217 (2018); DOI: 10.1063/1.5045570).
4. Masoud Shabaninezhad, and Guda Ramakrishna."Theoretical Investigation of Plasmonic Properties of Quantum-Sized Silver Nanoparticles". Under review.
5. Masoud Shabaninezhad, Muaaz. G. Awan and Guda Ramakrishna. " MATLAB Toolbox for Discrete Dipole Approximation by Graphics Processing Unit: One Dimensional Fast Fourier Transform and Biconjugate Gradient ". Under review.
6. Masoud Shabaninezhad, and Guda Ramakrishna. "Optical Properties of Embedded Plasmonic Nanoparticles Using Discrete Dipole Approximation". Under Process.

In addition, the results of this dissertation have been presented in the following American Physics Society (APS) meetings:

1. Size, Shape and Aspect Ratio Effect on the LSPR Sensitivity of Hollow-Gold Nanoshells, Annual Spring Meeting of the APS, Ohio- Region Section (Wooster, 2019), Oral presentation.

2. An overview of discrete dipole approximation by means of Graphics Processing Unit, Fast Fourier Transform, and Biconjugate Gradient in MATLAB, Annual Spring Meeting of the APS, Ohio- Region Section (Wooster, 2019), Poster presentation.
3. Theoretical Investigation of Plasmonic Properties of Quantum-Sized Silver Nanoparticles, Annual March Meeting of the APS (Boston, 2019), Oral Presentation.
4. Electron-Phonon Relaxation Dynamics of Thiolate-Protected Plasmonic Gold Clusters, Annual Fall Meeting of the APS, Ohio- Region Section (Toledo, 2018), Oral presentation.

A DDA package written in MATLAB also provided that is available in the Appendices for use by other researchers.

1.7. Structure of the Dissertation

The overall structure of this dissertation takes the form of six chapters, excluding this introductory chapter.

A. Chapter 2: Electromagnetic Methods
B. Chapter 3: Theoretical Investigation of Plasmonic Properties of Quantum-Sized Silver Nanoparticles
C. Chapter 4: Ultrafast Electron Dynamics in Thiolate-Protected Plasmonic Gold Clusters: Size and Ligand Effect
D. Chapter 5: Theoretical Investigation of Size, Shape and Aspect Ratio Effect on the LSPR Sensitivity of Hollow-Gold Nanoshells
E. Chapter 6: Optical Properties of Embedded Plasmonic Nanoparticles Using Discrete Dipole Approximation
F. Chapter 7: Conclusion and Future works

CHAPTER 2

COMPUTATIONAL METHODS

2.1. Introduction

This chapter discusses the theoretical models that have been used in this dissertation to describe the optical properties of the metallic nanoparticles. The first section of this chapter begins with the Drude model to describe the dielectric function of bulk metals [75], then discusses the modified version of the Drude model to represents the dielectric function of the bare and ligand conjugated metallic nanoparticles [76, 77]. The section follows by explaining the quantum model that has been applied to obtain the electric permittivities of the quantum-sized NPs [78, 79]. The second section starts with describing the Mie theory as an exact solution for the light scattering, and absorption field by a spherical shape target that inserted in a homogeneous and isotropic medium and illuminated by a plane wave [1, 80]. Also, the equations for calculating the electric and magnetic fields inside and around spherical NPs have been provided [1]. The section continues by explaining the particular case of Mie theory, Quasistatic approximation, that provides a solution for modeling the optical response of spherical and ellipsoid NPs with sizes much smaller than the incident light wavelength [1, 81]. In the last part of this section, we explain the Multi-layered Mie theory for calculating the optical properties of the Multi-layered spherical NPs [82].

The LSPR properties of the metallic NPs strongly depends on the shape and configuration of the NPs [1, 9, 64, 65, 83]. However, there is no analytical solution to model the optical response of the non-spherical nanoparticles or multimer structures. In this dissertation, the discrete dipole approximation [1, 9, 64, 65, 83–88]. has been used to compute the optical properties of the monomer or multimer nanostructures with arbitrary shape and configuration. The third section of this chapter describes the DDA and all of the techniques that have been applied in this work to reduce the computational time and memory. At the end of this chapter, we provided some examples of the optical properties of the plasmonic NPs that can be obtained using DDA.

2.2. Dielectric Function

2.2.1. Drude's Model

For calculating the plasmonic properties of the metallic NPs, at first step, it is required to calculate their corresponding dielectric function. The classical Drude Model is a well known theoretical model to describe the dielectric function of bulk metals [75]. In this classical model, the metal is made of free electrons moving in a positive ions background [75]. According to this theory, the electric response of the metals is dispersive and varying by changing the frequency of the incident light. The dielectric function of the bulk metals in the Drude Model is given by [75]

$$\varepsilon_{\mathrm{Bulk}}(\omega) = \varepsilon_{\mathrm{IB}}(\omega) - \frac{\omega_{\mathrm{p}}^2}{\omega^2 + \mathrm{i}\Gamma_0\omega} \tag{2.1}$$

where ω, Γ_0 and ω_{p} are representing the frequency of the incident light, scattering frequency of the electrons in bulk metal and the plasma frequency, respectively. In the above equation, $\varepsilon_{\mathrm{IB}}$ demonstrates the contribution of the interband transitions in the electric response of the metal to the incident light that is due to transferring the electrons from the valence d-band to the conduction band.

2.2.2. Modified Drude Model for Nanoparticles

In metallic nanostructures, the mean free path of conduction electrons is less than bulk material due to the interaction of the free electrons with the surface of the nanoparticles [9, 75, 77, 83]. The mean free path of the NPs reduces more by further decreasing their size, which leads to the additional increasing of the collision frequency and more damping of the surface plasmons [9, 75, 77, 83]. Thus, to fully describe the electric response of the metallic NPs, a modification term, which inversely proportional to the size of the particles, needs to be considered in their dielectric function. By adding this size effect, the electric permittivity of nano-sized metallic particles can be described by modifying the Drude model as following [75, 83]

$$\varepsilon_{\mathrm{NP}}(\omega, \mathrm{r}_{\mathrm{eff}}) = \varepsilon_{\mathrm{bulk}}(\omega) + \frac{\omega_{\mathrm{p}}^2}{\omega^2 + \mathrm{i}\Gamma_0\omega} - \frac{\omega_{\mathrm{p}}^2}{\omega^2 + \mathrm{i}\Gamma(\mathrm{r}_{\mathrm{eff}})\omega} \tag{2.2}$$

where $\mathrm{r}_{\mathrm{eff}}$ is the effective radius which is defined as a radius the sphere has a volume equal to that of the nanoparticle. $\Gamma(\mathrm{r}_{\mathrm{eff}})$ represents the modified damping frequency which is given by [75, 77, 83]

$$\Gamma(r_{eff}) = \Gamma_0 + A\frac{V_f}{r_{eff}} \tag{2.3}$$

where V_f is Fermi velocity, and A is an empirical parameter that has been used for the matching of calculated damping with the experimental one.

One common way to stabilize the small-sized NPs in a solution in order to prevent the amalgamation of them is conjugating them with chemical ligands [76, 77, 89–93]. However, integrating the NPs with the chemical ligands will reduce free electron density on the conduction band of the nanoparticles due to a chemical interaction between the ligand and the metallic NPs. Accordingly, it reduces plasma frequency ($\omega_P = \sqrt{\frac{ne^2}{m\varepsilon_0}}$) and damps the plasmon spectra [76, 77, 89–93]. It should be noted that the conductivity of the surface layer of the NPs will reduce more in comparison to the core region due to the direct interaction between this layer and the chemical ligands. To consider these effects, the electron density of the core region and the skin layer of the NPs need to be modified by multiplying them to a factor of g^2_{core} and g^2_{skin}, respectively [76, 77]. By applying these factors in Eq. (2.3), the revised dielectric function of the ligand- conjugated metallic NPs can be expressed as below [76, 77]

$$\varepsilon_{CNP}(\omega, r) = \varepsilon_{bulk}(\omega) + \frac{\omega_p^2}{\omega^2 + i\Gamma_0\omega} - \frac{g^2\omega_p^2}{\omega^2 + i\Gamma(r_{eff})\omega} \tag{2.4}$$

where g^2 is free electrons density correction factor and is g^2_{core} and g^2_{skin} in the core and the skin region, respectively.

2.2.3. Dielectric Function of the Quantum-Sized Nanoparticles

By further reducing the size of the NPs the modified classical Drude model is no longer valid for describing the electric response of the metallic NPs to the incident light [78, 79, 94]. For the NPs with an effective diameter below 10 nm the conduction band is not continuous anymore [78, 79, 94]. The inter-level discretization energy for these small-sized NPs is more than the thermal energy which increases more by further reducing the size of the particles [78, 79, 94]. Thus, to calculate the electric permittivity of these quantum-sized NPs all allowed inter-level transitions should be taken into account. By considering these effects, the dielectric function of the ultra-small NPs is given by [78, 79]

$$\varepsilon_{QNP}(\omega) = \varepsilon_{IB}(\omega) + \omega_p^2 \sum_i \sum_f \frac{S_{if}}{(\omega_{if}^2 - \omega^2 - i\Gamma(r_{eff})\omega)} \quad (2.5)$$

where summations are taken on the all allowed initial (i) and final (f) states. S_{if} and ω_{if} are representing the weight factor of the transition (or oscillator strength) and the transition frequency from the initial state i to final state f, respectively. The weight factor of allowed inter-level transitions can be calculated as [78, 79]

$$S_{if} = \frac{2m\omega_{if}\hbar}{N} |\langle i|z|f\rangle|^2 \quad (2.6)$$

where m is mass of the electron, and N is the number of the conduction electrons in the NPs.

For the ligand-conjugated quantum-sized metallic NPs the modified electric permittivity can be expressed as below

$$\varepsilon_{QNP}(\omega) = \varepsilon_{IB} + g^2\omega_p^2 \sum_i \sum_f \frac{S_{if}}{(\omega_{if}^2 - \omega^2 - i\Gamma(r_{eff})\omega)} \quad (2.7)$$

As already mentioned, the g^2 is representing the conductivity correction factor for the core or surface region of the NPs.

2.3. Mie Theory

Mie theory presents the exact solution for the light scattering, and absorption by a spherical shape target that is inserted in a homogeneous and isotropic medium and illuminated by a plane wave.[1, 80] The electric and magnetic fields inside and outside of the nanoparticles must satisfy the Maxwell equations

$$\nabla.(\varepsilon E) = 0 \quad (2.8.a)$$

$$\nabla.H = 0 \quad (2.8.b)$$

$$\nabla \times E = i\omega\mu H \quad (2.8.c)$$

$$\nabla \times H = -i\omega\varepsilon E \quad (2.8.d)$$

where ε and μ are continuous at all points and exp(-iωt) time dependence is assumed for both E and H field. In addition, a time-harmonic electromagnetic field in a homogeneous, linear and isotropic medium must satisfy the wave equations

$$\nabla^2 E + k^2 E = 0 \tag{2.9.a}$$

$$\nabla^2 H + k^2 H = 0 \tag{2.9.b}$$

where k is wavevector. By solving the above-mentioned equations the scattering field coefficients outside of a sphere with a refractive index of n_s and radius of r are given by [1]

$$a_n = \frac{\mu m^2 j_n(mx)[x j_n(x)]' - \mu_s j_n(x)[mx j_n(mx)]'}{\mu m^2 j_n(mx)\left[x h_n^{(1)}(x)\right]' - \mu_s h_n^{(1)}(x)[mx j_n(mx)]'} \tag{2.10.a}$$

$$b_n = \frac{\mu j_n(mx)[x j_n(x)]' - \mu_s j_n(x)[mx j_n(mx)]'}{\mu j_n(mx)\left[x h_n^{(1)}(x)\right]' - \mu_s h_n^{(1)}(x)[mx j_n(mx)]'} \tag{2.10.b}$$

and the electric field coefficients inside the sphere are [1]

$$c_n = \frac{\mu_s j_n(x)\left[x h_n^{(1)}(x)\right]' - \mu_s h_n^{(1)}(x)[x j_n(x)]'}{\mu_s j_n(mx)\left[x h_n^{(1)}(x)\right]' - \mu h_n^{(1)}(x)[mx j_n(mx)]'} \tag{2.11.a}$$

$$d_n = \frac{\mu_s m j_n(x)\left[x h_n^{(1)}(x)\right]' - \mu_s m h_n^{(1)}(x)[x j_n(x)]'}{\mu m^2 j_n(mx)\left[x h_n^{(1)}(x)\right]' - \mu_s h_n^{(1)}(x)[mx j_n(mx)]'} \tag{2.11.b}$$

where $m = \frac{|n_s|}{|n_m|}$, $x = k_m r = \frac{2\pi n_m r}{\lambda}$, and μ and μ_s represent the permeability of the surrounding medium and the sphere, respectively. n_s, n_m and k_m are the refractive index of the target particle, the refractive index of the surrounding medium, and the wavevector of the incident light in the medium, respectively. In the above equations, the $j_n(\rho)$ and $h_n^{(1)}(\rho)$ are the spherical Bessel function and the spherical Hankel function, respectively [1, 95]. It is worth mentioning that full derivation of the coefficients presented in equations 2.10 and 2.11 can be found elsewhere [1].

Important optical properties such as scattering, absorbing, and extinction cross-sections of the spherical particle can be calculated using the scattered field coefficients, which are provided in Eq. 2.10. These cross-sections can be expressed as follows [1]

$$C_{scat} = \frac{2\pi}{k_m^2} \sum_{n=1}^{\infty} (2n+1)\left(|a_n|^2 + |b_n|^2\right) \tag{2.12.a}$$

$$C_{ext} = \frac{2\pi}{k_m^2}\sum_{n=1}^{\infty}(2n+1)\,\mathrm{Re}(a_n + b_n) \qquad (2.12.b)$$

$$C_{abs} = C_{ext} - C_{scat} \qquad (2.12.c)$$

where C_{scat} , C_{ext} and C_{abs} are representing the scattering, extinction and absorption cross-sections, respectively. n=1, 2, 3, … corresponds to dipole, quadrupole, octopole modes, … . By dividing the optical cross-sections (Eq.2.12) to the geometrical cross-section of spherical nanoparticles the corresponding efficiency factors or Q-factor of the particle are given by

$$Q_{scat} = \frac{C_{scat}}{\pi r^2} \qquad (2.13.a)$$

$$Q_{ext} = \frac{C_{ext}}{\pi r^2} \qquad (2.13.b)$$

$$Q_{abs} = \frac{C_{abs}}{\pi r^2} \qquad (2.13.c)$$

where Q_{scat}, Q_{ext} and Q_{abs} are the scattering, extinction and absorption efficiency factors, respectively. Figure 2.1 shows an example of the extinction, absorption and scattering efficiencies of a spherical gold nanoparticle which have been calculated using Mie theory.

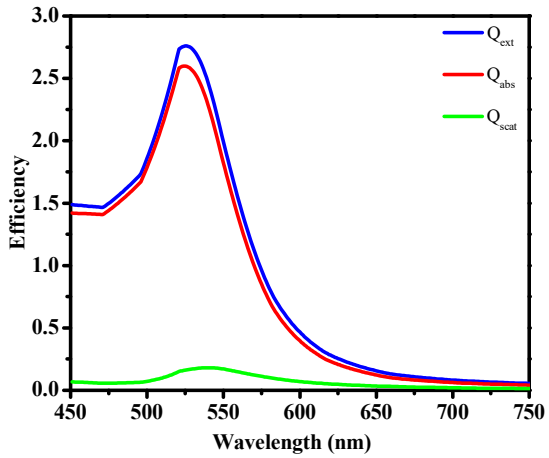

Figure 2.1. Extinction, absorption and scattering efficiencies of a spherical gold nanoparticle with diameter of 40 nm that is dispersed in water (n_b = 1.34).

The expansion of the electric and magnetic fields inside the particle and the scattered fields by the spherical target are other important optical properties that can be obtained by the Mie coefficients provided in the equations 2.10 and 2.11. These fields can be expressed as [1]

$$E_{in} = \sum_{n=1}^{\infty} E_n \left(c_n M_{o1n}^{(1)} - i d_n N_{e1n}^{(1)} \right) \tag{2.14.a}$$

$$H_{in} = \frac{-k_s}{\omega \mu_s} \sum_{n=1}^{\infty} E_n \left(d_n M_{e1n}^{(1)} + i c_n N_{o1n}^{(1)} \right) \tag{2.14.b}$$

$$E_S = \sum_{n=1}^{\infty} E_n \left(i a_n N_{e1n}^{(3)} - b_n M_{o1n}^{(3)} \right) \tag{2.14.c}$$

$$H_s = \frac{k}{\omega \mu} \sum_{n=1}^{\infty} E_n \left(i b_n N_{o1n}^{(3)} + a_n M_{e1n}^{(3)} \right) \tag{2.14.d}$$

where $E_n = i^n E_0 (2n+1)/n(n+1)$, and k_s is the wavevector inside the sphere.The $M_{o1n}^{(q)}$, $N_{o1n}^{(q)}$, $M_{e1n}^{(q)}$ and $N_{e1n}^{(q)}$ are the vector spherical harmonics generated by the scalar wave equations in spherical polar coordinates [1]

$$M_{emn}^{(q)} = \frac{-m}{\sin\theta} \sin m\varphi \, P_n^m(\cos\theta) Z_n^{(q)}(\rho) \hat{e}_\theta - \cos m\varphi \frac{dP_n^m(\cos\theta)}{d\theta} Z_n^{(q)}(\rho) \hat{e}_\varphi \tag{2.15.a}$$

$$M_{omn}^{(q)} = \frac{m}{\sin\theta} \cos m\varphi \, P_n^m(\cos\theta) Z_n^{(q)}(\rho) \hat{e}_\theta - \sin m\varphi \frac{dP_n^m(\cos\theta)}{d\theta} Z_n^{(q)}(\rho) \hat{e}_\varphi \tag{2.15.b}$$

$$N_{emn}^{(q)} = \frac{Z_n^{(q)}(\rho)}{\rho} \cos m\varphi \, n(n+1) P_n^m(\cos\theta) \hat{e}_r + \cos m\varphi \frac{dP_n^m(\cos\theta)}{d\theta} \frac{1}{\rho} \frac{d}{d\rho} \left[\rho Z_n^{(q)}(\rho) \right] \hat{e}_\theta - m \sin m\varphi \frac{P_n^m(\cos\theta)}{\sin\theta} \frac{1}{\rho} \frac{d}{d\rho} \left[\rho Z_n^{(q)}(\rho) \right] \hat{e}_\varphi \tag{2.15.c}$$

$$N_{omn}^{(q)} = \frac{Z_n^{(q)}(\rho)}{\rho} \sin m\varphi \, n(n+1) P_n^m(\cos\theta) \hat{e}_r + \sin m\varphi \frac{dP_n^m(\cos\theta)}{d\theta} \frac{1}{\rho} \frac{d}{d\rho} \left[\rho Z_n^{(q)}(\rho) \right] \hat{e}_\theta + m \cos m\varphi \frac{P_n^m(\cos\theta)}{\sin\theta} \frac{1}{\rho} \frac{d}{d\rho} \left[\rho Z_n^{(q)}(\rho) \right] \hat{e}_\varphi \tag{2.15.d}$$

where $\rho = kr$ and is a dimensionless variable. In the above equations, the q=1,3 where $Z_n^{(1)}(\rho)$ and $Z_n^{(3)}(\rho)$ are the spherical Bessel function (j_n) and the spherical Hankel function ($h_n^{(1)}$), respectively [1].

The total electric and magnetic field around the NP is the superposition of the incident light electric field and scattered field by particle

$$\vec{E}_t = \vec{E}_i + \vec{E}_s \qquad (2.16.a)$$

$$\vec{H}_t = \vec{H}_i + \vec{H}_s \qquad (2.16.b)$$

where the incident light and scattered light electric field can be expressed as below

$$E_i = E_0 \exp(ik.r - i\omega t) \qquad (2.17.a)$$

$$H_i = H_0 \exp(ik.r - i\omega t) \qquad (2.17.b)$$

As an example, the electric field enhancement of a 40 nm spherical gold nanoparticle that is obtained using Mie theory is provided in Figure 2.2.

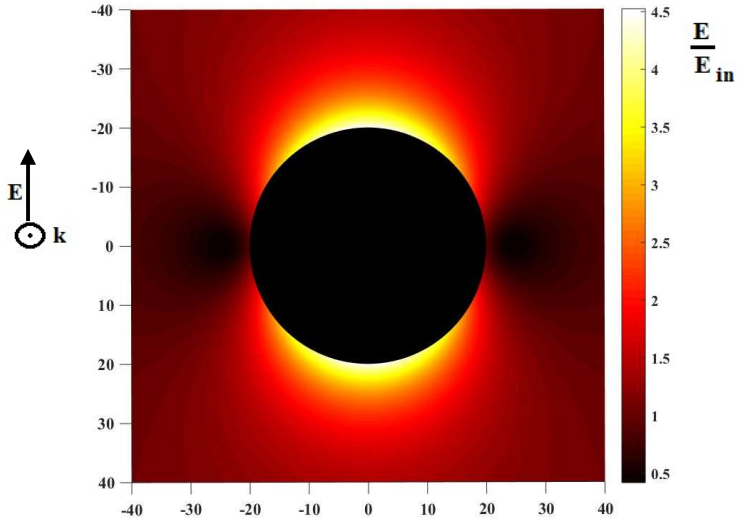

Figure 2.2. Electric field enhancement of a spherical gold nanoparticle with a diameter of 40 nm in vacuum.

2.4. Quasi-Static Approximation

When the size of the NP is very small in comparison to the incident light wavelength, the phase shift (kr) inside the Np is negligible. In this limit, which is called Quasi-static approximation regime, the electric field and polarization inside the NP are almost constant [1, 81]. Since the contribution of the higher-order modes is negligible in this regime, the scattering, absorption and extinction cross-sections of the spherical NPs can be calculated by considering only the dipole

term in the Mie coefficients [1, 81]. Interestingly, in this regime an analytical solution, named Mie-Gans solution, is also available for calculating optical properties of the spheroidal particles [1, 81, 96]. The scattering, absorption and extinction cross-sections of the spherical and spheroidal NPs in the Quasi-static approximation can be computed as below [1, 81]

$$C_{scat} = \frac{8\pi}{3} k_m^4 |\alpha|^2 \quad (2.18.a)$$

$$C_{abs} = 4\pi k_m \mathrm{Im}(\alpha) \quad (2.18.b)$$

$$C_{ext} = C_{scat} + C_{abs} \quad (2.18.c)$$

where α is the polarizability of the particle.The polarizability of the small spherical and spheroidal NPs in each direction in the Quasi-static approximation can be expressed using the Clausius - Mossotti [1, 81, 96]

$$\alpha_i = \frac{V}{4\pi}\left(L_i + \frac{1}{\varepsilon_r - 1}\right)^{-1}, \quad i = 1, 2, 3 \quad (2.19)$$

where V and ε_r are the volume and effective dielectric function (ratio of the dielectric function of the NP to the surrounding medium). L_i is the depolarization factor which depends on the shape and structure of the NPs and always fulfills the sum rule $L_1+L_2+L_3= 1$ [1, 96]. For a prolate spheroidal particle (c > a = b) the depolarization factor along different semi-axises can be calculated as below [1, 96]

$$L_1 = L_2 = \frac{1}{2}(1 - L_3) \quad (2.20.a)$$

$$L_3 = \frac{(1 - f^2)}{f^2}\left(-1 + \frac{1}{2f}\ln\frac{1 + f}{1 - f}\right) \quad (2.20.b)$$

and for oblate (c < a = b) we have

$$L_1 = L_2 = \frac{1}{2}(1 - L_3) \quad (2.21.a)$$

$$L_3 = \frac{(1 + f^2)}{f^2}\left(1 - \frac{1}{f}\tan^{-1}(f)\right) \quad (2.21.b)$$

where $f = \left|\left(\frac{a^2}{c^2}\right) - 1\right|$.

For a spherical particle $L_1 = L_2 = L_3 = \frac{1}{3}$ [1, 96].

After calculating L_i and α_i in different directions, the polarizability α can be expressed as $\alpha = \sum_{i=1}^{3} \alpha_i \hat{e}_i$ ($\hat{e}$ is the polarization direction of the incident light).

2.5. Multi-Layered Mie Theory

Electromagnetic (EM) radiation scattering by multi-layered spheres has attracted much research attention due to their application in several studies [1, 10, 27, 76, 77]. As an example, Peng et. al modeled the optical properties of the ligand conjugated silver NPs by considering three-layered Mie theory [76]. In this study, we used the recursive algorithm developed a few years ago by Yang that overcomes most of the numerical problems that exist in the previous models [82]. In this model, as demonstrated in Figure 2.3, the multilayered sphere composed of L layers which each one is characterized by a size parameter $X_l = k_m r_l$ and relative refractive index of $m_l = n_l/n_m$, l=1, 2, …, L , where k_m, r_l, n_l and n_m are the wave vector of the incident light in the surrounding medium, the outer radius of the l-th layer, the refractive index of l-th layer and the surrounding medium, respectively.

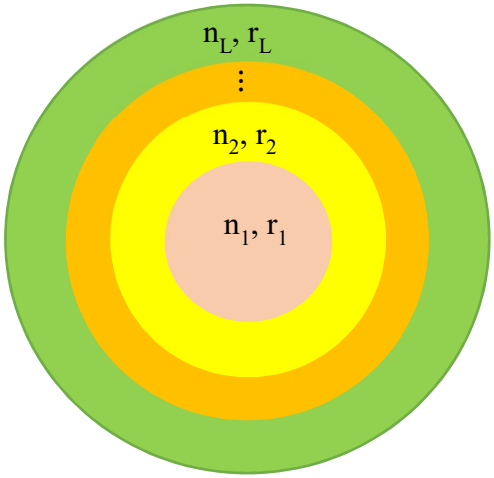

Figure 2.3. Schematic of a multilayered spherical particle.

It is assumed these concentric spheres are illuminated by an x-polarized electric field $E_i = E_0 \exp(ik_m r\cos(\theta))$ with time-harmonic factor $\exp(-i\omega t)$. The total space of this model is divided into two different regions: inside and outside of the sphere. Similar to Mie theory for a single sphere, inward and outward electric and magnetic fields of the *l*-th layer of the multi-layered spherical particle can be expressed using Eq. 2.14. The total E and H of each layer can be computed by superposition of the inward and outward fields in that layer and for the *l*-th layer are given by:

$$E^l = \sum_{n=1}^{\infty} E_n \left[c_n^{(l)} M_{o1n}^{(1)} - i d_n^{(l)} N_{e1n}^{(1)} + i a_n^{(l)} N_{e1n}^{(3)} - b_n^{(l)} M_{o1n}^{(3)} \right] \quad (2.22.a)$$

$$H^l = \frac{-k_l}{\omega \mu} \sum_{n=1}^{\infty} E_n \left[d_n^{(l)} M_{e1n}^{(1)} + i c_n^{(l)} N_{o1n}^{(1)} - i b_n^{(l)} N_{o1n}^{(3)} - a_n^{(l)} M_{e1n}^{(3)} \right] \quad (2.22.b)$$

where $E_n = i^n E_0 (2n+1)/n(n+1)$ and $M_{o1n}^{(q)}$, $N_{o1n}^{(q)}$, $M_{e1n}^{(q)}$ and $N_{e1n}^{(q)}$ are the vector spherical harmonics which have been provided in Eq. 2.15. However, each layer has its own specific Mie coefficients which can be calculated by applying boundary conditions at each layer. By applying boundary conditions, it can be inferred that the expansion coefficients $a_n^{(1)} = b_n^{(1)} = 1$, and $c_n^{(L+1)} = d_n^{(L+1)} = 1$ [82]. It should be noted that the scattering coefficients of this multi-layered nanostructure are the expansion coefficients of the outward field in the outside region of the sphere which can be expressed by [82]

$$a_n = a_n^{L+1} = \frac{\left[\frac{H_n^a(Z_L)}{m_L} + \frac{n}{X_L}\right] \psi_n(X_L) - \psi_{n-1}(X_L)}{\left[\frac{H_n^a(Z_L)}{m_L} + \frac{n}{X_L}\right] \xi_n(X_L) - \xi_{n-1}(X_L)} \quad (2.23.a)$$

$$b_n = b_n^{L+1} = \frac{\left[\frac{H_n^b(Z_L)}{m_L} + \frac{n}{X_L}\right] \psi_n(X_L) - \psi_{n-1}(X_L)}{\left[\frac{H_n^b(Z_L)}{m_L} + \frac{n}{X_L}\right] \xi_n(X_L) - \xi_{n-1}(X_L)} \quad (2.23.b)$$

where $Z_L = n_L X_L$ and $X_L = k_m r_L$. ψ_n and ξ_n are Riccati-Bessel functions:

$$\psi_n(X_L) = X_L j_n(X_L) \quad (2.24.a)$$

$$\xi_n(X_L) = X_L h_n(X_L) \quad (2.24.b)$$

The explicit expressions for H_n^a and H_n^b can be found elsewhere [82]. By calculating Mie coefficients of the multi-layered sphere, the scattering, extinction, and absorbing cross-sections and their corresponding efficiency factors can be obtained using Eq. 2.12 and Eq. 2. 13, respectively. As an example, the extinction, absorption and scattering efficiencies of a two-layers spherical gold nanoparticle have been computed using Multi-layered Mie theory and the spectra is presented in Figure 2.4. In our simulation, the core region is chosen to be vacuum and the thickness of the gold layer has set to be t = 0.4 r where r is the radius of the nanoparticle.

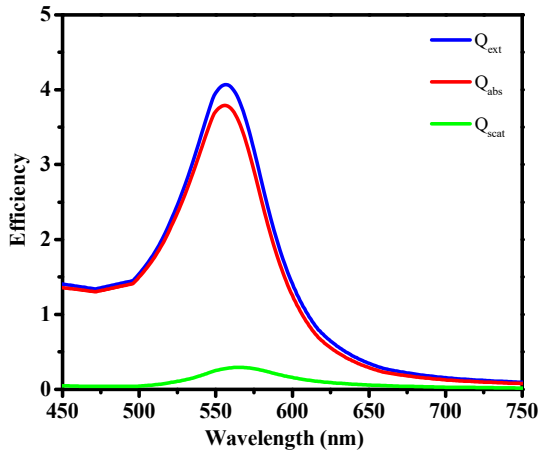

Figure 2.4. Extinction, absorption and scattering efficiencies of a two-layered gold nanosphere. The core region is vacuum, and the total radius and shell thickness of the particles are 20 nm and 8 nm, respectively.

2.6. Discrete Dipole Approximation

Several theoretical methods were used by researchers to describe the optical properties of the arbitrary shaped plasmonic NPs [1, 84–86, 97–100]. Among them, the discrete dipole approximation (DDA) has been widely used due to its computational simplifications in comparison to other electromagnetic methods [84–88]. DDA is a powerful and general technique to calculate scattering and absorption of the arbitrarily shaped particles. This electromagnetic method was initially proposed by Purcell and Pennypacker to calculate light scattering from grains in the interstellar medium [85]. In the last 25 years, DDA has been applied to calculate optical properties of the non-spherical plasmonic nanoparticle [9, 64, 65, 83] such as scattering [1, 9, 64, 65, 83], absorption [1, 9, 64, 65, 83], extinction [1, 9, 64, 65, 83], localized plasmon resonance sensitivity [27, 60, 61, 101, 102], and electric field enhancement around them [65, 103].

In DDA, the particle is discretized into N cubic array of polarizable elements with the almost constant electric field and polarization inside each nanocube. The optical response of each element (dipole) is the summation of the electric fields of the incident light and its N-1 neighboring elements [84–88].

The primary objective in DDA is to compute the polarization of each dipole (nanocube) in order to calculate the optical properties of the NPs, which includes solving 3N linear equations [87, 104–112]. Calculating 3N elements of the polarization vector using direct method is computationally very expensive, and computing time and memory increases dramatically with increasing N [87, 104–112]. The aforementioned problems have been addressed by combining complex conjugate gradient (CCG) method and Fast Fourier Transform technique (FFT) in literature, which reduced the computational time and required memory from the order of N^2 to Nlog(N) [87, 104–112]. However, in other electromagnetic scattering problems, biconjugate gradient (BCG) technique has been used as an iterative method, which is three- to six- times faster than the corresponding CCG [105, 113].

Several attempts have been made to increase the performance of the DDA [104, 106, 108–112, 114–118]. One of the pioneering works was carried out by Drain and Flatau, who popularized the DDA by releasing an open-source package named DDASCAT that was written in FORTRAN [104, 106]. By applying 3D FFT with a number of iterative methods such as BCG and CCG, they significantly reduced the required time and computational memory to calculate the polarizability of each element [104, 106]. In another work, Mc Donald et al. developed an open-source package named OpenDDA to optimize DDA by developing new Discrete Fourier Transform (DFT) kernel which performs 3-D DFTs as assemble of 1-D DFTs [108]. They were able to reduce over 80% the required memory to calculate the polarizability vector of the particles. Other works modified the DDA by adding capabilities to simulate the light scattering of the particles on a planar surface by developing packages written in FORTRAN [109, 110]. However, these packages were not open source. In another study, Loke et al. released an open-source MATLAB package to calculate the light scattering of the particles in free space and on a planar surface [111]. Despite its user-friendliness, the toolbox suffers from a lack of optimized methods like BCG and FFT, which made it computationally very expensive. In another attempt, to calculate scattering of the ice particles using DDA, Huntemann et al. performed their simulation on GPUs by implementing Amsterdam

DDA (ADDA) program package in open computing language (OpenCL), and calculated the scattering of the ice particles in GPUs,which was 5 times and 15 times faster than CPU in double and single precision, respectively [112].

Although the aforementioned works have made significant progress in decreasing the computational cost and required memory but no MATLAB package with accelerated methods to calculate DDA is available. The aim of this section is to provide a conceptual theoretical framework using a MATLAB package for all the steps of DDA and link them to the corresponding computational functions. All of the packages are provided in the appendices. To significantly reduce the computational time and memory in DDA, we applied FFT and BCG on the corresponding functions in MATLAB, which have not implemented in previous MATLAB packages [111, 119], inspired by Drain and Flatau [104, 106]. Also, GPU function in MATLAB has been used in our problem to significantly reduce the time of the calculation in comparison to CPU. Functions for creating NPs with cubic mesh, obtaining coordinates of dipoles, calculating extinction, scattering and absorption efficiencies of the monomeric and dimeric structures for four different shapes of plasmonic NPs, electric field enhancement in monomeric, and hot spots in dimeric structures are provided in the packages (see the appendices).

The remaining part of chapter 2 proceeds as follows: 1) Explaining the conceptual basis of the DDA, 2) Discussing BCG as an iterative method, 3) Outlining the Toeplitz matrices and the way to convert them to the corresponding circulant matrices, 4) Converting the tensor blocks of the interaction matrix in DDA to Toeplitz structures in order to accelerate their multiplication to the polarization vectors by transforming them to the circulant structures and 5) applying GPU to accelerate our problem more. Calculation of the optical cross-section efficiencies of the different shaped NPs, electric field enhancement around single NPs and the hot spot in dimeric structures along with their corresponding MATLAB scripts have been explained in the end.

2.6.1. Discrete Dipole Approximation Formalism

The DDA is a general and effective electromagnetic technique to compute the optical properties of monomeric or multimeric structures with arbitrary shapes and compositions [84, 85, 88, 104, 120]. As demonstrated in Figure 2.5, in this method the particle is divided into N nanocubes with size much smaller than the incident wavelength. The size of each cube should be

small enough to represent the particle shape satisfactory and to obtain a negligible phase shift inside each [85, 104]. To fulfill the aforementioned criteria we have

$$kd = \frac{2\pi\, n(\omega)}{\lambda} d \ll 1 \tag{2.25}$$

where k, d, and λ are wavevector, length of each cube, and wavelength of the incident light, respectively. The n(ω) represents the refractive index of the NPs which is dispersive and changing with the frequency of the incident light.

The corresponding functions to calculate the position of each dipole and obtain the shape of an arbitrary NP are provided in the appendix A.

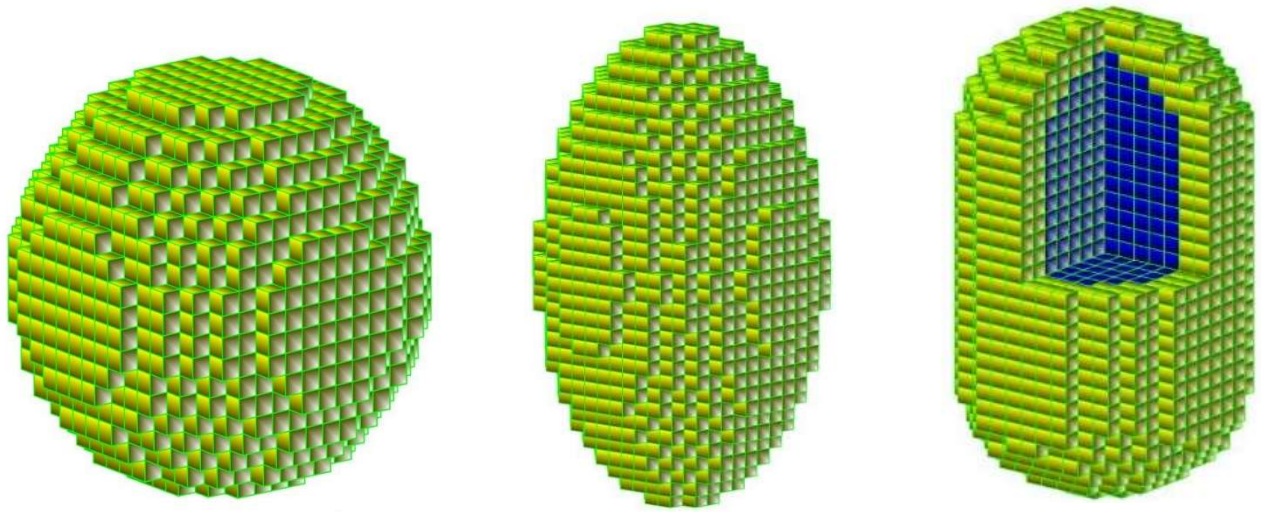

Figure 2.5. Schematic of (a) spherical NP, (b) ellipsoid NP, and (c) rod shape nanoshell, which are made of N=10648, N = 10422, and N = 8192 dipoles, respectively.

Each cube in NP is representing a point dipole that interacts with the electric fields of the incident light and N-1 other dipoles [85]. The polarization of each dipole can be expressed by [85, 87]

$$P_i = \alpha_i E_{loc}(r_i) \tag{2.26}$$

where α_i and $E_{loc}(r_i)$ are the polarizability and the total electric field at location r_i, respectively. In an anisotropic particle, the polarizability of each cube is changing with varying the direction. This

can be explained by the fact that the light passing through an anisotropic material will experience different refractive indices in different directions inside the material. However, the metal and the medium that have been used in this work are isotropic, and their corresponding polarizabilities are direction independent. Lattice dispersion relation polarizability is the most common used α_i in literature [104, 111] and is given by [121]

$$\alpha_i^{LDR} = \frac{\frac{3d^3}{4\pi}\left(\frac{\varepsilon_i - 1}{\varepsilon_i + 2}\right)}{1 + \frac{3d^3(\varepsilon_i - 1)}{4\pi d^3(\varepsilon_i + 2)}[(b_1 + m^2 b_2 + m^2 b_3 S)(kd)^2 - \frac{2}{3}i(kd)^3]} \tag{2.27.a}$$

$$b_1 = -1.891531, b_2 = 0.1648469, b_3 = -1.7700004 \tag{2.27.b}$$

$$S = \sum_{j=1}^{3}\left(\hat{a}_j \hat{e}_j\right)^2 \tag{2.27.c}$$

where $\hat{a}$ and $\hat{e}$ are unit vectors that are representing the direction and polarization of the incident light, respectively. The m-file "Polarizability.m" has been provided in the appendix D.5 to calculate the polarizability of each dipole in the NP.

As can be understood from Eq. 2.26, to compute the polarization of each dipole we need to obtain the total electric field at its position. Each dipole or nanocube inside the particle interacts with the incident light field and the electric field of N-1 neighboring dipoles [104]. Thus, the total electric field interacting with a dipole located at position r_i is given by

$$E_{loc}(r_i) = E_{inc,\,i} + E_{other\ dipoles,\,i} = E_0 \exp(ik.\,r_i - i\omega t) - \sum_{j \neq i}^{N} A_{ij} P_j \tag{2.28}$$

where N is the number of the dipoles, and A_{ij} is a complex matrix which represents the interaction between a receiving dipole at r_i and the radiating dipole at r_j, and P_j is the polarization of radiating dipole at r_j. A_{ij} can be expressed as following [104]

$$A_{ij} = \frac{\exp(ikr_{ij})}{r_{ij}}\left[k^2\left(\hat{r}_{ij}\hat{r}_{ij} - \mathbf{1}_3\right) + \frac{(ikr_{ij} - 1)}{r_{ij}^2}\left(3\hat{r}_{ij}\hat{r}_{ij} - \mathbf{1}_3\right)\right] \tag{2.29}$$

In Eq. 2. 29, the r_{ij} is the distance from the dipole i to j, $\hat{r}_{ij}$ is a unit vector in the direction from the dipole i to dipole j, and $\mathbf{1}_3$ represents the 3×3 identity matrix. The diagonal elements of the interaction matrix are defined as $A_{ii} = \alpha_i^{-1}$ which leads to a simplified format of Eq. 2.28 [104]

$$\sum_{i=1}^{N} A_{ij} P_j = E_{inc,\,i} \tag{2.30}$$

The above equation can be shown in a matrix-vector format as following

$$\begin{bmatrix} A_{xx} & A_{xy} & A_{xz} \\ A_{yx} & A_{yy} & A_{yz} \\ A_{zx} & A_{zy} & A_{zz} \end{bmatrix} \begin{bmatrix} P_x \\ P_y \\ P_z \end{bmatrix} = \begin{bmatrix} E_{inc,x} \\ E_{inc,y} \\ E_{inc,z} \end{bmatrix} \tag{2.31}$$

where A_{nm} (n and m = x,y or z) is an N×N matrix that represents the interaction matrix between n-th and m-th components of the dipoles. P_n and $E_{inc,\,n}$ are N×1 arrays representing the n-th components of the polarization vector and the incident electric field, respectively. Since the nine blocks of the interaction matrix are symmetric regarding changing the indices (refer to Eq. 2.29) we have

$$A_{xy} = A_{yx} \tag{2.32.a}$$

$$A_{xz} = A_{zx} \tag{2.32.b}$$

$$A_{yz} = A_{zy} \tag{2.32.c}$$

The aforementioned property reduces the computational burden of the interaction matrix from 9 tensor blocks (A_{xx}, A_{xy}, , A_{xz}, A_{yx}, A_{yy}, A_{yz}, A_{zx}, A_{zy} and A_{zz}) to 6 (A_{xx}, A_{xy}, A_{xz}, A_{yy}, A_{yz} and A_{zz}). The simplified format of Eq. (2.30) can be expressed as following

$$\begin{bmatrix} A_{xx} & A_{xy} & A_{xz} \\ A_{xy} & A_{yy} & A_{yz} \\ A_{xz} & A_{yz} & A_{zz} \end{bmatrix} \begin{bmatrix} P_x \\ P_y \\ P_z \end{bmatrix} = \begin{bmatrix} E_{inc,x} \\ E_{inc,y} \\ E_{inc,z} \end{bmatrix} \tag{2.33}$$

The primary objective of the DDA is to solve Eq. 2.33 to compute the polarization of each dipole and consequently calculate the optical properties of the NPs. By calculating the polarization of each dipole inside NP, the optical properties of NP structures such as absorption, scattering and extinction cross-sections, dipole force, Poynting vector, filed enhancement around a single NP, and hot spot in multimeric structures can be computed. In the remaining part of this chapter, we

focus on how to implement the accelerative techniques such as BCG, 1D FFT, and GPU to solve Eq. 2.33. In the following subsection, we provide a short review of the iterative technique (BCG) that has been applied to solve Eq. 2.33.

2.6.2. Computational Techniques

2.6.2.1. Biconjugate Gradient

As already mentioned in this chapter, using the direct method to solve the Eq. 2.33 is computationally very expensive. However, it has been demonstrated that iterative methods are effective and efficient than the direct method to solve Eq. 2.33 for obtaining the polarization of each dipole inside the particle [87, 104, 105, 113]. Here, we review the BCG method [113] that has been used as an iterative technique in our problem to solve Eq. 2.33. By setting the initial guess of P to zero we have

$$\mathrm{P}_0 = 0 \tag{2.34.a}$$

$$\mathrm{r}_0 = \mathrm{q}_0 = \mathrm{E}_{\mathrm{in}} - \mathrm{AP}_0 \tag{2.34.b}$$

$$\tilde{\mathrm{r}}_0 = \tilde{\mathrm{q}}_0 = \mathrm{r}_0^{*} \tag{2.34.c}$$

$$\mathrm{P}_{k+1} = \mathrm{P}_k + \alpha_k \mathrm{q}_k \tag{2.34.d}$$

$$\mathrm{r}_{k+1} = \mathrm{r}_k - \alpha_k \mathrm{A}\mathrm{q}_k \tag{2.34.e}$$

$$\mathrm{q}_{k+1} = \mathrm{r}_{k+1} + \beta_k \mathrm{q}_k \tag{2.34.f}$$

where A, P, and r_0^{*} are the interaction matrix, the polarization vector and the complex conjugate of r_0, respectively. The α_k and β_k can be calculated as

$$\alpha_k = \frac{\langle \tilde{\mathrm{r}}_k | \mathrm{r}_k \rangle}{\langle \tilde{\mathrm{q}}_k | \mathrm{A}\mathrm{q}_k \rangle} \tag{2.35.a}$$

$$\beta_k = \frac{\langle \tilde{\mathrm{r}}_{k+1} | \mathrm{r}_{k+1} \rangle}{\langle \tilde{\mathrm{r}}_k | \mathrm{r}_k \rangle} \tag{2.35.b}$$

It is worth to mention that the iterative process will be terminated if the error of the residual fulfill the following equation [105, 113]

$$\mathrm{Error} = \frac{|\mathrm{r}_k|}{|\mathrm{E}_{\mathrm{in}}|} \leq 10^{-3} \tag{2.36}$$

The flowchart of the BCG to compute the polarization vector of the dipoles inside the NP in DDA using the iterative process is provided in Figure 2.6.

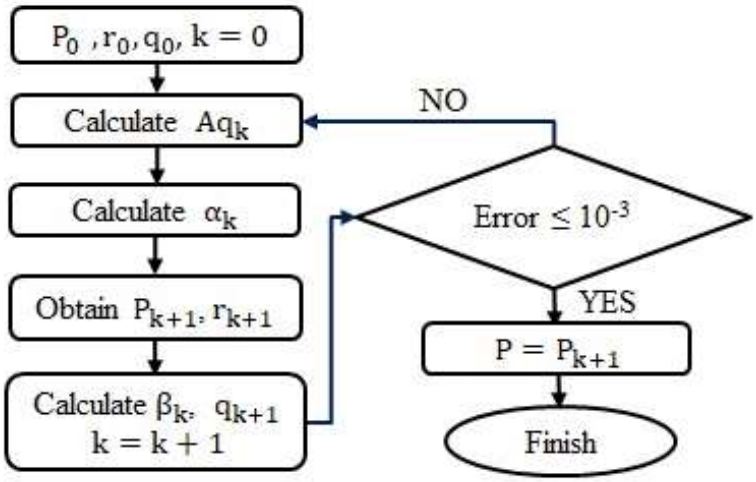

Figure 2. 6. Flowchart of Biconjugate Gradient as an iterative method to find the polarization of each dipole.

It is worth to mention that as the elements of the interaction matrix are complex numbers and each block requires $8(N/1000)^2$ Mb to be stored, where N is the number of the nanocubes or dipoles inside the NP. By increasing N not only the required storage memory increases but also the computational time drastically increases. So, using the iterative method solely is not a particle way to solve the DDA problems of the NPs with a number of the dipoles more than a few thousand.

In the following subsections, first, we explain Toeplitz matrices and how to convert them to circulant ones. Then, we will discuss how to convert the blocks of the interaction matrix to Toeplitz structures and consequently to the circulant ones in order to significantly reduce the computational time and memory by performing matrix-vector multiplication of A.P in Fourier domain.

2.6.2.2. Toeplitz Matrix and the Way to Convert it to a Circulant One

A Toeplitz matrix of order n is made of 2n-1 independent elements where all elements in each diagonal are constant [107, 108]. This kind of matrix can be entirely defined by its first row and the first column as following [107]

$$T^{(n)} = \begin{bmatrix} t_0 & t_{-1} & t_{-2} & \cdots & t_{-(n-1)} \\ t_1 & t_0 & t_{-1} & \ddots & \vdots \\ t_2 & t_1 & t_0 & \ddots & t_{-2} \\ \vdots & \vdots & \vdots & \ddots & t_{-1} \\ t_{n-1} & t_{n-2} & t_{n-3} & \cdots & t_0 \end{bmatrix} \tag{2.38}$$

A typical case of the Toeplitz matrix is a circulant matrix. In this particular case, every row of the matrix is a right cyclic shift of the row above it so that the last element of each row is the same as the first element of the next row [107, 122]. To convert a Toeplitz matrix of order n to a circulant one with the order of 2n-1, first we need to obtain its first column and then each column can be defined by down cyclic of the column in the left side of it. The first column can be obtained in three steps: (1) taking the first column of the Toeplitz matrix, (2) joining the first row to the first column in reverse order, and (3) excluding the last element which is the first element of the first row [107]:

$$c^{(2n-1)} = \begin{bmatrix} t_0 & t_{-1} & t_{-2} & \cdots & t_{-(n-1)} & t_{(n-1)} & t_{(n-2)} & \cdots & t_1 \end{bmatrix}^{\text{transpose}} \tag{2.39}$$

and the full (2n-1)×(2n-1) circulant matrix is

$$C^{(2n-1)} = \begin{bmatrix} t_0 & t_1 & \ddots & t_{(n-1)} & t_{-(n-1)} & \ddots & t_{-2} & t_{-1} \\ t_{-1} & t_0 & \ddots & t_{(n-2)} & t_{(n-1)} & \ddots & t_{-3} & t_{-2} \\ \vdots & \vdots & \ddots & \vdots & \vdots & \ddots & \vdots & \vdots \\ t_{-(n-1)} & t_{-(n-2)} & \ddots & t_0 & t_1 & \ddots & t_{(n-2)} & t_{(n-1)} \\ t_{(n-1)} & t_{-(n-1)} & \ddots & t_{-1} & t_0 & \ddots & t_{(n-3)} & t_{(n-2)} \\ t_{(n-2)} & t_{(n-1)} & \ddots & t_{-2} & t_{-1} & \ddots & t_{(n-4)} & t_{(n-3)} \\ \vdots & \vdots & \ddots & \vdots & \vdots & \ddots & \vdots & \vdots \\ t_1 & t_2 & \ddots & t_{-(n-1)} & t_{-(n-2)} & \ddots & t_{-1} & t_0 \end{bmatrix} \tag{2.40}$$

It should be noted that the circulant matrix can completely be defined by its first column elements which result in significant simplification. Interestingly, a circulant matrix can be diagonalized by the Fourier matrix. This property reduces the computational load of the problems (such as in DDA) that need to compute the multiplication of this kind of the matrices to an arbitrary vector by carrying out the product in the Fourier domain [86, 105, 107, 108, 110, 122].

2.6.2.3. Performing Matrix-Vector Multiplication in DDA using FFT

As mentioned already the Fourier domain can be applied to accelerate matrix-vector multiplication of the matrices that have Toeplitz structures. However, six tensor blocks of the

interaction matrix in DDA have only level-three single element Toeplitz structure for the rectangular particles [88]. The aforementioned matrices can be converted to Toeplitz structures for an arbitrary shaped NP by embedding the NP in the smallest rectangular block in such a way that the new lattice completely encompasses the NP (see Figure 2.7) [86, 107, 108]. It should be noted that the diagonal terms of the dipoles inside the NP are nonzero while the corresponding terms for the dipole outside the NP in the extended lattice are zero (light blue region in Figure 2.7) which are breaking the Toeplitz symmetry [86, 107, 108]. To prevent this effect, the diagonal terms must be negated initially and be added in the end to the resultant of the matrix-vector multiplications (see Appendix D.7) [86, 107, 108].

Figure 2.7. Schematic of embedding a rod shape NP inside a rectangular block.

The extended lattice is divided into N_x, N_y and N_z dipoles in the x, y and z directions, respectively. In other words, the new structure is made of $N_x \times N_y \times N_z$ nanocubes or dipoles. As mentioned already, the first column and first row of a Toeplitz matrix are sufficing to define the whole matrix. Interestingly, the six tensor blocks in the interaction matrix are symmetric respect to changing of the indices, which provide the opportunity to define the whole matrix using their first column. Thus, it is required only to calculate the first column of each tensor block which represents the interaction of the first dipole in the extended lattice with other dipoles. After computing the first column of each tensor block, the first element should be negated by zeroing it and then the column be rearranged in a $N_x \times N_y \times N_z$ three-dimensional matrix (see Appendix D.7) [86, 107, 108].

To perform matrix-vector multiplication using the Fourier domain in DDA it is required first compute FFT of the six 3D tensor blocks, second calculate FFT of the three components of the polarization vector, third perform the element-wise multiplication and finally operate inverse FFT of each. The FFT of the obtained 3D matrices of the first column of the block tensors can be carried out by taking FFT in x, y, and z-direction, consecutively, as following:

1. Take each line of obtained 3D matrices in the x-direction, expand them to the length of $2N_x-1$ by mirroring each in the reverse order and excluding the first element (refer to Eq. 2.39). After expanding each line, compute the FFT of each and insert the resultant in a matrix with a dimension of $(2N_x-1)\times(N_y)\times(N_z)$. It should be noted that as there are $(N_y)\times(N_z)$ lines in the x-direction, it is required to perform $(N_y)\times(N_z)$ FFTs in this step.
2. Take each y-direction's lines of the modified matrices obtained in step 1 and expand them to the arrays with the length of $(2N_y-1)$ using Eq. 2.39. Then, perform the FFT of each line in the y-direction and insert the result in matrices with the dimension of $(2N_x-1)\times(2N_y-1)\times(N_z)$. In this step, it is needed to perform FFT of $(2N_x-1)\times(N_z)$ lines in the y-direction.
3. Take z-direction's lines of the obtained matrices in step 2, expand them to the vector with the length of $(2N_z-1)$ using Eq. 2. 39. And finally, calculate the FFT of each line in the z-direction and insert the resultant in matrices with the dimension of $(2N_x-1)\times(2N_y-1)\times(2N_z-1)$. In this step, it is required to perform $(2N_x-1)\times(2N_y-1)$ FFTs in the z-direction.

It is worth mentioning that the mirror elements in steps 1, 2 and 3 must be multiplied to appropriate coefficients provided in Table 1 [107, 108]. The schematic of the performing FFT of the six tensor blocks of the interaction matrix has been demonstrated in Figure 2.8. Also, the 'FFT_Interaction' file provided in the Appendix D.8 to calculate the aforementioned FFTs.

Table 2.1. Coefficients which should be multiplied to the mirror elements for operation DFT [107, 108]

	A_{xx}	A_{xy}	A_{xz}	A_{yy}	A_{yz}	A_{zz}
X-DFT	+1	-1	-1	+1	+1	+1
Y-DFT	+1	-1	+1	+1	-1	+1
Z-DFT	+1	+1	-1	+1	-1	+1

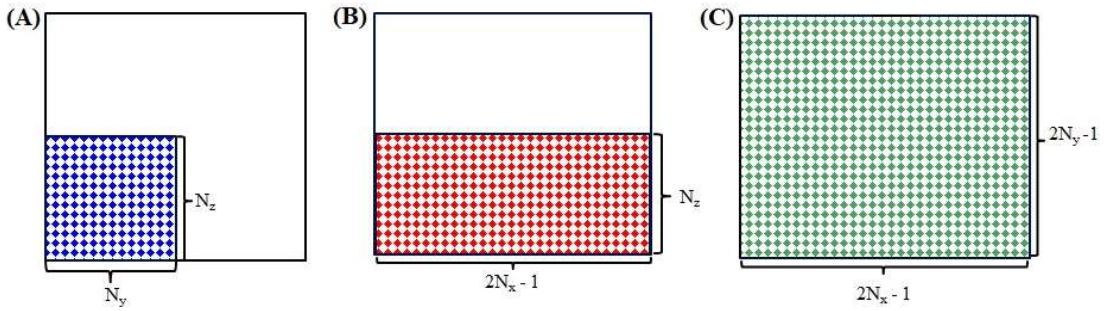

Figure 2.8. Schematic is representing the procedures of applying 1D FFT to the six 3D blocks of the interaction matrix. (A) Applying FFT to the $N_y \times N_z$ lines with the length of $(2N_x - 1)$ in the x-direction, (B) Performing FFT to $(2N_x - 1) \times (N_z)$ lines with the length of $(2N_y - 1)$ in the y-direction and (C) Obtaining FFT of the $(2N_x - 1) \times (2N_y - 1)$ lines with the length of $(2N_z - 1)$ in the z-direction.

In the next step, we need to obtain the FFT of each component of the polarization vector (P_x, P_y, and P_z). Similar to the 3D blocks, before performing the FFT of each component they must be transferred from a vector with a length of N ($N_x \times N_y \times N_z$) to a 3D matrix with the dimension of $N_x \times N_y \times N_z$. To fulfill the dimension requirement to perform element-wise multiplication of FFT(A) and FFT(P), the 3D components of the polarization vector must be extended from 3D matrices with dimension of $N_x \times N_y \times N_z$ to the matrices with dimension of $(2N_x - 1) \times (2N_y - 1) \times (2N_z - 1)$. The FFT of P_x, P_y and P_z can be carried out by taking 1D FFT in y, x, and z-direction, consecutively, as following:

1) Take each line in the y-direction and expand them to the length of $(2N_y - 1)$ by zero paddings, perform the FFT for the $N_x \times N_z$ lines in this direction and embed the results in the matrices with the dimension of $(N_x) \times (2N_y - 1) \times (N_z)$. This can be computed in MATLAB as

$$\mathrm{FFT}(P_i) = \mathrm{fft}(P_i, 2N_y - 1, 2) \tag{2.41}$$

where i represents the x, y or z-direction. It should be noted that $2N_y$-1 is presenting $(2N_y$-1)-point FFT along each line in the y-direction. Since the length of each line in P_x, P_y and P_z is N_y, before computing FFT, MATLAB will extend the length of each by zero paddings them to length $2N_y$-1 [123].

2) Take the results of the previous step, expand the lines in the x-direction to the lines with a length of $(2N_x - 1)$ by zero paddings, calculate the FFT of $(2N_y - 1) \times N_z$ lines in this direction and embed the results in a matrix with dimension of $(2N_x - 1) \times (2N_y - 1) \times (N_z)$. Similar to the previous step, this can be done as below in MATLAB

$$FFT(P_i) = fft(P_i, 2N_x - 1, 1) \quad (2.42)$$

3) Take the results of the step (2) and expand the length of the lines in the z-direction from N_z to $(2N_z - 1)$ by zero paddings them, perform the FFT for the $(2N_x - 1)\times(2N_y - 1)$ lines in z-direction and embed the results in the matrices with the dimension of $(2N_x - 1)\times(2N_y - 1)\times(2N_z - 1)$.

Figure 2.9 shows the procedures of applying 1D FFT to the 3 components of the polarization vector in DDA (see Appendix D.10).

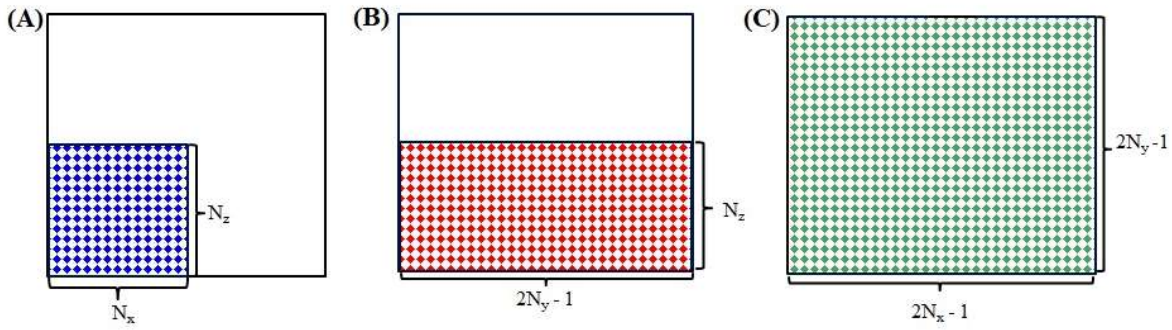

Figure 2.9. Schematic representing applying the 1D FFT to the three components of the polarization vector in the (A) y-direction, (B) x-direction and (C) z-direction.

By calculating the FFT of the tensor blocks of the interaction matrix and three components of the polarization vector the element-wise multiplication of the FFT(A) and FFT(P) can be performed as below (see Appendix D.10)

$$FFT(A.P)_{x,ex} = \left[FFT(A_{xx,ex}).* FFT(P_{x,ex}) + FFT(A_{xy,ex}).* FFT(P_{y,ex}) + FFT(A_{xz,ex}).* FFT(P_{z,ex})\right] \quad (2.43.a)$$

$$FFT(A.P)_{y,ex} = \left[FFT(A_{xy,ex}).* FFT(P_{x,ex}) + FFT(A_{yy,ex}).* FFT(P_{y,ex}) + FFT(A_{yz,ex}).* FFT(P_{z,ex})\right] \quad (2.43.b)$$

$$FFT(A.P)_{z,ex} = \left[FFT(A_{xz,ex}).* FFT(P_{x,ex}) + FFT(A_{yz,ex}).* FFT(P_{y,ex}) + FFT(A_{zz,ex}).* FFT(P_{z,ex})\right] \quad (2.43.c)$$

where $FFT(A.P)_{x,ex}$, $FFT(A.P)_{y,ex}$, and $FFT(A.P)_{z,ex}$ are presenting the matrix-vector element-wise multiplication resultant in the x, y, and z-direction, respectively. The subscribe 'ex' in the above equations represents an extended matrix and the symbol '.*' denotes element-wise multiplication.

To transfer A.P from the Fourier domain to the main domain, it is needed to carry out the inverse FFT of each component obtained in Eq.24. This can be taken by computing inverse FFT in the z, x, and y-direction, consecutively. As shown in Figure 2.10, this computation can be expressed in three steps as below (see Appendix. D.10):

1) Performing inverse FFT of the $FFT(A.P)_{x,ex}$, $FFT(A.P)_{y,ex}$ and $FFT(A.P)_{z,ex}$ for $(2N_x -1)\times(2N_y -1)$ lines in the z-direction.
2) Take $(2N_y -1)\times(N_z)$ lines in the x-direction of the results obtained in the step (1) and perform the inverse FFT for the lines in the x-direction.
3) Take $N_x \times N_z$ lines in the y-direction of the results obtained in the step (2) and perform the inverse FFT for all of the lines in the y-direction.

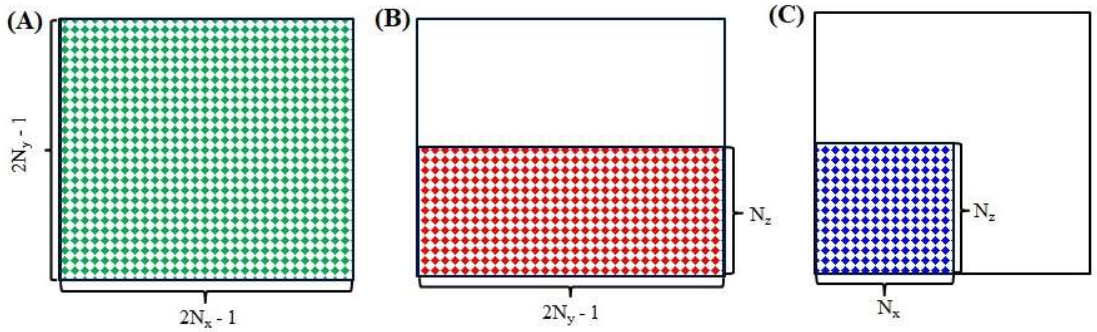

Figure 2.10. Schematic of applying 1D inverse FFT for calculating matrix-vector multiplication of (A.P) in DDA.

After obtaining the results of the matrix-vector multiplication (A.P) in all directions, in the final step, it is required to nullify the contribution of the dipoles which lie outside of the NP boundary and add the first elements which have been negated in the previous steps. The aforementioned operations can be applied as below:

$$(A.P)_{Np,x} = (A.P)_{x}.* B + \alpha^{-1}P_{x}.* B \qquad (2.44.a)$$

$$(A.P)_{Np,y} = (A.P)_{y}.* B + \alpha^{-1}P_{y}.* B \qquad (2.44.b)$$

$$(\mathrm{A.P})_{\mathrm{Np,z}} = (\mathrm{A.P})_{\mathrm{z}} .* \mathrm{B} + \alpha^{-1}\mathrm{P}_{\mathrm{z}} .* \mathrm{B} \qquad (2.44.\mathrm{c})$$

where $(A.P)_{Np,\,x}$, $(A.P)_{Np,\,y}$ and $(A.P)_{Np,\,z}$ are the results of the A.P in the x, y, and z-direction, respectively, and the symbol '.*, denotes the element-wise multiplication. In the above equations, the matrix B is a 3D matrix with a dimension of $N_x \times N_y \times N_z$ which its elements are one and zero for the nanocubes inside and outside of the NP, respectively. This matrix has been applied to nullify the contribution of the dipoles which lie outside of the NP. The second terms in the above equations are representing the contribution of the first elements in the corresponding direction which have been negated in the previous steps (see Appendix D.10).

A flowchart of the matrix-vector multiplication (A.P) steps using FFT and inverse FFT is presented in Figure 2.11. Also, the corresponding MATLAB scripts for calculating all of the steps in Figure 2.11 are provided in the Appendices. D.8, D.9, and D.10.

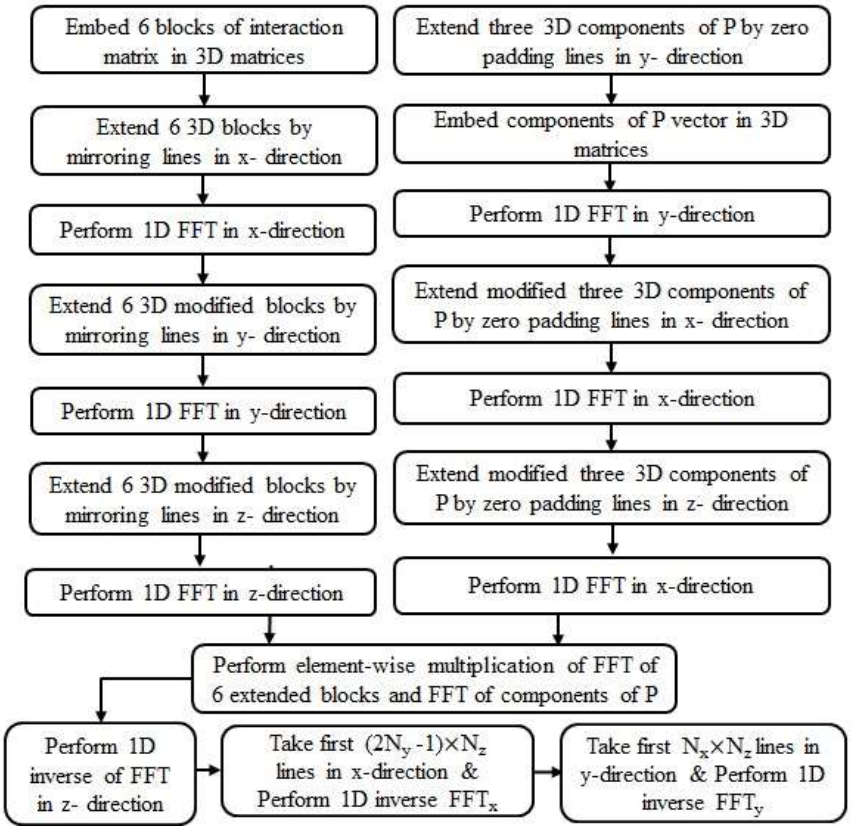

Figure 2.11. Flowchart of all of the required procedures to obtain matrix-vector multiplication A.P results in DDA in the Fourier domain.

As already mentioned, to obtain the polarization vector of the plasmonic nanoparticles using iterative methods after obtaining the results of the matrix-vector multiplication (A.P) the corresponding components of the polarization vector will be updated using BCG iterative method. The iteration process will continue until satisfying the terminating criterion that is provided in Eq. 2.35. The MATLAB script of the iterative technique (BCG) to modify the P_x, P_y and P_z is provided in Appendix D.9.

2.6.2.4. Running DDA in Graphics Processing Units (GPUs)

Graphics Processing Units (GPUs) have shown to be a cost-effective, energy-efficient and successful solution in comparison to CPUs for running a large amount of data in modern scientific studies [124]. In contrast to CPUs which typically have cores in the range of 2-8, GPU's architecture is unique in its design and typically has thousands of cores (see Figure 2.12) [125–128]. Although modern CPUs can have an even larger number of cores, it is still very small as compared to GPUs.

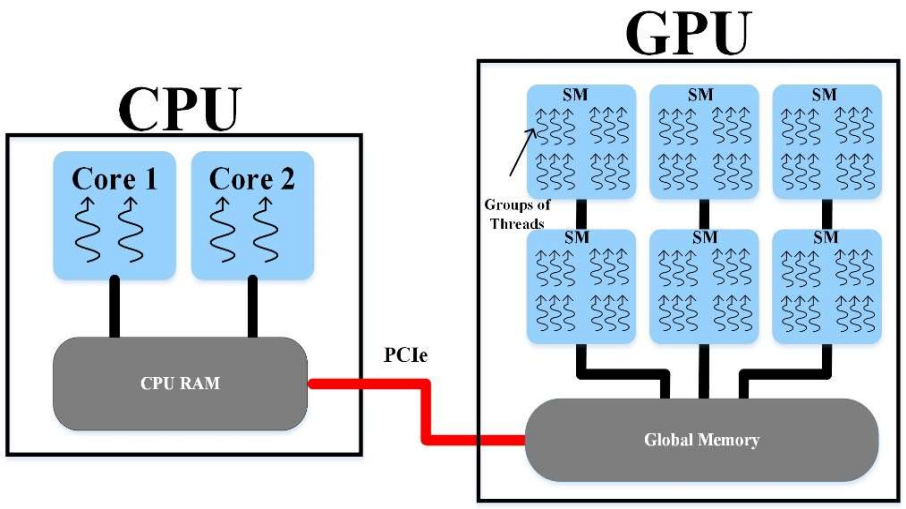

Figure 2.12. Schematic of CPU and GPU architecture and PCIe cable for transferring data from CPU to GPU and vice versa.

To accelerate DDA more, I modified the codes to run them using the GPU toolbox in the MATLAB. Since GPU is considered a foreign device, any data which needs to be processed in it should be transferred from CPU to it, and after finishing the processing of the data in the GPU it

must be offloaded back to the CPU. Offloading data from CPU to GPU and transferring it back from GPU and CPU can be done using 'gpuArray' and 'gather' commends in MATLAB, respectively [129]. Figure 2.13 demonstrates the flowchart of the data transferring in DDA from CPU and GPU and vice versa. It should be noted that a PCIe cable is responsible to move data between CPU and GPU device, which is highly limited in data communication speeds, and transfer of larger datasets may cause bottlenecks. In some cases, data transfer times can even exceed the processing time thus nullifying any advantage gained in the first place [128]. Hence, to accelerate our algorithms, the amount of data transferring from CPU to GPU and vice versa should be minimized. As demonstrated in Figure 2.13, only two communications happen between CPU and GPU in the whole algorithm in DDA. First, we transferred input parameters (wavelength, dielectric function and position of the dipoles) from CPU to GPU, run all intensive portions of DDA in GPU and then transferred final results from GPU to CPU.

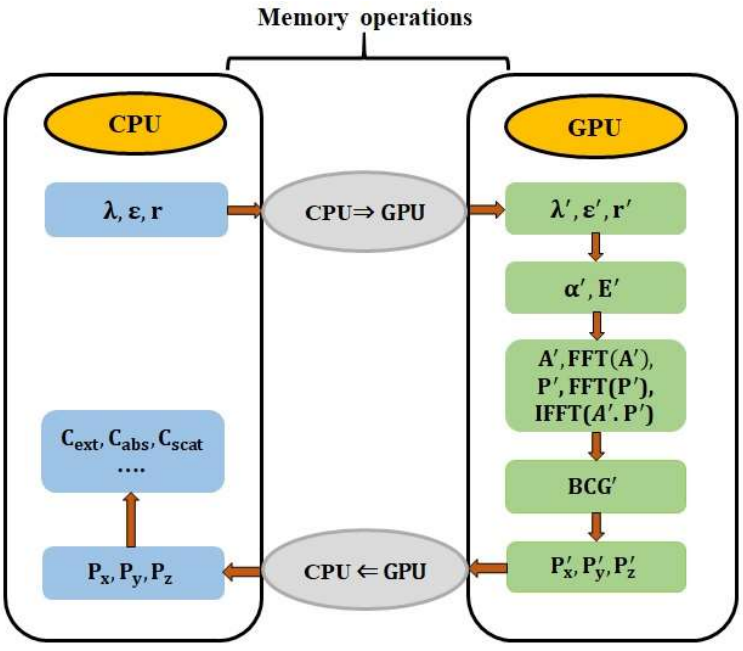

Figure 2.13. Flowchart of the data transfer from CPU to GPU and vice versa.

To compare the speed of the calculation of DDA in CPU and GPU, we computed absorption efficiency of a spherical gold NP with a diameter of 40 nm. Figure 2.14A shows the computational times of DDA versus number of the dipoles in CPU and GPU. By comparing the results, it can be

inferred from Figure 2.14B that the overall relative speedup of GPU aided implementation to CPU method enhances more with further increasing the number of the dipoles. The results demonstrate that for a nanoparticle that consists of ~10^6 dipoles the GPU computational time is almost 10 times less than CPU. Figure 2.15 shows the overall flowchart of the DDA using GPU.

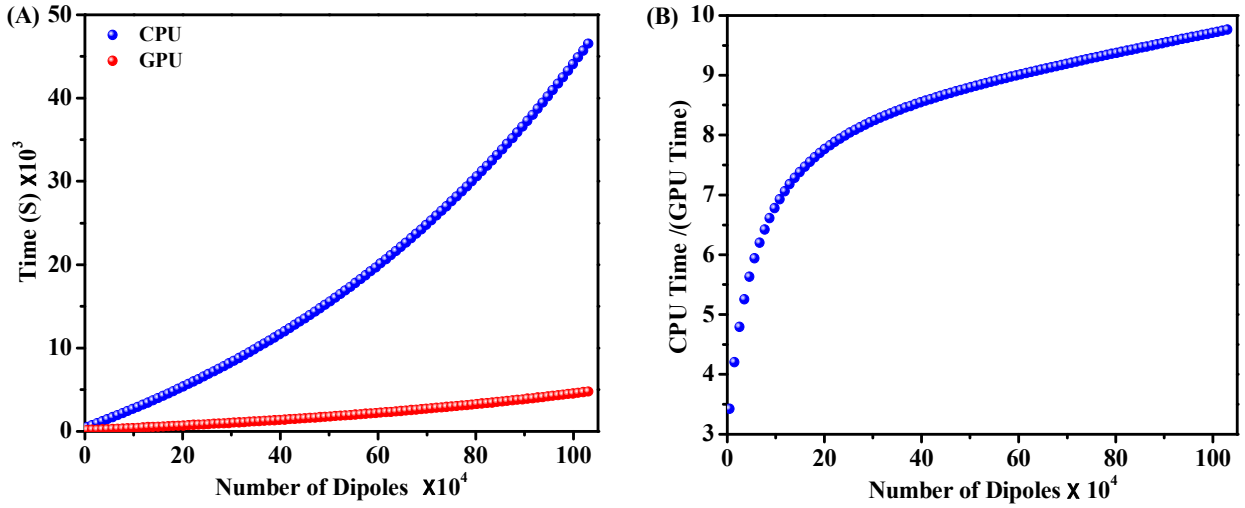

Figure 2.14. (A) Comparison computation time of DDA in CPU and GPU and (B) their ratio versus the number of the dipoles.

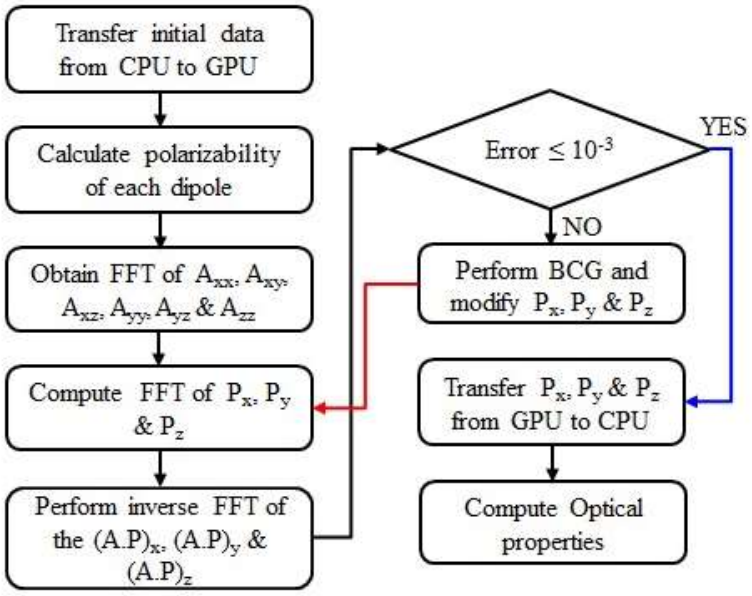

Figure 2.15. Flowchart of DDA for computing optical properties of the NPs using FFT, BCG, and GPU.

Table 2.2 presents a summary of some important MATLAB commands used in the proposed package.

Table 2.2. Description of some MATLAB functions applied in DDA

MATLAB function	Description
fft(A,[],i)	Compute 1D FFT of the lines of matrix A in i-direction
ifft(A,[],i)	Calculate inverse 1D FFT of the lines of matrix A in i-direction
gpuArray	Transfer data from CPU to GPU and running codes in GPU
gather	Transfer data from GPU to CPU

In the next section, we provide some examples of the optical properties of the metallic NPs that have been computed using the package provided in the Appendices.

2.6.3. Calculating Optical Properties of the Metallic NPs

2.6.3.1. Absorption, Scattering and Extinction Efficiencies

After calculating the polarization vector of the dipoles of an arbitrary shaped NP at different wavelengths, the absorption, extinction, and scattering cross-sections of the NP can be calculated using the following equations [87]

$$C_{abs} = \frac{4\pi|k|}{|E_0|^2}\sum_{i=1}^{N}[Im(\frac{P_i . P_i^*}{\alpha_i^*}) - \frac{2}{3}|k|^3|P_i|^2] \quad (2.44.a)$$

$$C_{ext} = \frac{4\pi|k|}{|E_0|^2}\sum_{i=1}^{N}[Im(E_{inc,i}^*) . P_i] \quad (2.44.b)$$

$$C_{scat} = C_{ext} - C_{abs} \quad (2.44.c)$$

where 'Im' and '*' are representing the imaginary part and complex conjugate, respectively. The absorption, extinction and scattering efficiencies factors are defined as $C_{abs}/ \pi r_{eff}^2$, $C_{ext}/ \pi r_{eff}^2$ and $C_{scat}/ \pi r_{eff}^2$, where πr_{eff}^2 and r_{eff} are geometrical cross-sections and effective radius of the NP. For a nonspherical nanoparticle with the volume of V, the r_{eff} is equal to the radius of a sphere with equal volume as NP that can be defined as $r_{eff} = (3V/4\pi)^{1/3}$.

Figure 2.16 shows the extinction efficiency of a spherical gold NP with a diameter of 40 nm obtained using DDA for two different mesh sizes of d=0.5 nm and 0.25 nm. To verify our code, the extinction efficiency of the mentioned NP has been obtained using the exact solution (Mie theory [1]) and the result has been added to Figure 2.16. By comparing the spectra obtained through the exact solution and DDA code, it can be inferred that the approximation method spectra converge more to the exact solution by further decreasing the size of the cubic mesh. The results show that the average error between the extinction spectra of DDA and Mie theory reduced from 6.7% to 1.4 % by reducing the size of the mesh from 0.5 nm to 0.25 nm.

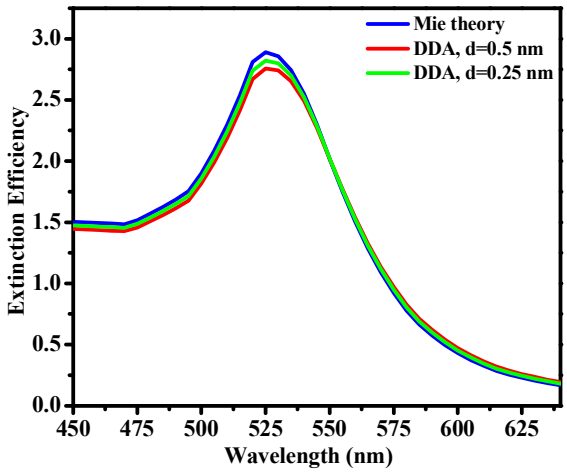

Figure 2.16. Extinction efficiency of a spherical Au Np with r = 20 nm using Mie theory (exact solution), and DDA with two different mesh sizes of 0.5 and 0.25 nm.

As mentioned already, approximation methods such as DDA [85–88, 104, 109, 130] mainly have been used to simulate the optical properties of non-spherical NPs due to lack of exact solution. Figure 2.17 demonstrates the extinction, absorption and scattering efficiencies of a gold nanorod. As demonstrated in Figure 2.5c, the rod NP is made of a cylinder and two semi-spheres caps at both ends. In our simulation, we set the effective radius of the NP to 20 nm and chose the aspect ratio (AR), which is defined as the ratio of the longer axis to shorter one, to be 2. Also, the incident light field is polarized along the long axis of the NP. Interestingly, by comparing the results of Figure 2.16 and 2.17 it can be inferred that the rod shape NP absorb and scatter the incident light much stronger than spherical one, despite the fact that they have the same volume. The extinction

spectra presented in Figure 2.16 and 2.17 have been computed using the m-file presented in Appendix B and the functions provided in Appendix D.

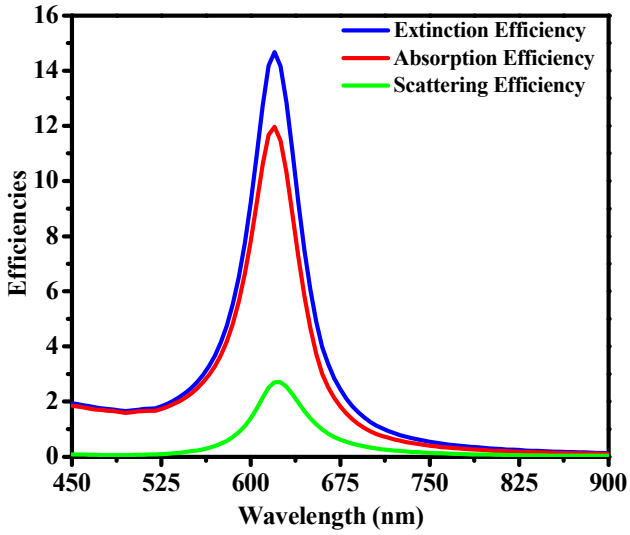

Figure 2.17. Extinction, absorption and scattering efficiencies of the longitudinal mode of a rod shape Au Np with r_{eff}= 20 nm, AR=2 and d = 0.5 nm using the DDA.

2.6.3.2. Calculating Electric Field Enhancement Around Plasmonic NPs

The total electric field at position r_i around a nanoparticle can be calculated by the summation of the incident light field and the scattered fields of N-1 other dipoles at position r_i , and is given by [111]

$$E_{tot}(r_i) = E_{inc}(r_i) + E_{scat}(r_i) \tag{2.45}$$

where the incident and scattered field at position r_i are

$$E_{inc}(r_i) = E_0 \exp(ikr_i) \tag{2.46}$$

$$E_{scat}(r_i) = \sum_{j=1}^{N} \frac{\exp(ikr_{ij})}{r_{ij}} \left[k^2(\hat{r}_{ij}\hat{r}_{ij} - \mathbf{1}_3) + \frac{(ikr_{ij} - 1)}{r_{ij}^2}(3\hat{r}_{ij}\hat{r}_{ij} - \mathbf{1}_3) \right] . P_j \tag{2.47}$$

where r_{ij} is the distance between the position of dipole i and j. Figure 2.18A and 2.18B show electric field enhancement around a spherical and a rod shape Au NP with an effective radius of 20 nm, respectively, at their corresponding localized surface plasmon resonance (LSPR)

wavelength. For the nanorod, the incident light electric field is aligned to be parallel to the long axis of the NP which creating longitudinal mode. Although the NPs in Figure 2.18A and 2.18B have the same volume, the average distance between the positive and negative charges in the longitudinal mode of the rod shape nanoparticle is bigger than the spherical NP, which leads to much stronger polarization and field enhancement in comparison to the spherical case [27, 131].

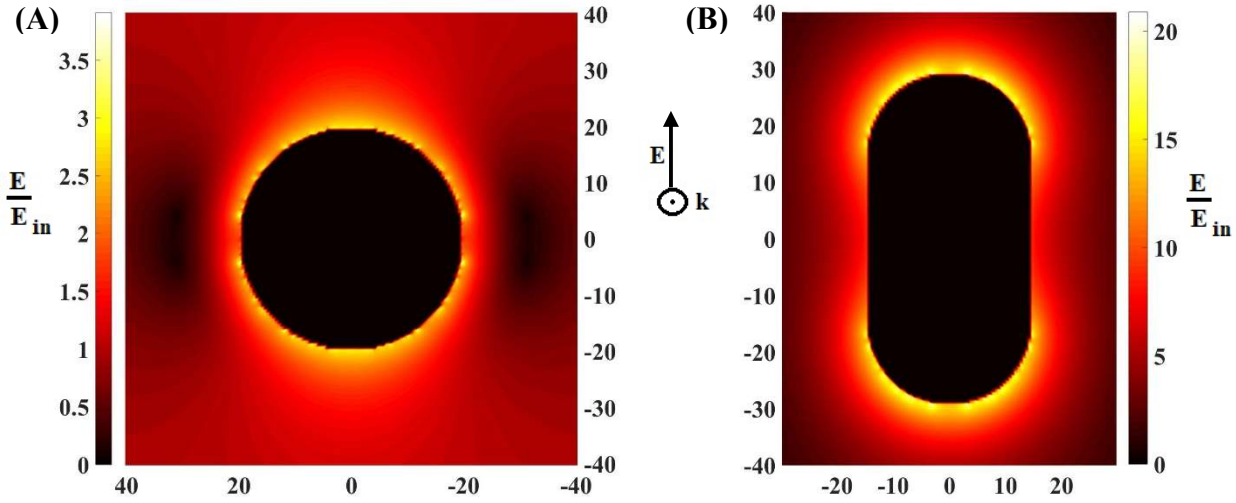

Figure 2.18. Electric field enhancement around (A) a spherical Au Np with r= 20 nm (λ_{LSPR}= 525 nm) (B) a rod shape Au Np with r_{eff}= 20 nm and AR= 2 for longitudinal mode (λ_{LSPR}= 620 nm), using DDA. The mesh size for both cases has been set to d= 0.5 nm.

2.6.3.3. Computing Hot Spots Between Nanoparticles in Dimeric Structures

When the distance between the two nanoparticles is small enough in comparison to the incident light wavelength the electric dipoles of the one NP can interact with the dipoles of another particle [63, 102, 103, 132]. This coupling, which depends on the polarization direction of the incident light [63, 103, 132], the orientation of the nanoparticles [63, 103, 132] and the inter-particle distances [63, 103, 132, 133], can create a bright or dark mode between the NPs. Figure 2.19A, 2.19B, and 2.19C show three different configurations, as examples, of the plasmonic coupling between two neighboring nanoparticles. In Figure 2.19A, the nanoparticles are oriented head-by-tail and the incident light electric field polarized in the direction of the long inter-particles axis. This interaction enhances absorption and scattering efficiencies and redshifts LSPR peak in comparison to the single NP due to the constructive coupling between neighboring particles, which

reduces the restoring Coulombic force between the positive and negative charges [27, 63], This constructive coupling leads to huge enhancing of the electric field between the NPs by creating a hot spot between them (see Figure 2.20A). In Figures 2.19B and 2.19C, the NPs are linked together in a side- by- side configurations. In Figure 2.19B, the electric field of the incident light is parallel to the long axis of each NP, while in Figure 2.19C it is oriented in the direction of the short inter-particles axis. The electric field enhancement in both structures is much weaker than the configuration presented in Figure 2.19A. In Figure 2.19B, the side by side parallel orientation of the electric dipoles of the neighboring NPs leads to a destructive coupling, which creates dark mode between them (See Figure 2.20B). In Figure 2.19C, although head to tail orientation of the dipoles of the neighboring NPs leads constructive coupling between them, the electric field enhancement of the transversal mode of each particle is weak in comparison to the longitudinal one due to smaller average distances between positive and negative charges in each NP which increases the required electromagnetic energy for exciting the conduction electrons of each particle (See Figure 2.20C).

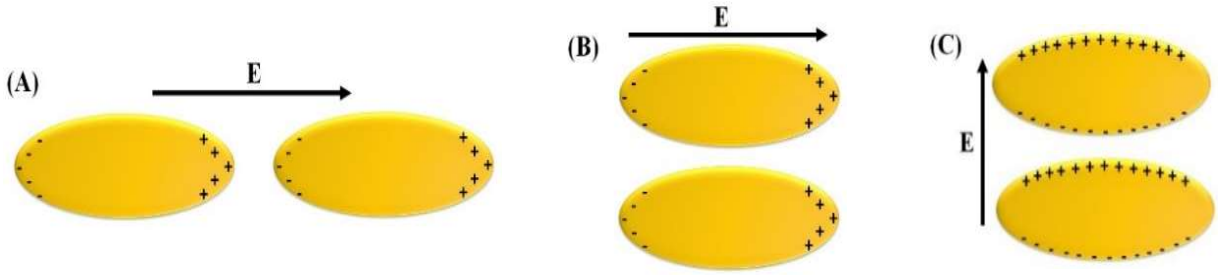

Figure 2.19. Schematic of the charge distribution around the plasmonic NPs in the dimeric structures (A) for head to tail orientation with incident light parallel to the long interparticle axis, (B) for side by side orientation with incident light parallel to the long axis of the NPs, and (C) for side by side orientation with incident light perpendicular to the long axis of the NPs.

The electric field enhancement in the monomeric and dimeric structures can be computed using the m-file ('$E\_field\_Enhancement.m$') that is provided in the Appendix C along with the MATLAB functions that are provided in Appendix D.

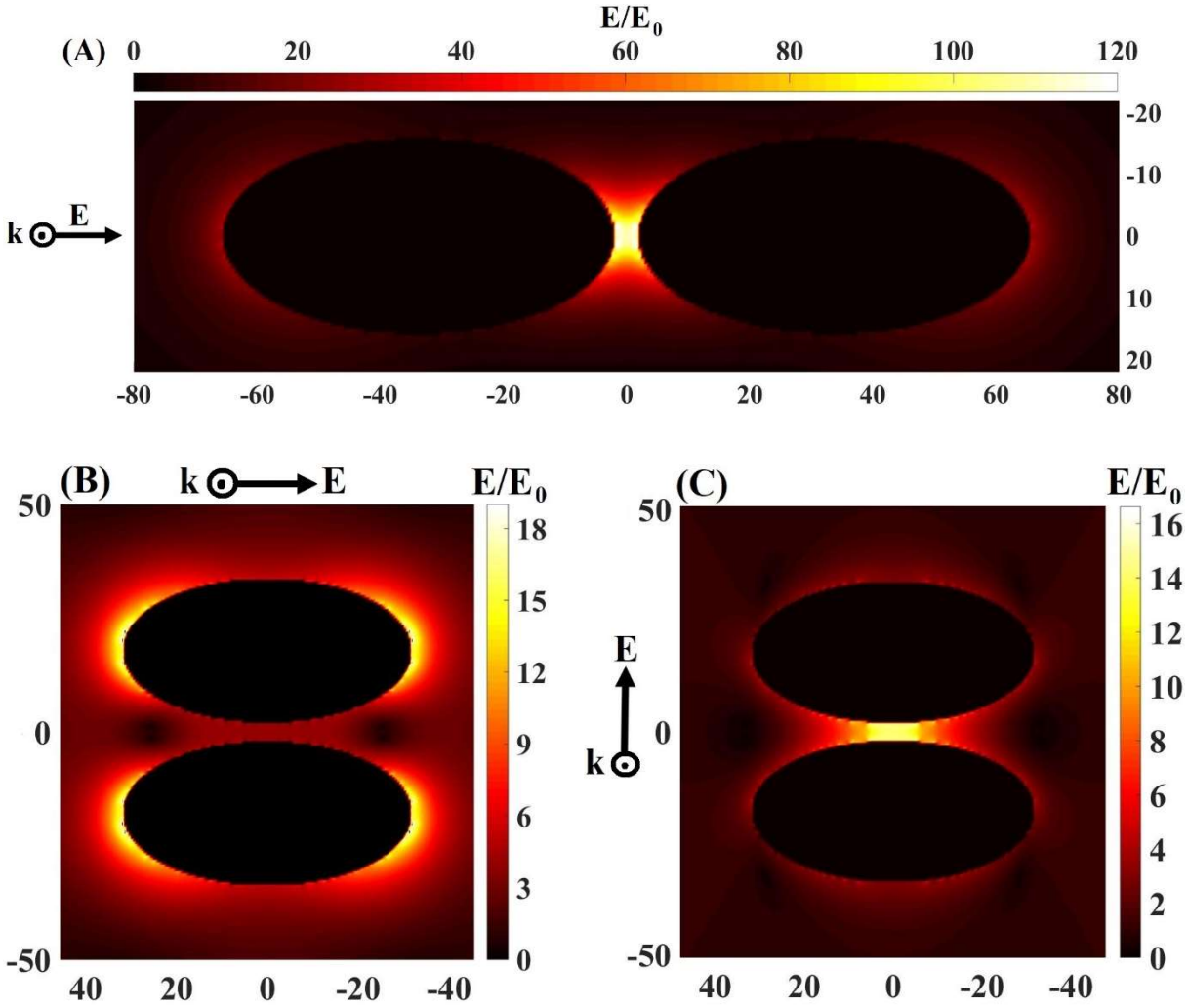

Figure 2.20. Surface plot representing the creation of (A) longitudinal hot spot, (B) dark mode and (C) transversal hot spot, between ellipsoid Au NPs in the dimeric structures presented in Figure 19A, 19B, and 19C, respectively. In our simulation, the effective radius of each NP, the aspect ratio, the interparticle distances, and the mesh sizes are chosen to be 20 nm, 2 nm, 4 nm and 0.5 nm, respectively.

CHAPTER 3

THEORETICAL INVESTIGATION OF PLASMONIC PROPERTIES OF QUANTUM - SIZED SILVER NANOPARTICLES

3.1. Introduction

Localized surface plasmon resonance (LSPR) is produced by strong coupling of the incident light and the oscillation of conduction band electrons in metallic NPs [1, 134, 135]. This phenomenon leads to strong scattering and absorption of the light as well as significant electric field enhancement around the NPs at LSPR frequency [49]. These optical properties, which resulted from the LSPRs of metallic NPs, have found applications in the fields of photonics [11, 14, 43, 102, 136–141], medicine [12, 14, 20, 142, 143], biological imaging [11, 14, 144, 145], biosensing [27, 29, 31, 146–152], plasmonic resonance energy transfer (PRET) [136–138], fluorescence enhancement [102, 147], and surface-enhanced Raman scattering (SERS) [43, 139]. Also, it was shown that plasmonic NPs can transfer the extra heat to the surrounding medium through electron-electron, electron-phonon, and phonon-phonon interactions [153–155]. which can be applied for destroying malignant cells [12, 14, 20, 143, 144]. As an example, gold nanorods conjugated with anti-epidermal growth factor receptor (anti-EGFR) antibody has been used to heat up and destroy the cancer cells [12, 14, 20, 143, 144]. Owing to overexpressed EGFR on the cytoplasmic membrane of the malignant cells, the anti-EGFR antibody integrated nanorods attached with higher affinity to the surface of the malignant cells [12, 14, 20, 143]. By continuous irradiation of these nanoparticles by low power laser light at the LSPR frequency, it was observed that malignant cells were photothermally destroyed when compared to healthy cells [12, 14, 20, 143].

The LSPR frequency of plasmonic NPs can be tuned by different parameters such as shape, size, the refractive index of the surrounding medium, the polarization direction of the incident light, and inter-particle plasmonic coupling [9, 49, 61, 63-65, 83, 103, 132, 156–165]. Reducing the size of the NPs would enable them to integrate more into biological cells for biological imaging

or photothermal therapy. The small-sized plasmonic NPs can be ideal candidates to detect and sense a single molecule or electron or few electron transfer phenomena [79]. Although a significant amount of the theoretical and experimental research was carried out on understanding the LSPR properties of the classical-sized metallic NPs(> 10 nm) [9, 49, 61, 63-65, 83, 103, 132, 156–162], few studies concentrated on the LSPR properties of the quantum-sized (≤ 10 nm) NPs [76, 79, 166–173]. For instance, Scholl et al. investigated optical properties of small-sized Ag NPs using aberration-corrected transmission electron microscope (TEM) imaging and scanning TEM electron energy- loss microscopy [79]. Using an analytical quantum model, they observed 0.5 eV blue shift of the LSPR frequency by decreasing the size of the NPs from 20 nm to less than 2 nm [79]. Varas et al. studied the anisotropy effect on the plasmon coupling, field enhancement, and electron tunneling in dimer junction of Na_{279} for different inter-particle distances using ab initio study [166]. In another study, Barbry et al. explored the atomic distribution dependence of plasmonic hot spots of the ultra-small sodium NPs using time-dependent density functional theory (TDDFT) [167]. They demonstrated that formation of the subnanometric hot spot in the inter-particle junction is due to the distribution of the near-field close to the NPs. Recently, Mokkath observed shape- anisotropy effect on the optical properties of the quantum-sized spherical aluminum NPs (made of 807 atoms) using TDDFT [168]. He demonstrated that stretching of the NPs in one or two directions caused significant enhancement of the plasmon spectra and led to the appearance of distinct plasmon peaks in optical spectra of the aluminum NPs in UV- visible region.

To describe the optical properties of the NPs, it is required to define their dielectric function, which plays a vital role in determining their LSPR properties. The classical Drude model is a commonly used approach to calculate the dielectric function of the bulk metals and big-sized plasmonic NPs [1, 174]. However, by reducing the size of the NPs, the mean free path of the electrons decreases due to the increased number of the collisions of the electrons with the boundary of the nanoparticles [1, 174, 175]. To consider this effect, an additional term, which is inversely proportional to the size of the NPs, has been applied to intrinsic collision frequency for describing the electric permittivity of the classical-sized NPs (d > 10 nm) [174]. However, this classical approach failed to predict the optical properties of the ultra-small NPs, which can be described as quantum-sized NPs (d ≤ 10 nm) [79]. This can be ascribed to the discretization of the band structure of the NPs by further reducing the size [78, 79, 94], where demanding quantum calculations, and solving many-body problems might be needed. Few theoretical models have been proposed to

calculate the electric permittivity of the quantum-sized NPs [78, 79, 94, 176, 177]. The first theoretical model was developed by Gonzel and Martin in 1975 using a simple model of electrons in a box [78]. This model was able to observe the ultrafine structures in the spectra of ultra-small NPs. However, the drawback of this is model is that it overestimated the plasmon peak broadening of the quantum-sized NPs with countable atoms [176]. In another study, the permittivity of ultra-small silver NPs (up to 586 atoms) has been calculated using density functional theory (DFT) [94]. In this work, He and Zeng derived an empirical equation as a function of the radius of NPs and frequency of the incident light for the intraband term of the imaginary part of the dielectric constant and calculated the real part of the dielectric function using the Kramer-Kronig relation [177]. In another work, Scholl and coworkers developed an analytical equation to model the optical properties of the quantum-sized NPs [79]. They used Lorentzian oscillation terms to describe allowed quantum electron transition frequencies for NPs with a diameter less than 10 nm. Their results successfully explained the blueshifts and reducing of the absorption efficiency as the size of the isolated ultra-small NPs is decreased [79]. Although these studies have improved the understanding of ultrasmall plasmonic NPs, several factors remain to be understood that include a systematic size effect, effect of the surrounding medium and the effect of passivating ligands on the optical properties of the plasmonic NPs.

In this chapter, we focused on the size and refractive index (RI) of surrounding medium effects on plasmonic absorption, LSPR frequency shift, and field enhancement of the individual ultrasmall spherical Ag NPs in size range of 3 to 20 nm. To understand the optical properties of the Ag NPs theoretically, first, the dielectric function of the NPs was calculated. For NPs with size ranges from 10 to 20 nm, the modified classical Drude model was used to calculate the dielectric function, whereas for quantum-sized NPs (3 to 10 nm), the quantum model proposed by Scholl et al. has been utilized [79]. Utilizing the standard Mie theory, the size, and surrounding medium effects on the plasmonic properties were explored using both classical and quantum models. By comparing the results of these two models, it is conceivable that the quantum model could predict a blue shift of LSPR peak when the size of NPs decreases from 10 to 3 nm while the classical model failed to observe this effect. We studied the effect of RI of the surrounding medium on the LSPR peak position and field enhancement around NPs. Also, the evolution of the enhanced electric field against the distance from the surface of the NP has been investigated, and interesting results were obtained. Then, the dependence of the aforementioned optical properties for ligand

passivated NPs has been studied in detail for spherical Ag NPs conjugated with oleylamine (OAM) using multi-layered Mie theory. Both models predicted an enhancement for the LSPR wavelength difference ($\Delta\lambda$) between the ligand-conjugated and ligand-free samples by shrinking the dimension of the NPs. However, the quantum model demonstrated a larger $\Delta\lambda$ than the classical one for NPs less than 10 nm.

In the following section, we discuss the theoretical methods that have applied to describe electric permittivity and calculate the optical properties of the quantum-sized nanoparticles.

3.2. Theoretical Methods

3.2.1. Electric Permittivity

Values of the electric permittivity of a bulk Ag at different wavelengths were taken from experimental data provided by Johnson and Christy [78]. In nanoscale regime, when the size of NPs is smaller than the mean free path of the free electrons in bulk metal, the collision frequency has been modified using Eq. 2.3. The revised electric permittivity of the classical-sized NPs (d > 10 nm) has been calculated using Eq. 2.2. In the quantum regime (d < 10 nm), we obtained the imaginary part of the permittivity of these quantum-sized NPs for the sizes ranging from 3 to 10 nm by calculating the imaginary part of the interband contribution through the analytical equation that is given in Eq. 2.5. Then, the Kramer- Kronig relation [177] has been applied to compute the real part of the dielectric function of each NP

$$\varepsilon_1(\omega) = 1 + \frac{2}{\pi} P \int_0^{\infty} d\omega' \frac{\omega'^2 \varepsilon_2(\omega')}{\omega'^2 - \omega^2} \tag{3.1}$$

here P is the Cauchy principal value.

Also, the dielectric permittivities of the classical and quantum-sized ligand-conjugated Nps have been calculated using Eq. 2.4 and Eq. 2.7, respectively.

It is worth mentioning that, in our simulation, ε_{IB} was considered to be independent of the size of the NPs in the energy range that we performed our calculations [79, 94]. Also, the bulk collision frequency, plasma frequency, Fermi velocity and empirical parameter in Ag NPs were

taken to be $\Gamma_0 = 2.43 \times 10^{13}\,\frac{\text{rad}}{\text{s}}$ [78], $\omega_p = 1.37 \times 10^{16}\,\frac{\text{rad}}{\text{s}}$ [178], $V_F = 1.39 \times 10^{6}\,\frac{\text{m}}{\text{s}}$ [179], and A = 0.25 [79], respectively.

3.2.2. Calculation Methods

For ligand-free samples, we performed standard Mie theory to study the size and the surrounding medium influence on the LSPR resonance wavelength and the optical efficiencies of the spherical Ag NPs [80]. The incident, scattered and total electric fields have been obtained from [180]

$$E_{in} = \sum_{n=1}^{\infty} \frac{\left[M_{01n}^{(1)} - iN_{e1n}^{(1)}\right] i^n (2n+1)}{[n(n+1)]E_0} \tag{3.2}$$

$$E_s = \frac{\sum_{n=1}^{\infty}\left[ia_n N_{e1n}^{(3)} - b_n M_{01n}^{(3)}\right] i^n (2n+1)}{[n(n+1)]E_0} \tag{3.3}$$

$$\vec{E}_t = \vec{E}_{in} + \vec{E}_s \tag{3.4}$$

where n is the summation index of the partial waves, E_0 is the magnitude of the incident wave at the origin, and E_{in}, E_s and E_t are the incident, scattered and the total electric field, respectively. The $M_{01n}^{(j)}$ and $N_{e1n}^{(j)}$ (j = 1, 3) are the vector spherical harmonics, where detailed information about them can be found elsewhere [180].

In the case of ligand-conjugated samples, we employed three-layered Mie theory [82, 181] to investigate chemical bonding effects on the plasmon damping, LPSR wavelength shifting, electron conductivity and field enhancement around the NPs. Inspired by Peng [76], this three-layered model consists of an inner or core region with a diameter of $d_{cor} = d - 2t$, outermost atomic layer with a thickness of t and the chemical ligand layer with a width of *l* (see Figure 3.1).

We performed our simulation for different size spherical Ag NPs which integrated with OAM ligand and dispersed in Hexane solution. The ligand layer and outermost shell thickness were taken to be 2 and 0.25 nm, respectively [76]. Also, the dielectric constant was chosen 1.4596 for OAM ligand and 1.379 for the Hexane solution [76].

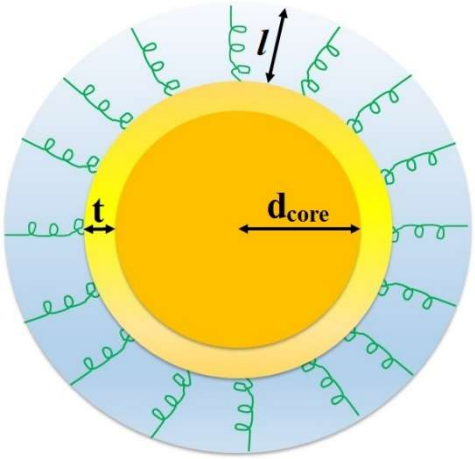

Figure 3.1. Schematic illustration of a three-layered nanosphere consists of the core region of diameter d_{core}, and the skin and surrounding chemical ligand with a thickness of t and *l*, respectively.

3.3. Results and Discussion

3.3.1. Electric Permittivity of the Quantum-Sized NPs

Figure 3.2A and 3.2B show dispersion spectra of the real and the imaginary part of the dielectric function of the spherical Ag NPs with the diameter ranged from 3 to 10 nm using the quantum model, respectively. These quantities have been calculated using Eq. 2.7 by setting g =1. Our results show that by decreasing the size of the NPs some small peaks appeared in both the real and imaginary parts of the dielectric function which their magnitude increases more by the further shrinking the dimension of the NPs. The appearance of new peaks in the dielectric function spectra can be attributed to the inter-level transitions of the electrons due to the discretization of the conduction band. A likely explanation for the increasing size of peaks is that the inter-level transition frequency between the initial state of i and the final state of f, which is inversely proportional to the square of the radius of NPs ($\omega_{if} \propto \frac{1}{R^2}$), increases with reducing the size of the NPs, resulting in enhanced oscillator strength for the transition. As a comparison, the dielectric function of the NP with d = 10 nm was calculated using the classical model and has been added to Figure 3.2. In the classical approach, the experimental permittivity of the bulk metal has been altered only by adding size modification term to the damping frequency of the electrons, whereas, in the quantum modeling both the surface and the conduction band discretization effects have been considered for calculating the permittivity. Our simulation results show that the calculated

permittivity from these two models overlaps for the desired range of wavelengths (300 - 500 nm) for sizes greater than or equal to10 nm.

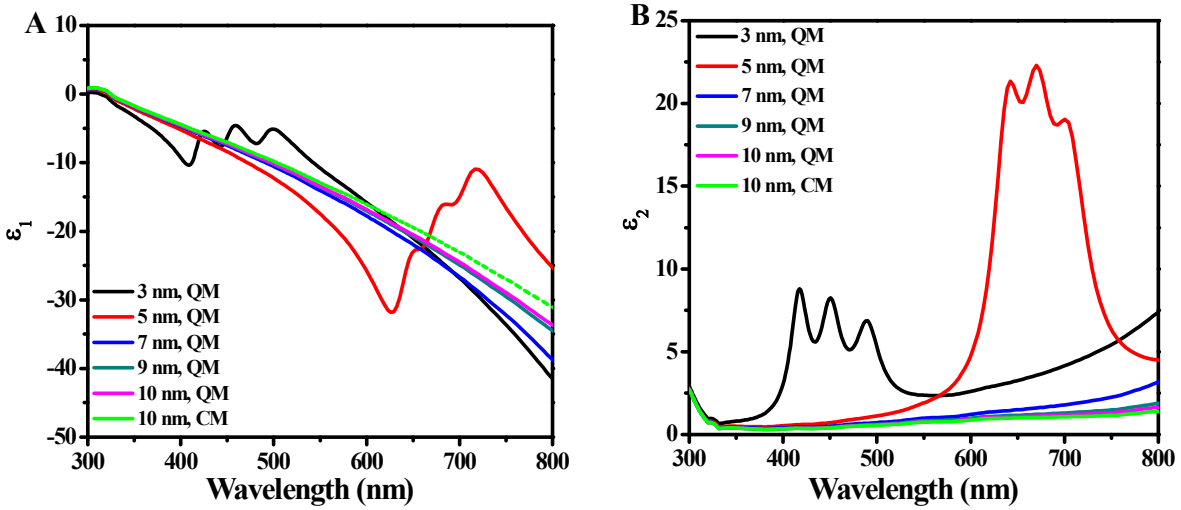

Figure 3.2. Quantum modeling (QM) of the real (A) and imaginary (B) part of the dielectric function of the spherical Ag NPs with diameters ranged from 3 nm to 10 nm. Green lines represent the permittivity of the Ag NPs with d =10 nm that have been obtained using the classical model.

3.3.2. Absorption Efficiency and LSPR Wavelength

In this section, the absorption efficiency of the spherical Ag NPs in the size range of 3 to 20 nm was determined using standard Mie theory. To show the discrepancies between the classical and quantum model, we simulated the aforementioned optical property using both models and represented the results in Figure 3.3. In our simulation, the refractive index of the medium was set to be 1.34. It is expected that LSPR peak magnitude increases and shifts to longer wavelengths by increasing the size of the NPs.[9] The results of both models show that the absorption efficiency grows with an increase in the size of the NPs, and the maximum amount of the absorption remains relatively the same for both approaches. However, the LSPR peak wavelength obtained from the quantum model significantly differs from the classical calculation. To present this discrepancy clearly, the full evolution of the LSPR peak position against the diameter of the Ag NPs was shown in Figure 3.4 for both models. It is observed from the figure that the classical model does not show a noticeable shift for the LSPR maximum, and it stays around 380 nm as the diameter of the NPs decreased from 20 to 3 nm. By comparing the results of both models, a slight difference was observed between the predicted LSPR peak positions of the quantum and classical model when

the size of the NP decreased from 20 to 10 nm. However, by further reducing the size of the NP, the calculated LSPR peak energy of the quantum model diverges from the classical one and it predicts a noticeable (~ 30 nm) blue shift for the plasmon resonance wavelength as the NP size decreased from 10 to 3 nm and matched relatively well with the experimental result [79]. Thus, the classical calculation has failed to predict the expected LSPR shift for the small-sized NPs ($d \leq 10$ nm), while the quantum simulation has shown the expected plasmon resonance shift.

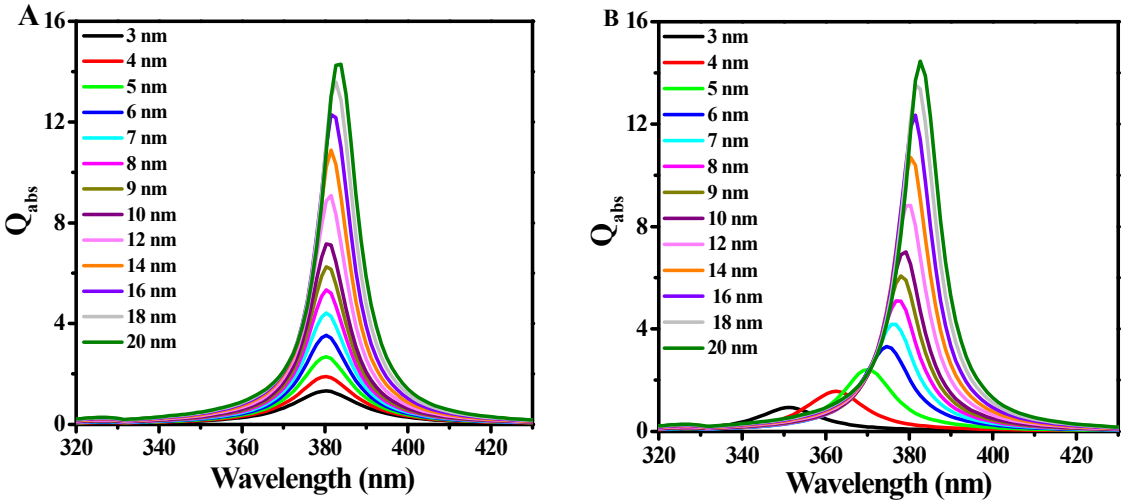

Figure 3.3. Absorption efficiency of the different size spherical Ag NPs inserted in water ($n_b = 1.34$) using (A) classical and (B) quantum Model. The quantum model predicts a redshift for LSPR peak wavelength with the increasing dimension of the NPs ,while the classical model obtains an almost constant value for LSPR with changing the size of the NPs.

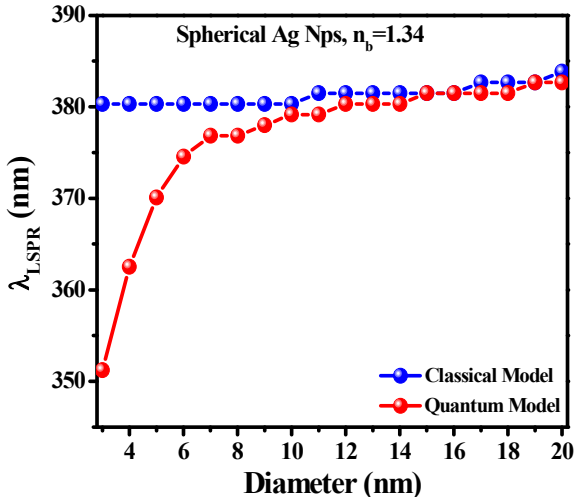

Figure 3.4. Comparing the Classical Model (CM) and Quantum Model (QM) LSPR peak wavelength evolution versus diameter of the Ag NPS dispersed in water.

3.3.3. Medium Effect on the LSPR Wavelength

Absorbing molecules on the surface of the NPs change the RI of the medium around their surface, leading to the shifting of the LSPR energy. This leads to changing the peak color of the spectra and provides opportunities for the NPs to be potential candidates for imaging and single-molecule detection [9, 14, 67, 182, 183]. Our group has shown recently that LSPR sensitivity depends on the shape, size, and structure of the NPs [27]. Although absorption and scattering efficiencies of the plasmonic NPs decreases by reducing their size [27], their surface to volume atoms ratio increases by shrinking the size that makes them very sensitive to few absorbates on their surface.[67, 79] In this section, we explored the effect of changing RI of the surrounding medium on the LSPR wavelength shift of the quantum-sized Ag NPs with varying RI of the medium from 1 to 2 (See Figure 3.5). For comparison, the results of the classical-sized spherical Ag NPs with diameters of 20, 30, and 40 nm have been added to Figure 3.5. In our simulation, the quantum model was applied to calculate the LSPR wavelength of the NPs in the size range from 3 to 10 nm, whereas the classical model was used for NPs with sizes bigger than 10 nm.

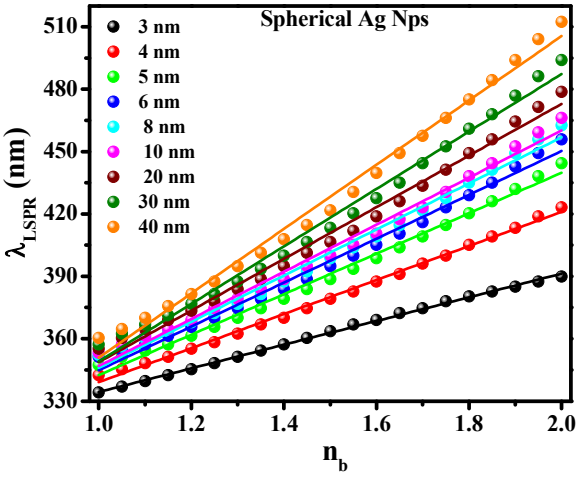

Figure 3.5. Evolution of the LSPR peak wavelength of the spherical Ag NPs versus RI of the surrounding medium. LSPR shift rate increases by increasing the size of the NPs.

As shown in Figure 3.5, the LSPR wavelength of the NPs increased by increasing the RI of the medium. The observed result could be attributed to enhanced electric field shielding effect by increasing n_b, which decreases the attractive coulombic force between the electron clouds and positive ions, and consequently reduces the required energy to excite electrons on the surface of

the NPs [61]. Similar to the results observed by Lee and El-Sayed for large-sized NPs, our results show that the LSPR wavelength follows a clear linear trend of increasing with increasing RI of the medium [184]. Interestingly, as demonstrated in Figure 3.5, the LSPR shift increases with increasing the size of the NPs. This result can be explained by the fact that the contribution of the higher-order plasmonic modes increases by increasing the size of the NPs [185].

3.3.4. Medium Effect on the E-field Enhancement

Interaction of the incident light with plasmonic NPs results in a strong localized electric field around their surface at corresponding LSPR frequency that decays exponentially with increasing the distance from the surface of the NPs. This property, which depends on the shape, size, and configuration of the NPs and RI of the medium, creates a small sensing volume around the NPs that increases their capability to effectively detect the target molecules in their close vicinity through observing the LSPR peak shift or enhancing the targets signals [67, 79, 186]. As explained already, owing to the smaller size and higher surface-to-volume ratio, the quantum-sized NPs are potential candidates to detect single molecules [79]. It is therefore of interest to see how the electric field around the quantum-sized NPs will alter with varying the size of NPs, the distance from their surface, and changing RI of the surrounding medium.

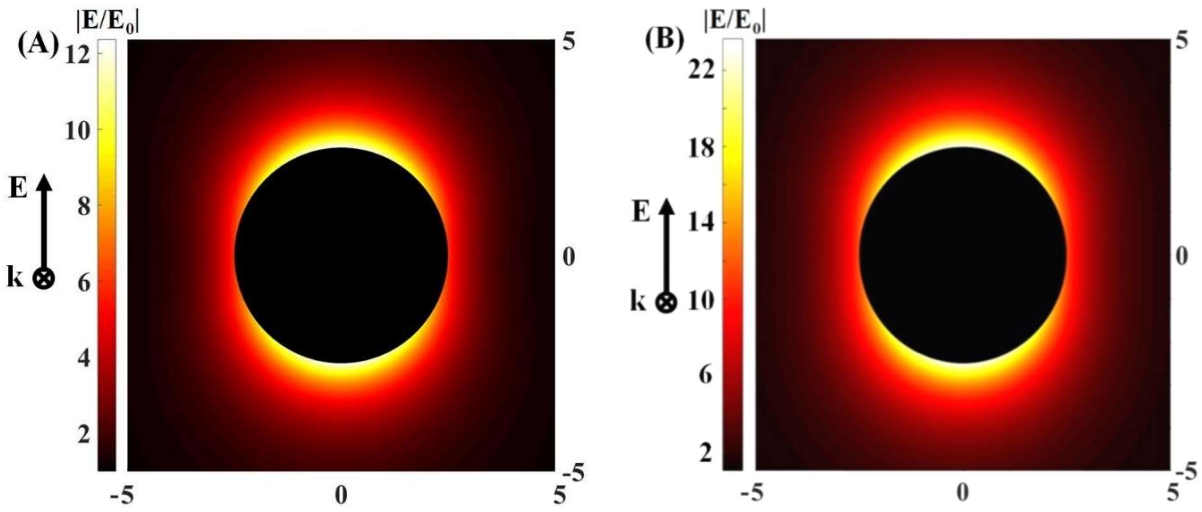

Figure 3.6. Surface plot of the normalized electric field enhancement of the spherical Ag NPs with D=5 nm in (A) vacuum (B) aqueous solution.

Figures 3.6A and.3.6B show the surface-plot of E field enhancement around the Ag NPs with a diameter of 5 nm that was dispersed in two different mediums with $n_b = 1$ and $n_b = 1.34$, respectively, at corresponding LSPR wavelengths. The electric field around the NPs has been normalized to the incident light electric field. Our results show that the electric field enhancement around the NPs reaches its maximum value of 12.37 in vacuum, whereas this amount increases in aqueous solution and gets to 23.65.

To further understand the trend of the electric field evolution of the quantum-sized NPs by varying the RI of the medium, we obtained the field enhancement factor (FEF) of the different size Ag NPs (See Figure 3.7) against the normalized distance (normalized to each particle diameter) from the surface of each one. FEF, which is a dimensionless parameter, quantifies the ability of an NP to enhance the electric field around itself and described by

$$\mathrm{FEF} = \left|\frac{\mathrm{E}}{\mathrm{E}_0}\right|^2 \tag{3.5}$$

where E and E_0 are the total electric field around the NP and the incident light electric field at the origin, respectively.

The simulation was performed for the NPs with a diameter in the range of 3 - 6 nm and for different RI of the medium, which varied from 1 to 1.6. As expected, the FEF enhances by increasing the diameter of the NPs due to the increasing volume of the NPs. For example, at the $n_b = 1.6$ maximum FEF for the NP with a diameter of 6 nm is 1170, which is 4.7 times greater than FEF of the NP with a diameter of 3 nm. Also, it can be seen that the FEF is rising by increasing the RI of the medium. This observation can be ascribed to enhancing the polarizability of the NPs with increasing n_b in the studied range. However, the decay length of the scattered field of each NP is independent of the RI of the medium and is almost 0.2 times of their corresponding diameters. This result suggests that sensing volume of the NPs is enlarged by increasing the size of the NPs while it remains unchanged by varying the RI of the surrounding medium.

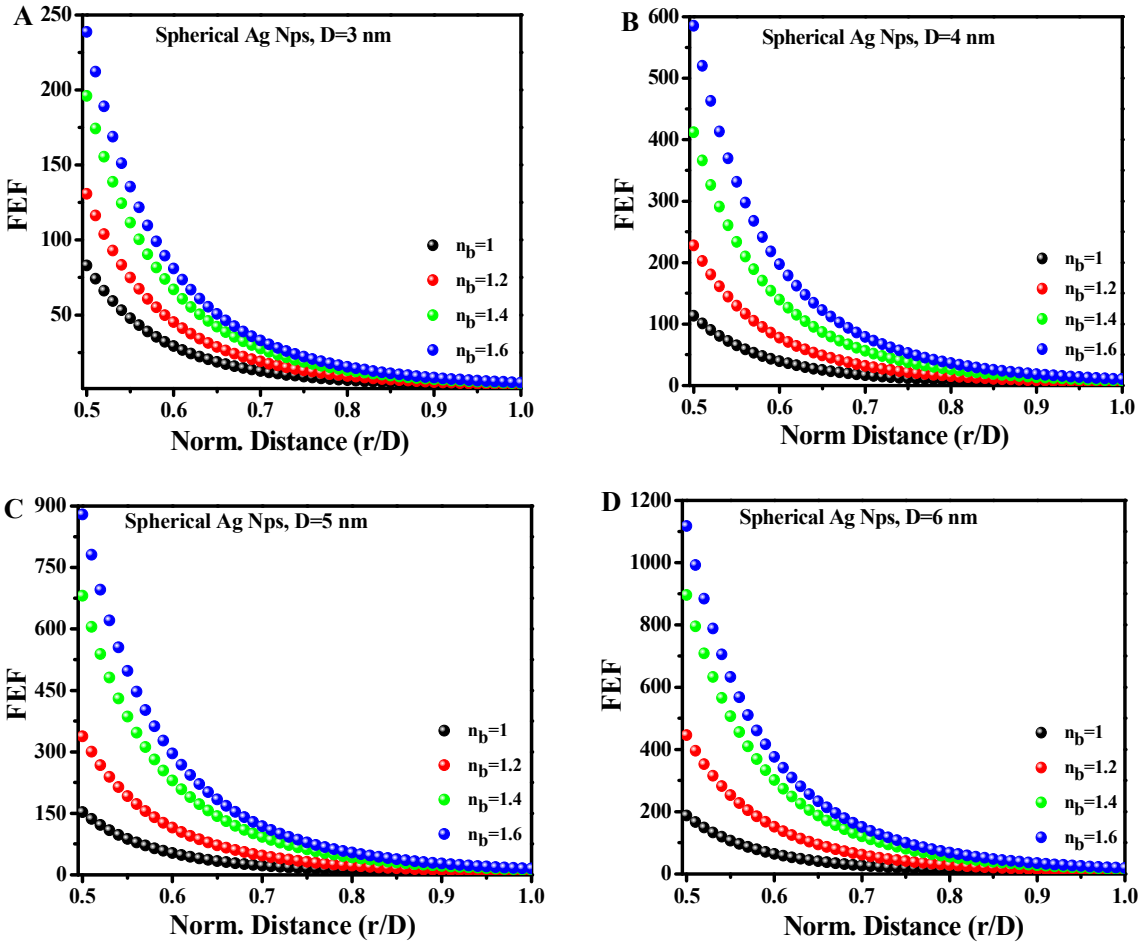

Figure 3.7. Evolution of FEF of the spherical quantum-sized Ag NPs versus distance from the surface of each, which normalized by the diameter of the particles. FEF has been calculated with varying n_b from 1 to 1.6 for different sizes: (A) D= 3 nm, (B) D= 4 nm, (C) D= 5 nm, and (D) D= 6 nm.

3.3.5. Chemical Ligand Effect

Synthesized NPs in solution agglomerates due to van der Waals attractive forces, which prevents them to obtain small-sized clusters [77, 187]. To prevent this effect, it is common to conjugate the NPs with ligands that help the stabilization of the particles by counterbalancing the van der Waals forces [77, 187]. However, the chemical bonding between the NPs and the ligands dampens the surface plasmons of the NPs and reduces their free electron density, especially on the surface atoms [76, 188]. Reducing the conductivity alters the optical properties of the NPs such as increasing plasmon damping and shift of LSPR frequency to longer wavelengths. In this section, we have studied the optical properties of different sized spherical Ag NPs that were dispersed in hexane and bound to OAM ligand. The absorption spectra were calculated using multi-layered

Mie theory [76], and for clarity, the absorption spectrum of each NP is multiplied by an arbitrary factor mentioned in the parentheses (See Figure 3.8).

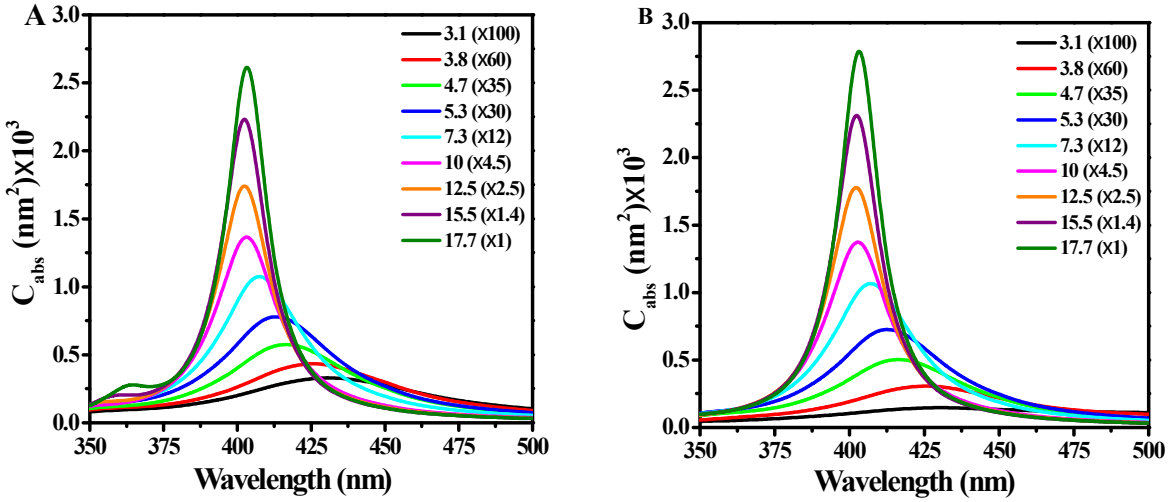

Figure 3.8. The absorption spectrum of different sized spherical Ag NPs that dispersed in Hexane solution and conjugated with OAM ligand using (A) the classical, and (B) the quantum model. In the inset, the numbers outside of the parentheses represent the diameter of the NPs, whereas the numbers inside them express an arbitrary factor that multiplied to their corresponding spectra for clarity.

These spectra were obtained by fitting the LSPR peaks to the experimental results that were reported by Peng et al.[76] through adjusting the conductivity of the core and the skin regions. As shown in Figure 3.8, both classical and quantum models predict that by decreasing the size of the NPs the absorption spectrum diminishes, while its full width at half maximum (FWHM) increases. These effects are due to reducing the volume of the NPs and increasing the electron-surface collision rate by reducing the size of the NPs. Similar to Peng et al. work, it is obtained that the plasmon absorption spectra of the ligand-conjugated spherical Ag NPs show an anomalous behavior by reducing the size of the NPs. It started with a gradual blue shift, then followed by strong redshift as the size of the NPs decreased further. This abnormal behavior is ascribed to increasing surface effects by decreasing the size of the NPs, and the chemical bonding between the ligand and NPs that reduces the conductivity of the NPs, especially the surface layer that is in direct contact with chemical ligands [76].

Figure 3.9 shows the conductivity correction factors of the core and skin regions of the studied ligand-conjugated Ag NPs using both models. In the classical model, the conductivity

correction factor of the core region (g^2_{core}) was set to be 1, while the g^2_{skin} varied slightly from its proposed simulated value (0.632) [76] in order to obtain perfect matching between the experimental and the theoretical spectra peak. The quantum model, on the other hand, predicted a reduced conductivity for both core and skin regions due to the chemical bonding between the ligand and the NPs. As expected, the conductivity of the surface atoms reduced more than core ones due to the direct interaction between the chemical ligand and surface atoms. Interestingly, it is shown that in size range of 18 to 10 nm the conductivity correction factor of the surface and core layers are almost independent of the size of the NPs, while both are reduced by decreasing the size of particles from 10 to 3 nm. These findings further support the observed anomalous LSPR peak behavior of the ligand-conjugated samples by reducing the size of the NPs.

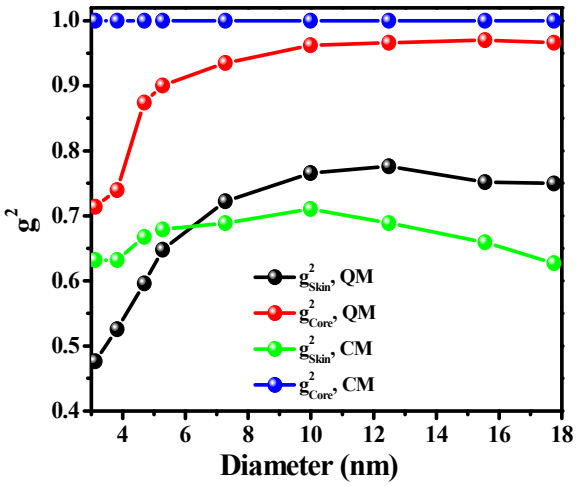

Figure 3.9. The conductivity correction factors of the core and skin regions of the Ag NPs versus the diameter using both quantum and classical models.

To further verify the validity of the quantum model, we calculated the absorption spectra of ligand-free samples with different diameters dispersed in hexane solution using both models (Figure 3.10). The absorption spectra were calculated using the standard Mie theory [80], and for clarity, the absorption spectrum of each NP is multiplied by an arbitrary factor mentioned in the parentheses. A comparison of the two models reveals that LSPR peak position in the classical calculation remains almost constant ($\lambda_{LSPR} \approx 390$ nm) by changing the dimension of the Ag nanoparticles, whereas in the quantum model the absorption maximum redshifts from 346 to 390.5

nm as the size of the NPs changes 3.1 to 17.8 nm. The LSPR peak shift of the NPs due to the chemical ligand was calculated by subtracting corresponding ligand-free values from the ligand-conjugated one ($\Delta\lambda = \lambda_{Lc} - \lambda_{Lf}$, where Lc and Lf are representing the Ligand-conjugated and Ligand-free NPs, respectively). As shown in Figure 3.11A, both models predict that the LSPR peak redshifts because of the chemical ligand binding, and the shift is increased by reducing the size of the NPs. However, the quantum model results deviate from the classical one by predicting a large redshift as the size of the NPs reduces. Also, the absorption spectra change versus the diameter of the NPs was calculated using both models (See Figure 3.11B). These changes were obtained by subtracting the peak absorption spectra of ligand-free samples from ligand integrated ones and normalized to absorption spectra of ligand-free ones ($\Delta A = \frac{(A_{Lc} - A_{Lf})}{A_{Lf}}\%$). From Figure 3.11B we can see that the classical model predicts that the |ΔA| reduces by reducing the size of the NPs from ≈ 18 nm to 10 nm, and then turns over and slightly increases by further reducing the size. On the other hand, the quantum model predicts that in size range from ≈ 18 nm to 10 nm the |ΔA| stays almost constant, while increases exponentially by further reducing the size of the NPs. As explained already, this is ascribed to the further reduction of the conductivity correction factors of the core and skin region due to increasing the surface effect by reducing the size of the NPs.

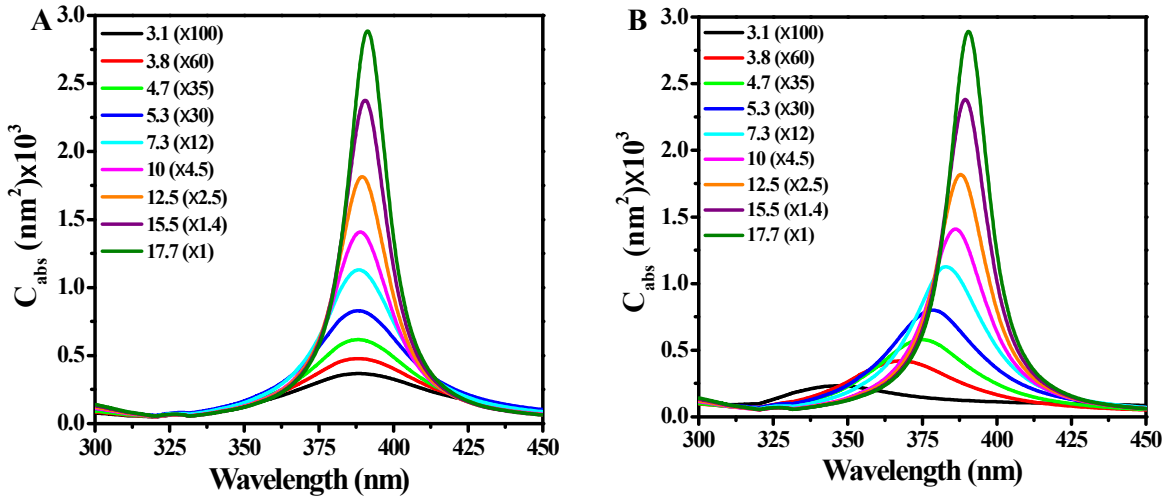

Figure 3.10. Size-dependent absorption spectra of the different size Ag NPs dispersed in Hexane solution using the (A) classical model, and (B) quantum model.

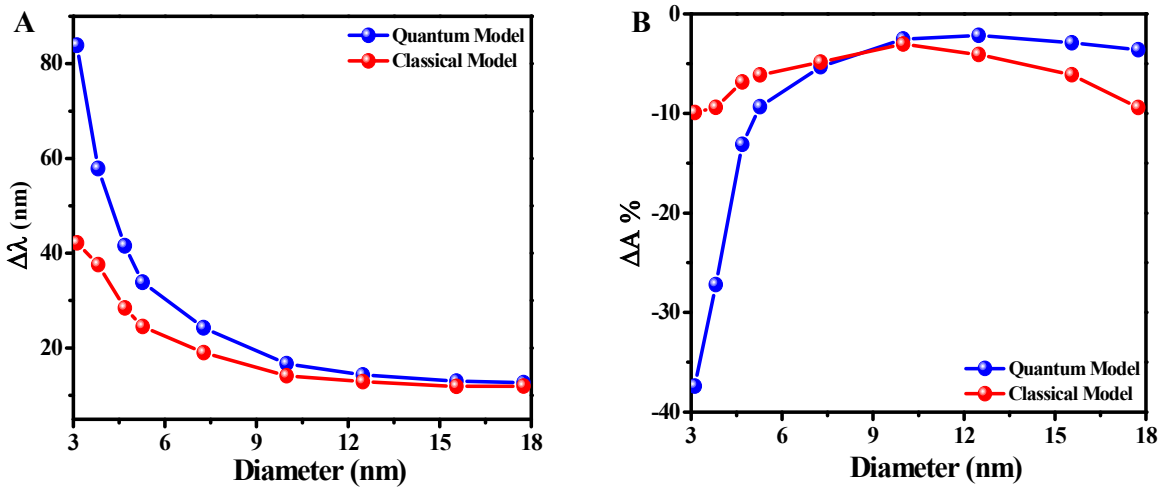

Figure 3.11. Size evolution of (A) LSPR peak shift, and (B) normalized LSPR peak absorption spectra changes of the spherical Ag NPs, dispersed in Hexane solution, due to adding OAM ligand to the Hexane solution.

Concerning the ligand effect on the field enhancement around the NPs, the evolution of the FEF versus normal distance from the surface of the NPs has been calculated using both models, and the results are presented in Figure 3.12. As shown, both models demonstrate that the electric field jumps from a particular distance for all NPs. This increase, which occurs in the boundary of the ligand and hexane solution, is due to changing RI of the medium when the electric field crosses the boundary of the ligand and solvent. By passing the electric field from the ligand to hexane solution, RI of the medium decreases, resulting in decreasing electric field shielding and consequently enhancing the electric field. However, by comparing the results of both models, it can be inferred that the quantum model predicts less amount of the electric field enhancement for the small size NPs as it accurately predicts decreased electronic conductivity. For comparison, The electric field evolution versus distance from the surface of bare nanoparticles has been presented in Figure 3.13.

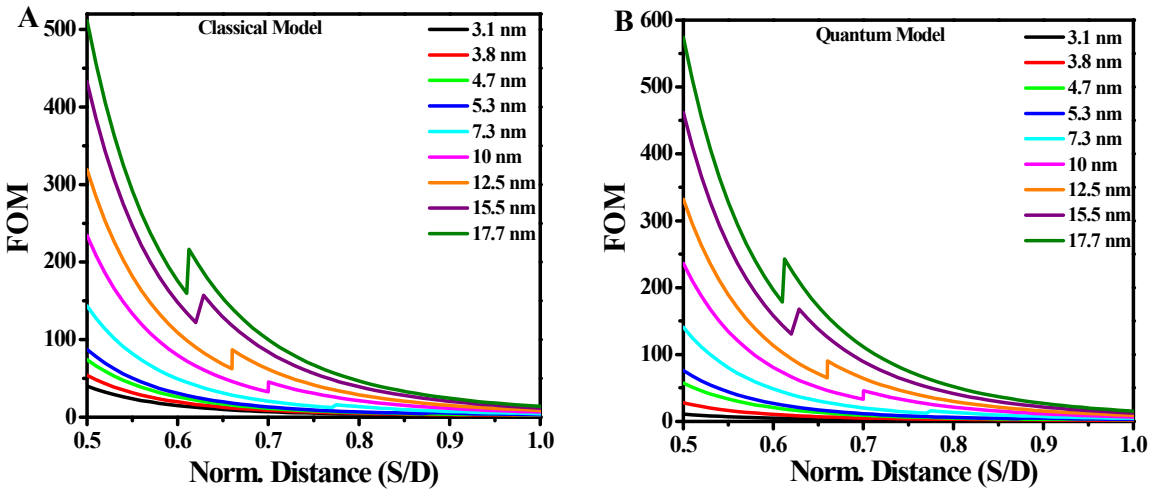

Figure 3.12. Distance evaluation of normalized FEF of the ligand-conjugated spherical Ag NPs that dissolved in Hexane solution using: (A) Classical model, and (B) Quantum model. We calculated FEF evaluation from the surface of the NPs and normalized distance from the center to the diameter of each NPs.

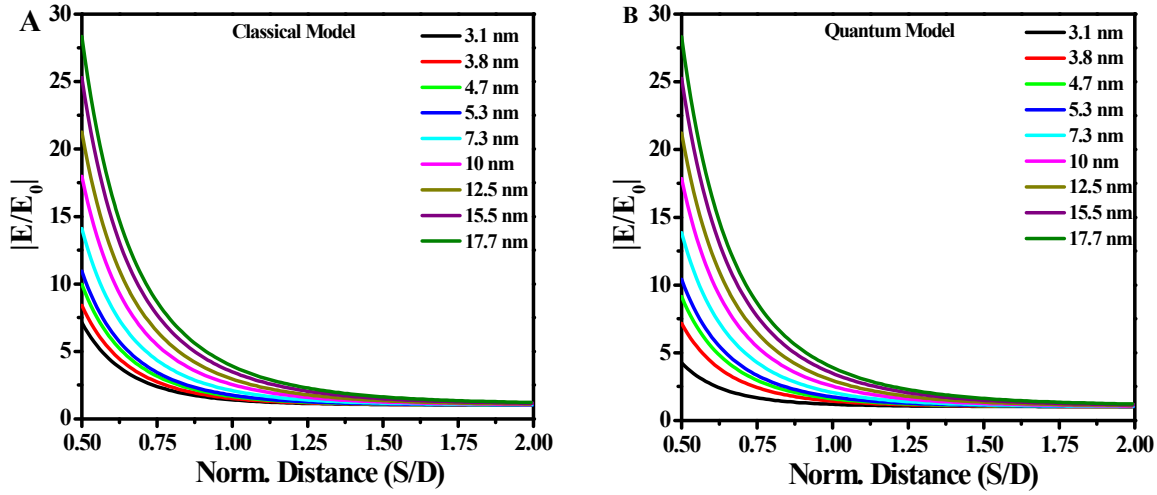

Figure 3.13. Distance evaluation of the normalized electric field of the ligand-free spherical Ag NPs that dissolved in Hexane solution using: (A) Classical model, and (B) Quantum model. We calculated E field evaluation from surface of the NPs and normalized distance from center to the diameter of each NPs.

The changing of the electric field on the surface of the Ag NPs due to the chemical ligand is calculated by (See Figure 3.14)

$$\Delta E = \frac{(E_{Lc} - E_{Lf})}{E_{Lf}} \tag{3.6}$$

where E_{Lc} and E_{Lf} are the electric field around ligand conjugated and ligand-free nanoparticles, respectively. As it is clear from Figure 3.14, the classical model failed to predict the electric field changes due to the chemical ligand and shows a reduction of ΔE by increasing the size of the NPs. On the other hand, the quantum model accurately demonstrates that the electric field of the ligand-conjugated NPs following a similar trend as ΔA, and in size range from ≈ 18 nm to 10 nm stays almost constant, while exponentially decreases by shrinking the dimension of the particles from 10 to 3 nm.

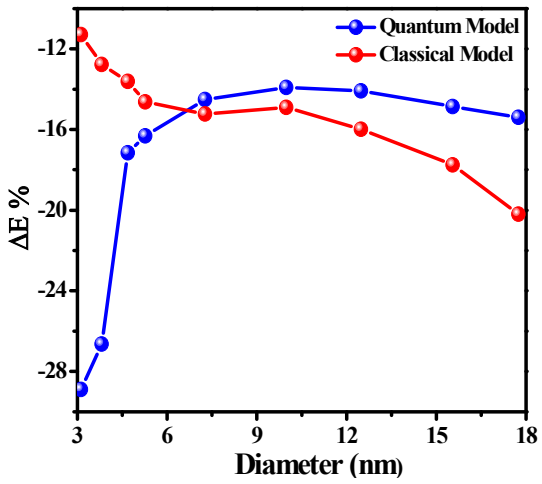

Figure 3.14. Size evolution of the changing the electric field around NPs due to adding OAM ligand. Electric field change has been normalized by the electric field of the corresponding ligand-free samples

CHAPTER 4

ULTRAFAST ELECTRON DYNAMICS IN THIOLATE-PROTECTED PLASMONIC GOLD CLUSTERS: SIZE AND LIGAND EFFECT[1]

4.1. Introduction

Optical properties of noble-metal nanoparticles (NPs) have been the subject of widespread research interest for the past two decades [7, 20, 47, 49]. The coupling of the electromagnetic field to free electrons in metal NPs creates quasi-particles named surface plasmons and was the focus of research for both theoreticians and experimentalists alike [50]. The surface plasmon resonance (SPR) of metal NPs strongly depends on the density of electrons, shape, type, size, the composition of the NPs, the polarization direction of the incident light, as well as the chemical environment that surrounds them [50, 60, 61–65, 75, 83, 189, 190, 191]. Among plasmonic NPs, gold NPs have attracted significant interest owing to their high chemical and physical stability, biocompatibility, photo-stability, and large optical cross-sections [69, 192, 193]. The SPR of gold NPs found applications in manifold areas [45] that included optical sensing [27, 194], biological imaging [9, 12, 195], plasmonic photo-thermal therapy [20], molecular diagnostics [11, 12, 47], surface-enhanced Raman spectroscopy [47], metal-enhanced luminescence and plasmonic rulers [49].

Enormous research has focused on the plasmonic properties of Au NPs and significant breakthroughs were made in the field [9, 11, 12, 47, 49, 62, 64, 69, 90, 92, 192, 196–198]. However, a bulk of the surface plasmon research has focused on gold NPs passivated with surfactants or gold nanomaterials in different matrices [196, 199–205]. The SPR properties seem to be influenced by the chemical environment around the NPs and can be greatly altered if the surface of the gold NPs is chemically bound to ligands [196, 199–202]. The ligands that are chemically bound to Au NPs prevent coalescence of the NPs by counterbalancing the van der-

[1] The chapter 4 is reprinted by permission from ref [188]
J. Phys. Chem. C 2019, 123, 13344−13353; DOI:10.1021/acs.jpcc.9b01739

Waals attractive forces [76, 206, 207]. Coupling NPs with chemical ligands potentially reduces the electron density of the conduction electrons, thereby, altering the effective optical refractive index in the near field of the NPs [76, 77, 207]. A remarkable work was carried out by Peng et al.[76] on the plasmon absorption spectrum of spherical silver (Ag) NPs with diameters in the range of 2-20 nm. They observed an interesting trend where the absorption peak of the ligand-conjugated Ag NPs shifted to higher energies when size was decreased from 20 to 12 nm, whereas the absorption peak shifted to longer wavelengths with the further reduction of the size. This unusual trend was assigned to the ligand effect on SPR absorption. Although significant progress was made on gold NPs of varying sizes and shapes, corresponding research on ligand-protected plasmonic gold NPs such as thiolated gold NPs was rather limited [9, 11, 12, 20, 47, 61, 64, 65, 69, 131, 162]. In recent years, thiolate-protected gold clusters have received enormous research attention as the clusters with sizes less than 2 nm seem to show interesting quantum size behavior and excitonic properties [90, 109, 196–198, 208–210]. The advent of modern synthetic and characterization techniques has made the science of atomically precise thiolate-protected gold clusters interesting for theoreticians and experimentalists. Even thiolate-protected gold clusters show plasmonic properties and Au_{329} protected with hexane thiol was found to be the smallest aliphatic thiolate protected plasmonic Au NPs [86, 211, 212]. The composition of 76.3 kDa aliphatic or aliphatic-like (SC_2Ph) thiolate-protected gold cluster has been found to be $Au_{329}(SR)_{84}$ (where SR is the thiolate ligand) by employing SC_2Ph, SC_6, and SC_{12} ligands with and without Cs^+ adducts [213]. A closely related composition of $Au_{333}(SR)_{79}$ has been reported for the 76.3 kDa cluster based on Cs^+ adduct peaks and it remains to be addressed [93, 214]. Recently, hexane thiolate-protected $Au_{\sim 1400}$ and $Au_{\sim 2000}$, two new sizes in aliphatic thiolate-protected plasmonic Au NPs of size ~3.6 and ~3.8 nm, respectively, have been reported [89, 215].

One common way to study plasmons in metal nanoparticles is via the use of ultrafast transient spectroscopy and corresponding pump-power dependence that yields information of electron dynamics [92, 93, 131, 216–223]. Illuminating the metallic nanoparticles by a femtosecond laser pulse will perturb the electron distribution in them due to absorption of the heat. This phenomenon creates non-thermalized electrons that have a higher temperature in comparison to other conduction band electrons [93, 131, 215–218, 220]. These electrons transfer their extra

heat to the surrounding medium in three processes: 1) electron-electron collision, 2) electron-phonon scattering and 3) phonon-phonon interaction (see Figure 4. 1) [93, 131, 215–218, 220].

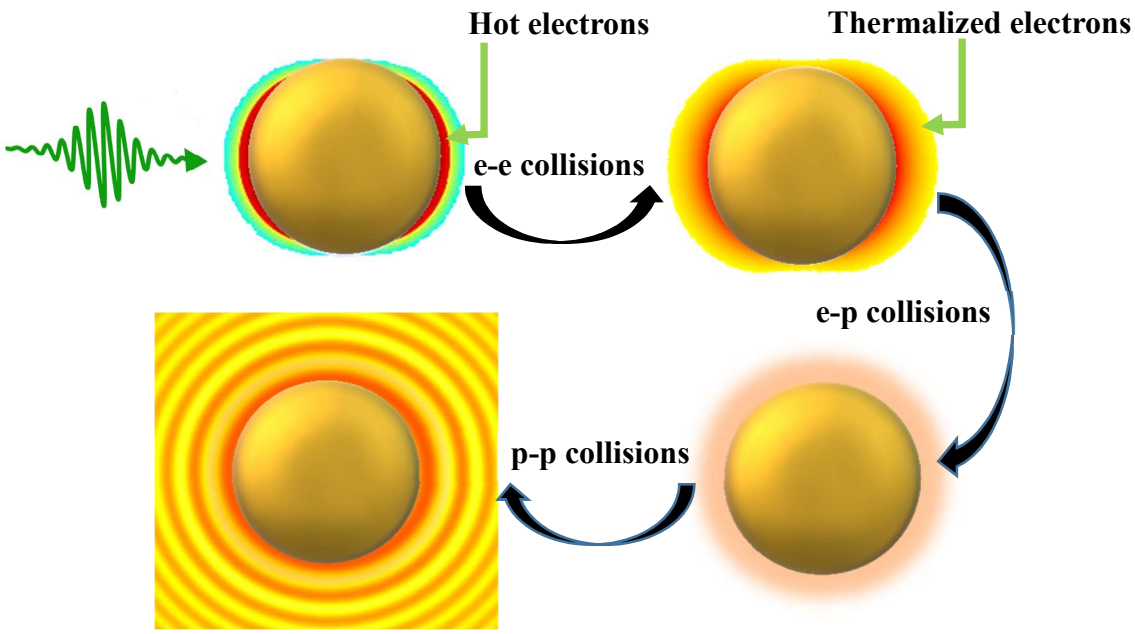

Figure 4.1. Schematic of the relaxation dynamics of the heated NP through electron-electron collision (~ 0.1 ps), electron-phonon scattering (~1 ps) and phonon-phonon interaction (~ 10-100 ps).

Comprehensive understanding of the relaxation processes of metal NPs yielded valuable information that was useful for applications like exciton-plasmon energy transfer and optical switching [217–222]. Link and El-Sayed investigated pump-power, size, and shape effects on electron-phonon (e-p) relaxation dynamics in gold and silver nanospheres and nanorods in size range from 10 to 100 nm [131]. The studies demonstrated that e-p relaxation dynamics was independent of the size and shape of NPs [131]. Similarly, Hodak and co-workers reported a size-independent electron-phonon coupling in Au NPs in the 2.5-8 nm range in aqueous solution [217]. Link et al. embedded 14.5 nm and 12.1 nm Au NPs in $MgSO_4$ powder and solution to test the effect of the surrounding medium on the recovery time of plasmon bleach [218]. They found that electron-phonon relaxation time of Au NPs in $MgSO_4$ powder is higher than in solution by a factor of 2 that was assigned to the effect of the medium. In recent work, e-p dynamics of the different-sized gold NPs conjugated with the chemical-ligand have been studied [93]. By mapping the

bleach recovery dynamics of these NPs, Zhou et al. demonstrated that Au clusters with diameters larger than 2.3 nm show metallic behavior, whereas NPs with a diameter smaller than 1.7 nm display pure molecular behavior. In addition, it was shown that particles with 1.7 to 2.3 nm range show both metallic and excitonic behavior. In a recent study, the first crystal structure of plasmonic gold nanocrystal, TBBT-protected Au_{279} has been reported [224]. More recently, our group studied the optical properties of $Au_{36}(SR)_{24}$, $Au_{44}(SR)_{28}$, $Au_{133}(SR)_{52}$, and $Au_{279}(SR)_{84}$ using steady-state and transient absorption (TA), time-dependent density function theory, and density of state calculations [92]. By observing power-dependent bleach recovery kinetics in Au_{279} $(SR)_{84}$, our group reported that it is the smallest gold thiolate NP that has shown metallic behavior and supports localized SPR.

The type of ligand (aliphatic/aromatic/bulky) being used determines the structure and properties of metal clusters [91, 225]. Although significant research has focused on molecule-like properties of gold clusters and how ligands alter their optical properties, the same influence of ligands on the e-p relaxation dynamics of ultra-small clusters has not been addressed. In addition, previous theoretical studies have neglected the chemical ligand effect on the conductivity of Au NPs and consequently on their e-p relaxation. In the present work, e-p relaxation dynamics of smallest-sized plasmonic gold clusters conjugated with different thiolate ligands was studied using ultrafast pump-probe spectroscopy. To explore the effect of aromatic and aliphatic ligands on the electron dynamics, investigations were carried out on Au_{279} ($d \approx 2.1$ nm [224]) passivated with TBBT and Au_{329} ($d \approx 2.2$ nm [226]) passivated with phenylethane thiol (SC_2Ph), and hexane thiol (SC_6). To understand the ligand effects theoretically, the free electron density of the clusters was modeled using three-layered Mie theory [181], inspired by Peng et al.[76]. The size effect on the electron dynamics in aliphatic thiolate protected plasmonic gold clusters was investigated by studying the optical properties of hexane thiolate protected Au_{329} ($d \approx 2.2$ nm), $Au_{\sim 1400}$ ($d \approx 3.6$ nm), and $Au_{\sim 2000}$ ($d \approx 3.8$ nm).

4.2. Methods

4.2.1. Synthesis and Characterization of the Clusters

Au_{279} $(TBBT)_{84}$, Au_{329} $(SC_2Ph)_{84}$, Au_{329} $(SC_6)_{84}$, $Au_{\sim 1400}$ (SC_6) and $Au_{\sim 2000}$ (SC_6) were synthesized following the reported protocols from ref. [224], ref. [226], ref. [212], ref. [89], and

ref. [215], respectively. Citrate stabilized gold NPs were synthesized following a procedure published elsewhere [227].

4.2.2. Transient AbsorptionMeasurements

Femtosecond TA measurements were carried out at the Center for Nanoscale Materials, Argonne National Laboratory [212]. In brief, a Spectra Physics Tsunami Ti:Sapphire, 75 MHz oscillator was used to seed a 5 KHz Spectra-Physics Spit-fire Pro regenerative amplifier. 95% of the output from the amplifier is used to pump a TOPAS optical parametric amplifier, which is used to provide the pump beam in a Helios TA setup (Ultrafast Systems Inc.). A pump beam of 370 nm was used for the measurements. The remaining 5% of the amplified output is focused onto a sapphire crystal to create a white light continuum that served as the probe beam in our measurements (450-700 nm). The pump beam was depolarized and chopped at 2.5 kHz, and both pump and probe beams were overlapped in the sample for magic-angle transient measurements.

4.2.3. Theoretical Modeling

From the TA measurements, it was shown that the ligand plays an important role in the surface plasmon bleach spectral width as well as e-p relaxation time and coupling strength. To understand this behavior, the SPR bleach was modeled with three-layered Mie theory (refer to chapter 2) [76, 82, 181]. We considered the modeling geometry as a single NP because of the fact all of the investigated clusters characterized by mass spectrometry [89, 212, 215, 224, 226] and have very narrow size distribution. In our simulation, the NP has been considered to be a sphere in order to take into account all of the possible orientations of the icosahedral NPs to the incident light beam. In addition, as these NPs are coated with the ligand layer which alters the conductivity of the surface and core region of the NP differently, the three-layered Mie theory has been used to simulate their optical properties (refer to chapter 2).

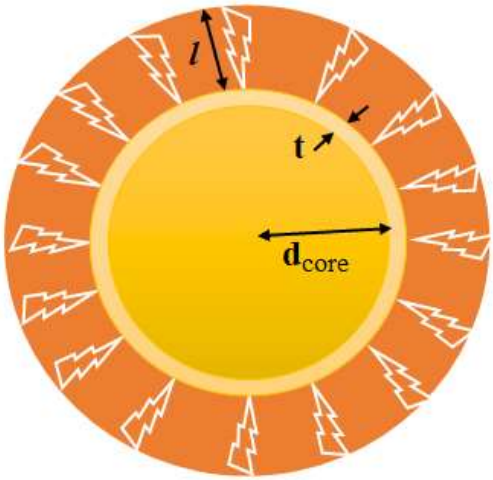

Figure 4.2. Schematic illustration of three layers structure of spherical NPs consists of the core region of diameter d_{core}, and skin and surrounding chemical ligand with a thickness of t and *l*, respectively.

As illustrated in Figure 4.2, the three layers structure of gold clusters consists of a core region with a diameter of $d_{core} = d_{NPs} - 2t$, skin layer with a thickness of *t*, and chemical ligand with a width of *l*. We fixed *t* to be roughly the thickness of an atomic Au layer (or Au-Au bonding length), t = 0.28 nm. In addition, in our simulation, the diameter of clusters were obtained from the literature and are taken as: $d_{279} = 2.1$ nm [224], $d_{329} = 2.2$ nm [226], $d_{\sim 1400} = 3.6$ nm [89], and $d_{\sim 2000} = 3.8$ nm [215]. The thickness of chemical ligands was fixed to $l = 0.8$ nm. Finally, the refractive index was used as 1.492, 1.43, and 1.375 for the TBBT, SC_2Ph, and SC_6 ligands, respectively [228]. In this work, values of the electric permittivity of a bulk Au at different wavelengths were taken from experimental data provided by Johnson and Christy [78]. We applied Eqs. 2.4 and 2.7 to obtain the dielectric function of the Au_{13nm} and all ligand-protected clusters, respectively.

4.3. Results and Discussion

4.3.1. Ultrafast Transient Absorption Measurements

The optical absorption spectra of the investigated gold clusters are shown in Figure 4.3. The linear absorption maxima of smaller sized ligand-protected gold clusters are appearing at around 500- 510 nm, much below the expected surface plasmon absorption of larger-sized gold NPs. This condition is arising because of the overlapping of inter-band transitions with the surface

plasmon absorption, thereby shifting the shape and maximum of absorption maximum to higher energies. Because of this reason, the linear absorption of the thiolate-protected clusters is unable to represent the true surface plasmon absorption. Thus, to model the ligand effects on the SPR, we used the bleach spectrum obtained from TA measurements.

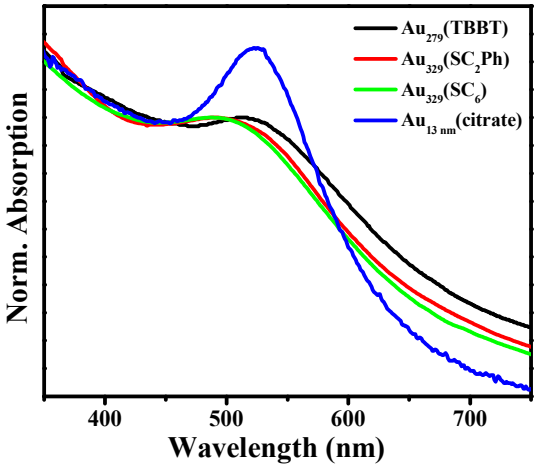

Figure 4.3. Normalized absorption spectra of Au_{279}(TBBT), $Au_{329}(SC_2Ph)$, $Au_{329}(SC_6)$ and 13-nm citrate stabilized gold nanoparticles.

TA measurements were carried out after excitation at 370 nm for all clusters and probing in the visible region. Pump-power dependent TA measurements were carried out to follow the electron dynamics. Parts A, B, C, D, E, and F of Figure 4.4 show the TA spectra at a pump energy of 120 nJ for Au_{279} (TBBT), Au_{329} (SC_2Ph), Au_{329} (SC_6), Au_{1400} (SC_6), Au_{2000} (SC_6), and $Au_{13\ nm}$ (citrate), respectively. Excitation of the NPs creates hot electrons and their relaxation is often monitored using pump-power dependent TA measurements [131, 215, 216, 220]. As observed in Figure 4.4, a negative absorption with two positive wings was observed for all investigated gold clusters. The bleach maximum is attributed to SPR absorption of the clusters and the accurate maximum was determined by the fit of the bleach curve [93, 131, 220, 223, 229, 230]. The bleach maximum has shifted to higher energies for all samples with an increase in time, except for Au_{329} (SC_2Ph) that has shown two peaks (see Figure 4.4). The presence of two peaks for Au_{329} (SC_2Ph) in the bleach spectrum was also observed by Zhou and co-workers and is quite interesting to see why such behavior was observed for this cluster [93].

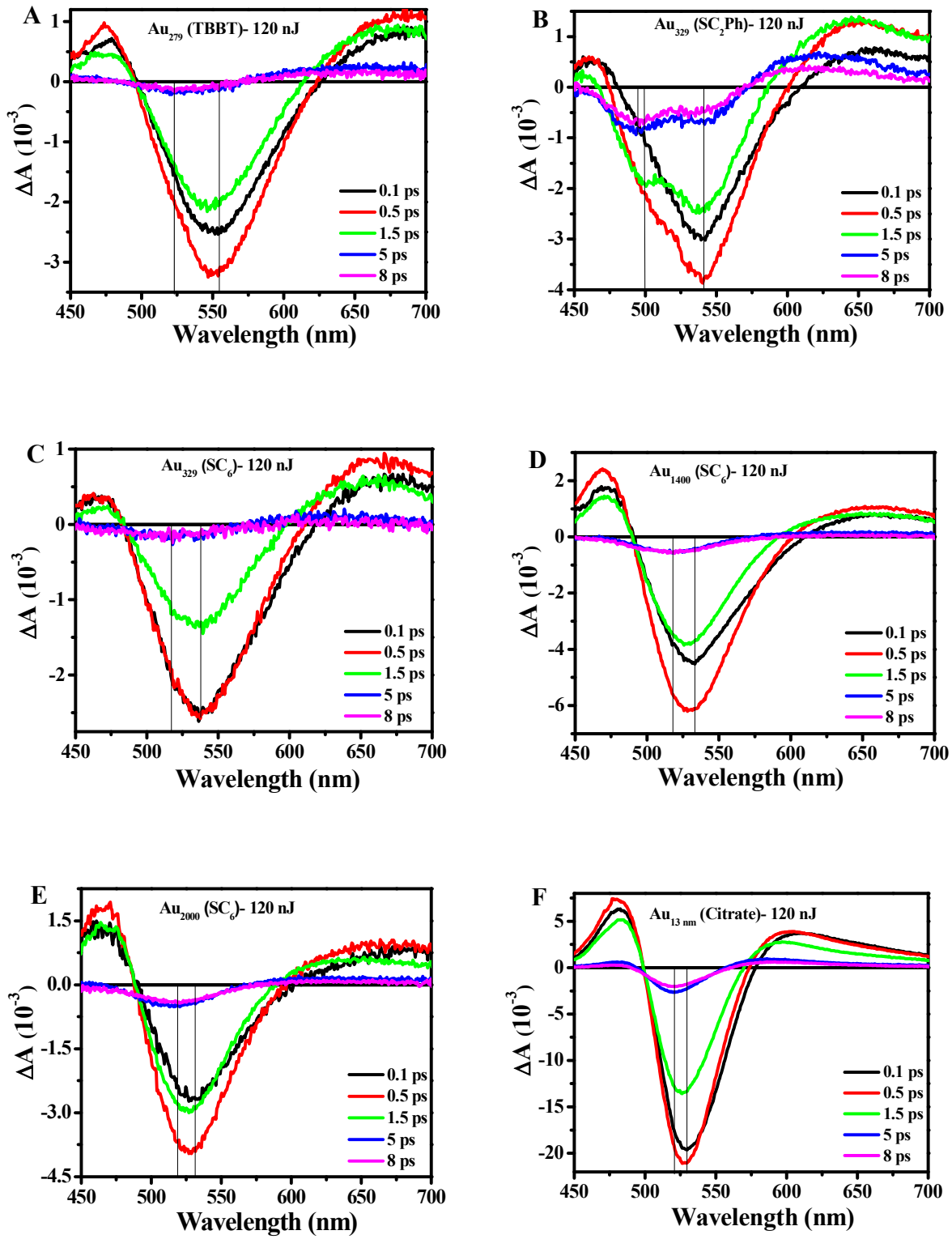

Figure 4.4. Transient absorption spectra at different time delays for (A) Au_{279} (TBBT), (B) Au_{329} (SC_2Ph) (C) Au_{329} (SC_6), (D) Au_{1400} (SC_6) and (E) Au_{2000} (SC_6) and (F) $Au_{13\ nm}$ (citrate) after excitation at 370 nm.

The shift of the bleach maximum to the higher energies is attributed to a decreased electronic temperature of the illuminated clusters because of the heat transfer to the phonon bath. From Figure 4. 4, it can be seen that the bleach maximum of the ligand-passivated gold clusters is shifted to lower energies as well as broadened when compared to ligand-free gold nanoparticles [76].

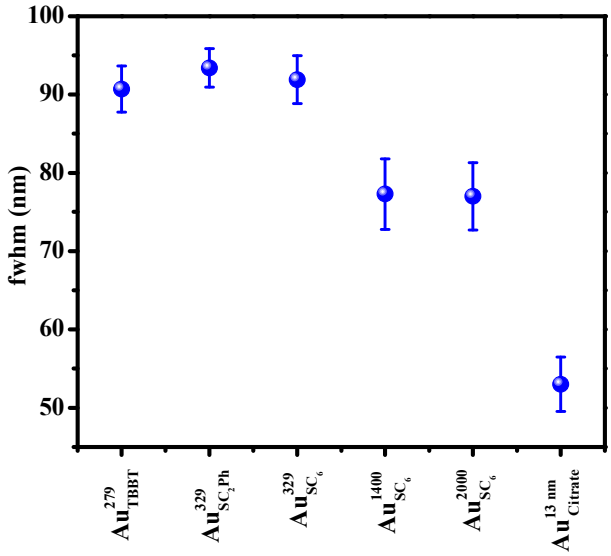

Figure 4.5. fwhm of the studied samples at a time delay of 0.5 ps for the pump energy of 120 nJ.

The full width at half maximum (fwhm) depends on many factors, such as the size of NPs, polydispersity in size and shape, and chemical bonding between the NPs and ligand [76]. Although the ligand exchange can diphase the oscillations of the plasmonic electrons by adding an additional decay channel due to the transient in and out tunneling in interfacial orbitals with the NP and ligand [231–233], the size of the NPs plays a dominant role in plasmonic damping (see Figure 4.5). As demonstrated in the Figure 4.5 and Figure 4.6, the fwhm of the smaller samples (Au_{279} (TBBT), Au_{329} (SC_2Ph), and Au_{329} (SC_6)) at a delay time of 0.5 ps were determined to be ~92 nm, which decreases with further increasing the size of the samples and reaches to ~53 nm for 13 nm - Au.

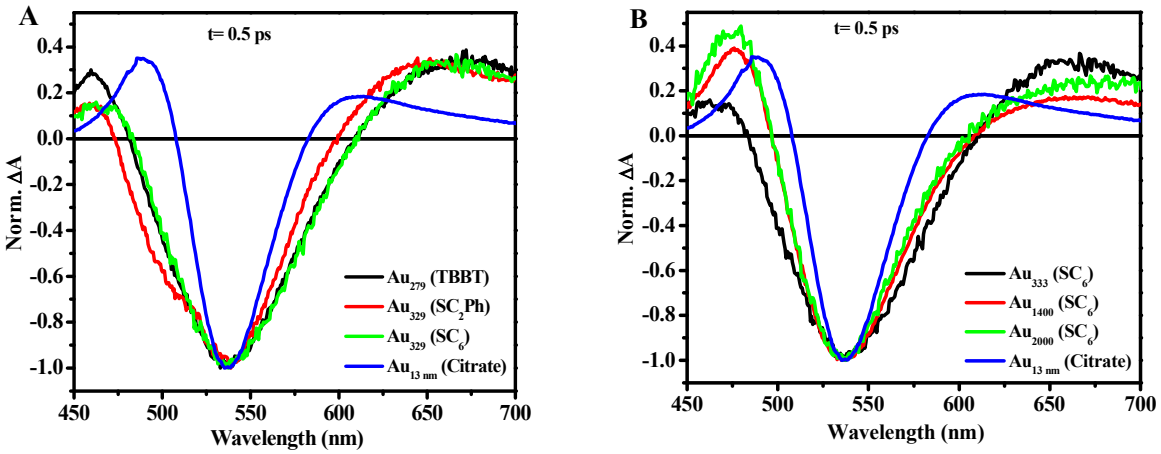

Figure 4.6. Comparison the plasmon damping of (a) Au_{279} (TBBT), Au_{329} (SC_2Ph), Au_{329} (SC_6), and $Au_{13\ nm}$ (citrate), and (b) Au_{329} (SC_6), Au_{1400} (SC_6), Au_{2000} (SC_6), and $Au_{13\ nm}$ (citrate) at a time delay of 0.5 ps for the pump energy of 120 nJ. As guides to the eye, the bleach maximum of all samples shifted to ~535 nm and normalized to -1.

As the central aim of the study is to understand the influence of passivating ligand on the electron dynamics, transient bleach recovery dynamics was monitored as a function of pump power. Pump-power dependence of bleach recovery kinetics is a key feature for plasmonic NPs as it alters the electronic temperature of the NPs. Figure 4.7 A-F shows the bleach recovery kinetic traces for the investigated clusters at different pump powers. As expected with an increase in pump-power, the bleach signal increases as the local temperature of cluster increases. Increasing pump energy will heat up more electrons and decelerating the e-p coupling leads to slowing down of electron relaxation [93, 234]. The pump-power dependence of bleach recovery can be modeled using a two-temperature model [235–238]:

$$C_e(T_e)\frac{\partial T_e}{\partial t} = -\gamma(T_e - T_l) + \alpha N \tag{4.1}$$

$$C_l\frac{\partial T_e}{\partial t} = \gamma(T_e - T_l) + \beta N \tag{4.2}$$

where C_e, T_e, and C_l, T_l are heat capacity and temperature of the electron gas and lattice, respectively. αN describes the heating of the electron gas by the initial non-thermalized electrons, βN represents the direct coupling between the non-thermalized electrons and the lattice occurs during the electron gas thermalization process [235], and γ is the e-p coupling constant [13, 217, 239, 240]. The electron heat capacity of the metals is proportional to the electron gas temperature.

Increasing the temperature of electron gas reduces the e-p effective coupling rate ($\gamma/C_e(T_e)$), deaccelerating the e-p coupling time.

4.3.2. Calculating Electron-Phonon Coupling Time

The non-normalized (ΔA) and normalized bleach recovery (-Norm. ΔA) for the investigated clusters are shown in Figure 4.7 A-F and Figure. 4.8 A-F, respectively. To extract electron-phonon relaxation for each cluster, the bleach recovery dynamics was fitted (see Figure 4.7 and 4.8) using [93, 241, 242]:

$$\Delta A(t) = \int_{-\infty}^{\infty} H(\tau)\left[A\left(1 - e^{-\tau/\tau_{ee}}\right)e^{-\tau/\tau_{ep}} + B\left(1 - e^{-\tau/\tau_{ep}}\right)\right] e^{-(\tau-t)^2/\tau_0^2}\, d\tau \quad (4.3)$$

where H(τ) is the Heaviside function, A and B are e-e and e-p scattering amplitudes, where $|B| < |A|/10$. τ_{ee} is e-e coupling time and is on the order of a few hundred femtoseconds, and τ_{ep} is e-p coupling time and is on order of ~ 1 ps. τ_0 is the instrument response obtained by the cross-correlation of the pump and probe beams. From the intercept and slope of the linear fit of e-p relaxation lifetime versus pump energy, intrinsic e-p coupling time and e-p coupling strength for all samples were determined and are provided in Table 4.1.

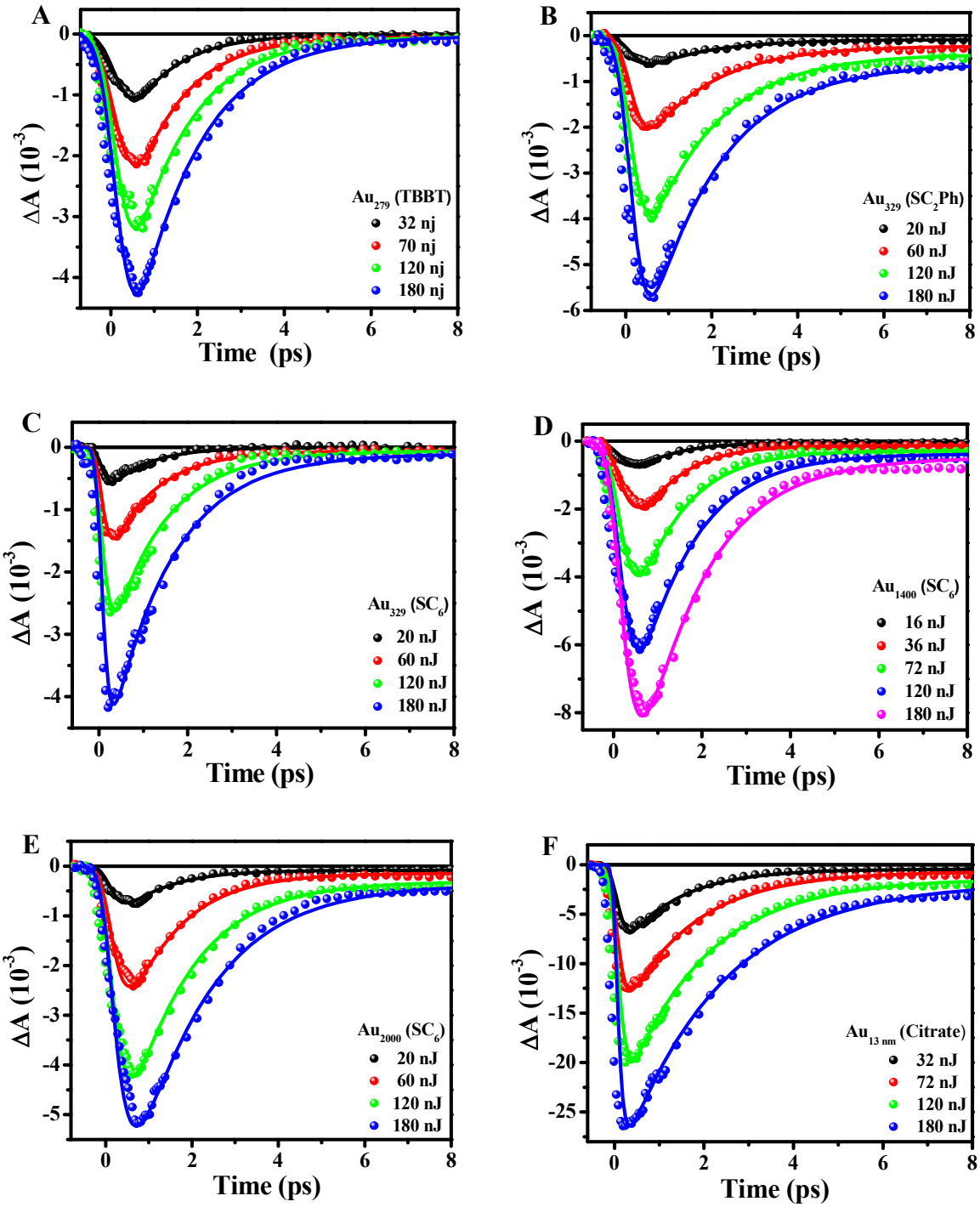

Figure 4.7. Temporal evolution of the e-p dynamics of (A) Au_{279} (TBBT), (B) Au_{329} (SC_2Ph), (C) Au_{329} (SC_6), (D) Au_{1400} (SC_6), (E) Au_{2000} (SC_6), and (F) $Au_{13\ nm}$ (citrate) for different pump powers at their corresponding bleach maximum wavelength. Solid lines are the fit of the bleach curve.

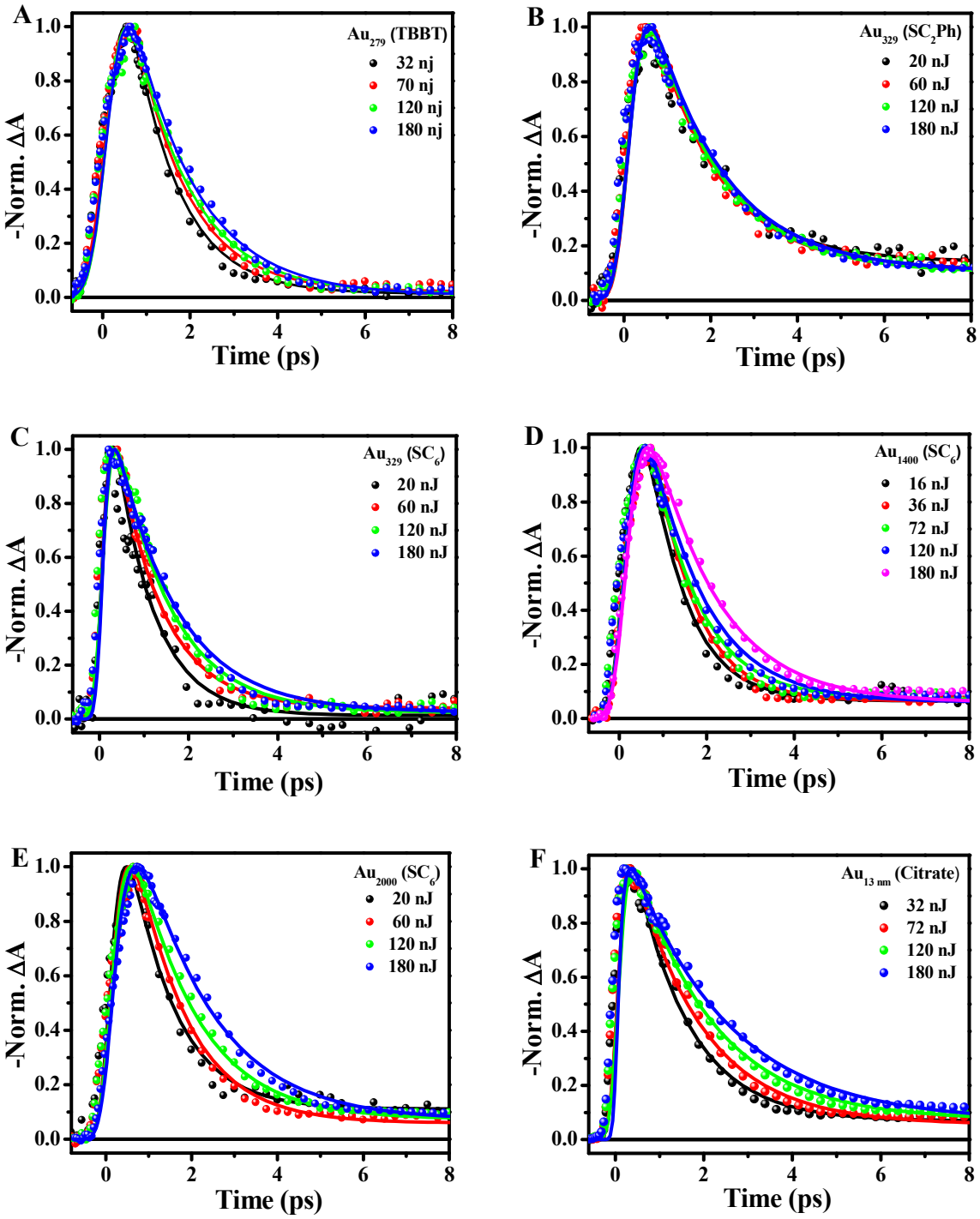

Figure 4.8. Normalized bleach recovery kinetics (-ΔA) of (A) Au_{279} (TBBT), (B) Au_{329} (SC_2Ph), (C) Au_{329} (SC_6), (D) $Au_{\sim 1400}$ (SC_6), (E) $Au_{\sim 2000}$ (SC_6), and (F) $Au_{13\ nm}$ (citrate) at different pump powers.

Figure 4.9A shows the plot of calculated τ_{ep} at different pump energies for Au_{279} (TBBT), Au_{329} (SC_2Ph), Au_{329} (SC_6), and $Au_{13\ nm}$ (citrate) NPs. As seen from the figure, the slopes and intercepts varied for different clusters. Au_{279} (TBBT) and Au_{329} (SC_6) has shown an intercept of close to 1 and 0.8 ps, respectively, whereas Au_{329} (SC_2Ph) has shown an intercept of 1.4 ps. Similar higher intercept was also observed by Zhou et al.[93] for Au_{329} (SC_2Ph). One another interesting observation is the difference in slopes for Au_{279} (TBBT), Au_{329} (SC_6), and the 13 nm Au cluster. The slope is smaller for Au_{279} (TBBT) when compared to Au_{329} (SC_6), which is much smaller than that of 13 nm Au NP (see Table 4.1). This is attributed to differences in electric conductivities because of the nature of passivating ligands. Aromatic passivating ligands seem to have smaller slopes and higher intercepts when compared to hexane thiol ligand. Also, the plot of e-p relaxation as a function of pump power for different-sized SC_6-protected gold cluster is shown in Figure 4.9B. It can be observed from the Figure 4.9B and Table 4.1 that with an increase in size, total electric conductivity increases slightly due to a decrease of the surface to volume ratio, and thereby increasing the intercept (intrinsic electron-phonon coupling time) and slope (electron-phonon coupling strength). However, the slope is definitely smaller when compared to $Au_{13\ nm}$ NP that was passivated with a surfactant, again signifying the importance of the ligand on electron-phonon relaxation dynamics.

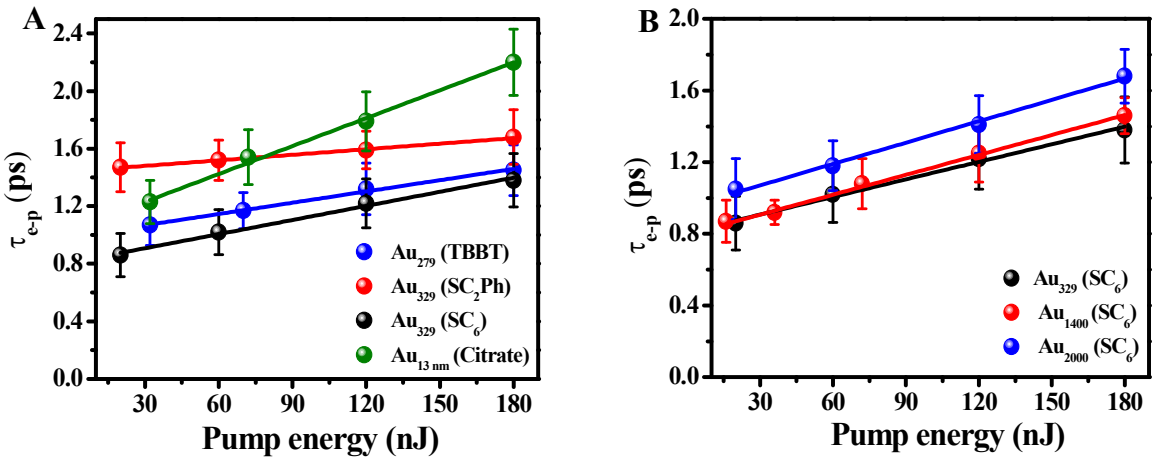

Figure 4.9. Electron-phonon relaxation as a function of pump pulse energy for (A) Au_{279} (TBBT), Au_{329} (SC_2Ph), Au_{329} (SC_6), and $Au_{13\ nm}$ (citrate), (B) Au_{329} (SC_6), $Au_{\sim 1400}$ (SC_6), and $Au_{\sim 2000}$ (SC_6).

Table 4.1. Electron-Phonon coupling time and coupling strength obtained from power-dependent bleach recovery kinetics of the investigated clusters

	Au_{279}-TBBT	Au_{329}-SC_2Ph	Au_{329}-SC_6	$Au_{\sim1400}$-SC_6	$Au_{\sim2000}$-SC_6	Au_{13nm}-citrate
Slope	$(2.6 \pm 0.3)\times10^{-3}$	$(1.2 \pm 0.2)\times10^{-3}$	$(3.2 \pm 0.3)\times10^{-3}$	$(3.7 \pm 0.3)\times10^{-3}$	$(3.9 \pm 0.3)\times10^{-3}$	$(6.0 \pm 0.4)\times10^{-3}$
Intercept	1.0± 0.2	1.4 ± 0.2	0.8 ± 0.2	0.8± 0.1	1.0± 0.2	1.0 ± 0.2

4.3.3. Ligand Effect on Electron Conductivity

Among all investigated clusters, unique behavior was observed for Au_{329} (SC_2Ph). The transient bleach of Au_{329} (SC_2Ph) has shown two negative bleach peaks around ~493 and 540 nm. A similar result was reported by Zhou and co-workers and assigned to the excitonic and plasmonic behavior of the cluster [93].

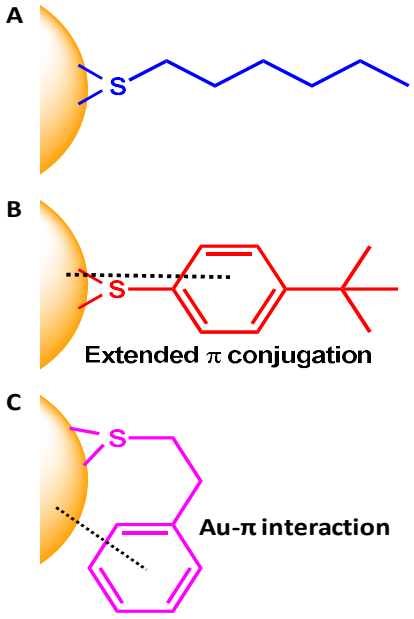

Figure 4.10. Cartoon diagram depicting the interaction of (A) SC_6, (B) STBBT, and (C) SC_2Ph, with the surface of gold atoms.

Interestingly, a closer look to the TA spectrum of the samples in Figure 4.4 reveals that transient bleach of the Au_{329} (SC_2Ph) is higher than Au_{279} (TBBT) and Au_{329} (SC_6), respectively. This unusual result can be ascribed to specific Au-π interaction between the aromatic ring in

phenylethane thiol and surface gold atom of Au_{329} (SC_2Ph), significantly reducing the electric conductivity of the surface and core layers of the cluster (see Figure 4.10). This specific Au-π interaction potentially reduces the free electron density of Au_{329} significantly (refer to Theoretical Modeling section), thereby creating a hybrid state [93] (metallic/molecular) for it. Additional modeling is necessary to understand the influence of passivating ligands on electron density in these clusters.

As the transient bleach at initial times represents the SPR bleach, the spectrum at a time delay of 500 fs has been used into the fit to the theoretical absorption spectra (see Figure 4.11) in order to obtain the electronic conductivities and corresponding g_{core} and g_{skin} [93, 131, 220, 223, 229, 230]. Obtained g_{core}^2 and g_{skin}^2 from the analysis for different samples are shown in Figure 4. 12A. A closer inspection of Figure 4.12A reveals interesting trends. Both g_{core}^2 and g_{skin}^2 values for aromatic passivating ligands are much smaller when compared to the hexane thiol passivating ligand. Also, the g_{skin}^2 obtained for SC_2Ph is much smaller than that for TBBT, and the results are consistent with experimentally observed electron dynamics in these clusters. The modeling suggests that it is the electron density difference, which is crucial for electron dynamics in these clusters. Due to the direct interaction between the chemical ligand and surface layer, electron conductivity of the outermost layer of the metallic NPs is decreased more when compared to the core region. In agreement with our experimental results, aromatic ligands, especially SC_2Ph, lowered the conductivity of the NPs more when compared to hexane thiol. As mentioned above, owing to the specific Au-π interaction between the surface gold and SC_2Ph ligand, the free electron density of the skin and core regions of Au_{329} are lowered by a factor of 0.64 and 0.9, respectively. This significant reduction of the electron conductivity, especially for the outermost layer, is a further justification of deaccelerated electron-phonon dynamics in Au_{329} (SC_2Ph) and is the reason for observed smaller power dependence for this cluster. Also, smaller electron conductivity was also observed for Au_{279} (TBBT) that can be attributed to the Au-π interaction. However, this interaction is probably the reason for observing plasmon behavior for this cluster even though its size is smaller when compared to Au_{329}.

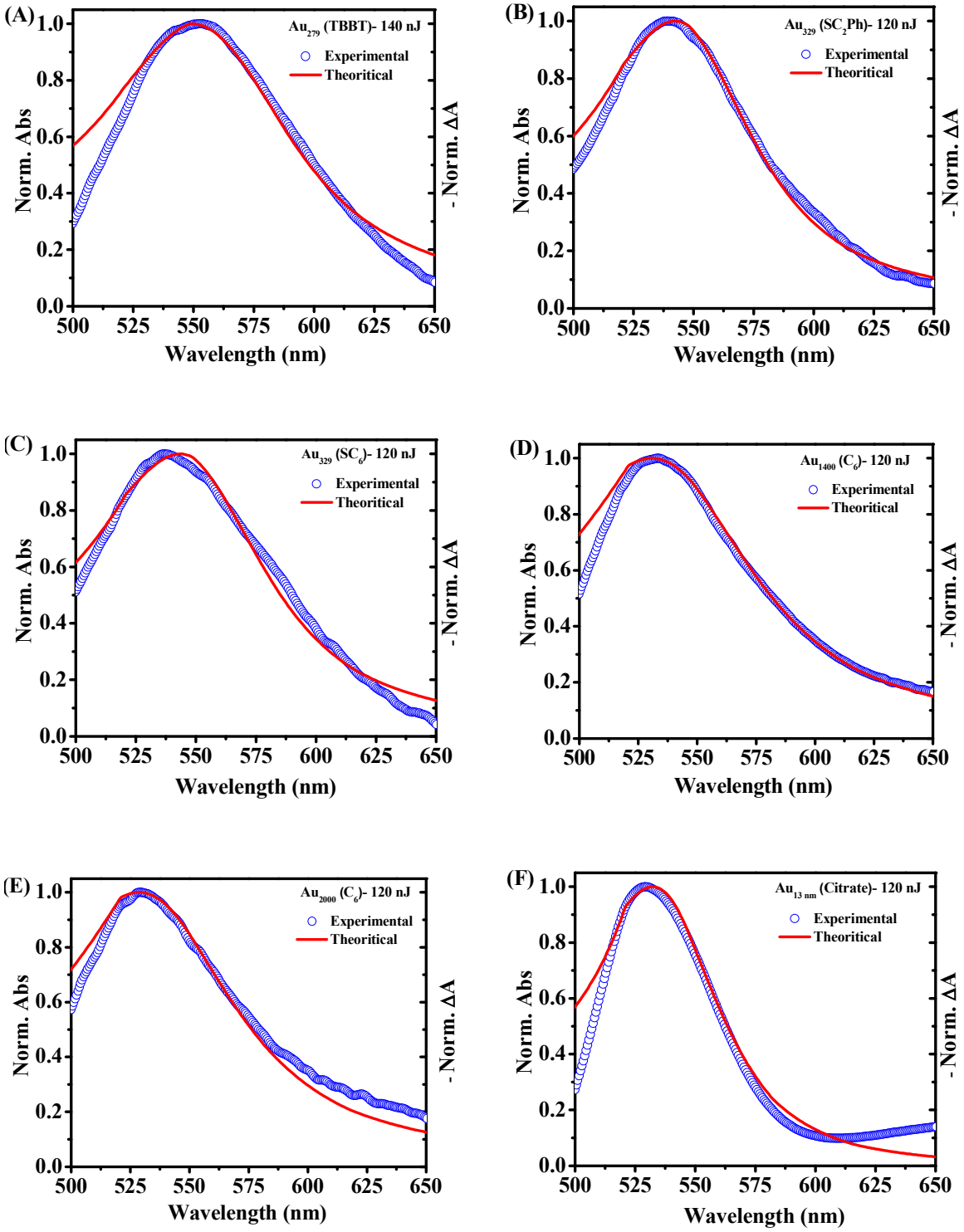

Figure 4.11. Normalized theoretical absorption spectra which fitted into the normalized experimental bleach at t≈ 500 fs: (A) Au_{279} (TBBT), (B) Au_{329} (SC_2Ph), (C) Au_{329} (SC_6), (D) Au_{1400} (SC_6), (E) Au_{2000} (SC_6), and (F) $Au_{13\ nm}$ (citrate) for their corresponding pump power mentioned on their corresponding legend.

For the clusters with same SC_6 passivating ligand, the g_{skin}^2 values have slightly increased with an increase in cluster size, whereas g_{core}^2 values are the same as those of 13 nm Au NP and increased electron conductivity with increase in the size of the cluster (see Table 4.2). Present results show zero reduction in the number of free electrons in citrate-capped 13 nm Au NPs. The total conductivity correction factor of each cluster has been calculated by

$$g_t^2 = g_{core}^2 f_{core} + g_{skin}^2 f_{skin} \quad (4.4)$$

where f_{core} and f_{skin} are core and skin volume fraction, respectively. As shown in Figure 4.12B, the total conductivity correction factor of Au_{329} (SC_2Ph) is smaller than other samples. In addition, for the clusters with the same SC_6, owing to the decreasing surface to volume ratio, the total modified conductivity increases with increasing size of the samples. The three-layered Mie theory results were able to accurately model the influence of the ligand on electron density and their effect on plasmon quality factor. This ligand influence can have consequences for electric field enhancement offered by ligand-protected plasmonic clusters.

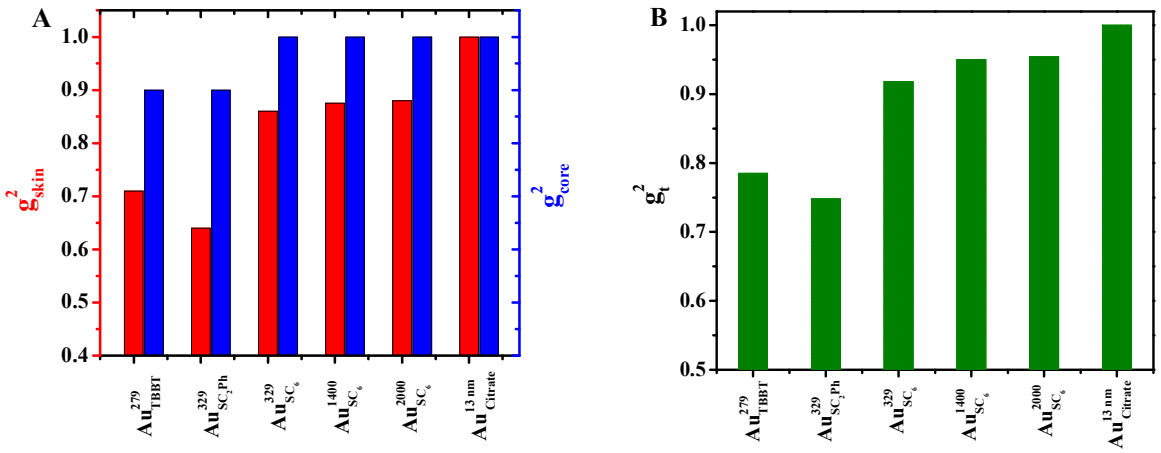

Figure 4.12. (A) Free electron density correction factor of the outermost layer (g_{skin}^2) and core region (g_{core}^2), (B) total free electron density correction factor (g_t^2) of the investigated Au clusters.

Table 4.2. Summary of the studied samples and their characteristics. FWHM of each sample has been at the delay time of 0.5 ps for the pump energy of 120 nJ

Samples	Size (nm)	FWHM (nm)	g_{core}^2	g_{skin}^2	$t_{e\text{-}ph}$
Au_{279} (TBBT)	2.1	91 ± 3	0.9	0.71	1.0 ± 0.2
Au_{329} (SC_2Ph)	2.2	93 ± 3	0.9	0.64	1.4 ± 0.2
Au_{329} (SC_6)	2.2	92 ± 3	1	0.86	0.8 ± 0.2
$Au_{\sim 1400}$ (SC_6)	3.6	77 ± 5	1	0.875	0.8 ± 0.1
$Au_{\sim 2000}$ (SC_6)	3.8	77 ± 4	1	0.88	1.0 ± 0.2
$Au_{13\ nm}$ (Citrate)	13	53 ± 4	1	1	1.0 ± 0.2

CHAPTER 5

THEORETICAL INVESTIGATION OF SIZE, SHAPE AND ASPECT RATIO EFFECT ON THE LSPR SENSITIVITY OF HOLLOW-GOLD NANOSHELLS[2]

5.1. Introduction

Plasmonic sensors have attracted enormous scientific interest in recent years as the optical properties are governed by strong coupling between the incident light and conduction electrons leading to LSPR [11, 12, 14, 25, 37–39, 43, 60, 101, 146, 151, 186, 243–256]. The LSPR leads to strong scattering and absorption of incident light, resulting in highly localized and amplified electric field around the NPs [1, 12, 14, 61, 64, 101, 151, 185] and plays a vital role in applications of plasmonic NPs [11, 12, 14, 25, 37–39, 43, 60, 101, 146, 151, 186, 243–256]. Among plasmonic NPs, gold NPs have received significant attention for biological and chemical applications as they are non-toxic, biocompatible, inert and ease of synthesis [67, 68]. Also, Au nanoparticles possess strong extinction spectra with LSPR peak that can be tuned from visible to near infrared region based on their size, shape and configuration [256]. The tunability of LSPR peak into the near infrared region is highly desirable, especially for biological applications as the human tissue has the highest transparency in this frequency region [248, 257]. The LSPR maximum of plasmonic NPs is very sensitive to the refractive index (RI) of the surrounding medium and shifts to longer wavelengths with an increase in RI. Since the RI of biological or chemical analytes is usually higher than the RI of the surrounding medium [258], binding of the molecules to the surface of the plasmonic NPs alters the effective RI of the surrounding medium, redshifts the LSPR maximum and changes the electric field intensity around the NP [11, 12, 14, 25, 37-39, 43, 60, 101, 146, 151, 186, 243–256]. In addition, the localized enhanced electric field around plasmonic NPs decay exponentially with increasing distance from the surface that creates a small sensing volume and

[2] The Chapter 5 is reprinted by permission from ref [27]
J. Chem. Phys. 150, 144116 (2019); https://doi.org/10.1063/1.5090885

detects the target molecules in the close vicinity of the NPs [25]. The LSPR peak shift, which is the basis of the majority of LSPR sensing applications, can be detected by measuring scattered light from the NPs [25]. However, to sense the RI change induced LSPR peak shift of the small-sized NPs that weakly scatter incident light, ensemble extinction methods are commonly used [25].

LSPR biosensors offer a wide range of advantages such as low-cost, higher surface to volume ratio, facile surface chemistry, detecting of several different targets at the same time and monitoring binding of molecules in real-time [186, 250, 251, 256]. For example, a gold nanorod with different aspect ratios have been used for multiplex sensing by monitoring the distinct LSPR peak shift caused by the binding of three different molecules on their surfaces [186]. In another study, to determine the concentration of the microRNAs (miRs) in the plasma or blood of pancreatic cancer patients, Joshi et al. applied nanoprism Au nanoparticles to detect and measure miRs [259]. Using LSPR sensing technique, they observed that concentration of miR-10b is almost four times greater than of miR-21 in pancreatic cancer patients [259]. More recently, Sriram et al. developed an analyzing technique to detect interleukin-6 (IL-6) protein based on the changing in color from plasmonic gold nanoparticles using dark field microscopy and digital camera with a CMOS sensor [260]. They were able to detect 4.76 nM (100 ng/mL) of IL-6 using this technique. However, the main drawback of this method is that its working wavelength range is from 450 nm to 625 nm and can be applied only for NPs that have single plasmon peak.

In contrast to the vast majority of the biological sensors, which need labels such as fluorophores, radioisotopes or enzyme to generate and enhance target signals [38], LSPR based biosensors are label-free [37, 261, 262]. Due to enhanced electric field around NPs, the target molecule signals can be amplified and be used to detect the molecules without chemical or biological labels [37, 261, 262]. In addition, unlike surface plasmon resonance (SPR) sensing that has been widely used for detecting bimolecular interactions [263], LSPR sensing is not sensitive to temperature and requires simple instrumentation [264]. At the same time, LSPR leads to enhanced localized electric field around plasmonic NPs that have shorter decay length in comparison to SPR and results in better sensitivity to changing RI in the close vicinity of the NPs [25, 248]. However, despite the advantages mentioned above, the sensitivity and the signal-to-noise ratio of LSPR sensing is much less than the SPR sensing technique [25, 256]. Thus, designing

and optimizing different LSPR plasmonic nanostructures to obtain higher sensitivity by changing the refractive index of the surrounding medium is desirable for sensing applications [249, 256].

Attaching target molecules to the surface of the NP (see Figure 5.1) alters the effective refractive index of the surrounding medium. Since the refractive index of the target molecules is more the refractive index of the medium, it increases the RI of the surrounding medium and consequently redshifts the LSPR peak wavelength.

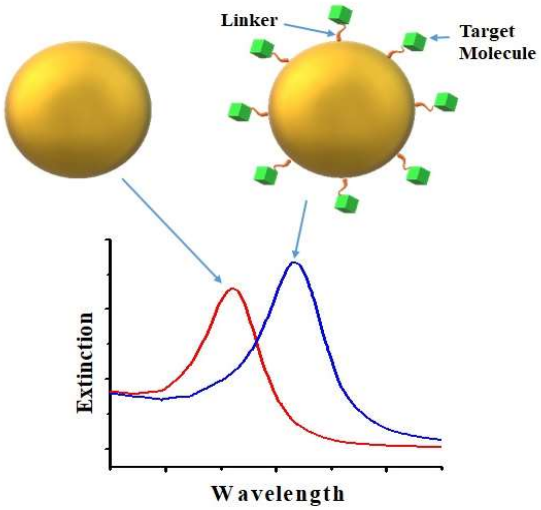

Figure 5.1. Red-shifting of the LSPR peak shift due to attaching target molecules at the surface of the NP.

The LSPR sensitivity of plasmonic NPs is widely defined as LSPR peak shift per surrounding medium refractive index unit (RIU) [23]

$$S = \frac{d\lambda_{LSPR}}{dn} \tag{5.1}$$

In addition to medium effect, the LSPR peak position and its shift, electric field enhancement and its decay length can be adjusted by changing parameters such as shape and size of the NPs, and the polarization direction of incident light [9, 64, 76, 83, 158, 180, 185, 211, 245, 248, 252, 265–267]. All these optical properties can also be adjusted by varying inter-particle distances of neighboring nanoparticles in dimer or trimer structures [63, 77, 103, 132, 156] or

varying shell thickness in core-shell nanostructures [20, 268]. Several research efforts have focused on the shape, size and other parameter effects on the sensitivity of the plasmonic NPs [33, 37, 38, 76, 244, 254, 265, 269, 270]. For example, a sensitivity factor of 408.8 nm/RIU has been reported for a spherical hollow core- Au nanoshells with a mean total size of 50 nm and shell thickness of 4.5 nm, which was almost 6- times stronger than the solid Au NPs with the same diameter [270]. In this study, the core region was filled out with the surrounding medium [270]. In a theoretical work, Jain et al. investigated LSPR sensitivity of spherical silica- gold core-shell with a total diameter of 80 nm and demonstrated that LSPR sensitivity of nanoshells versus shell-to-core ratio shows universal scaling behavior [271]. In addition, due to increased plasmonic coupling between inner and outer surface layers of shell by reducing shell thickness, they had observed significant enhancement of LSPR sensitivity from 129 nm/RIU to 363 nm/RIU when shell thickness decreased from 40 nm (solid sphere) down to 4 nm [271]. In another study, a nanorice nanoshell with longitudinal diameter of 340± 20 nm, transverse diameter of 54± 4 nm and shell thickness of 13.1± 1.1 nm has shown LSPR sensitivity of 801.4 and 103.0 nm/RIU for longitudinal and transverse plasmon modes, respectively [76]. Lee et al. have shown that the LSPR sensitivity of Au nanoparticles increases with increase in the size and the AR. Interestingly, they observed 491.4 (nm/RIU) LSPR sensitivity for Au nanorod with an aspect ratio of 3.4 and effective radius of 20 nm was almost 3.2 and 1.5 times higher when compared to spherical Au NPs with r=20 nm and r=60 nm, respectively [248]. In another study, by varying AR of gold nanorods (with an effective diameter of 50 nm) from 2 to 6, LSPR sensitivity in the range of 200-600 (nm/RIU) has been obtained from FDTD simulations [272]. Dondapati and coworkers have used biotin-modified gold nanostars to sense binding of streptavidin with concentrations as low as 0.1 nM by measuring the plasmon shift [37]. These nanoparticles have shown average sensitivity of 218 nm/RIU [37]. In recent work, Woo et al. elucidated anisotropic property of arrays of Au nanodisks with a structural dimension of 162 and 340 nm, and measured sensitivity of 327 nm/RIU and 167 nm/RIU for longitudinal and transverse modes, respectively [256].

Although extensive research has been carried out on LSPR sensitivity of the different shape solid plasmonic NPs [37, 186, 244, 248, 261, 262, 269, 273] and spherical nanoshells [76, 211, 270, 271], there has been little quantitative analysis of size, shape, shell thickness and aspect ratio effects on the LSPR sensitivity of the hollow/Au nanoshells. In this chapter, we focused on

understanding these parameters' effects on the plasmonic properties of hollow/Au nanoshells in order to obtain structures with higher sensitivity. The main objectives of this study are to probe the effect of (1) size and shell thickness, (2) shape and shell thickness, and (3) aspect ratio on LSPR sensitivity. Multi-layered Mie theory was used to calculate the size effect of LSPR sensitivity for different size gold spheres from 20 to 80 nm. Then, to understand the shape effect, we have performed simulations on disk, rod, ellipsoid, rectangular block, and prism shape NPs with an effective diameter of 40 nm by varying shell thicknesses (see Figure 5.2).

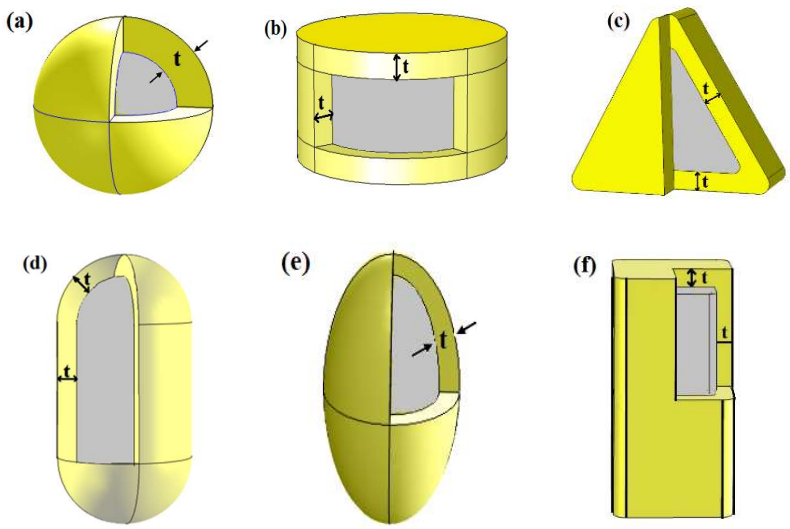

Figure 5.2. Schematic of (a) Spherical, (b) Disk, (c) Triangular Prism, (d) Rod, (e) Ellipsoid and (f) Rectangular block, hollow/Au nanoshells that have been investigated in this work. Sharp corners of the rectangular block and prism have been rounded. To specify the sizes of the non-spherical nanoparticles with volume V, the effective radius is defined as radius of a sphere per equal volume of the particle: $r_{eff} = (3V/4\pi)^{1/3}$. In addition, the rounding radius for the outer surface set to be 2 nm and the inner radius has been calculated by multiplying ratio of the core-to-total size to 2 nm.

Also, we have studied the AR effect on plasmonic properties of rod and rectangular block shaped hollow/Au nanoshells while varying AR from 1 to 5 for a fixed effective diameter of 40 nm. Section 5.2 describes the calculation methods and results and discussion is provided in Section 5.3.

5.2. Calculation Methods

In this work, for bulk Au, values of the dielectric function at different wavelengths were taken from experimental data provided by Johnson and Christy [274]. The modified dielectric function of the hollow-gold nanoshells has been calculated using Eq. 2.2. In addition, $\omega_p = 1.35 \times 10^{16}\ \mathrm{rads}^{-1}$ [274], $\Gamma_0 = 1.06 \times 10^{14}\ \mathrm{rads}^{-1}$ [64], $V_F = 1.4 \times 10^{6}\ \mathrm{ms}^{-1}$ and A=1 have been chosen in our simulation.

In the simulation, multi-layered Mie theory [80, 82, 181] and discrete dipole approximation (DDA) [104, 107, 108, 275, 276] have been used to obtain optical properties of the spherical and non-spherical nanoshells, respectively. All codes were developed by our group in MATLAB Software. To test the DDA codes, the results of DDA code for spherical nanoshells were compared against multi-layered Mie theory, and there was an excellent agreement in the calculation of extinction, absorption and scattering efficiencies by both methods. Then, to check our DDA codes for non-spherical hollow/Au nanoshells, we compared the results with available spectra of solid NPs in the literature [266] for three cases: 1) setting the refractive index of core to be equal to refractive index of the shell, 2) setting the effective radius of the core to be zero, and 3) vanishing shell thickness. In all of the cases, there was an excellent agreement between our results and available data in the literature. Figure 5.2 shows the schematic of six different (Sphere, Disk, Triangular Prism, Rod, Ellipsoid, and Rectangular block) hollow-Au core-shell structures that have been investigated in this research. Rod NPs are made of one cylinder and hemisphere caps at both ends. In addition, to obtain appropriate mesh size for the non-spherical nanoshells, C_{ext} of samples was calculated with different mesh sizes (d= 0.25 nm, d= 0.35 nm, and d = 0.5 nm) to show convergence in the simulation.

Extinction spectra of Rod, ellipsoid, and rectangular block with shell thickness of $t > 0.3\ r_{eff}$ have been converged at d = 0.5 nm, while for $t \leq 0.3\ r_{eff}$, d= 0.25 nm has been employed to collecting data. For Disk and Prism hollow nanoshells, d has been set to 0.25 nm to collect the data. Figure 5.3 shows an example of the convergence of extinction spectra of 40 nm ellipsoid hollow/Au nanoshells with a shell thickness of a) $t = 0.1\ r_{eff}$ and b) $t = 0.2\ r_{eff}$.

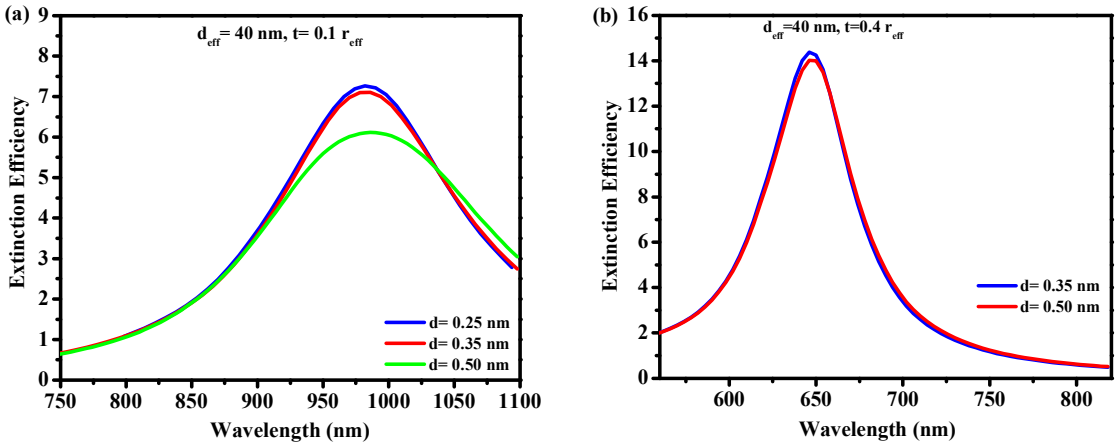

Figure 5.3. Convergence of the extinction spectra of the ellipsoid hollow/Au nanoshells with an effective diameter of 40 nm and a shell thickness of a) t = 0.1 reff and b) t = 0.2 reff. As shown in these figures, for t=0.1 r_{eff} and t=0.2 r_{eff} extinction spectra converge at d = 0.35 nm and d = 0.5 nm, respectively. The incident light electric field is parallel to the main axis of the NPs.

5.3. Results and Discussion

5.3.1. Dielectric Function Effect on Sensitivity and FWHM

In order to theoretically elucidate the shell thickness influence on the dielectric function and consequently on plasmon sensitivity and FWHM of the hollow/Au nanoshells, Quasi-static approximation was used. In this approximation, the size of the NPs is much smaller than incident light wavelength (kd<<1) whereby the electromagnetic phase shift and electric field and polarizability variation are negligible inside the Np [277]. In this model, by considering dipole mode and ignoring higher-order modes, the absorption spectrum inside Np is given by [277]

$$\sigma_{abs}(\omega) = \frac{V}{3c}\varepsilon_m^{1.5}\sum_{i=1}^{3}\frac{1}{L_i^2}\frac{\omega\varepsilon_2}{\left[\varepsilon_1 + \varepsilon_m\left(\frac{1}{L_i} - 1\right)\right]^2 + \varepsilon_2^2} \tag{5.2}$$

where V, c and ε_m are the volume of the nanoparticle, the speed of the light in a vacuum and the dielectric function of the surrounding medium. L_i represent shape factors related to depolarization effect and are equal to 1/3, 1 and 0 for spherical, flat disk and infinite spheroid (when the incident light is in direction of the long axis) [277]. In addition, ε_1 and ε_2 are the real and imaginary part of the dielectric function of the metallic nanoparticles. In order to obtain the corresponding wavelength of LSPR, the denominator of the Eq. 5.2 should be minimum that gives [277]

$$\varepsilon_1 + \varepsilon_m\left(\frac{1}{L_i} - 1\right) = 0 \tag{5.3}$$

with minimizing the denominator of σ_{abs} in Eq. 5.2, LSPR frequency can be expressed as [277]

$$\omega_{LSPR} = \frac{\omega_p}{\left[\varepsilon_{IB} + \varepsilon_m(\frac{1}{L_i} - 1)\right]^{\frac{1}{2}}} \tag{5.4}$$

From the above equation, it is evident that ω_{LSPR} decreases with increasing the refractive index of the medium. This shift to longer wavelengths can be ascribed to decreasing the restoring Coulombic force due to increased shielding effect between the oscillating electrons and positive ions that results in a reduction of the required incident light energy to excite coherent oscillation of the electrons [252].

To evaluate hollow/Au nanoshells electric permittivity, we used the composition-weighted average to calculate ε_{eff} of the structure [248, 278–280]

$$\varepsilon_{eff}(\omega) = X_{core}\,\varepsilon_{core}(\omega) + (1 - X_{core})\varepsilon_{shell}(\omega) \tag{5.5}$$

where X_{core} , and $(1 - X_{core})$ are core and shell volume fractions, respectively.

Figure 5.4a and 5.4b show real part of the effective dielectric function of spherical hollow/Au nanoshells with a diameter of the 40 nm for different shell thicknesses without and with electron-surface collision effect, respectively. It is evident from Figure 5.4 and Figure 5.5 that electron-surface collision has little to no effect on the real part of the electric permittivity. However, as can be understood from these figures, the slope and amount of ε_{1eff} significantly alter with changing the shell thickness. Since the dielectric function of the air ($\varepsilon_{air} = 1$) is dispersionless, and ε_1 of Au is negative and varying with the wavelength of incident light, the core volume fraction will increase that results in increase of ε_{1eff} , and reducing the slope with a decrease in shell thickness. On the other hand, ε_{2eff} depends on two factors: volume fraction of the shell and electron-surface scattering rate. As shown in Figure 5.4c and 5.4d, the ε_{2eff} decreases by reducing shell thickness. However, it has already been noted above that by decreasing effective size of the shell electron-surface collision frequency increases. As demonstrated in Figure 5.5b, the electron-surface effect will become important for longer wavelengths and leads to increasing

ε_{2eff} with reducing shell thickness. In hollow nanoshell structures, reducing shell thickness increases the real part of the dielectric function while decreases its gradient (See Figure 5.4a and 5.4b). To satisfy Eq. 5.3 for plasmon resonance, with a decreasing gradient of the real part of the dielectric function, it requires the LSPR peak to shift significantly with changing the refractive index of the medium. Thus, decreasing shell thickness for fixed total size leads to increased sensitivity for hollow-Au nanoshells.

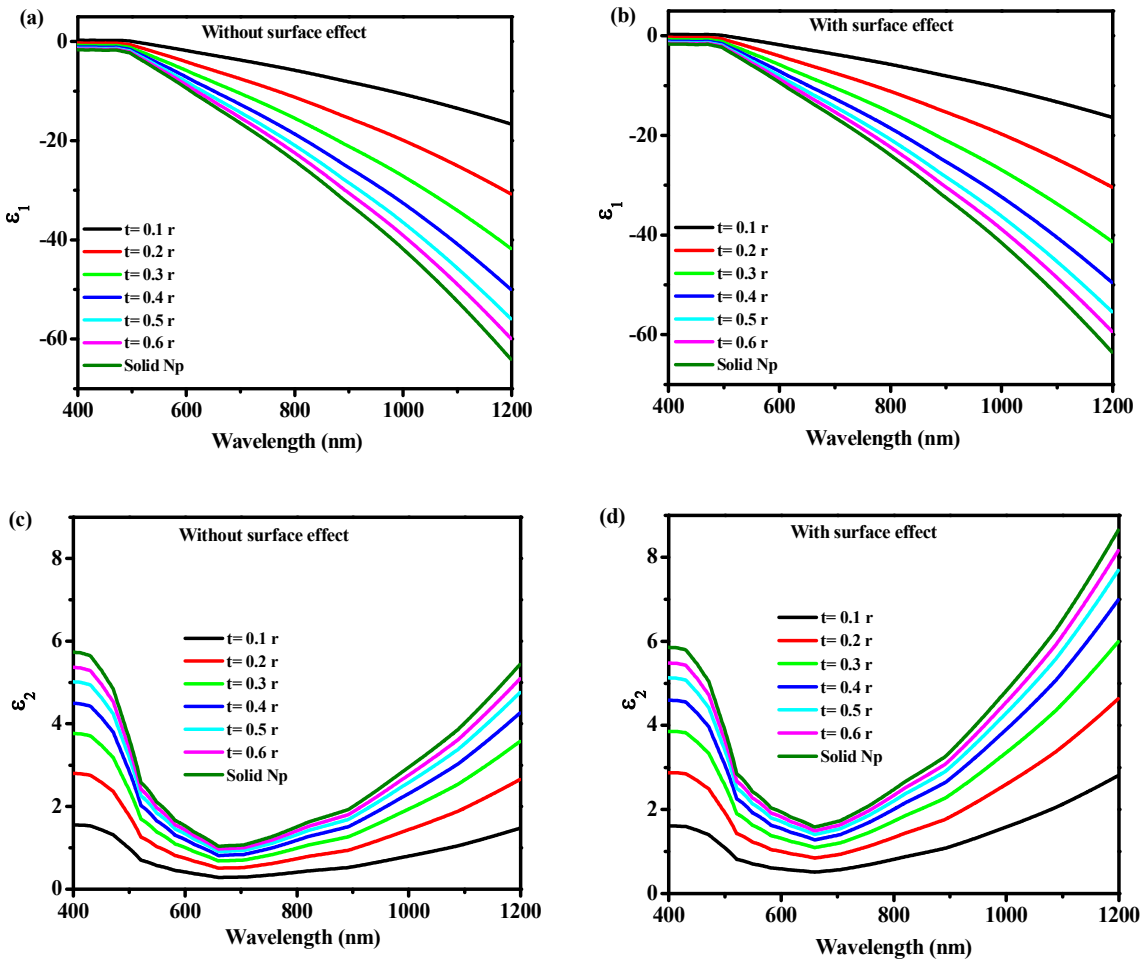

Figure 5.4. Changing real (ε_1) and imaginary part (ε_2) of the dielectric function of hollow Au nanoshell with a total diameter of 40 nm for different shell thicknesses versus incident light wavelength: (a) and (c) without considering electron-surface scattering effect, (b) and (d) with considering electron-surface scattering effect in damping frequency. For comparison, electric permittivity of solid NPs in both cases has been added.

To characterize the LSPR sensitivity, the FWHM of the LSPR resonance spectrum has been obtained by Taylor expansion of the absorption spectrum at LSPR wavelength as [248, 281]

$$\Delta\lambda_{1/2} \approx 2\left|\lambda_R - \lambda_{1/2}\right| \approx \frac{2\varepsilon_2(\lambda_{LSPR})}{\frac{d\varepsilon_1(\omega)}{d\lambda}|_{\lambda=\lambda_{LSPR}}} \tag{5.6}$$

FWHM plays an important role to determine relative scattering and absorption to extinction. Eq. 5.6 suggests that in order to have narrower bandwidth it is required to optimize NP structures to have smaller imaginary part of the dielectric function and steeper derivative of the real part at the resonance frequency. As it is demonstrated in Figure 5.4 for spherical hollow-Au nanoshells with a total diameter of 40 nm, both the imaginary part and slope of the real part of the dielectric function reduce by decreasing shell thickness. From this result, it can be concluded that the imaginary part of dielectric functions and gradient of the real part of structures play important role to obtain higher sensitivity and lower FWHM.

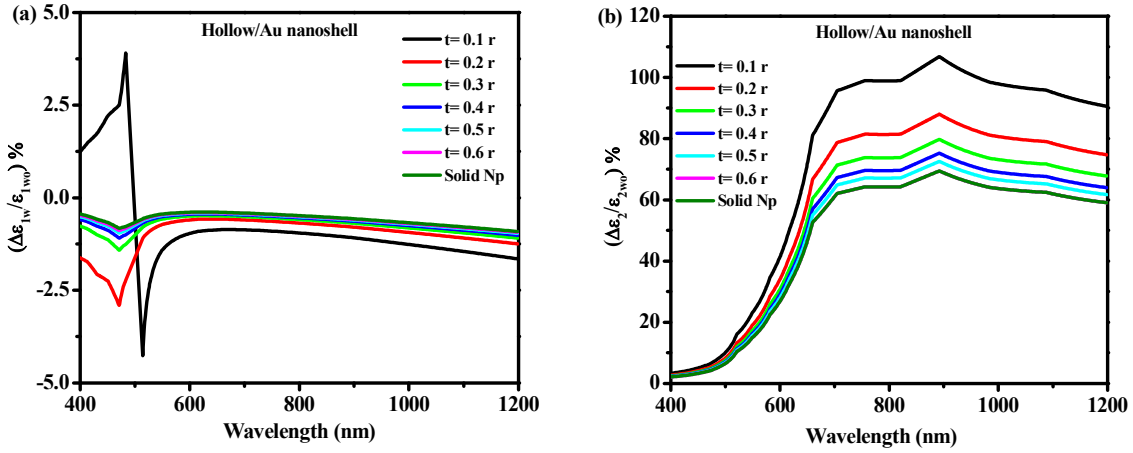

Figure 5.5. Percentage of changing of the (a) real part and (b) the imaginary part, of the dielectric function of spherical hollow/Au nanoshells with a total size of d=40 nm with varying shell thickness due to considering surface effect ($\Delta\varepsilon = \varepsilon_w - \varepsilon_{wo}$, where ε_w and ε_{wo} are the dielectric function of the hollow/Au nanoshell with and without considering the surface effect, respectively). Here ε_{1w} and ε_{2wo} are real and imaginary part of the dielectric function of hollow/Au nanoshells without electron- surface scattering effect.

5.3.2. Size Effect on the LSPR Sensitivity

In this section, the size effect on the LSPR sensitivity of spherical hollow-Au nanoshells with varying shell thickness was studied. Two-layered Mie theory was used to calculate the extinction spectrum and corresponding LSPR wavelength of each sample (See Figure. 5.6).

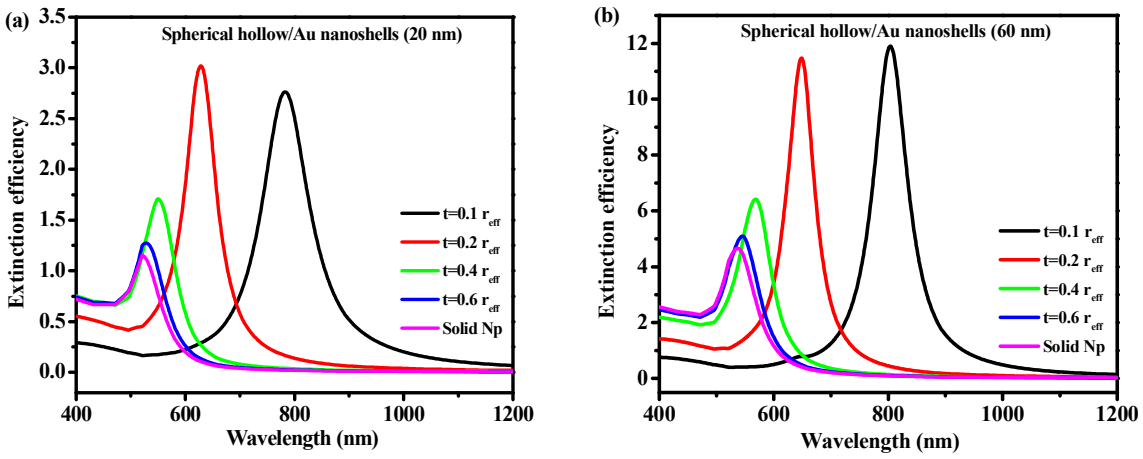

Figure 5. 6. Extinction spectrum of spherical hollow/Au nanoshells for different shell thickness with a total diameter of (a) 20 nm and (b) 60 nm.

Figure 5.7a-5.7d show LSPR peak wavelength versus the refractive index of the medium for different shell thicknesses for nanoparticles with a total diameter of d=20 nm, d=40 nm, d=60 nm, and d=80 nm, respectively. As shown in Figure 5.7, λ_{LSPR} and its corresponding gradient significantly increases with reducing the ratio of shell thickness-to-total radius (t/r). The two possible explanations for this result are: 1) enhancing inner and outer layers plasmonic coupling due to reducing the shell thickness [44, 49, 271], 2) decreasing gradient of the real part of the dielectric function ($\frac{d\varepsilon_1(\omega)}{d\lambda}$).

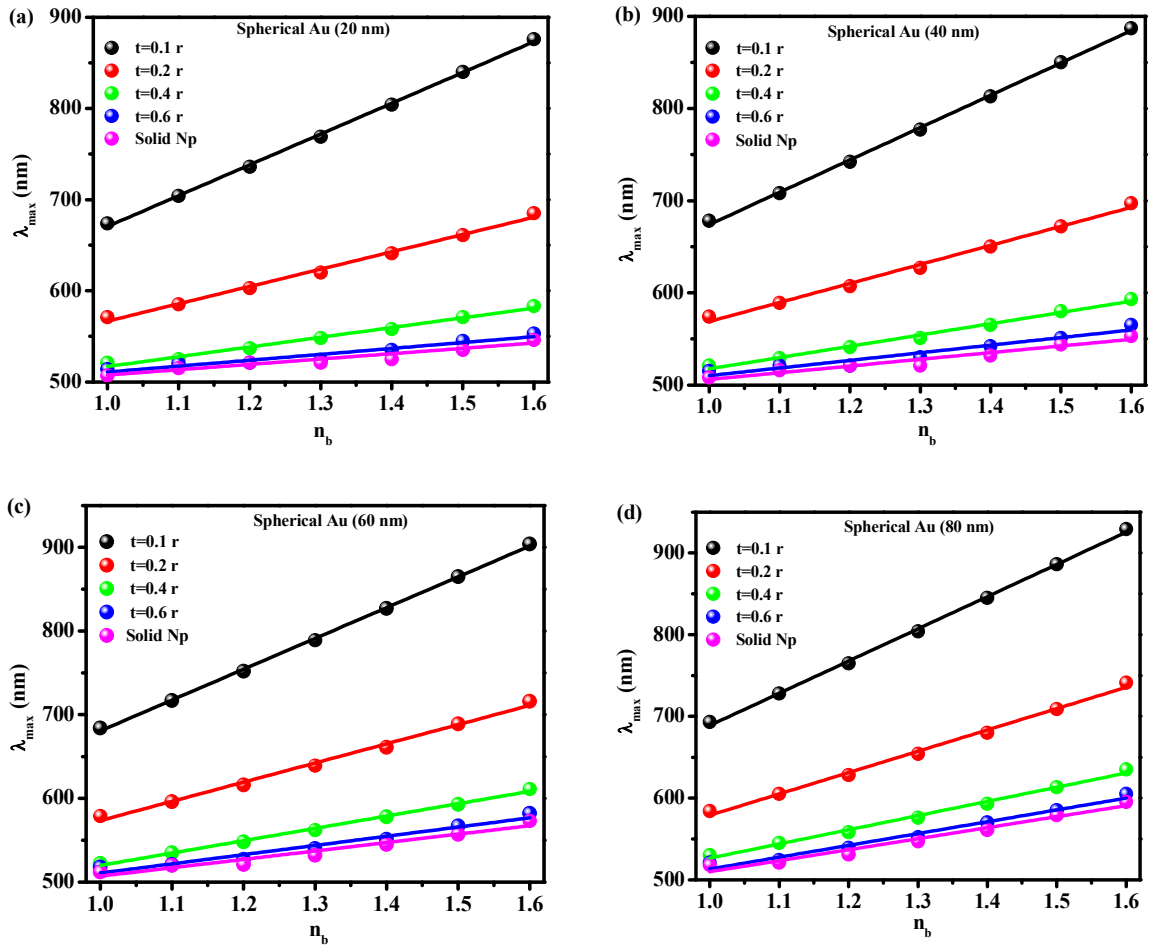

Figure 5.7. LSPR peak wavelength of the spherical hollow/Au nanoshells for different shell thicknesses versus RI of the surrounding medium with the diameter of (a) d=20 nm (b) d=40 nm, (c) d=60 nm and (d) d= 80 nm.

Figure 5.8 shows the LSPR peak shift at different refractive index of the surrounding medium for different size spherical nanoshells. The shift calculated respect to the LSPR peak of the corresponding particle at vacuum.

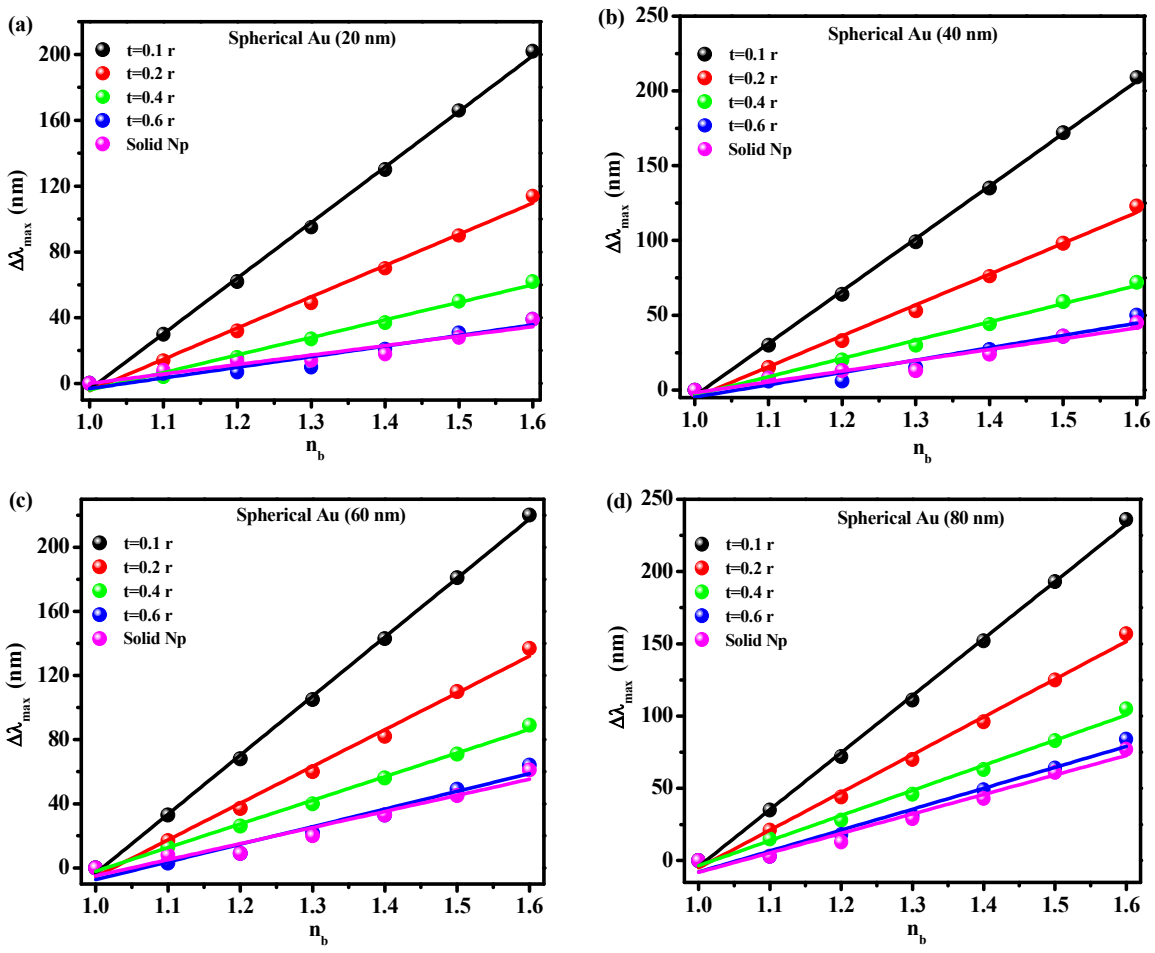

Figure 5.8. LSPR peak wavelength shift of the spherical hollow/Au nanoshells with varying shell thicknesses for the diameter of (a) d = 20 nm, (b) d = 40 nm (c) d = 60 nm, and (d) d= 80 nm, versus the RI of the surrounding medium.

The LSPR sensitivity is obtained by the slope of the linear fit of the LSPR wavelength versus RI of the surrounding medium and is presented in Figure 5.9. Similar to previous studies [76, 271], our finding shows that the LSPR sensitivity increases with reducing shell thickness, at an exponential rate. As an example, for Np with d=20 nm, the LSPR sensitivity increases significantly from 57.5 to 338 nm/RIU by reducing shell thickness from t=1 r (Solid Sphere) to t=0.1 r. In addition, the sensitivity increases with increasing the size due to increased contribution from higher-order modes [248, 282]. However, by reducing the shell thickness, the LSPR sensitivity of the different size NPs converge. This can be ascribed to the decrease in contribution of the higher-order modes leading to size-independent behavior of LSPR sensitivity for thin shells.

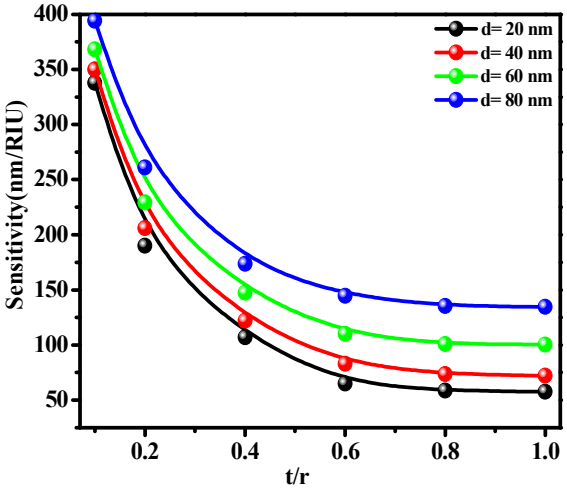

Figure 5.9. Size effect on the LSPR sensitivity of the spherical hollow/Au nanoshells for the NPs with the total diameter of d=20 nm, d=40 nm, d=60 nm, and d= 80 nm. Lines are added as guides to the eye.

In order to easily detect the LSPR peak shift with changing RI of the surrounding medium, structures with lower FWHM that have higher extinction (See Figure 5.10) are desirable [248]. FWHM in nanoshells depends on several factors: electron- surface scattering at the boundaries of the nanoshell; shell to core volume ratio; and retardation effect, including the contribution of higher-order plasmon modes [248, 282]. Figure 5.11 shows the calculated FWHM of the different size spherical nanoshells that were obtained using Gaussian fit to extinction spectrum of the NPs in aqueous solution ($n_m = 1.34$). Interestingly, the plasmon bandwidth is minimum at t=0.2 r for all sizes. This observation could be attributed to the fact that the reduction in imaginary part of the dielectric function is dominated by a decrease of $\frac{d\varepsilon_1(\omega)}{d\lambda}$ leading to a decrease of the FWHM of the nanoshells. Interestingly, the results also show that with an increase in the size of NPs from 20 nm to 40 nm, FWHM decreases and then increases by further enlarging the NPs size. The inconsistency may be due to the increased retardation effect and contribution of the higher plasmonic modes that overcome the reduced electron-surface scattering rate effect with increasing size of the NP from 40 to 80 nm, and results in a net increase of the plasmon bandwidth.

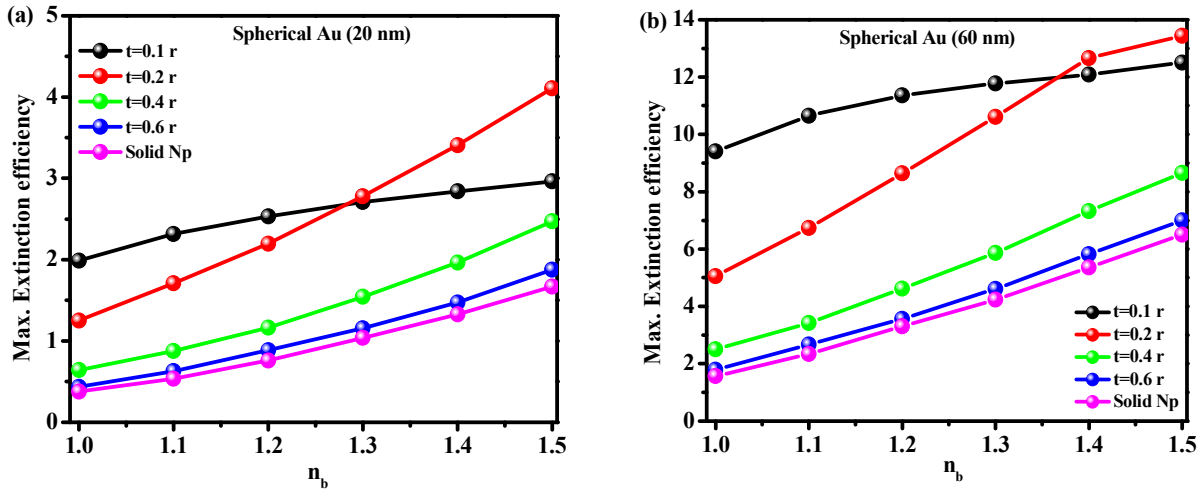

Figure 5. 10. Maximum extinction efficiency of the spherical hollow/Au nanoshells against RI of the surrounding medium for different shell thickness with a total diameter of (a) 20 nm and (b) 60 nm.

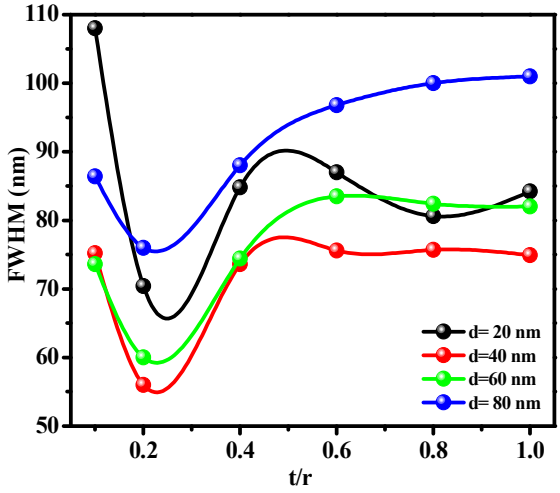

Figure 5.11. Evolution of FWHM of spherical hollow/Au nanoshells versus shell thickness-to-total radius (t/r) for the NPs with the total diameter of d=20 nm, d= 40 nm, d=60 nm and d= 80 nm. Lines are added as guides to the eye.

5.3.3. Shape Effect on LSPR Sensitivity

In order to explore the shape effect on the LSPR peak wavelength, and LSPR sensitivity, we have performed DDA simulation for five different shapes (disk, prism, rod, ellipsoid, and rectangular block) with an effective diameter of 40 nm and compared their optical properties with same sized spherical hollow/Au nanoshells. With changing the particle shape, the curvature of the nanoparticles change that alters the charge distribution, electric field enhancement and LPSR peak

position, and consequently effects LSPR sensitivity. In addition, by changing the shape of the nanoparticles, the effective distance between the positive and negative charges will change that result in shifting LSPR peak wavelength and altering LSPR sensitivity. For the rod, ellipsoid and rectangular block, the aspect ratio was set to 2 and direction of the incident light electric field has been considered parallel to the long axis of the nanoshells. For the prism, the thickness was considered to be half of the side length of equilateral triangular and incident light has been chosen in the direction of the trigonal axis. The thickness of the disk nanoshell was set to be equal to its radius, and the electric field was chosen in the direction of its main axis. DDA calculation was performed for varying shell thickness of each sample while the total effective diameter of each was fixed to 40 nm. Figure 5.12 shows the evolution of the LSPR peak wavelength of each sample with changing RI of the medium for different shell thicknesses. As a reference, the calculated LSPR of the spherical hollow/Au nanoshells with a total diameter of 40 nm was added to the figure. It is observed that LSPR shift for a given surrounding medium RI increases by reducing shell thickness in all samples. As shown in Figure 5.12, for a given RI change of the surrounding medium, the LSPR peak of the ellipsoid, rod, and rectangular block nanoshells shifted to longer wavelengths more than other shaped shells and can be tuned from visible to infrared region by changing the shell thickness. These results are mainly due to lower depolarization factor or higher polarizability of the ellipsoid, rod, and rectangular block nanoshells when compared to other structures [252]. By decreasing the depolarization factor, the restoring Coulombic force between the positive ions and oscillating electrons decreases which decreases the required incident light energy to excite the free electrons of the nanoshell [252]. The results show that the sensitivity of the rectangular block and the disk is the highest and lowest for all shell thicknesses, respectively (see Figure 5.13). For example, at $t = 0.1\ r_{eff}$, the LSPR sensitivity of the rectangular block is 594.9 nm/RIU which is almost 1.7 times of the sphere (350 nm/RIU) and 2.1 times of the disk (278.4 nm/RIU) with same shell thickness. In addition, LSPR sensitivity of rod and ellipsoid converge to rectangular block by further reducing the shell thickness. The sensitivity of rod nanoshells is slightly higher than ellipsoid in all shell thickness, which can be ascribed to the larger average distance between positive ions and excited electrons in rod nanoshell.

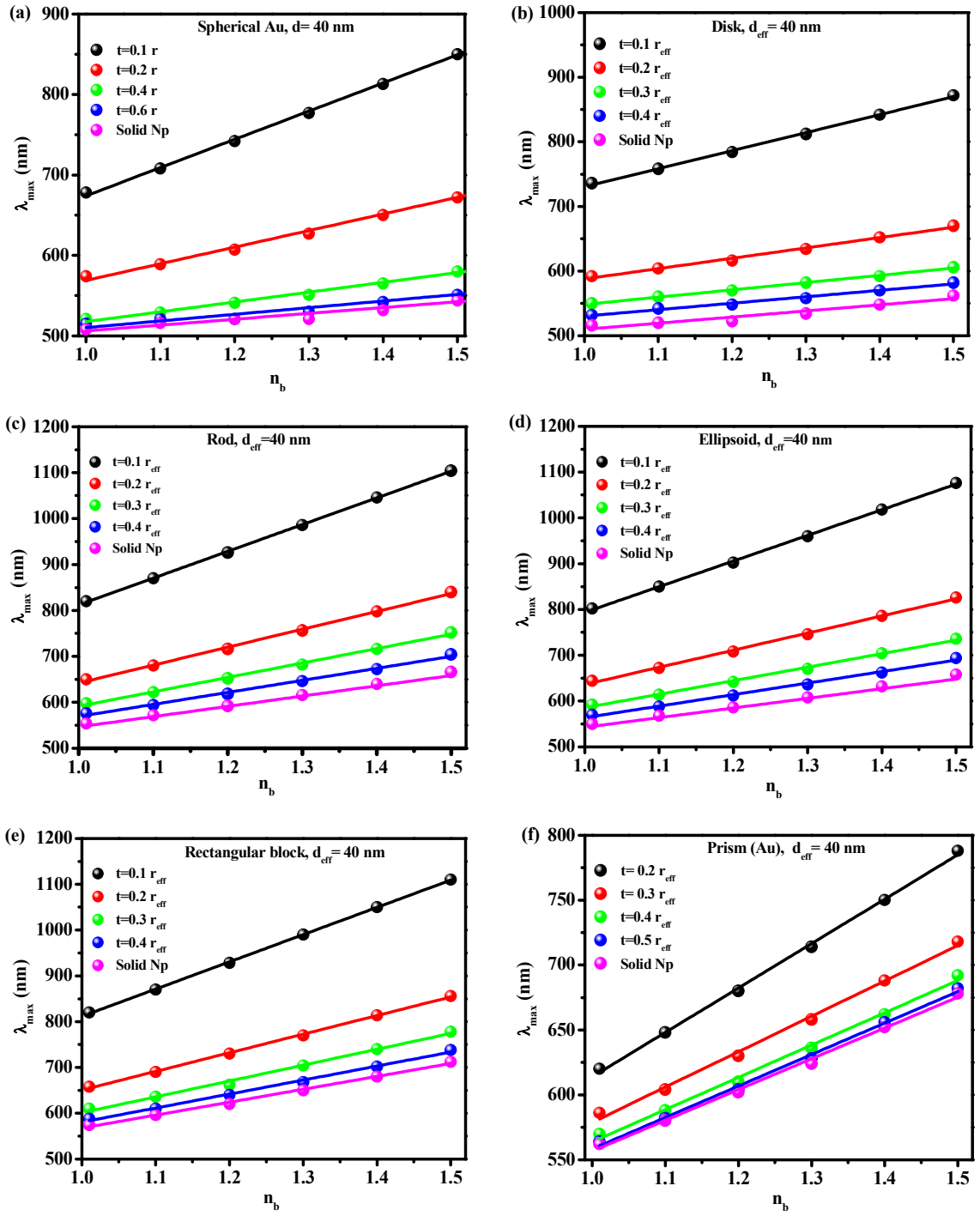

Figure 5.12. LSPR peak wavelength of the hollow/Au nanoshells versus RI of the surrounding medium for different shapes: (a) Spherical, (b) Disk, (c) Rod, (d) Ellipsoid, (e) Rectangular block and (f) Prism, with d_{eff} = 40 nm. The incident light electric field was chosen to be parallel to the main axis of the NPs.

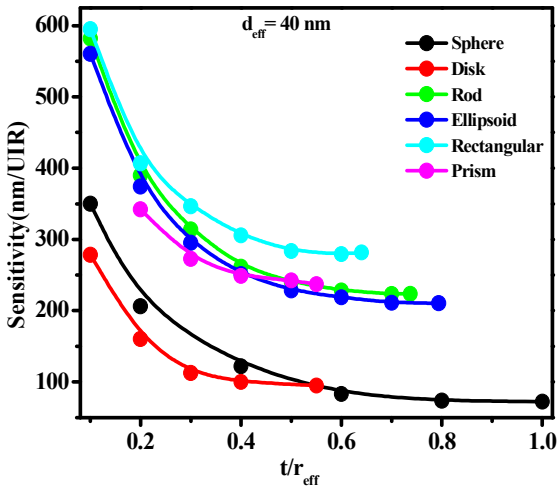

Figure 5.13. Influence of shape and shell thickness on the LSPR sensitivity of the sphere, disk, rod, ellipsoid, rectangular block, and prism, shaped hollow/Au nanoshell with an effective diameter of d_{eff} = 40 nm. Lines are added as guides to the eye.

As mentioned earlier, structures with lower FWHM that have higher extinction are desirable LSPR sensitivity applications [248]. Owing to inner and outer layers coupling the maximum extinction efficiency in most of the shell structures is more than the solid particles (See Figure 5.14). As shown in Figure 5.14, the extinction spectra's maximum of all of the structures increases by reducing shell thickness until 0.2 r_{eff}, however, it increases by further decreasing the outer layer thickness. This can be attributable to increasing electron-surface scattering rate by reducing the thickness of the gold layer. Figure 5.15 shows the summary of the FWHM of the studied samples with varying shell thickness. It shows a clear trend of exponential decreasing of the FWHM for ellipsoid, rod, rectangular block, and prism with increasing shell thickness. The significant reduction has happened when the shell thickness varied from t=0.1 r_{eff} to t=0.2 r_{eff}. At t=0.2 r_{eff}, the FWHM reaches 86.8, 75.62, 73.1 and 74.3 nm for ellipsoid, rod, rectangular block, and prism, respectively. However, the FWHM of spherical and disk reduces just in the range of t=0.1- 0.2 r_{eff} and reaches its minimum value at t= 0.2 r_{eff}, and then increases with further increasing the shell thickness. In the next section, the aspect ratio effect on the optical properties of the rectangular block and rod hollow/Au nanoshells is presented.

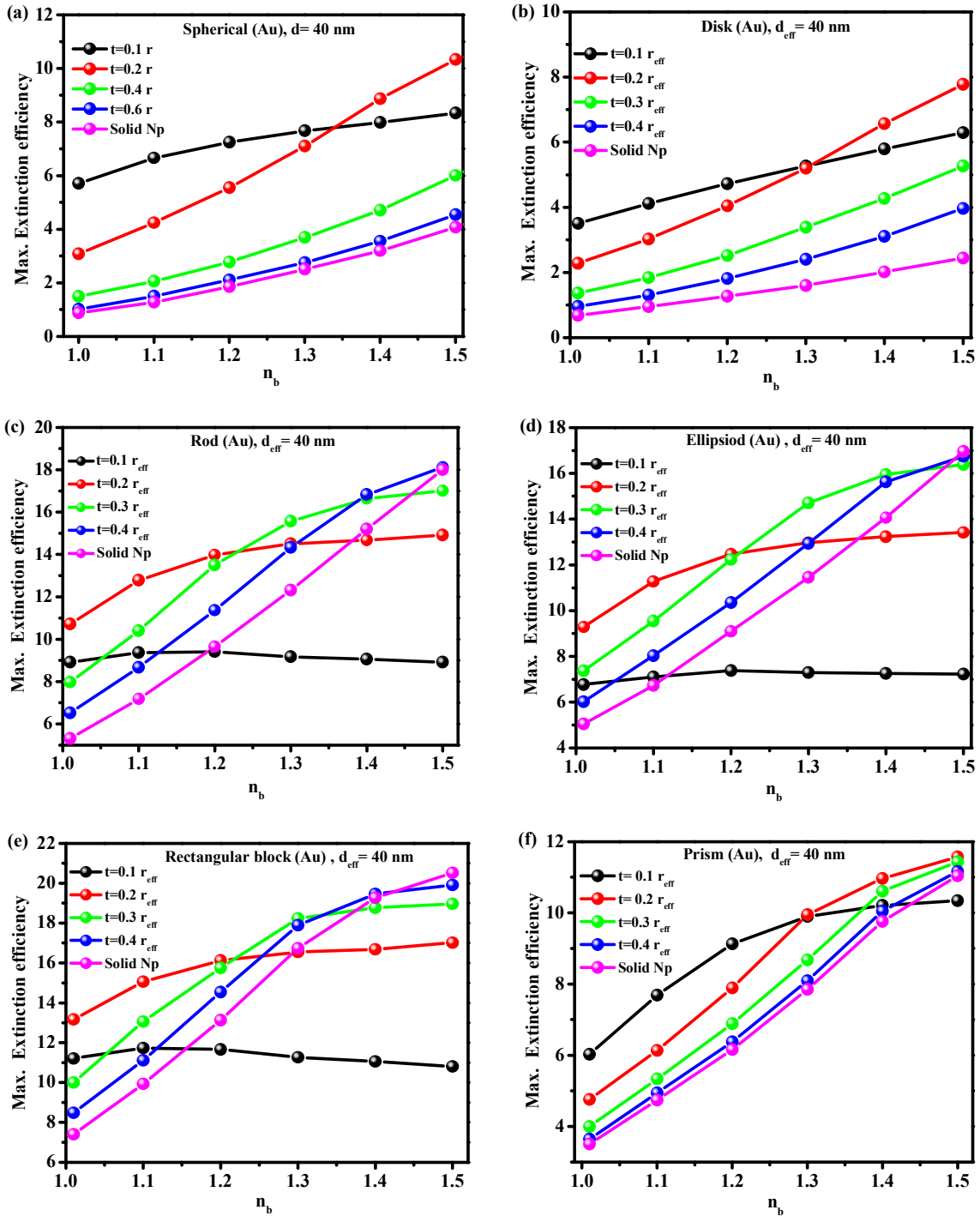

Figure 5.14. Maximum extinction efficiency of spherical hollow Au nanoshells versus RI of the surrounding medium for different shapes: (a) Spherical, (b) Disk, (c) Rod, (d) Ellipsoid, (e) Rectangular block and (f) Prism, with deff = 40 nm. The incident light electric field is parallel to the main axis of the NPs.

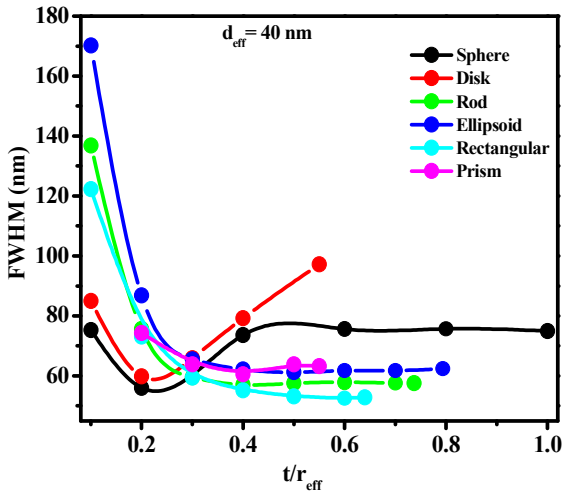

Figure 5.15. Influence of shape and shell thickness on the FWHM of the sphere, disk, rod, ellipsoid, rectangular block, and prism, shaped hollow/Au nanoshell with an effective diameter of the d_{eff} = 40 nm. Lines are added as guides to the eye.

5.3.4. Aspect Ratio Effect on the LSPR Sensitivity

Increasing AR of the NPs will enhance surface area-to-volume ratio that can make sensing of target molecules easy by providing enhanced active area [67]. To study AR effects in LSPR sensitivity, we investigated the optical properties of the rectangular block and rod nanoshells which have shown higher sensitivity for AR = 2 when compared to other structures, as discussed in the previous section. The effective total diameter of the samples was set to 40 nm, and the AR was varied from 1 to 5. Note that at AR = 1, Rod and Rectangular block will convert to spherical and cube, respectively. The DDA calculation was performed for three different cases: 1) Solid Np, 2) nanoshell with fixed t = 0.2 r_{eff} and 3) nanoshell with fixed shell volume. In the third case, the volume of the shell for all aspect ratios was set to be equal to the volume of the shell with AR=2 and t = 0.2 r_{eff}.

Figure 5.16a and 5.16b show the LSPR sensitivity of the rod and the rectangular block versus AR, respectively. It is observed that sensitivity for all cases increases with increasing AR. This observation, first, can be attributed to enhancing polarizability or decreasing depolarization factor due to increasing the effective distance between the positive and negative charges in the NPs which reduces the required energy to excite electrons on their surface. Second, it can be ascribed to increasing the surface to volume ratio by increasing aspect ratio which leads to

enhancement of surface effect and more shifting of the LSPR peak with changing RI of the surrounding medium. Also, it was demonstrated that the sensitivity for both hollow/Au nanoshells is significantly higher than the solid NPs due to strong plasmon coupling between the inner and outer layer of the shell. However, it must be noted that the sensitivity of the structures with fixed shell volume diverges and become higher than the case with fixed shell thickness with an AR greater than 2. This observation is due to the fact that in the case with fixed shell volume, shell thickness slightly reduces with increase in AR. For example, at an AR of 5 and for fixed shell volume, the LSPR sensitivity of rectangular block is 800 nm/RIU that is ,despite its smaller size, almost same as the longitudinal plasmons mode of the nanorice (801.4 nm/RIU) with longitudinal diameter of 340± 20 nm, transverse diameter of 54± 4 nm and shell thickness of 13.1± 1.1 nm [76]. A comparison of the two results reveals that for small AR (<3), the sensitivity of the rectangular block is more than the rod, whereas by further increase in AR, the rod sensitivity exceeds that of rectangular block. The interesting finding was that the LSPR sensitivity of the nanorod with an AR of 5 and for fixed shell volume is 829.5 nm/RIU, which is higher than the structures mentioned above (rectangular block and nanorice).

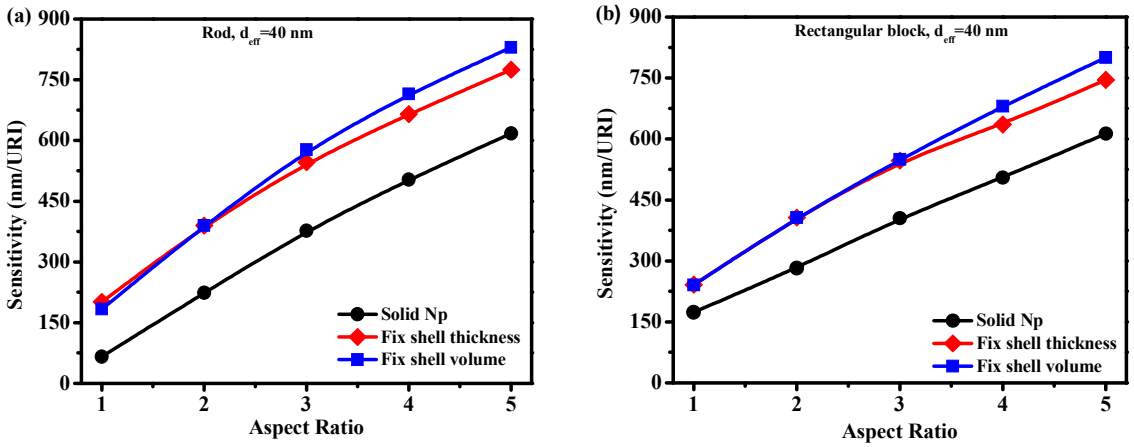

Figure 5.16. The sensitivity of the hollow/Au nanoshells, (a) Rod and (b) Rectangular block, with d_{eff} = 40 nm versus aspect ratio. Lines are added as guides to the eye.

However, it must be noted that a further increase of the AR reduces the extinction spectra due to increasing electron-surface scattering rate, which makes detection of the wavelength

changes experimentally difficult. As shown in Figure 5.17, by increasing the AR of both rod and rectangular block the extinction spectra and FWHM will increase.

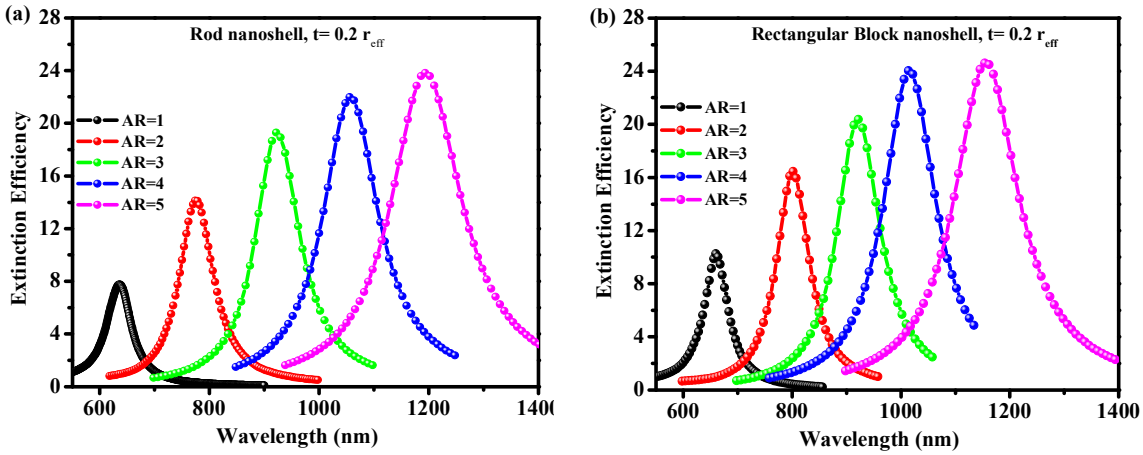

Figure 5.17. Extinction efficiency spectra of the (a) rod shape, and b) rectangular block, hollow/Au nanoshells with an effective diameter of 40 nm, and shell thickness of t=0.2 $r_{eff,}$ for varying the AR from 1 to 5.

In summary, it has been shown that both the rectangular block and rod hollow/Au nanoshells provide higher sensitivity in comparison to other structures. Also, due to their smaller sizes, the RI of the surrounding medium can change effectively with a low binding concentration of the target molecules, which offers the possibility to sense and detect the analytes such as DNA which have low concentrations. The tunability of the sensitivity of these structures with changing the shell thickness and AR provides the opportunity to further enhance LSPR sensitivity and molecules detecting capabilities of the single NP.

CHAPTER 6

OPTICAL PROPERTIES OF EMBEDDED PLASMONIC NANOPARTICLES USING DISCRETE DIPOLE APPROXIMATION

6.1. Introduction

Collective oscillations of the conduction band electrons of plasmonic NPs lead to a fundamental property called localized surface plasmon resonance (LSPR) [1, 49, 134, 135]. Owing to strong scattering and absorption of the incident light due to LSPR, and significant enhancement of the electric field, which is highly localized around the surface of the nanostructures, plasmonic NPs have received considerable attention in nanophotonic research [1, 49, 134, 135]. Due to higher scattering and absorption of the incident light, noble metallic nanoparticles such as Au and Ag have been subjected to extensive studies with potential application in biomedical field [9–26], solar cells [7, 8], plasmonic sensors [21–40], catalysis [283], surface-enhanced Raman spectroscopy [41–47], and metal-fluorescence enhancement [48], For example, El-Sayed and his group have shown that scattered light of the Au NPs bounded to the surface of malignant cells can be used to construct the image of the cancerous tissues [12]. In another study, Joshi and coworkers via LSPR sensing technique, by monitoring plasmonic wavelength shift of the NPs due to changing the refractive index of the surrounding medium, observed that concentration of miR-10b is almost four times greater than of miR-21 in the plasma or blood of pancreatic cancer patients [259]. Zhang et al. fabricated tubular Ag NPs/silica nanotubes nanocomposites catalysts by assembling size-controlled Ag NPs on the inner and outer surface of the nanotubes, which could be easily recycled without decreasing of the catalytic activity [283]. Since the redox potential and the surface-to-volume ratio of the Ag NPs are size-dependent, they demonstrated that the catalytic activity of the nanocomposite can be increased by reducing the size of the Ag NPs [283]. Liu et al. used Au nanorods that have two LSPR peaks to significantly enhance the fluorescence of the Oxazine-725 molecules embedded in silica shell around the NP [74]. They simultaneously enhanced excitation and emission of the dye molecules by matching the LSPR wavelengths of the transversal and

longitudinal modes to the excitation and emission wavelengths, respectively, which results in 20.8 times stronger fluorescence enhancement in comparison to the emission from the same amount of dye molecules in solution [74]. Recently, researchers have shown an increased interest in plasmonic properties of the copper (Cu) NPs due to their large extinction cross-section, high conductivity and photosensitivity, cost-effectiveness when compared to Au and Ag, and their capability of insertion in host polymer matrices [284, 285]. The aforementioned properties of the metallic Cu NPs provide a wide range of applications in chemistry, material science, catalysis, and nonlinear optics [286–288]. For example, a recent study has shown that chemically grown Cu NPs onto TiO_2 leads to significant improvement of the electrocatalytic activity in oxygen reduction in alkaline media [286].

LSPR properties of the plasmonic NPs can be tailored by their size, shape, composition, the refractive index of the medium, and the polarization direction of the incident light [9, 64, 76, 83, 158, 180, 185, 211, 245, 248, 252, 265–267]. The LSPR properties of the metallic NPs also can be tuned by changing the interparticle distances in multimeric structures [63, 77, 103, 132, 156]. or changing shell thickness and core size in nanoshell compositions [20, 27, 268]. Several studies have been carried out to investigate the effect of the parameters mentioned above on the LSPR properties of the plasmonic NPs [9, 20, 27, , 63, 64, 76, 77, 83, 103, 132, 156, 158, 180, 185, 211, 245, 248, 252, 265–268]. In one well-known study, Jain et al. explored the size, shape, and composition effect on the absorption and scattering properties of Au nanoparticles [9]. By studying three different structures viz. silica-Au nanoshells, Au nanosphere, and Au nanorods, they observed that extinction cross-section and relative scattering contribution of the NPs enhance by increasing the size of the NPs. Also, it has been shown that LSPR peak of the Au nanospheres lies in the visible range, whereas the plasmonic resonance peak of the nanorods and nanoshells structures can be tuned to in the near-infrared region by altering aspect ratio (AR) and shell thickness, respectively, which makes them a potential candidate for vivo applications [9]. In another work, Jain and coworkers investigated the plasmonic coupling effect on the optical properties of Au nanorods assemblies [61]. By studying extinction efficiencies of side-by-side and head-to-tail linkage of Au nanorods, they observed that LSPR peak of a longitudinal plasmon mode blue shifts in the first configuration whereas redshifts in the latter case. They also demonstrated that the amount of shifting of the plasmon resonance peak increases further by decreasing

interparticle distances [61]. More recently, we investigated the size, shape, shell thickness, and aspect ratio effect on the LSPR sensitivity of the hollow-Au nanoshells [27]. It was conclusively shown that reducing the shell thickness increases the LSPR sensitivity of the nanoshell structures due to the inner and outer surface coupling effect. Also, by studying different shaped hollow-Au nanoshells (sphere, disk, prism, ellipsoid, rectangular block, and nanorod), we demonstrated that rectangular block and rod shape hollow-Au nanoshells have higher LSPR sensitivity in comparison to other nanostructures that enhances more by a further increase in the aspect ratio [27].

Chemical ligands are widely used to stabilize small-sized nanoparticles in a solution [76, 77, 187, 188]. Conjugating the NPs with chemical ligands prevents the integration of the NPs in the solution by counterbalancing the Vander Waals attractive forces between them and helps the stabilization of the NPs [76, 77, 187, 188]. However, the chemical ligands usually alter the electron conductivity of the NPs due to the chemical bonding between the ligands and conduction electrons of the NPs and consequently changing the optical properties of the NPs [8, 76, 77, 187, 188]. In one of the well-known study, Peng et al. used chemical ligand to synthesize small-sized Ag nanoparticles with uniform morphologies and narrow size distribution [76]. They observed that the plasmonic peak blue shifts by reducing the size of the NPs from 20 to 12 nm, however, it turns over and redshifts by further reducing the size of NPs [76]. Peng and coworkers justified their results by the fact that the chemical bonding between the NPs and the ligand reduces the electron conductivity of the surface atoms in NPs that results in unusual behavior in LSPR peak [76]. Addition to the above-mentioned effect, transient in and out tunneling of the plasmonic electrons in interfacial orbitals with the NP and ligand alters hot electron relaxation processes in NP and adds an extra decay channel to their oscillations which results in dampening of the plasmonic band [188, 231–233]. For example, our group recently has shown that conjugating Au clusters with aromatic passivating ligands decelerate electron-phonon relaxation dynamics more than alphabetic ones due to the special Au-π interaction between the NPs and the ligands which reduces the electron conductivity of the NPs significantly [188].

An alternative method to control the size distribution and interparticle distances of the NPs is embedding them in a matrix [289–294]. The ion implementation method is one of the most promising techniques that has been used to embed NPs into a matrix [147, 293]. This technique offers an effective way to control the distance between the embedded NPs and the surface of the

matrix by adjusting the incident energies of the ion beam [147, 295]. Recently, researchers have shown an increased interest in the embedded plasmonic NPs [7, 147, 289–298]. By placing fluorophore molecules on the surface of the matrix, the electric field of the embedded NPs can enhance the fluorescence of these molecules [147]. For example, our group carried out a study to investigate the fluorescence enhancement of the Coumarin515 (C515) dye molecules via the plasmonic field of the embedded Ag nanoparticles in a quartz matrix. We have shown a fluorescence enhancement factor ranging from 1.0 to 2.1 with a maximum enhancement for larger NPs [147]. Interestingly, it has been suggested that trapping of the incident light by exciting LSPR of the embedded plasmonic NPs in a semiconductor can be used to design solar cells with 10- to-100 folds thinner photovoltaic layer thickness [7, 296–298]. The strong enhanced electric field around the NPs can also be used to increase the absorption in the semiconductor matrix [7, 296–298].

Although some experimental research was carried out on embedded plasmonic NPs, there is very little theoretical understanding of the optical properties of these kinds of nanostructures [7, 147, 289–298]. The main objectives of this research are to investigate optical properties such as the extinction cross-section, scattering quantum yield, and electric field enhancement of the embedded NPs. We studied size, shape, interparticle distances, and the number of the NPs effects on plasmonic properties of the Au, Ag, and Cu embedded NPs in a silica matrix. Figure 6.1 shows a schematic of nanospheres and nanorods Au NPs that embedded in a matrix. It has been observed that nanorods possess higher extinction cross-section and produce a stronger electric field in comparison to spherical NPs. Ag nanoparticles show stronger plasmonic properties against other samples. In addition, interesting results have been observed about field enhancement and concentration of the electric field in the multimeric structures.

This work has been organized in the following way. Section 6.2 is concerned with the computational method used in this study. Section 6.3 represents the results and discussions of the research. This section begins with studying how the shape, size, aspect ratio and type of embedded monomeric structures influence their corresponding optical properties, then will go on to investigate coupling effects in extinction spectra, and enhancement and concentration of the electric fields in the dimeric structures, and will end by exploring the number of the NPs influence on the aforementioned optical properties.

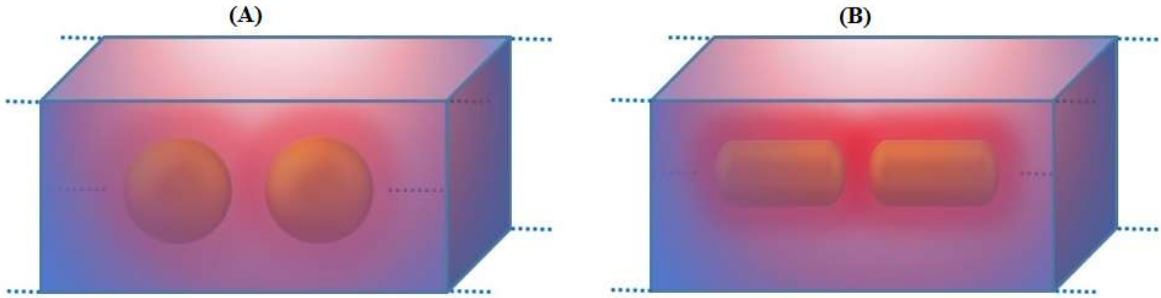

Figure 6.1. Schematic of an embedded gold (A) nanosphere, and (B) nanorod in the matrix.

6.2. Computational Methods

The optical properties of the embedded Au, Ag and Cu nanoparticles were quantified in terms of their calculated extinction (C_{ext}), absorption (C_{abs}) and scattering (C_{scat}) cross-sections, scattering quantum yield, LSPR wavelength, and electric field enhancement inside and on the surface of the matrix. The aforementioned optical properties are calculated using the DDA (refer to chapter 2, section 6.2) [84, 85, 88, 104, 120]. In DDA the particle is divided into N cubic meshes with dimensions much smaller than the incident light wavelength [84, 85, 88, 104, 120]. Each cube represents a point dipole that interacts with the incident light field and the electric field of N-1 neighboring cubes [84, 85, 88, 104, 120]. It is worth mentioning that we applied the biconjugate gradient (BCG) and fast Fourier transform (FFT) techniques to significantly reduce the time and required memory of the calculation [87, 104–113]. Our codes have been tested in the following ways. First, by vanishing the difference between the refractive index of the matrix and the surrounding medium the optical spectrum of a single spherical embedded nanoparticle was in excellent agreement with the spectrum of the same size spherical nanoparticle obtained using Mie theory. Second, by setting the dielectric function of the matrix to be equal to the dielectric function of the embedded nanoparticle the spectra of the spherical and rod shape embedded nanoparticles converged to the spectrum of a single rectangular block shaped nanoparticle with the size same as the matrix. Third, by vanishing the size of the embedded nanoparticle, the optical spectrum was in good agreement with the result of a silica matrix.

The C_{ext}, C_{abs}, and C_{scat} of each studied case can be calculated as follows [87]

$$C_{ext} = \frac{4\pi|k|}{|E_0|^2}\sum_{i=1}^{N}[Im(E_{inc,i}^{*}).P_i] \tag{6.1a}$$

$$C_{abs} = \frac{4\pi|k|}{|E_0|^2}\sum_{i=1}^{N}[Im(\frac{P_i.P_i^{*}}{\alpha_i^{*}}) - \frac{2}{3}|k|^3|P_i|^2] \tag{6.1b}$$

$$C_{scat} = C_{ext} - C_{abs} \tag{6.1c}$$

where k, E_0, and $E_{inc,i}$ are representing wavevector, the amplitude of the incident light filed, and the incident light field at the position of the dipole i, respectively. α_i [121] and P_i [85, 87] are the polarizability and polarization of each dipole, respectively. Also, in Eq. 6.1 'Im' denotes the imaginary part, and the symbol '*' represents the complex conjugate. The whole procedure of DDA, such as calculating α_i and P_i has been explained in full detail in the second chapter of this dissertation.

The total electric field at position r_i around a plasmonic nanoparticle can be obtained by summing the electric field of the incident light and scattered field of the N-1 neighboring dipoles at position r_i [111]

$$E_{tot}(r_i) = E_{inc}(r_i) + E_{scat}(r_i) \tag{6.2}$$

where the incident and scattered field at position r_i are

$$E_{inc}(r_i) = E_0 \exp(ikr_i) \tag{6.3}$$

$$E_{scat}(r_i) = \sum_{j=1}^{N}\frac{\exp(ikr_{ij})}{r_{ij}}\left[k^2(\hat{r}_{ij}\hat{r}_{ij} - \mathbf{1}_3) + \frac{(ikr_{ij}-1)}{r_{ij}^2}(3\hat{r}_{ij}\hat{r}_{ij} - \mathbf{1}_3)\right].P_j \tag{6.4}$$

where r_{ij} is the distance between the position of dipole i and j, $\hat{r}_{ij}$ is a unit vector in the direction from the dipole i to j, and $\mathbf{1}_3$ represents the 3×3 identity matrix.

The total electric field has been calculated in two different planes (see Figure 6.2): (1) at x-z plane inside the matrix at y = 0, and (2) at the x-y plane on the surface of the matrix. It is worth mentioning that the origin is chosen at the center of the matrix.

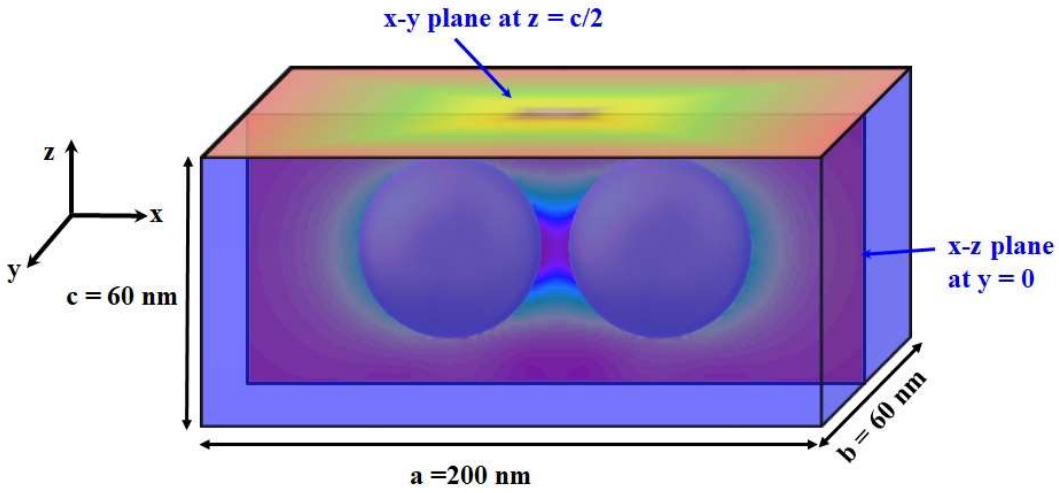

Figure 6.2. Schematic of embedded nanoparticles in a matrix and two planes (x-y plane at z = c/2, and x-z plane at y = 0) that electric field enhancement has been calculated.

The bulk dielectric function of the Au, Ag, and Cu at different wavelengths were obtained from Johnson and Christy [78]. However, due to increasing electron-surface scattering rate in nanostructures, it is required to modify the scattering frequency of the electrons in bulk metal [77]. This modification can be applied by adding an extra term to the collision frequency which is inversely proportional to the size of the NP. The corrected dielectric function for the nanostructures can be expressed as below [77]

$$\varepsilon_{NP}(\omega, r_{eff}) = \varepsilon_{bulk}(\omega) + \frac{\omega_p^2}{\omega^2 + i\Gamma_0\omega} - \frac{\omega_p^2}{\omega^2 + i\Gamma(r_{eff})\omega} \tag{6.5}$$

where ε_{bulk}, ω, ω_p, and Γ_0 are representing the bulk dielectric function, frequency of the incident light, plasma frequency, and the collision frequency of the electrons in bulk metal, respectively. The r_{eff} is the effective radius of the nanoparticle, which is defined as a radius the sphere that has a volume equal to that of the nanoparticle ($r_{eff} = (3V/4\pi)^{1/3}$). $\Gamma(r_{eff})$ is the corrected collision frequency for nanostructures which is given by [174]

$$\Gamma(r_{eff}) = \Gamma_0 + A\frac{V_F}{r_{eff}} \tag{6.6}$$

where A is the empirical fitting parameter, and V_F is the Fermi velocity. The A was chosen to be 1, 0.25, and 0.5 for Au, Ag, and Cu, respectively. The values of the ω_p, Γ_0, and V_F that have been used in our simulation provided in Table. 6.1.

Table. 6.1. Summary of the plasma frequency, bulk collision frequency, and Fermi velocity of the Au, Ag, and Cu

Metal	**Au**	**Ag**	**Cu**
ω_p [78]	1.35×10^{16} rad s^{-1}	1.39×10^{16} rad s^{-1}	1.34×10^{16} rad s^{-1}
Γ_0 [78]	1.07×10^{14} rad s^{-1}	3.22×10^{13} rad s^{-1}	1.45×10^{14} rad s^{-1}
V_F [299]	1.40×10^{6} m/s	1.39×10^{6} m/s	1.59×10^{6} m/s

In our simulation, the nanoparticles were embedded in a silica matrix with the refractive index of 1.55 at all wavelengths and dimensions of 200 × 60 × 60 nm (see Figure 6.2). The polarization and propagation directions of the incident light are aligned to be parallel to the x and y-axis, respectively, otherwise, they are given. The surrounding medium in all studied cases was considered to be a vacuum with a refractive index of 1+0i. To calculate the aforementioned optical properties of the embedded NPs, the mesh size was set to be 0.6 nm for all investigated cases.

6.3. Results and Discussion

6.3.1. Monomeric Structures

6.3.1.1. Size Effect on the Extinction Spectra

Figure 6.3 shows the calculated longitudinal mode (the electric field parallel to the long axis of the particle) extinction cross-section (C_{ext}) spectra of the single embedded Au, Ag, and Cu NPs. The spectra have been obtained for two different shapes viz. nanosphere and nanorod at different sizes. The nanorods are made of a cylinder capped with two hemispheres, and their aspect ratio (AR), defined as the ratio of the long-to-short axis of the NP, is fixed to be 2. As shown in Figure 6.3A-6.3F, the extinction spectra of all investigated cases show a clear trend of increasing by an increase in the size of the NP while the LSPR peak wavelengths experience small redshifts. It is apparent from these figures that the embedded nanorods in each case show stronger extinction spectra as well as redshifted LSPR peak when compared to the corresponding spherical NPs. For

example, Au nanorod with an effective diameter of 40 nm has a calculated maximum extinction cross-section of 3.67×10^4 nm^2 at λ_{max} = 656 nm that is almost four times higher than the corresponding value of the spherical-shaped embedded Au NP with the same volume (C_{ext} = 9.76×10^3 nm^2 at λ_{max} = 544 nm). This observation, which clearly demonstrates that plasmonic properties of the NPs depend on the shape of the NPs, can be attributed to the fact that in longitudinal mode the average distance between the positive and negative charges increases by stretching the NPs. This effect, which increases the polarizability of the NP, decreases the Coulombic attractive force between the positive and negative charges and consequently reduces the required excitation energy of the NPs and redshifts the plasmonic peak [27]. Also, the surface area of the NPs increases by stretching them which leads to an enlarged extinction spectrum in comparison to the nanospheres. A comparison of the extinction spectra of the embedded monomeric structures in Figure 6.3 reveals that Ag NPs have higher extinction spectra and narrower plasmon width in comparison to the Au and Cu NPs. On the other hand, spherical-shaped Cu NPs possess weak plasmonic spectra among the simulated samples.

The observed differences may be explained in part by looking to plasmonic bandwidth formulas of the plasmonic NPs in Quasi-static approximation, which is given as below [248, 281]

$$\Delta\lambda_{1/2} \approx 2\left|\lambda_{LSPR} - \lambda_{1/2}\right| \approx \frac{2\varepsilon_2(\lambda_{LSPR})}{\frac{d\varepsilon_1(\omega)}{d\lambda}|_{\lambda=\lambda_{LSPR}}} \tag{6.7}$$

where ε_1, and ε_2 are the real and imaginary parts of the dielectric function of the NP, respectively. As suggested by equation 6.7, the NPs that have smaller ε_2 and higher $\frac{d\varepsilon_1(\omega)}{d\lambda}|_{\lambda=\lambda_{LSPR}}$ at their corresponding LSPRs wavelengths have a narrower plasmonic peak. As can be seen from Figure 6.4, the amount of slopes of the real part of the dielectric functions of the Au, Ag, and Cu at a constant effective diameter of 40 nm are almost the same and slightly increases by increasing the wavelength of the incident light. However, the imaginary part of the dielectric function of the Ag is significantly less than the ε_2 of Au and Cu at all wavelengths. Thus, Eq. 6.7 and the results of Figure 6.4 further explain why Ag NPs possess higher and narrower extinction spectra in comparison to Au and Cu NPs.

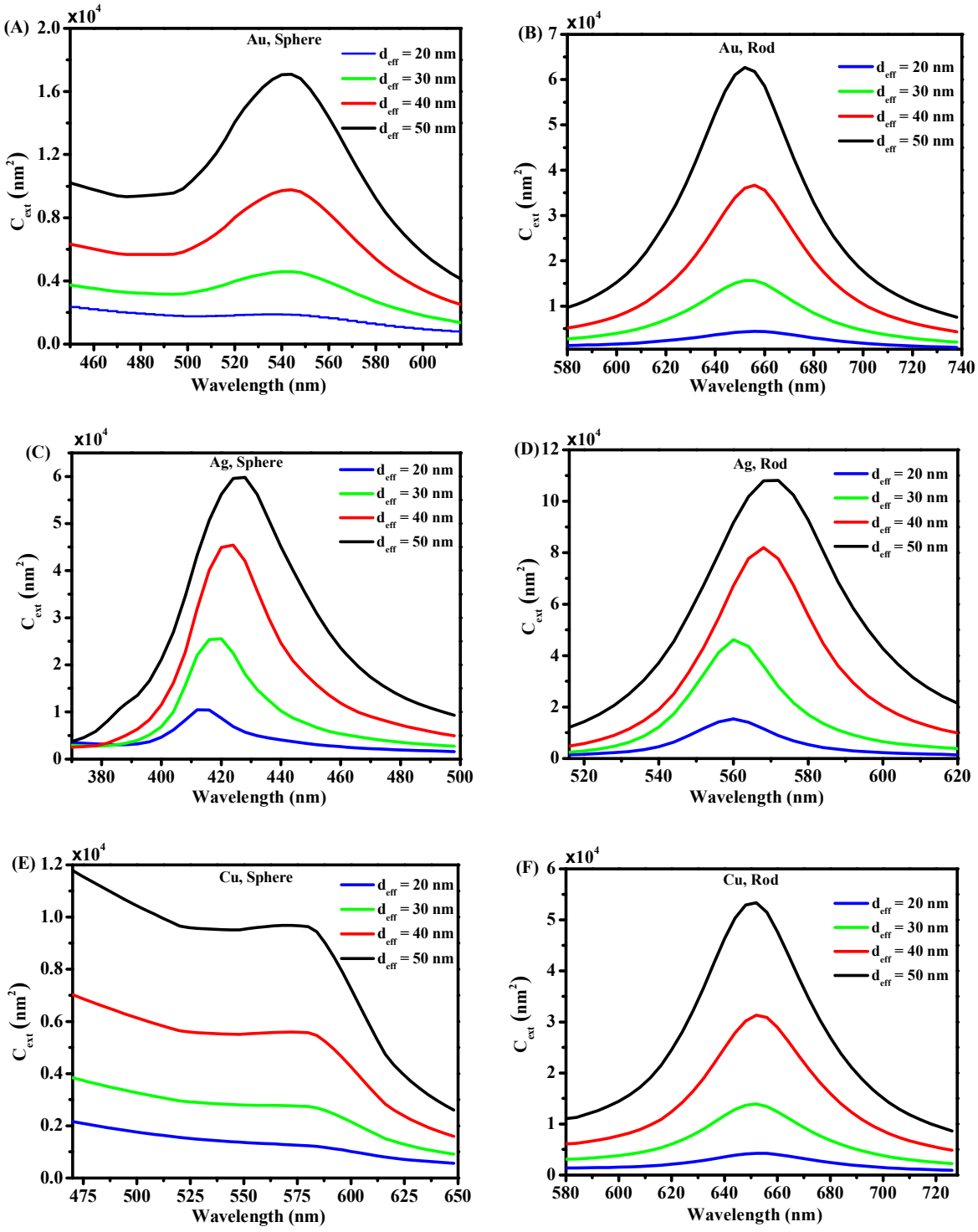

Figure 6.3. Extinction spectra of the different size and shape embedded monomeric NPs: (A) Au nanosphere, (B) Au nanorod, (C) Ag nanosphere, (D) Ag nanorod, (E) Cu nanosphere, and (F) Cu nanorod.

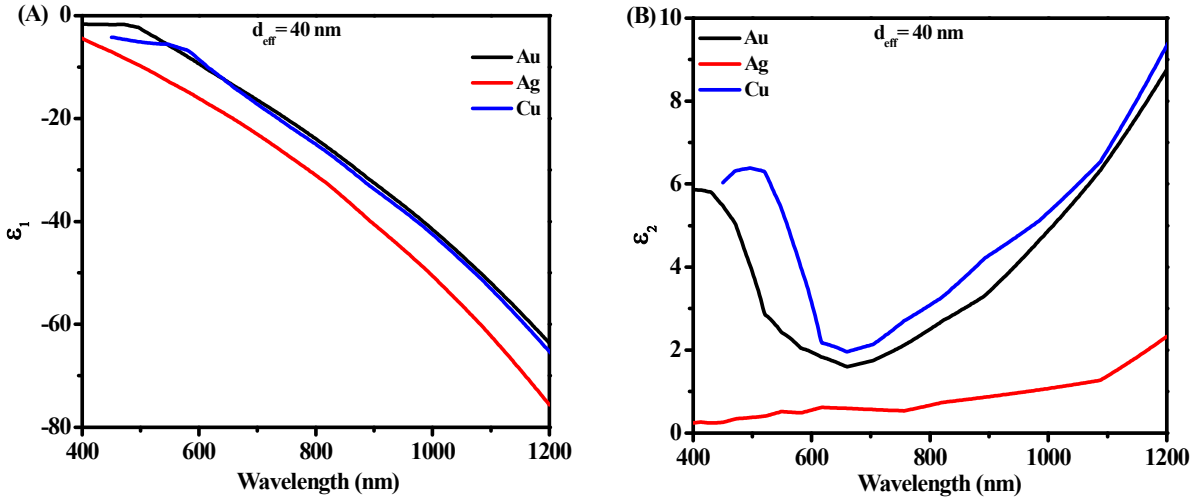

Figure 6.4. (A) Real, and (B) imaginary part of the dielectric function of Au, Ag, and Cu at d_{eff} = 40 nm.

6.3.1.2. Evolution of the LSPR Peak Wavelength with Aspect Ratio

In nanorod geometry, changing the AR alters the LSPR peak wavelength, the optical scattering, and absorption cross-sections as well as their relative contributions to the total extinction cross-section. Here, we investigated the AR ratio effect on the longitudinal mode properties of the single embedded Au, Ag, and Cu nanorods in a silica matrix with an effective diameter of 40 nm. Figure 6. 5 presents the change of the LSPR wavelength of the studied nanorod geometries versus the change of the AR. It should be noted that AR=1 is corresponding to the spherical NP. From this figure, we can see that the λ_{max} of all studied cases increases linearly with increasing the AR. The linear redshift of the λ_{max} on the aspect ratio of the embedded Au, Ag, and Cu nanorods are λ_{max} = 418 + 121 AR, λ_{max} = 290 + 137.2 AR, and λ_{max} = 444 + 109.8 AR, respectively. A similar trend has been seen in experiments [300] and simulations [9, 301] for nanorods in solution. As mentioned already, this observation is ascribed to increasing the polarizability and outer surface of the NP by increasing the AR which results in reducing the required excitation energy and redshifting the plasmonic peak [27].

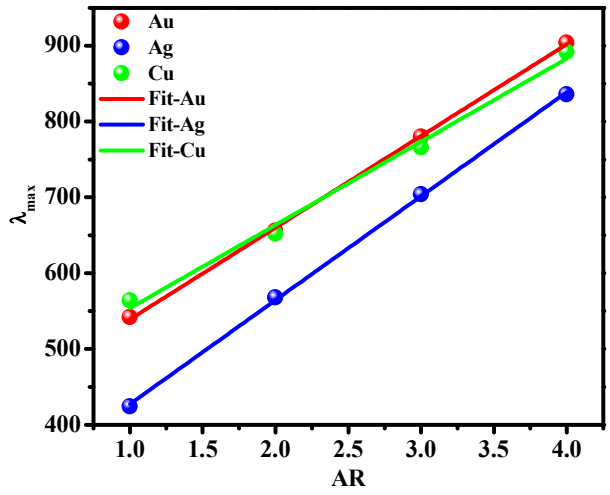

Figure 6.5. Changing the longitudinal mode LSPR wavelength of the extinction spectra of the Au, Ag, and Cu nanorods by altering their AR. In all cases, the effective diameter of the NPs is chosen to be 40 nm.

Besides the linear dependence of the LSPR wavelength to the AR, the peak of the extinction spectra of all investigated nanorods is increasing by increasing the AR (see Figure 6.6A). As can be seen from Figure 6.6A, the extinction spectra enhancing rates slow down by increasing the AR of Au and Cu nanorods, whereas, the extinction spectra of Ag nanorods show a clear linear increasing trend by further elongation and is much higher than the Au and Cu. Also, the relative enhancement of the scattering to the absorption can be influenced by changing the elongation of the NPs. To study this effect, the scattering quantum yield, which is defined as the ratio of the scattered cross-section to extinction one at each resonance wavelength, is given by

$$\eta = \frac{C_{scat}}{C_{ext}}|_{max} \tag{6.8}$$

where C_{scat} and C_{ext} are scattering and extinction cross-sections, respectively. Figure 6.6B shows the evolution of the η of the longitudinal mode in monomeric embedded Au, Ag, and Cu structures at a constant effective diameter of 40 nm. The results show that the embedded Ag NPs possess higher scattering quantum yield in comparison to the Au and Cu NPs. From this figure, we can see that by changing the AR from 1 to 2 in Au and Cu NPs the scattering quantum yields increase, reaches their maximum values at AR = 2, and then start to decrease by further stretching the NPs. It should be emphasized that by increasing the AR of the Au and Cu NPs from 1 to 2, their

corresponding scattering quantum yields increase from (0.084, 0.107) to (0.173, 0.187), respectively. However, the η of Ag NPs slightly depends on the elongation of the NP. The results mentioned above may be explained by carefully looking at the behavior of the imaginary part of the dielectric functions of each NP (see Figure 6.4B). Obviously, changing the AR of the Au and Cu from 1 to 2 shifts the corresponding LSPR wavelengths from ~ 550 nm to ~ 650 nm, and the further increase of the AR moves the LSPR peaks to the wavelengths longer than 650 nm (see Figure 6.5). As shown in Figure 6.4B, the ε_2 of both Au and Cu decrease in the wavelength range from ~ 550 nm to ~ 650 nm, whereas they show a clear trend of increasing by a further increase of the wavelength. The aforementioned trends of the imaginary part of the dielectric functions of the Au and Cu lead to increase of the corresponding scattering quantum yields in AR range from 1 to 2 and then result in reducing it with further elongation of the NPs as a consequence of increasing absorption contribution. However, the ε_2 of the Ag NPs is very small in the visible and near-infrared regions when compared to the Au and Cu (see Figure 6.4B) and increases slowly by increasing wavelength. This behavior of the ε_2 is the one possible reason for the higher observed η with a small shift in Ag NPs (see Figure 6.6B).

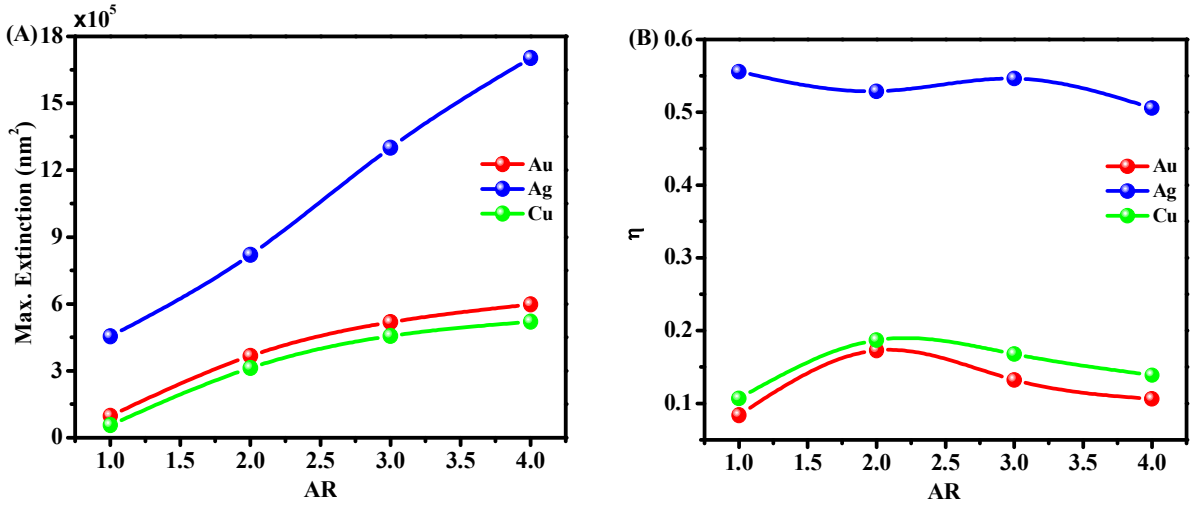

Figure 6.6. (A) Maximum of the extinction spectra and (B) Scattering quantum yield of the longitudinal mode versus aspect ratio of the NPs. In all cases, the effective diameter of the NPs is chosen to be 40 nm.

6.3.1.3. Electric Field Enhancement in Embedded Monomeric NPs

Figure 6.7 shows the DDA simulated electric field enhancement surface plot of the embedded plasmonic NPs with an effective diameter of the 40 nm at the x-z plane inside the matrix for y = 0.

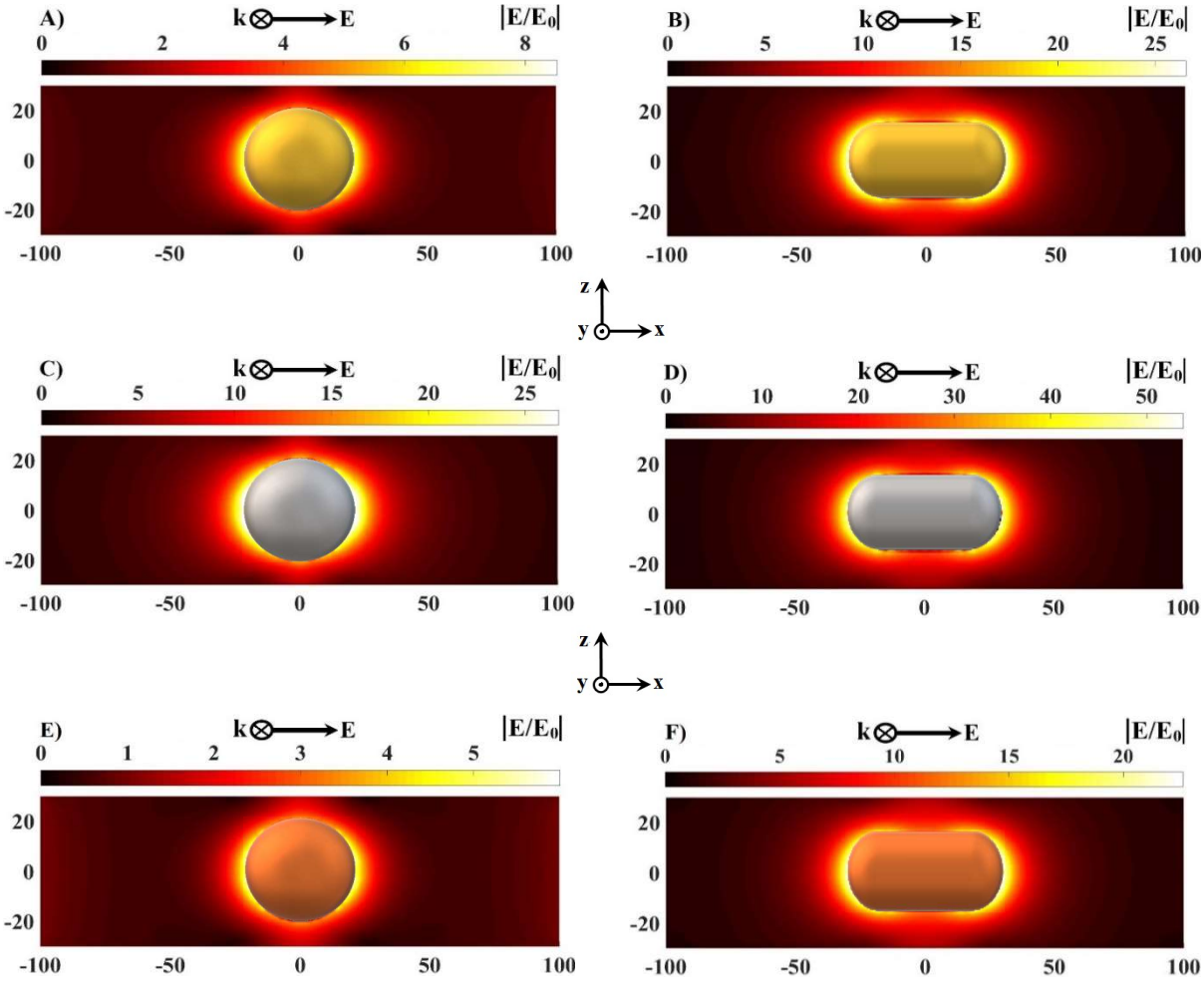

Figure 6.7. Electric field enhancement around single embedded plasmonic NPs at their corresponding LSPR wavelengths at the x-z plane and y = 0 for (A) spherical Au, (B) rod-shaped Au, (C) spherical Ag, (D) rod-shaped Ag, (E) spherical Cu, and (F) rod-shaped Cu. The effective diameter of each NP in each case is 40 nm.

It is worth mentioning that the aspect ratio of the embedded nanorods is set to be 2, and their electric fields have been calculated at their corresponding longitudinal LSPR wavelength. Here, we see that electric field enhancement for longitudinal mode around the rod-shaped NPs is

stronger than the corresponding spherical case. For example, the largest electric field around Au nanorod is 26 (times of the incident field), whereas it is 6 for the spherical case. This effect, again, can be attributable to the large polarizability and bigger surface area of the nanorod structures which results in stronger extinction spectra and higher electric field enhancement. A comparison of the results of Au, Ag, and Cu NPs reveals that the electric field enhancement of the Ag nanoparticles is much stronger than the Au and Cu. This observation is in agreement with the plasmonic spectra of these samples in the previous sections.

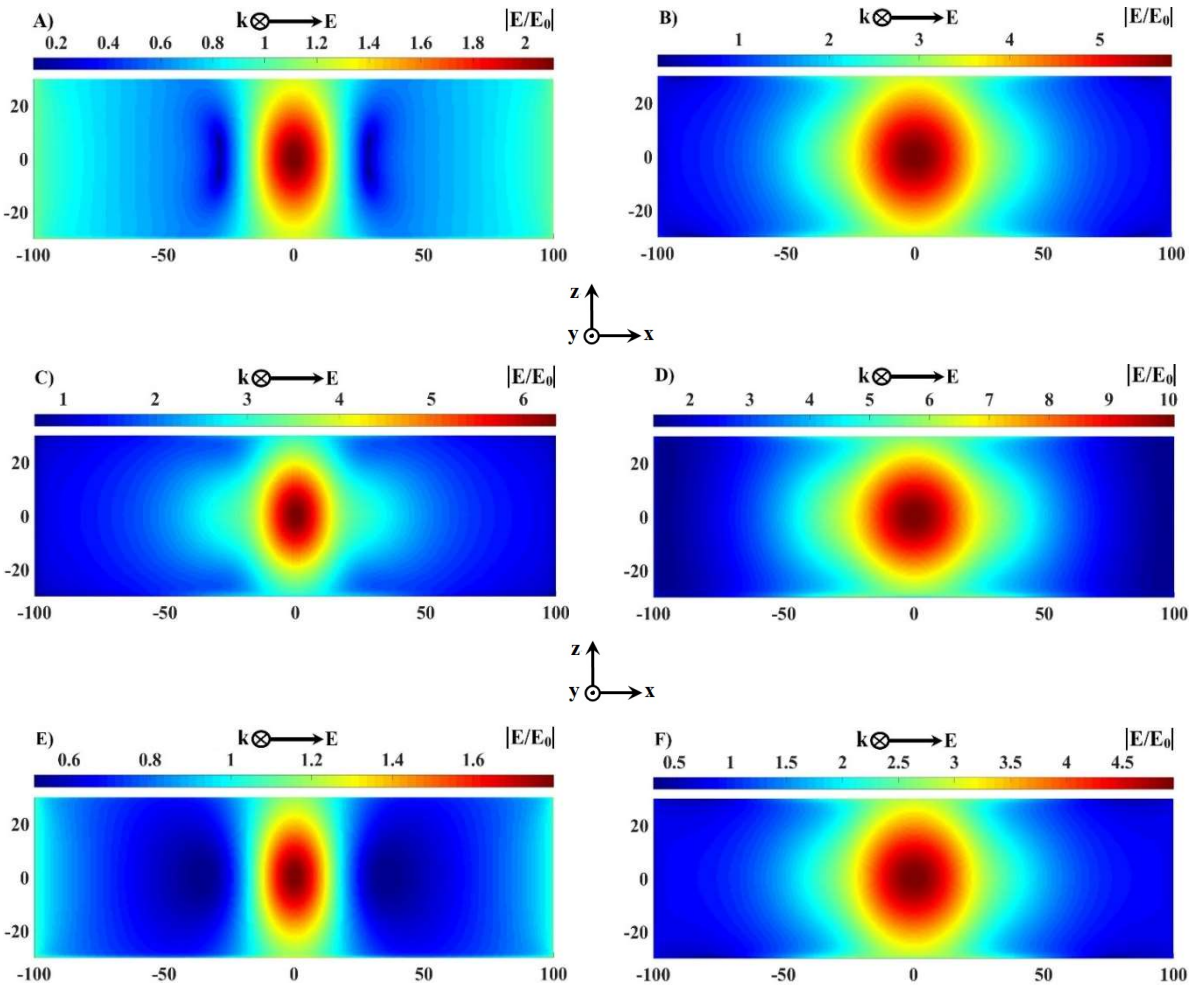

Figure 6.8. Electric field enhancement around single embedded plasmonic NPs at their corresponding LSPR wavelengths at x-z plane at surface of the matrix for (A) spherical Au, (B) rod-shaped Au, (C) spherical Ag, (D) rod-shaped Ag, (E) spherical Cu, and (F) rod-shaped Cu. The effective diameter of each NP in each case is 40 nm.

As mentioned in the introduction section, the electric field enhancement of the embedded NPs can be used to enhance the fluorescence of fluorophore molecules which placed on the surface of the matrix [147]. Thus, it is interesting to examine the electric field enhancement of the abovementioned structures at the surface of the matrix (see Figure 6.8). Since the effective diameter of the embedded NPs is constant, the average distance between the surface of the nanorod and the outer surface of the matrix is more than spherical ones. Interestingly, the results show that nanorods structures not only produce stronger electric fields at the outer surface of the matrix but also enhancing field at a larger surface area in comparison to the spherical ones. It is apparent from these figures that Ag nanorods are showing stronger electric field enhancement in comparison to other samples which make them a suitable candidate for embedded metal-fluorescence enhancement.

6.3.2. Embedded Dimeric Structures

When two nanoparticles are located in the close vicinity of each other, the electric dipoles of the one NP not only interact with other dipoles of that particle but also interact with the dipoles of the neighboring NP [61, 63, 103]. As a result of these interactions, plasmon oscillations of the two neighboring NPs become coupled. This coupling, which depends on the polarization direction of the incident light and the interparticle distance, can have a constructive or destructive effect on the nature of the plasmon excitation and electric field enhancement [61, 63, 103]. Here, we simulated the plasmonic properties of the longitudinal mode in the dimeric structures made of two embedded NPs with an effective diameter of 40 nm each. The polarization direction of the incident light is considered to be parallel to the long interparticle axis that leads to enhancing the extinction spectra and creating hot spot between the NPs. Also, the minimum separation distance from the surface of the one NP to other one was set to be 0.2 d_{eff}, since the electron cloud of one NP can tunnel to the neighbor NP at shorter distances which make the use of the dielectric function provided in Eq. 6.5 questionable [103].

6.3.2.1. Coupling Effect on the Optical Spectra

In this subsection, we have performed DDA calculations to simulate the coupling effect on the changing optical cross-sections and LSPR wavelength of the dimeric embedded structures. Figure 6.9 shows extinction, absorption, and scattering cross-sections of the embedded dimeric Au, Ag, and Cu structures for an interparticle distance of 0.2 d_{eff} (8 nm).

The spectra have been calculated for embedded nanospheres and nanorods. Also, for comparison, the optical spectra of the monomeric structure have been added to the figure. Since the direction of the incident light is set to be parallel to the interparticle distance, the coupling in the dimeric structures is constructive. As can be seen from Figure 6.9, the optical spectra of the dimeric structures not only enhanced due to the plasmonic coupling but also red-shifted when compared to the spectra of the corresponding monomeric structures.

The plasmonic coupling strength between the neighboring NPs depends on the spacing between NPs. To study this effect, we calculated the evolution of the LSPR peak in dimeric structures versus interparticle distance. As shown in Figure 6.10, the LSPR wavelength of all structures blue-shifts by increasing the separation distance between the neighboring NPs. This result may be explained by the fact that the coupling strength between NPs in dimeric structures reduces by increasing interparticle distance, which increases the required energy to excite plasmonic oscillations. It should be noted the spherical Cu NPs do not show a clear plasmonic peak at larger interparticle distances.

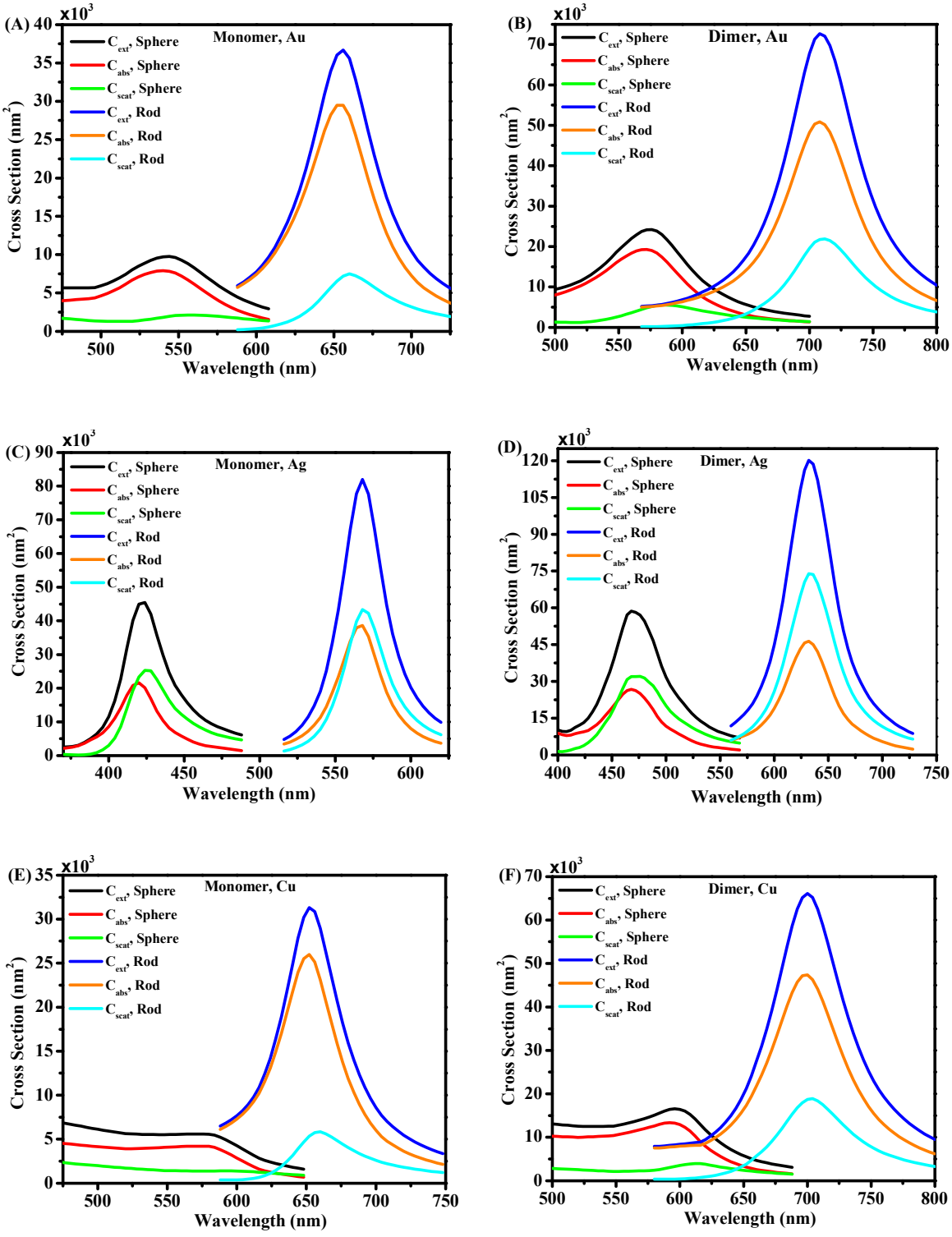

Figure 6.9. Optical spectra of the embedded nanosphere and nanorod: (A) monomeric Au, (B) dimeric Au, (C) monomeric Ag, (D) dimeric Ag, (E) monomeric Cu, and (D) dimeric Cu. The effective diameter of each nanoparticle is chosen to be 40 nm. In dimeric structures, the interparticle distance is 8 nm, and the incident light electric field is aligned to be parallel to the long interparticle axis.

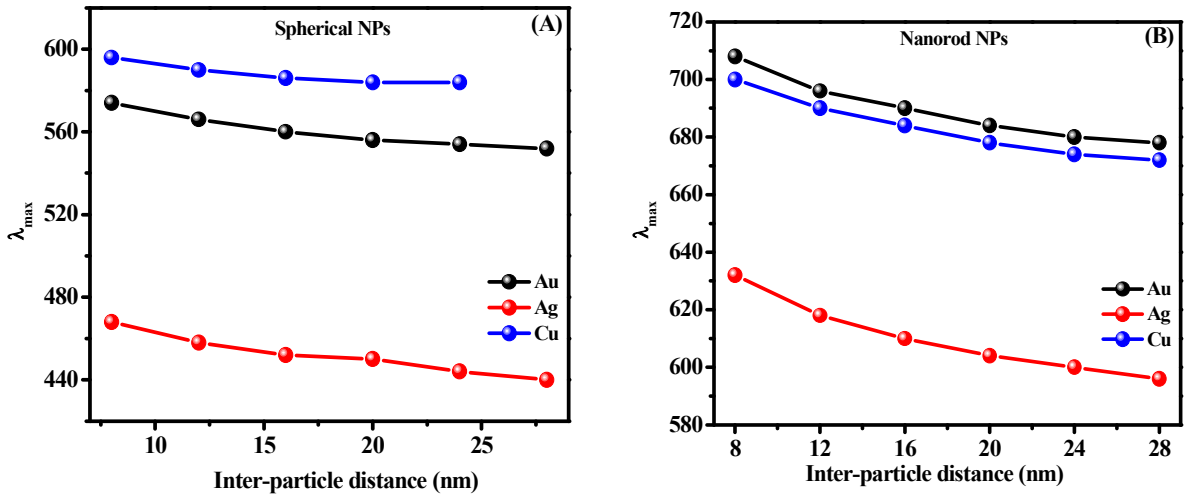

Figure 6.10. LSPR peak wavelength versus inter-particle distance in embedded dimeric Au, Ag, and Cu structures with (A) spherical, and (B) rod-shaped nanoparticles.

6.3.2.2. Coupling Effect on the Electric Field Enhancement

As noted in section 6.3.1.3., the single embedded nanoparticles create a strong electric field around themselves and also enhance the electric field at the outer surface of the matrix. It is therefore of interest to see how plasmonic coupling between the neighboring NPs will affect the electric field enhancement in dimeric structures. To study this effect, we have performed the DDA simulation to calculate the electric field of the aforementioned dimeric structures at the x-z plane inside the matrix for y = 0. The results have been obtained for the interparticle distance of 0.2 d_{eff} with the induced polarization along the interparticle long axis. Figure 6.11 shows the electric field enhancement surface plot of these structures for corresponding LSPR wavelengths (see Figure 6. 10). In all structures, we see a strong field enhancement between the pair of NPs. Again, this is attributable to the constructive plasmonic coupling, which produces a hot spot between the NPs. Similar to the monomeric structures, the rod-shaped Ag nanoparticles pairs produce stronger field enhancement in comparison to other dimeric structures. Comparing Figure 6.7 and 6.11 reveals that the maximum electric field in dimeric structures is at least two times stronger than the corresponding monomer structures. Interestingly, the ratio of field enhancement in a pair of nanospheres is more than the corresponding pair of the nanorods.

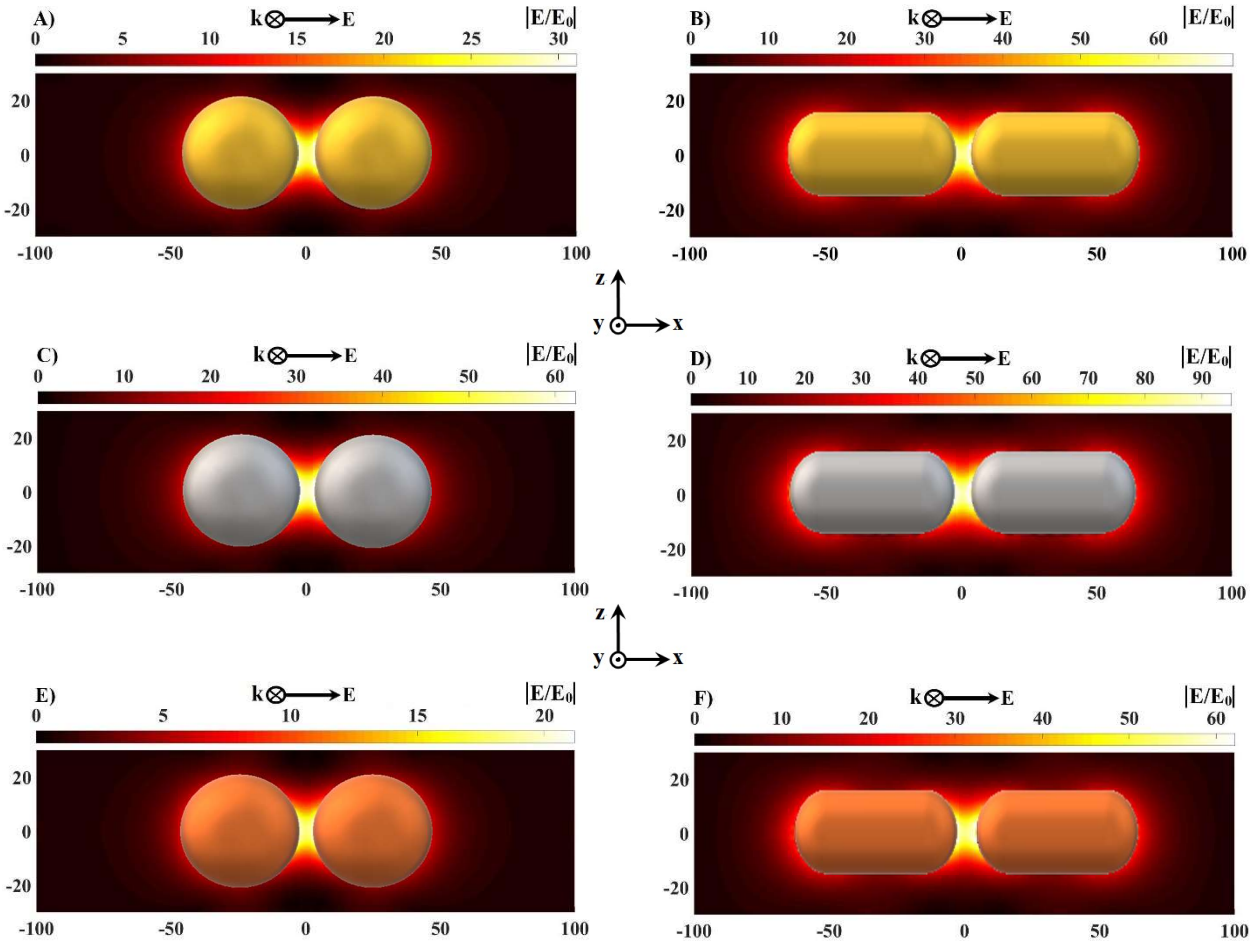

Figure 6.11. Creation of hot spot in the dimeric embedded NPs at their corresponding LSPR wavelengths at x-z plane and y = 0 for (A) spherical Au, (B) rod-shaped Au, (C) spherical Ag, (D) rod-shaped Ag, (E) spherical Cu, and (F) rod-shaped Cu. The effective diameter of each NP in each case is 40 nm, and the interparticle distance is set to be 8 nm.

Figure 6.12 shows the electric field enhancement of the above mentioned dimeric structures at the surface of the matrix. It can be seen that the plasmonic coupling has a small effect on the enhanced electric field on the surface of the NPs. The observed result could be attributed to a long distance between the center of the hot spot and the surface of the matrix. As the electric field is highly localized, the electric field between the NPs reduces by increasing the distance from the center of the hot spot and results in small field enhancement at the surface of the matrix due to the hot spot. It should be noted that there is a small difference between the maximum electric field on the surface of the matrix in the dimeric and monomeric structures of the Au and Cu. However, the main difference in the field pattern of the two structures is that in dimeric structures the effective

area that the electric field has been enhanced is bigger when compared with results of the monomeric structures, presented in Figure 6.8. By comparing Figure 6.8 and Figure 6.11, it can be observed that the maximum electric enhancement due to dimeric Ag NPs at the surface of the matrix is less than the corresponding monomeric structures. The reason for this unexpected result is not clear, but it may have something to do with the size of cubic meshes, which need to be reduced further in order to obtain a more accurate result.

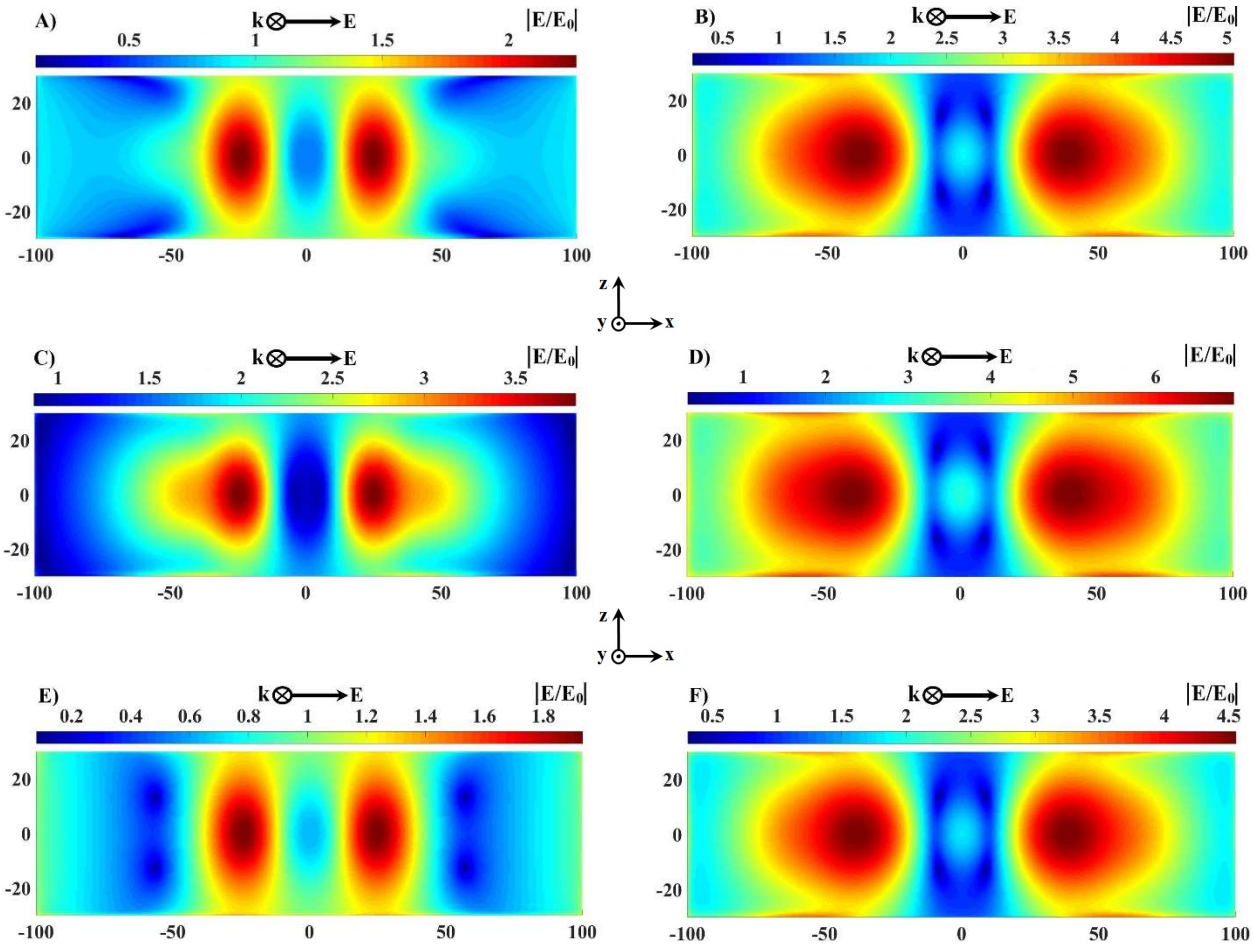

Figure 6.12. Field enhancement due to the embedded dimeric NPs at their corresponding LSPR wavelengths at the x-z plane for (A) spherical Au, (B) rod-shaped Au, (C) spherical Ag, (D) rod-shaped Ag, (E) spherical Cu, and (F) rod-shaped Cu, at the surface of the matrix. The effective diameter of each NP in each case is 40 nm, and interparticle distance is set to be 8 nm.

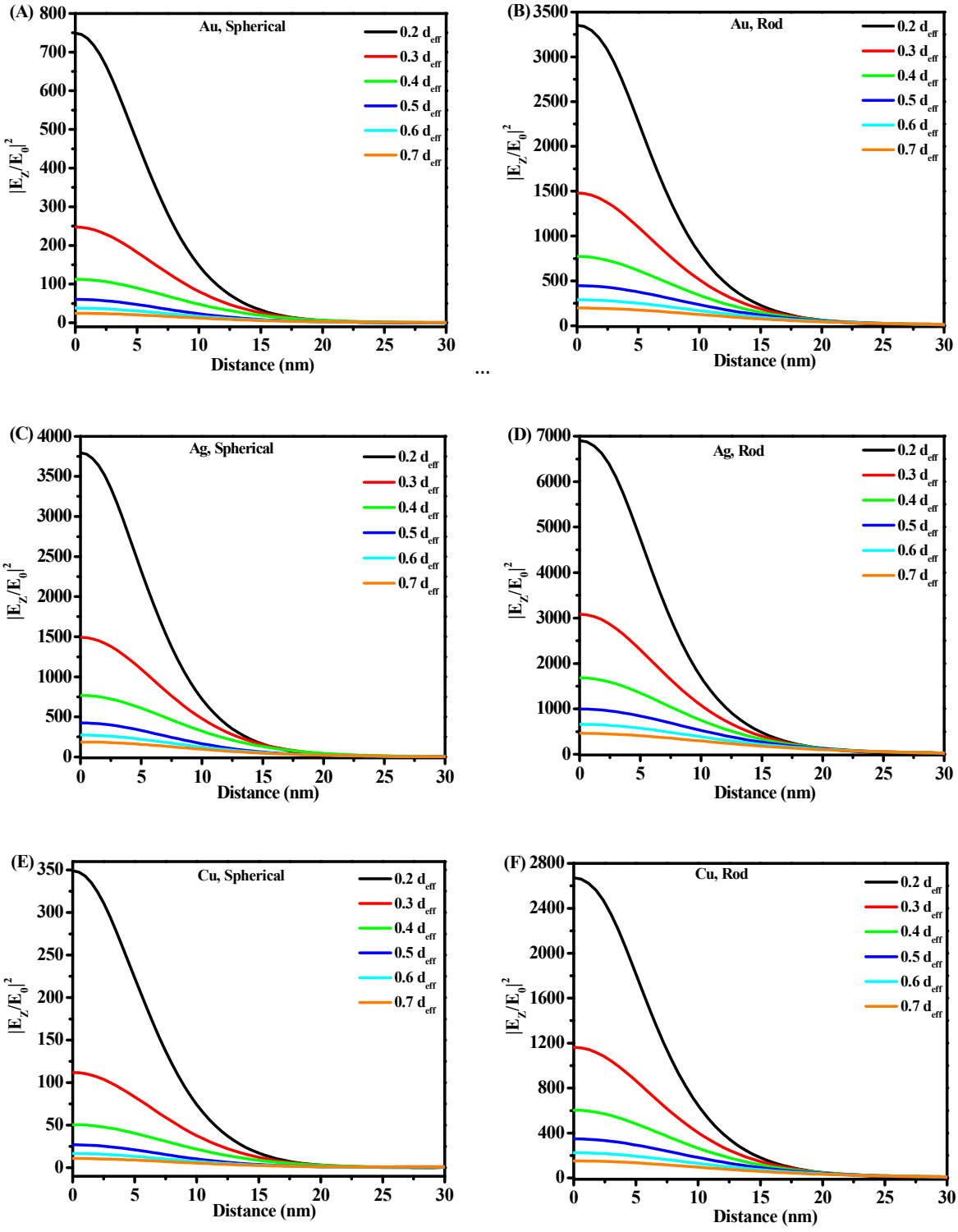

Figure 6.13. Evolution of the electric field versus distance from the center of the matrix in the dimeric structures for different interparticle distances: (A) spherical Au, (B) rod-shaped Au, (C) spherical Ag, (D) rod-shaped Ag, (E) spherical Cu, and (F) rod-shaped Cu. The effective diameter of each NP in each case is 40 nm.

To have a quantitative understanding of the localization length of enhanced electric field in the embedded dimeric structures, we simulated the evolution of $|E_z|^2$ from the center to the surface of the matrix for different interparticle spacing (see Figure 6.13). As expected, the E-field enhancement is very sensitive to the interparticle distance. The E-field enhancement is large for small interparticle separations due to the strong plasmonic coupling between neighboring NPs and significantly reduces by increasing the spacing between neighboring particles (see Figure 6.13). For example, for the spherical Au structure, at $d = 0.2\ d_{eff}$ the $|E_z/E_0|^2$ is 750 at the center of the hot spot which reduces three times by increasing interparticle distance to $d = 0.3\ d_{eff}$. Again, the rod-shaped Ag structure shows higher field enhancement in comparison to the other structures. The most interesting result to emerge from the data is that as the interparticle distance decreases, which leads to higher electric field enhancement between NPs, the $|E_z/E_0|^2$ decreases faster. In other words, the decay length is smaller for a higher amount of $|E_z/E_0|^2$. A possible explanation for this observation might be that the plasmonic coupling strength is increased by reducing the interparticle distance, which results in stronger localization of the enhanced electric field and reduction of the localization length.

6.3.3. Optical Properties of the Embedded Trimeric and Tetrameric Structures

In this section, we extended our calculation to the trimeric and tetrameric structures to investigate the effect of the number of embedded NPs on the optical extinction and plasmonic field enhancement. To do this, the effective diameter of each particle and interparticle distance were set to be 40 nm and $0.2\ d_{eff}$, respectively. The optical properties have been calculated for spherical-shaped embedded NPs, and the polarization direction of incident light was chosen to be parallel to the interparticle axis. Figure 6.14 shows the extinction cross-section of the trimeric and tetrameric configurations mentioned above. It is not surprising that the extinction spectra increase as the number of NPs increases. However, a comparison of the results of Figure 6.14 and Figure 6.9 reveals that the number of NPs has a small effect on the LSPR wavelength. This observation is due to the fact that the NPs only have strong interactions with the closest neighboring NPs.

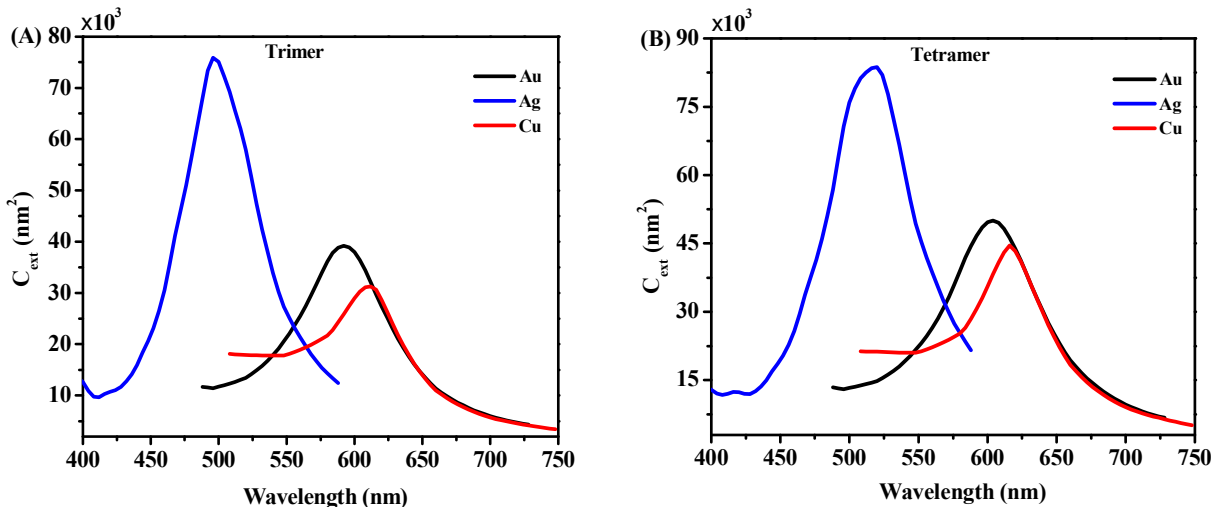

Figure 6.14. Extinction spectrum of the (A) Trimeric, and (B) Tetrameric embedded spherical structures of the Au, Ag, and Cu. The diameter of each NP is 40 nm, and the interparticle distance is set to be 8 nm. Also, the electric field is aligned to be parallel to the long interparticle axis (longitudinal mode).

To further investigate the number of NPs influence on the optical properties of the embedded NPs, we simulated electric field enhancement of the trimeric and tetrameric configurations mentioned above at two different planes: (1) x-z plane at y = 0, (2) at the surface of the matrix (see Figure 6.15 and 6.16). Except for Ag structures (for the same reason mentioned in the previous section), the maximum electric field enhancement between NPs (at x-z plane) increases by increasing number of the NPs. However, no significant differences were found between the maximum electric field enhancement in the dimeric, trimeric, and tetrameric structures.

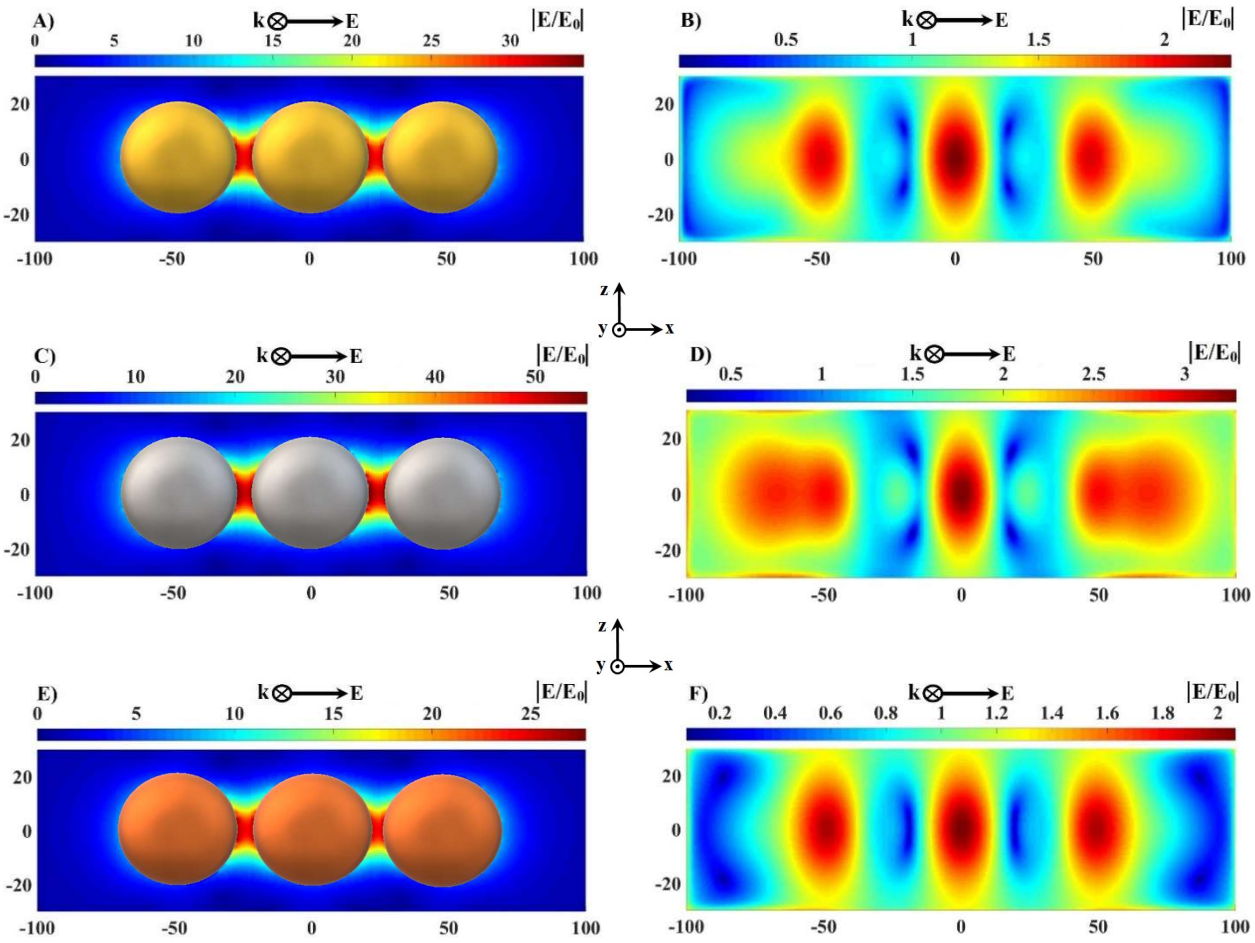

Figure 6.15. Field enhancement due to 3-embedded spherical NPs at their corresponding LSPR wavelengths and at x-z plane for (A) Au at y = 0, (B) Au at y = b/2, and (C) Ag at y = 0, (D) Ag at y = b/2, (E) Cu at y = 0, and (F) Cu at y = b/2. The effective diameter of each NP is 40 nm, and the interparticle distance is taken to be 8 nm.

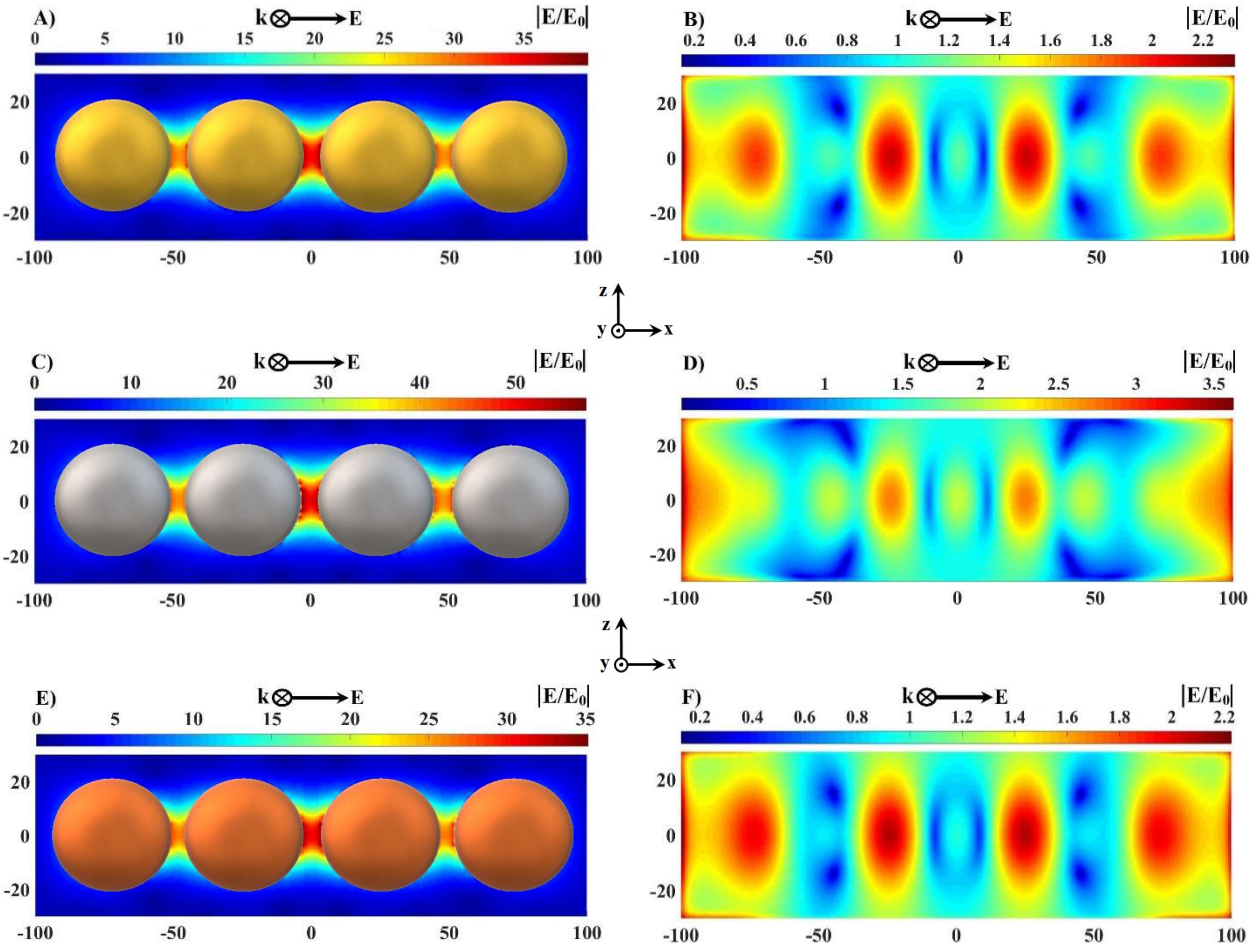

Figure 6.16. Field enhancement due to 4- embedded spherical NPs at their corresponding LSPR wavelengths and at xz plane for (A) Au at y=0, (B) Au at y=b/2, and (C) Ag at y=0, (D) Ag at y=b/2, (E) Cu at y=0, and (F) Cu at y=b/2. The effective diameter of each NP in each case is 40 nm and interparticle distance is 8 nm.

CHAPTER 7

CONCLUSIONS AND FUTURE WORKS

7.1. Conclusions

The plasmonic nanoparticles attracted enormous research interest in recent years due to their profound applications in inter-disciplinary areas of sciences such as biological imaging, plasmonic photo-thermal therapy, photovoltaics, plasmonic sensors, and molecular diagnostics. LSPR of the plasmonic NPs is responsible for novel spectroscopic fields such as surface-enhanced Raman spectroscopy, metal-enhanced luminescence, and plasmonic rulers. In this work, we investigated the following areas of the plasmonic NPs as detailed below:

E. This dissertation gives first a brief introduction regarding the characteristics of the plasmonic nanoparticles and reviews some of the LSPR applications.

B. In this dissertation, we reviewed the electromagnetic methods such as standard and Multi-layered Mie theory and discrete dipole approximation (DDA) as commonly used methods to describe optical properties of the nanoparticles. As part of the aim of this study, we introduced a package in MATLAB to calculate the optical properties of plasmonic NPs such as extinction, scattering and absorption efficiencies, electric field enhancement in monomeric structures and creation of the hot spots in dimeric structure using DDA. This study represents the first application of BCG, FFT to accelerate DDA in MATLAB software. All procedures of DDA discussed in detail and their corresponding MATLAB functions were introduced. In addition, to further accelerate the calculations of the polarization vector of the dipoles inside NPs, we transferred all of the initial data of the problem from CPU to GPU and run our simulation in it. By performing the calculations in GPU, the computation time decreased more with an increase in the number of the dipoles (decreasing size of mesh). For $N \sim 10^6$, the GPU performance is ~ 10 times faster than the CPU.

C. We explored the optical properties of the quantum-sized silver nanoparticles using both classical and quantum model. Due to discretization of the band structure by reducing the size of the NPs, the quantum model shows a different trend in comparison to the classical one by reducing the size of the NPs. We demonstrated that the quantum modeling LSPR prediction differs from the classical one for the particles with a diameter less than 10 nm. The quantum calculation has shown that LSPR energy of the quantum-sized Ag NPs blue shifts by reducing the size of the NPs while the classical simulation fails to predict this expected increase of the LSPR energy. Also, we observed that LSPR energy decreases linearly by increasing the refractive index of the surrounding medium. It has been observed that by increasing the size of the NPs the LSPR energy shift accelerated by changing the refractive index of the medium. Also, by calculating the total electric field around the NPs, we observed that FEF increases by increasing the size of the NPs and RI of the surrounding medium. Interestingly, the results show that the enhanced electric field decay length and consequently the sensing volume of the NPs increases by increasing the size of NPs, while it remains unchanged by changing the refractive index of the medium (~ 0.7 D). To further study the optical properties of quantum sized Ag NPs, we investigated the OAM ligand effect on the free-electron conductivity of surface and core regions, LSPR wavelength, absorption cross-sections, and the electric field enhancement using both classical and quantum models. By fitting the theoretical data to the corresponding experimental results in Pen et al. paper [76], the quantum model demonstrated that electron conductivity of both core and skin region decreased more by further reducing the size of NPs, while the classical simulation predicted a slight change in electron conductivity of the surface layer. The quantum simulations results were in agreement with the fact that by the shrinking dimension of the NPs the surface-to-volume ratios will increase, resulting in enhancing the surface effect and further reducing the conductivity of the core and skin region. Also, it has been observed that both models predicted that the amount of LSPR wavelength difference ($\Delta\lambda$) between the ligand-conjugated and ligand-free samples increases by reducing the size of the NPs. However, the quantum model observed larger $\Delta\lambda$ than the classical one for NPs less than 10 nm. By calculating the ΔA and ΔE, the quantum model predicted that these properties reduce more by further reducing the size of the NPs that are in agreement with increasing surface and ligand effect with reducing the size of the NPs.

D. We studied size and ligand effects on the electron-phonon relaxation time of the thiolate-protected plasmonic gold clusters using ultrafast transient absorption and multi-layered Mie theory. The electron-phonon relaxation dynamics measurements carried out on smallest-sized plasmonic gold clusters have shown interesting trends with regard to the effect of the ligand on the electron dynamics. The results show that the The electron dynamics of gold clusters with hexane thiol are in line with the results obtained for citrate-stabilized gold clusters as well as larger gold clusters with the same passivating ligand. The different electron dynamics observed for aromatic passivating ligands is ascribed to reduced electron conductivity offered by Au-π interaction and conjugation. The electron conductivity was modeled with three-layered Mie theory and the results have shown that all ligand passivated gold clusters have smaller surface conductivity when compared to citrate-stabilized gold NPs. Within the ligand-passivated clusters, TBBT, and SC_2Ph ligand passivated clusters have much smaller electron conductivity that can be attributed to the way the aromatic ligands interact with surface gold atoms. Especially, unique results were obtained for Au_{329} (SC_2Ph) that has shown smaller surface electron conductivity as well as two bleach maxima in TA spectra and can be attributed to specific π interactions between the ligand and Au on the surface creating a hybrid molecule/metallic state. However, similar π-conjugation was probably the reason for observing plasmon behavior for Au_{279}, which is smaller in size when compared to Au_{329}. In addition, it was found that the electron-phonon coupling of the samples conjugated with same chemical ligands (Au_{329} (SC_6), $Au_{\sim1400}$ (SC_6), and $Au_{\sim2000}$ (SC_6)) depend on the size of the cluster, wherein the electron conductivity increased with increase in the size of the cluster.

E. We investigated the effect of the size, shape, shell thickness and AR on the LSPR sensitivity of hollow-Au nanoshell structures. Six different shaped hollow/Au nanoshells structures were investigated that include: sphere, disk, rod, ellipsoid, rectangular block, and prism. From the results, it was observed that by reducing the shell thickness of the shells, the plasmonic coupling between the inner and outer surface of the Au shell increases that leads to shift of LSPR maximum to longer wavelengths and increasing its sensitivity. Also, results show that LSPR sensitivity increases with an increase in the size of NPs. From shape effect studies, it was demonstrated that rod and rectangular block nanoshells show

higher sensitivity when compared to other samples. In addition, the AR effect was simulated for rod and rectangular block nanoshells, which show higher sensitivity when compared to other structures. It is found that for both structures, LSPR peak shifts more and its sensitivity enhanced by increasing the AR of the nanoshells. This study has found that rod and rectangular block hollow/Au nanoshells possess higher LSPR sensitivity in comparison to other structures, which make them suitable candidates for sensing applications.

F. We studied the optical cross-sections and field enhancement of the sphere and rod-shaped embedded NPs, using the discrete dipole approximation method. To obtain a quantitative guide for the selection of nanoparticles for field enhancement applications such as metal-fluorescence enhancement and energy harvesting, a systematic study was performed to explore the aforementioned optical properties in embedded monomeric, dimeric, trimeric, and tetrameric NPs in silica matrix for three different metallic NPs viz. Au, Ag, and Cu. This theoretical study set out to determine the effect of the size, shape, aspect ratio, interparticle distance, and the number of the NPs effects on the aforementioned optical properties of the embedded NPs. By performing simulation in embedded monomeric structures, it was found that the plasmonic properties of all investigated cases significantly increase by increasing the size of the NPs. The results of this study have shown that longitudinal mode of the rod-shaped Ag NP possesses the highest extinction, and produces the strongest electric field around itself and at the surface of the matrix. Also, it was shown that by increasing the elongation of the embedded NPs not only the extinction spectra increases but also the LSPR wavelength redshifts due to increasing polarizability of the NPs. Interestingly, the scattering quantum yield of the Au and Cu NPs increases by increasing the AR from 1 to 2, shows saturation around AR = 2, and then turn over and starts to reduce by further increasing the elongation of the NPs. We observed that the η of Ag NPs is much higher than the Au and Cu at different AR but slightly changes with stretching the NP, possibly due to the small variation of the imaginary part of the dielectric function of the Ag NPs in the studied wavelength region. To study the coupling effect on the optical properties of the embedded NPs, we calculated the extinction, absorption, and scattering cross sections in embedded dimeric structures. The results of the longitudinal

modes in dimeric structures show an increase in the optical cross-sections and a strong field enhancement at the junction of the neighboring NPs as well as a redshift in LSPR wavelength when compared to the corresponding monomeric configurations. Moreover, it was observed that electric field enhancement between the embedded NPs is strong at shorter distances; however, it decays faster as the spacing between neighboring NPs decrease. An additional goal of this research was to investigate the influence of the number of embedded NPs on the optical properties of the NPs. The simulation results show that by increasing the number of the embedded plasmonic NPs in the matrix, the extinction spectra increases, while the LSPR wavelength and maximum field enhancement between NPs experience small changing.

7.2. Future Works

This research provides the following insights for future research:

I. Further work will need to be done to extend the DDA package to calculate the optical properties of the NPs near a planer surface and in periodic structures.

II. Further theoretical investigation of the ligand effect on the electron relaxation dynamics of the small-sized Au cluster using DFT is strongly recommended.

III. Another possible area of future research would be investigating LSPR sensitivity of the three-layered nanoparticles with a different shape. It is expected that coupling between the first and the second regions, and between the second and third regions redshifts LSPR peak significantly and increases the LSPR sensitivity and figure of merit (FOM). A three-layered structure will provide an additional adjusting parameter to design a structure with higher LSPR sensitivity and FOM.

REFERENCES

1. Bohren CF, Huffman DR (1983) Absorption and Scattering of Light by Small Particles. John Wiley & Sons.

2. Vilayurganpathy S (2013) Localized surface plasmon resonance induced structure-property relationships of metal nanostructures. Western Michigan University

3. Trügler A (2011) Optical properties of metallic nanoparticles. Karl–Franzens–Universität Graz.

4. Barmer DJ, Freestone IC (1990) An investigation of the origin of the colour of the Lycurgus cup by analytical transmission electron microscopy. Archaeometry 32:33–45. https://doi.org/10.1111/j.1475-4754.1990.tb01079.x

5. Wagner FE, Haslbeck S, Stievano L, et al (2000) Before striking gold in gold-ruby glass. Nature 407:691–692

6. https://www.britishmuseum.org/

7. Atwater HA, Polman A (2010) Plasmonics for improved photovoltaic devices. Nat Mater 9:205–213. https://doi.org/10.1038/nmat2629

8. Zhou M, Higaki T, Hu G, et al (2019) Three-orders-of-magnitude variation of carrier lifetimes with crystal phase of gold nanoclusters. Science (80-) 364:279–282. https://doi.org/10.1126/science.aaw8007

9. Jain PK, Lee KS, El-Sayed IH, El-Sayed MA (2006) Calculated absorption and scattering properties of gold nanoparticles of different size, shape, and composition: Applications in biological imaging and biomedicine. J Phys Chem B 110:7238–7248. https://doi.org/10.1021/jp057170o

10. Loo C, Lowery A, Halas N, et al (2005) Immunotargeted Nanoshells for Integrated Cancer

Imaging and Therapy. Nano Lett 5:709–711. https://doi.org/10.1021/nl050127s

11. El-Sayed IH, Huang X, El-Sayed MA (2005) Surface plasmon resonance scattering and absorption of anti-EGFR antibody conjugated gold nanoparticles in cancer diagnostics: Applications in oral cancer. Nano Lett 5:829–834. https://doi.org/10.1021/nl050074e

12. Huang X, El-Sayed IH, Qian W, El-Sayed MA (2006) Cancer cell imaging and photothermal therapy in the near-infrared region by using gold nanorods. J Am Chem Soc 128:2115–2120. https://doi.org/10.1021/ja057254a

13. Lermé J, Celep G, Broyer M, et al (2005) Effects of confinement on the electron and lattice dynamics in metal nanoparticles. Eur Phys J D 34:199–204. https://doi.org/10.1140/epjd/e2005-00107-8

14. Jain PK, Huang X, El-Sayed IH, El-Sayed MA (2008) Noble metals on the nanoscale: Optical and photothermal properties and some applications in imaging, sensing, biology, and medicine. Acc Chem Res 41:1578–1586. https://doi.org/10.1021/ar7002804

15. Huang X, Jain PK, El-sayed IH, El-Sayed MA (2008) Plasmonic photothermal therapy (PPTT) using gold nanoparticles. Lasers Med Sci 23:217–228. https://doi.org/10.1007/s10103-007-0470-x

16. Khlebtsov B, Zharov V, Melnikov A, et al (2006) Optical amplification of photothermal therapy with gold nanoparticles and nanoclusters. Nanotechnology 17:5167–5179. https://doi.org/10.1088/0957-4484/17/20/022

17. Huang X, El-sayed MA (2011) Plasmonic photo-thermal therapy (PPTT). Alexandria J Med 47:1–9. https://doi.org/10.1016/j.ajme.2011.01.001

18. Huang X, El-sayed MA (2010) Gold nanoparticles: Optical properties and implementations in cancer diagnosis and photothermal therapy. J Adv Res 1:13–28. https://doi.org/10.1016/j.jare.2010.02.002

19. El-sayed IH, Huang X, El-sayed MA (2006) Selective laser photo-thermal therapy of epithelial carcinoma using anti-EGFR antibody conjugated gold nanoparticles. Cancer Lett 239:129–135. https://doi.org/10.1016/j.canlet.2005.07.035

20. Hirsch LR, Stafford RJ, Bankson JA, et al (2003) Nanoshell-mediated near-infrared thermal therapy of tumors under magnetic resonance guidance. PNAS 100:13549–13554. https://doi.org/10.1073/pnas.2232479100

21. Sadrolhosseini AR, Shafie S, Fen YW (2019) Nanoplasmonic Sensor Based on Surface Plasmon-Coupled Emission : Review. Jouranl Appl Sci 9:1–13. https://doi.org/10.3390/app9071497

22. Zhu S, Li H, Yang M, Pang SW (2018) Label-free detection of live cancer cells and DNA hybridization using 3D multilayered plasmonic biosensor. Nanotechnology 29:1–13. https://doi.org/10.1088/1361-6528/aac8fb

23. Špačková B, Wrobel P, Bocková M, Homola J (2016) Optical Biosensors Based on Plasmonic Nanostructures: A Review. Proc IEEE 104:2380–2408. https://doi.org/10.1109/JPROC.2016.2624340

24. Spadavecchia J, Barras A, Lyskawa J, et al (2013) Approach for plasmonic based DNA sensing: Amplification of the wavelength shift and simultaneous detection of the plasmon modes of gold nanostructures. Anal Chem 85:3288–3296. https://doi.org/10.1021/ac3036316

25. Jans H, Huo Q (2012) Gold nanoparticle-enabled biological and chemical detection and analysis. Chem Soc Rev 41:2849–2866. https://doi.org/10.1039/c1cs15280g

26. Wu H-J, Henzie J, Lin W-C, et al (2012) Membrane-protein binding measured with solution-phase plasmonic nanocube sensors. Nat Methods 9:1189–1191. https://doi.org/10.1038/nmeth.2211

27. Shabaninezhad M, Ramakrishna G (2019) Theoretical investigation of size, shape, and aspect ratio effect on the LSPR sensitivity of hollow-gold nanoshells. J Chem Phys 150:1–9. https://doi.org/10.1063/1.5090885

28. Sun Y, Cai H, Wang X, Zhan S (2019) Optimization methodology for structural multiparameter surface plasmon resonance sensors in different modulation modes based on particle swarm optimization. Opt Commun 431:142–150. https://doi.org/10.1016/j.optcom.

2018.09.027

29. Fathi F, Rashidi MR, Omidi Y (2019) Ultra-sensitive detection by metal nanoparticles-mediated enhanced SPR biosensors. Talanta 192:118–127. https://doi.org/10.1016/j.talanta.2018.09.023

30. Jiang J, Wang X, Li S, et al (2018) Plasmonic nano-arrays for ultrasensitive bio-sensing. Nanophotonics 7:1517–1531. https://doi.org/10.1515/nanoph-2018-0023

31. Mejía-Salazar JR, Oliveira ON (2018) Plasmonic Biosensing. Chem Rev 118:10617–10625. https://doi.org/10.1021/acs.chemrev.8b00359

32. Luan J, Xu T, Cashin J, et al (2018) Environmental Stability of Plasmonic Biosensors Based on Natural versus Artificial Antibody. Anal Chem 90:7880–7887. https://doi.org/10.1021/acs.analchem.7b05470

33. Chang YC, Chung HC, Lu S-C, Guo T-F (2013) A large-scale sub-100 nm Au nanodisk array fabricated using nanospherical-lens lithography: A low-cost localized surface plasmon resonance sensor. Nanotechnology 24:1–7. https://doi.org/10.1088/0957-4484/24/9/095302

34. Valsecchi C, Brolo AG (2013) Periodic metallic nanostructures as plasmonic chemical sensors. Langmuir 29:5638–5649. https://doi.org/10.1021/la400085r

35. Abbas A, Tian L, Morrissey JJ, et al (2013) Hot spot-localized artificial antibodies for label-free plasmonic biosensing. Adv Funct Mater 23:1789–1797. https://doi.org/10.1002/adfm.201202370

36. Li Y, Jing C, Zhang L, Long Y-T (2012) Resonance scattering particles as biological nanosensors in vitro and in vivo. Chem Soc Rev 41:632–642. https://doi.org/10.1039/c1cs15143f

37. Swaim JD, Knittel J, Bowen WP (2011) Detection limits in whispering gallery biosensors with plasmonic enhancement. Appl Phys Lett 99:1–4. https://doi.org/10.1063/1.3669398

38. Vazquez-Mena O, Sannomiya T, Villanueva LG, et al (2011) Metallic nanodot arrays by stencil lithography for plasmonic biosensing applications. ACS Nano 5:844–853.

https://doi.org/10.1021/nn1019253

39. Lee S-W, Lee K-S, Ahn J, et al (2011) Highly sensitive biosensing using arrays of plasmonic Au nanodisks realized by nanoimprint lithography. ACS Nano 5:897–904. https://doi.org/10.1021/nn102041m

40. Guo L, Ferhan AR, Lee K, Kim D-H (2011) Nanoarray-based biomolecular detection using individual Au nanoparticles with minimized localized surface plasmon resonance variations. Anal Chem 83:2605–2612. https://doi.org/10.1021/ac200432c

41. Yu Q, Guan P, Qin D, et al (2008) Inverted size-dependence of surface-enhanced Raman scattering on gold nanohole and nanodisk arrays. Nano Lett 8:1923–1928. https://doi.org/10.1021/nl0806163

42. Zheng P, Kasani S, Shi X, et al (2018) Detection of nitrite with a surface-enhanced Raman scattering sensor based on silver nanopyramid array. Anal Chim Acta 1040:158–165. https://doi.org/10.1016/j.aca.2018.08.022

43. Talley CE, Jackson JB, Oubre C, et al (2005) Surface-enhanced Raman scattering from individual Au nanoparticles and nanoparticle dimer substrates. Nano Lett 5:1569–1574. https://doi.org/10.1021/nl050928v

44. Jackson JB, Westcott SL, Hirsch LR, et al (2003) Controlling the surface enhanced Raman effect via the nanoshell geometry. Appl Phys Lett 82:257–259. https://doi.org/10.1063/1.1534916

45. Amendola V, Pilot R, Frasconi M, et al (2017) Surface plasmon resonance in gold nanoparticles: a review. J Phys Condens Matter 29:1–48. https://doi.org/10.1088/1361-648X/aa60f3

46. Katyal J (2018) Plasmonic coupling in Au , Ag and Al nanosphere homo-dimers for sensing and SERS. Adv Electromagn 83–90. https://doi.org/10.7716/aem.v7i2.563

47. Huang X, El-Sayed IH, Qian W, El-Sayed MA (2007) Cancer cells assemble and align gold nanorods conjugated to antibodies to produce highly enhanced, sharp, and polarized surface Raman spectra: A potential cancer diagnostic marker. Nano Lett 7:1591–1597.

https://doi.org/10.1021/nl070472c

48. Masson JF (2017) Surface Plasmon Resonance Clinical Biosensors for Medical Diagnostics. ACS Sensors 2:16–30. https://doi.org/10.1021/acssensors.6b00763

49. Jain PK, Huang W, El-Sayed MA (2007) On the universal scaling behavior of the distance decay of plasmon coupling in metal nanoparticle pairs: A plasmon ruler equation. Nano Lett 7:2080–2088. https://doi.org/10.1021/nl071008a

50. Maier SA (2007) Plasmonics Fundamentals and Applications. Springer

51. Han Z, Bozhevolnyi SI (2013) Radiation guiding with surface plasmon polaritons. Reports Prog Phys 76:1–37. https://doi.org/10.1088/0034-4885/76/1/016402

52. Pitarke JM, Silkin VM, Chulkov E V., Echenique PM (2007) Theory of surface plasmons and surface-plasmon polaritons. Reports Prog Phys 70:1–87. https://doi.org/10.1088/0034-4885/70/1/R01

53. Barnes WL, Dereux A, Ebbesen TW (2003) Surface plasmon subwavelength optics. Nature 424:824–830

54. Raether H (1988) Surface Plasmons on Smooth and Rough Surfaces and on Gratings. Springer-Verlag, USA, New York

55. Jackson JD (1999) Classical Electrodynamics, Third Edit. JOHN WILEY & SONS, INC, Hoboken, NJ

56. Otto A (1968) Excitation of Nonradiative Surface Plasma Waves in Silver by the Method of Frustrated Total Reflection. Zeitschrift für Phys 216:398–410

57. Akowuah EK, Gorman T, Haxha S (2009) Design and optimization of a novel surface plasmon resonance biosensor based on Otto configuration. Opt Express 17:491–496

58. Leong H-S, Guo J, Lindquist RG, Liu QH (2009) Surface plasmon resonance in nanostructured metal films under the Kretschmann configuration. J Appl Phys 106:1–5. https://doi.org/10.1063/1.3273359

59. Willets KA, Duyne RP Van (2007) Localized Surface Plasmon Resonance Spectroscopy

and Sensing. https://doi.org/10.1146/annurev.physchem.58.032806.104607

60. Jain PK, El-Sayed MA (2008) Noble metal nanoparticle Pairs: Effect of medium for enhanced nanosensing. Nano Lett 8:4347–4352. https://doi.org/10.1021/nl8021835

61. Jain PK, Eustis S, El-Sayed MA (2006) Plasmon coupling in nanorod assemblies: Optical absorption, discrete dipole approximation simulation, and exciton-coupling model. J Phys Chem B 110:18243–18253. https://doi.org/10.1021/jp063879z

62. Jain PK, El-Sayed MA (2007) Universal scaling of plasmon coupling in metal nanostructures: Extension from particle pairs to nanoshells. Nano Lett 7:2854–2858. https://doi.org/10.1021/nl071496m

63. Jain PK, El-Sayed MA (2010) Plasmonic coupling in noble metal nanostructures. Chem Phys Lett 487:153–164. https://doi.org/10.1016/j.cplett.2010.01.062

64. Lee K-S, El-Sayed MA (2005) Dependence of the enhanced optical scattering efficiency relative to that of absorption for gold metal nanorods on aspect ratio, size, end-cap shape, and medium refractive index. J Phys Chem B 109:20331–20338. https://doi.org/10.1021/jp054385p

65. Kelly KL, Coronado E, Zhao LL, Schatz GC (2003) The optical properties of metal nanoparticles: The influence of size, shape, and dielectric environment. J Phys Chem B 107:668–677. https://doi.org/10.1021/jp026731y

66. (2019) Chemists manipulate the quantum states of gold nanoclusters. 1–2. https://doi.org/10.1126/science.aaw8007

67. Lee J-H, Cho H-Y, Choi HK, et al (2018) Application of gold nanoparticle to plasmonic biosensors. Int J Mol Sci 19:1–14. https://doi.org/10.3390/ijms19072021

68. Guo L, Jackman JA, Yang HH, et al (2015) Strategies for enhancing the sensitivity of plasmonic nanosensors. Nano Today 10:213–239. https://doi.org/10.1016/j.nantod.2015.02.007

69. Daniel M-C, Astruc D (2004) Gold Nanoparticles: Assembly, Supramolecular Chemistry, Quantum-Size Related Properties and Applications toward Biology, Catalysis and

Nanotechnology. Chem Rev 104:293–346. https://doi.org/10.1021/cr030698

70. Zharov VP, Kim J, Curiel DT, Everts M (2005) Self-assembling nanoclusters in living systems : application for integrated photothermal nanodiagnostics and nanotherapy. Nanomedicine Nanotechnology, Biol Med 1:326–345. https://doi.org/10.1016/j.nano.2005.10.006

71. Pitsillides CM, Joe EK, Wei X, et al (2003) Selective Cell Targeting with Light-Absorbing Microparticles and Nanoparticles. Biophys J 84:4023–4032

72. Lakowicz JR (2006) Principles of fluorescence spectroscopy, third edit. Springer-Verlag, USA, New York

73. Ming T, Zhao L, Yang Z, et al (2009) Strong Polarization Dependence of Plasmon-Enhanced Fluorescence on Single Gold Nanorods. Nano Lett 9:3896–3903. https://doi.org/10.1021/nl902095q

74. Liu S, Huang L, Li J, et al (2013) Simultaneous Excitation and Emission Enhancement of Fluorescence Assisted by Double Plasmon Modes of Gold Nanorods. J Phys Chem C 117:10636–10642. https://doi.org/10.1021/jp4001626

75. Kreibig U, Vollmer M (1995) Optical Properties of Metal Clusters. Springer

76. Peng S, McMahon JM, Schatz GC, et al (2010) Reversing the size-dependence of surface plasmon resonances. PNAS 107:14530–14534. https://doi.org/10.1073/pnas.1007524107

77. Romann J, Wei J, Pileni MP (2015) Computational matching of surface plasmon resonance: Interactions between silver nanoparticles and ligands. J Phys Chem C 119:11094–11099. https://doi.org/10.1021/jp511859p

78. Genzel L, Martin TP, Kreibig U (1975) Dielectric function and plasma resonances of small metal particles. Zeitschrift für Phys B Condens Matter 21:339–346. https://doi.org/10.1007/BF01325393

79. Scholl JA, Koh AL, Dionne JA (2012) Quantum plasmon resonances of individual metallic nanoparticles. Nature 483:421–428. https://doi.org/10.1038/nature10904

80. Mie G (1908) Beiträge zur Optik trüber Medien, speziell kolloidaler Metallösungen. Ann Phys 330:377–445. https://doi.org/10.1002/andp.19083300302

81. van de Hulst HC (1981) Light Scattering by Small Particles. Dover Publications, New York

82. Yang W (2003) Improved Recursive Algorithm for Light Scattering by a Multilayered Sphere. Appl Opt 42:1710–1720. https://doi.org/10.1364/AO.42.001710

83. Amendola V, Bakr OM, Stellacci F (2010) A study of the surface plasmon resonance of silver nanoparticles by the discrete dipole approximation method: Effect of shape, size, structure, and assembly. Plasmonics 5:85–97. https://doi.org/10.1007/s11468-009-9120-4

84. Zhao J, Pinchuk AO, Mcmahon JM, et al (2008) Methods for Describing the Electromagnetic Properties of Silver and Gold Nanoparticles. Acc Chem Res 41:1710–1720. https://doi.org/10.1021/ar800028j CCC

85. Purcell EM, Pennypacker CR (1973) Scattering and Absorption of Light by Nonspherical Dielectric Grains. Astrophys J 186:705–714. https://doi.org/10.1086/152538

86. Goodman JJ, Draine BT, Flatau PJ (1991) Application of fast-Fourier-transform techniques to the discrete-dipole approximation. Opt Lett 16:1198–1200

87. Draine BT (1988) The discrete-dipole approximation and its application to interstellar graphite grains. Astrophys J 333:848–872

88. Flatau PJ, Stephens GL, Draine BT (1990) Light scattering by rectangular solids in the discrete-dipole approximation: a new algorithm exploiting the Block–Toeplitz structure. J Opt Soc Am A 7:593–600. https://doi.org/10.1364/JOSAA.7.000593

89. Kumara C, Hoque MM, Zuo X, et al (2018) Isolation of a 300 kDa, Au∼1400 Gold Compound, the Standard 3.6 nm Capstone to a Series of Plasmonic Nanocrystals Protected by Aliphatic-like Thiolates. J Phys Chem Lett 9:6825–6832. https://doi.org/10.1021/acs.jpclett.8b02993

90. Jones TC, Sumner L, Ramakrishna G, et al (2018) Bulky t-Butyl Thiolated Gold Nanomolecular Series: Synthesis, Characterization, Optical Properties, and Electrocatalysis. J Phys Chem C 122:17726–17737. https://doi.org/10.1021/acs.jpcc.

8b01106

91. Rambukwella M, Sakthivel NA, Delcamp JH, et al (2018) Ligand Structure Determines Nanoparticles ' Atomic Structure , Metal-Ligand Interface and Properties. Front Chem 6:1–17. https://doi.org/10.3389/fchem.2018.00330

92. Sakthivel NA, Stener M, Sementa L, et al (2018) Au 279 (SR) 84 : The Smallest Gold Thiolate Nanocrystal That Is Metallic and the Birth of Plasmon. J Phys Chem Lett 9:1295–1300. https://doi.org/10.1021/acs.jpclett.8b00308

93. Zhou M, Zeng C, Chen Y, et al (2016) Evolution from the plasmon to exciton state in ligand-protected atomically precise gold nanoparticles. Nat Commun 7:1–7. https://doi.org/10.1038/ncomms13240

94. He Y, Zeng T (2010) First-Principles Study and Model of Dielectric Functions of Silver Nanoparticles. J Phys Chem C 114:18023–18030. https://doi.org/10.1021/jp101598j

95. Arfken. G. B WHJ (2005) Mathematical methods for physicsts, 6th ed. Elsevier

96. Voshchinnikov N V., Farafonov VG (2000) Applicability of Quasi-Static and Rayleigh Approximations for Spheroidal Particles. Opt Spectrosc 88:71–75

97. Yee KS (1966) Numerical Solution of Initial Boundary Value Problems Involving Maxwell's Equations in Isotropic Media. IEEE Trans Antennas Propag 14:302–306. https://doi.org/10.1109/TAP.1966.1138693

98. Hagness, S.; Taflove A (2005) Computational Electrodynamics: The Finite-Difference Time-Domain Method, 3rd ed. Artech: Boston

99. Teixeira FL (2007) Fdtd/Fetd Methods: A Review on Some Recent Advances and Selected Applications. Microw Optoelectron 6:83–95

100. Jin J (2002) The Finite Element Method in Electromagnetics, 2nd ed. Wiley: New York

101. Lee K, El-Sayed MA (2006) Gold and Silver Nanoparticles in Sensing and Imaging : Sensitivity of Plasmon Response to Size , Shape , and Metal Composition. J Phys Chem B 110:19220–19225. https://doi.org/10.1021/jp062536y

102. Kinkhabwala A, Yu Z, Fan S, et al (2009) Large single-molecule fluorescence enhancements produced by a bowtie nanoantenna. Nat Photonics 3:654–657. https://doi.org/10.1038/nphoton.2009.187

103. Hao E, Schatz GC (2004) Electromagnetic fields around silver nanoparticles and dimers. J Chem Phys 120:357–366. https://doi.org/10.1063/1.1629280

104. Draine BT, Flatau PJ (1994) Discrete-Dipole Approximation For Scattering Calculations. J Opt Soc Am A 11:1491–1499. https://doi.org/10.1364/JOSAA.11.001491

105. Zhang ZQ, Liu QH (2001) Three-Dimensional Weak-Form Conjugate- and Biconjugate-Gradient FFT Methods for Volume Integral Equations. Microw Opt Technol Lett 29:350–356

106. http://ddscat.wikidot.com/.

107. Mc Donald J (2007) OpenDDA - A Novel High-Performance Computational Framework for the Discrete Dipole Approximation. National University of Ireland

108. Mc Donald J, Golden A, Jennings SG (2009) Opendda: A novel high-performance computational framework for the discrete dipole approximation. Int J High Perform Comput Appl 23:42–61. https://doi.org/10.1177/1094342008097914

109. Taubenblatt MA, Tran TK (1993) Calculation of light scattering from particles and structures on a surface by the coupled-dipole method. J Opt Soc Am A 10:912–919. https://doi.org/10.1364/JOSAA.10.000912

110. Schmehl R, Nebeker BM, Hirleman ED (1997) Discrete-dipole approximation for scattering by features on surfaces by means of a two-dimensional fast Fourier transform technique. J Opt Soc Am A 14:3026–3036. https://doi.org/10.1364/JOSAA.14.003026

111. Loke VLY, Pinar Mengüç M, Nieminen TA (2011) Discrete-dipole approximation with surface interaction: Computational toolbox for MATLAB. J Quant Spectrosc Radiat Transf 112:1711–1725. https://doi.org/10.1016/j.jqsrt.2011.03.012

112. Huntemann M, Heygster G, Hong G (2011) Discrete dipole approximation simulations on GPUs using OpenCL-Application on cloud ice particles. J Comput Sci 2:262–271.

https://doi.org/10.1016/j.jocs.2011.05.011

113. Smith CF, Peterson AF, Mittra R (1990) The biconjugate gradient method for electromagnetic scattering. IEEE Trans Antennas Propag 38:938–940. https://doi.org/10.1109/8.55595

114. Draine BT, Flatau PJ (2008) Discrete dipole approximation for periodic targets: theory and tests. Opt Soc Am A 25:2693–2703. https://doi.org/10.1364/JOSAA.25.002693

115. Zimmermann M, Tausendfreund A, Patzelt S, Goch G (2012) In-process measuring procedure for sub-100 nm structures. J Laser Appl 24:1–6. https://doi.org/10.2351/1.4719936

116. Geuquet N, Henrard L (2010) EELS and optical response of a noble metal nanoparticle in the frame of a discrete dipole approximation. Ultramicroscopy 110:1075–1080

117. Mackowski DW (2002) Discrete dipole moment method for calculation of the T matrix for nonspherical particles. J Opt Soc Am A 19:881–893. https://doi.org/10.1364/JOSAA.19.000881

118. Bigelow NW, Vaschillo A, Iberi V, et al (2012) Characterization of the Electron- and of Metal Nanorods. ACS Nano 6:7497–7504. https://doi.org/10.1021/nn302980u

119. Loke VLY, Mengüç MP (2010) Surface waves and atomic force microscope probe-particle near-field coupling: discrete dipole approximation with surface interaction. J Opt Soc Am A 27:2293–2302. https://doi.org/10.1364/JOSAA.27.002293

120. Collinge MJ, Draine BT (2004) Discrete-dipole approximation with polarizabilities that account for both finite wavelength and target geometry. J Opt Soc Am A 21:2023–2028. https://doi.org/10.1364/JOSAA.21.002023

121. Draine BT, Goodman J (1993) Beyond Clausius-Mossotti - Wave propagation on a polarizable point lattice and the discrete dipole approximation. Astro J 405:685-697.

122. Gray RM (2006) Toeplitz and Circulant Matrices: A review. Found Trends® Commun Inf Theory 2:155–239. https://doi.org/http://dx.doi.org/10.1561/0100000006

123. https://www.mathworks.com/help/matlab/ref/fft.html.

124. Awan MG, Saeed F (2017) An Out-of-Core GPU based Dimensionality Reduction Algorithm for Big Mass Spectrometry Data and Its Application in Bottom-up Proteomics. In: Proceedings of the 8th ACM International Conference on Bioinformatics, Computational Biology,and Health Informatics. pp 550–555

125. Awan MG, Eslami T, Saeed F (2018) GPU-DAEMON : GPU algorithm design , data management & optimization template for array based big omics data. Comput Biol Med 101:163–173. https://doi.org/10.1016/j.compbiomed.2018.08.015

126. Chen Y, Xiang C, Hong M (2010) Large-Scale FFT on GPU Clusters. In: ICS '10 Proceedings of the 24th ACM International Conference on Supercomputing. pp 315–324

127. Warris S, Yalcin F, Jackson KJL, Nap JP (2015) Flexible, Fast and Accurate Sequence Alignment Profiling on GPGPU with PaSWAS. J Plos One 10:1–13. https://doi.org/10.1371/journal.pone.0122524

128. https://www.top500.org/lists/2018/11.

129. Hu Y, Zhang AQ, Li HJ, et al (2016) Synthesis, Study, and Discrete Dipole Approximation Simulation of Ag-Au Bimetallic Nanostructures. Nanoscale Res Lett 11:1–9. https://doi.org/10.1186/s11671-016-1435-4

130. Flatau PJ (2004) Fast solvers for one dimensional light scattering in the discrete dipole approximation. Opt Express 12:3149–3155. https://doi.org/10.1364/OPEX.12.003149

131. Link S, El-Sayed MA (2000) Shape and size dependence of radiative, non-radiative and photothermal properties of gold nanocrystals. Int Rev Phys Chem 19:409–453. https://doi.org/10.1080/01442350050034180

132. Kumar J, Wei X, Barrow S, et al (2013) Surface plasmon coupling in end-to-end linked gold nanorod dimers and trimers. Phys Chem Chem Phys 15:4258–4264. https://doi.org/10.1039/c3cp44657c

133. Jain PK, El-Sayed MA (2007) Universal scaling of plasmon coupling in metal nanostructures: Extension from particle pairs to nanoshells. Nano Lett 7:2854–2858.

https://doi.org/10.1021/nl071496m

134. El-Sayed MA (2001) Some interesting properties of metals confined in time and nanometer space of different shapes. Acc Chem Res 34:257–264. https://doi.org/10.1021/ar960016n

135. Hutter E, Fendler JH (2004) Exploitation of localized surface plasmon resonance. Adv Mater 16:1685–1706. https://doi.org/10.1002/adma.200400271

136. Gao MX, Zou HY, Gao PF, et al (2016) Insight into a reversible energy transfer system. Nanoscale 8:16236–16242. https://doi.org/10.1039/c6nr03262a

137. Liu GL, Long Y-T, Choi Y, et al (2007) Quantized plasmon quenching dips nanospectroscopy via plasmon resonance energy transfer. Nat Methods 4:1015–1017. https://doi.org/10.1038/nmeth1133

138. Choi Y, Park Y, Kang T, Lee LP (2009) Selective and sensitive detection of metal ions by plasmonic resonance energy transfer-based nanospectroscopy. Nat Nanotechnol 4:742–746. https://doi.org/10.1038/nnano.2009.258

139. Jiang J, Bosnick K, Maillard M, Brus L (2003) Single Molecule Raman Spectroscopy at the Junctions of Large Ag Nanocrystals. J Phys Chem B 107:9964–9972. https://doi.org/ 10.1021/jp034632u

140. Zhang X, Marocico CA, Lunz M, et al (2014) Experimental and theoretical investigation of the distance dependence of localized surface plasmon coupled förster resonance energy transfer. ACS Nano 8:1273–1283. https://doi.org/10.1021/nn406530m

141. Lunz M, Gerard VA, Gun'Ko YK, et al (2011) Surface plasmon enhanced energy transfer between donor and acceptor CdTe nanocrystal quantum dot monolayers. Nano Lett 11:3341–3345. https://doi.org/10.1021/nl201714y

142. Huang X, Jain PK, El-Sayed IH, El-Sayed MA (2006) Determination of the Minimum Temperature Required for Selective Photothermal Destruction of Cancer Cells with the Use of Immunotargeted Gold Nanoparticles. Photochem Photobiol 82:412–417. https://doi.org/10.1562/2005-12-14-RA-754

143. Jain PK, ElSayed IH, El-Sayed MA (2007) Au nanoparticles target cancer. Nano Today

2:18–29. https://doi.org/10.1016/S1748-0132(07)70016-6

144. Jain PK, Huang X, El-sayed IH, El-Sayed MA (2007) Review of Some Interesting Surface Plasmon Resonance-enhanced Properties of Noble Metal Nanoparticles and Their Applications to Biosystems. Plasmonics 2:107–118. https://doi.org/10.1007/s11468-007-9031-1

145. Yong K, Swihart MT, Ding H, Prasad PN (2009) Preparation of Gold Nanoparticles and their Applications in Anisotropic Nanoparticle Synthesis and Bioimaging. Plasmonics 4:79–93. https://doi.org/10.1007/s11468-009-9078-2

146. Anker JN, Hall WP, Lyandres O, et al (2008) Biosensing with plasmonic nanosensors. Nat Mater 7:442–453. https://doi.org/10.1038/nmat2162

147. Iqbal S, Shabaninezhad M, Hatshan M, et al (2018) Ion-implanted silver nanoparticles for metal-enhanced fluorescence. AIP Adv 8:1–12. https://doi.org/10.1063/1.5045570

148. Liu J, Ma Y, Shao J, et al (2018) Ultra-tall sub-wavelength gold nano pillars for high sensitive LSPR sensors. Microelectron Eng 196:7–12. https://doi.org/10.1016/j.mee.2018.04.007

149. Farmani A, Mir A, Bazgir M, Zarrabi FB (2018) Highly sensitive nano-scale plasmonic biosensor utilizing Fano resonance metasurface in THz range: Numerical study. Phys E Low-Dimensional Syst Nanostructures 104:233–240. https://doi.org/10.1016/j.physe.2018.07.039

150. Eftekhari F, Escobedo C, Ferreira J, et al (2009) Nanoholes as nanochannels: Flow-through plasmonic sensing. Anal Chem 81:4308–4311. https://doi.org/10.1021/ac900221y

151. Yu C, Irudayaraj J (2007) Multiplex biosensor using gold nanorods. Anal Chem 79:572–579. https://doi.org/10.1021/ac061730d

152. Popescu VA (2018) Simulation of Some Plasmonic Biosensors for Detection of Hemoglobin Concentration in Human Blood. Plasmonics 13:1507–1511. https://doi.org/10.1007/s11468-017-0657-3

153. Link S, El-Sayed MA (2000) Shape and size dependence of radiative, non-radiative and

photothermal properties of gold nanocrystals. Int Rev Phys Chem 19:409–453. https://doi.org/10.1080/01442350050034180

154. Link S, Burda C, Wang ZL, El-Sayed MA (1999) Electron dynamics in gold and gold-silver alloy nanoparticles: The influence of a nonequilibrium electron distribution and the size dependence of the electron-phonon relaxation. J Chem Phys 111:1255–1264. https://doi.org/10.1063/1.479310

155. Hodak JH, Henglein A, Hartland G V. (2000) Electron-phonon coupling dynamics in very small (between 2 and 8 nm diameter) Au nanoparticles. J Chem Phys 112:5942–5947. https://doi.org/10.1063/1.481167

156. Rechberger W, Hohenau A, Leitner A, et al (2003) Optical properties of two interacting gold nanoparticles. Opt Commun 220:137–141. https://doi.org/10.1016/S0030-4018(03)01357-9

157. Jain PK, El-Sayed MA (2008) Noble metal nanoparticle Pairs: Effect of medium for enhanced nanosensing. Nano Lett 8:4347–4352. https://doi.org/10.1021/nl8021835

158. Zhu J, Ren Y-J (2013) Tuning the plasmon shift and local electric field distribution of gold nanodumbbell: The effect of surface curvature transition from positive to negative. Appl Surf Sci 285P:649–656. https://doi.org/10.1016/j.apsusc.2013.08.106

159. Wiley BJ, Im SH, Li Z-Y, et al (2006) Maneuvering the surface plasmon resonance of silver nanostructures through shape-controlled synthesis. J Phys Chem B 110:15666–15675. https://doi.org/10.1021/jp0608628

160. Lermé J, Bonnet C, Lebeault MA, et al (2017) Surface Plasmon Resonance Damping in Spheroidal Metal Particles: Quantum Confinement, Shape, and Polarization Dependences. J Phys Chem C 121:5693–5708. https://doi.org/10.1021/acs.jpcc.6b12298

161. Nicolas R, Lévêque G, Adam PM, Maurer T (2018) Graphene Doping Induced Tunability of Nanoparticles Plasmonic Resonances. Plasmonics 13:1219–1225. https://doi.org/10.1007/s11468-017-0623-0

162. Coronado EA, Schatz GC (2003) Surface plasmon broadening for arbitrary shape

nanoparticles: A geometrical probability approach. J Chem Phys 119:3926–3934. https://doi.org/10.1063/1.1587686

163. Derkachova A, Kolwas K, Demchenko I (2016) Dielectric Function for Gold in Plasmonics Applications: Size Dependence of Plasmon Resonance Frequencies and Damping Rates for Nanospheres. Plasmonics 11:941–951. https://doi.org/10.1007/s11468-015-0128-7

164. Zhang JZ, Noguez C (2008) Plasmonic Optical Properties and Applications of Metal Nanostructures. Plasmonics 3:127–150. https://doi.org/10.1007/s11468-008-9066-y

165. Jie YM, Zhang ZL, Wu GJS (2011) Theoretical Analysis the Optical Properties of Multi-coupled Silver Nanoshell Particles. Plasmonics 6:705–713. https://doi.org/10.1007/s11468-011-9254-z

166. Varas A, García-González P, García-Vidal FJ, Rubio A (2015) Anisotropy Effects on the Plasmonic Response of Nanoparticle Dimers. J Phys Chem Lett 6:1891–1898. https://doi.org/10.1021/acs.jpclett.5b00573

167. Barbry M, Koval P, Marchesin F, et al (2015) Atomistic near-field nanoplasmonics: Reaching atomic-scale resolution in nanooptics. Nano Lett 15:3410–3419. https://doi.org/10.1021/acs.nanolett.5b00759

168. Mokkath JH (2017) Shapes matter: Examining the optical response evolution in stretched aluminium nanoparticles via time-dependent density functional theory. Phys Chem Chem Phys 20:51–55. https://doi.org/10.1039/c7cp07151e

169. Kulkarni V, Prodan E, Nordlander P (2013) Quantum plasmonics: Optical properties of a nanomatryushka. Nano Lett 13:5873–5879. https://doi.org/10.1021/nl402662e

170. Marchesin F, Koval P, Barbry M, et al (2016) Plasmonic Response of Metallic Nanojunctions Driven by Single Atom Motion: Quantum Transport Revealed in Optics. ACS Photonics 3:269–277. https://doi.org/10.1021/acsphotonics.5b00609

171. Sinha-Roy R, García-González P, Weissker HC, et al (2017) Classical and ab Initio Plasmonics Meet at Sub-nanometric Noble Metal Rods. ACS Photonics 4:1484–1493. https://doi.org/10.1021/acsphotonics.7b00254

172. Rossi TP, Kuisma M, Puska MJ, et al (2017) Kohn-Sham Decomposition in Real-Time Time-Dependent Density-Functional Theory: An Efficient Tool for Analyzing Plasmonic Excitations. J Chem Theory Comput 13:4779–4790. https://doi.org/10.1021/acs.jctc.7b00589

173. Kulkarni V, Manjavacas A (2015) Quantum Effects in Charge Transfer Plasmons. ACS Photonics 2:987–992. https://doi.org/10.1021/acsphotonics.5b00246

174. Kreibig U, Vollmer M (1995) Optical Properties of Metal Clusters. Springer

175. Etchegoin PG, Le Ru EC, Meyer M (2006) An analytic model for the optical properties of gold. J Chem Phys 125:1–3. https://doi.org/10.1063/1.2360270

176. Zheng J, Zhang C, Dickson RM (2004) Highly fluorescent, water-soluble, size-tunable gold quantum dots. Phys Rev Lett 93:1–4. https://doi.org/10.1103/PhysRevLett.93.077402

177. Palik, Edward D, Elsevier Inc V 5 (1997) Handbook of optical constants of solids. Academic Press

178. Rakic AD, Djurisic AB, Elazar JM, Majewski ML (1998) Optical properties of metallic films for vertical-cavity optoelectronic devices. Appl Opt 37:5271–5283. https://doi.org/10.1364/AO.37.005271

179. Kreibig U, Fragstein C v. (1969) The limitation of electron mean free path in small silver particles. Zeitschrift für Phys 224:307–323. https://doi.org/10.1007/BF01393059

180. Fu Q, Sun W (2001) Mie theory for light scattering by a spherical particle in an absorbing medium. Appl Opt 40:1354–1361. https://doi.org/10.1364/AO.40.001354

181. Peña O, Pal U (2009) Scattering of electromagnetic radiation by a multilayered sphere. Comput Phys Commun 180:2348–2354. https://doi.org/10.1016/j.cpc.2009.07.010

182. Raschke G, Brogl S, Susha AS, et al (2004) Gold Nanoshells Improve Single Nanoparticle Molecular Sensors. Nano Lett 4:1853–1857. https://doi.org/10.1021/nl049038q

183. Stewart ME, Anderton CR, Thompson LB, et al (2008) Nanostructured Plasmonic Sensors. Chem Rev 108:494–521. https://doi.org/10.1021/cr068126n

184. Lee K, El-sayed MA (2006) Gold and Silver Nanoparticles in Sensing and Imaging : Sensitivity of Plasmon Response to Size , Shape , and Metal Composition. J Phys Chem B 110:19220–19225. https://doi.org/10.1021/jp062536y

185. Noguez C (2007) Surface plasmons on metal nanoparticles: The influence of shape and physical environment. J Phys Chem C 111:3606–3619. https://doi.org/10.1021/jp066539m

186. Mayer KM, Hafner JH (2011) Localized Surface Plasmon Resonance Sensors. Chem Rev 111:3828–3857. https://doi.org/10.1021/cr100313v

187. Sun Y, Gray SK, Peng S (2011) Surface chemistry: A non-negligible parameter in determining optical properties of small colloidal metal nanoparticles. Phys Chem Chem Phys 13:11814–11826. https://doi.org/10.1039/c1cp20265k

188. Shabaninezhad M, Abuhagr A, Sakthivel NA, et al (2019) Ultrafast Electron Dynamics in Thiolate-Protected Plasmonic Gold Clusters : Size and Ligand Effect. J Phys Chem C 123:13344–13353. https://doi.org/10.1021/acs.jpcc.9b01739

189. Ghosh SK, Pal T (2007) Interparticle coupling effect on the surface plasmon resonance of gold nanoparticles: From theory to applications. Chem Rev 107:4797–4862. https://doi.org/10.1021/cr0680282

190. Mirin NA, Bao K, Nordlander P (2009) Fano Resonances in Plasmonic Nanoparticle Aggregates. J Phys Chem A 113:4028–4034. https://doi.org/10.1021/jp810411q

191. Zohar N, Chuntonov L, Haran G (2014) The simplest plasmonic molecules: Metal nanoparticle dimers and trimers. J Photochem Photobiol C Photochem Rev 21:26–39. https://doi.org/10.1016/j.jphotochemrev.2014.10.002

192. Dreaden EC, Alkilany AM, Huang X, et al (2012) The golden age: Gold nanoparticles for biomedicine. Chem Soc Rev 41:2740–2779. https://doi.org/10.1039/c1cs15237h

193. Amendola V, Meneghetti M (2009) Laser ablation synthesis in solution and size manipulation of noble metal nanoparticles. Phys Chem Chem Phys 11:3805–3821. https://doi.org/10.1039/b900654k

194. Fabrizio ED, Schlücker S, Wenger J, et al (2016) Roadmap on biosensing and photonics

with advanced nano-optical methods. J Opt 18:1–27. https://doi.org/10.1088/2040-8978/18/6/063003

195. Kawata S, Inouye Y, Verma P (2009) Plasmonics for near-field nano-imaging and superlensing. Nat Photonics 3:388–394. https://doi.org/10.1038/nphoton.2009.111

196. Jones TC, Sementa L, Stener M, et al (2017) Au21S(SAdm)15: Crystal Structure, Mass Spectrometry, Optical Spectroscopy, and First-Principles Theoretical Analysis. J Phys Chem C 121:10865–10869. https://doi.org/10.1021/acs.jpcc.6b12075

197. Pyo K, Ly NH, Han SM, et al (2018) Unique Energy Transfer in Fluorescein-Conjugated Au22 Nanoclusters Leading to 160-Fold pH-Contrasting Photoluminescence. J Phys Chem Lett 9:5303–5310. https://doi.org/10.1021/acs.jpclett.8b02130

198. Fortunelli A, Sementa L, Thanthirige VD, et al (2017) Au21S(SAdm)15: An Anisotropic Gold Nanomolecule. Optical and Photoluminescence Spectroscopy and First-Principles Theoretical Analysis. J Phys Chem Lett 8:457–462. https://doi.org/10.1021/acs.jpclett.6b02810

199. Kumar SS, Kwak K, Lee D (2011) Electrochemical sensing using quantum-sized gold nanoparticles. Anal Chem 83:3244–3247. https://doi.org/10.1021/ac200384w

200. Thanthirige VD, Sinn E, Wiederrecht GP, Ramakrishna G (2017) Unusual Solvent Effects on Optical Properties of Bi-Icosahedral Au25 Clusters. J Phys Chem C 121:3530–3539. https://doi.org/10.1021/acs.jpcc.6b10948

201. Kwak K, Kumar SS, Lee D (2012) Selective determination of dopamine using quantum-sized gold nanoparticles protected with charge selective ligands. Nanoscale 4:4240–4246. https://doi.org/10.1039/c2nr30481c

202. Devadas MS, Kim J, Sinn E, et al (2010) Unique Ultrafast Visible Luminescence in Monolayer-Protected Au25 Clusters. J Phys Chem C 114:22417–22423. https://doi.org/10.1021/jp107033n

203. Ryasnyanskiy AI, Palpant B, Debrus S, et al (2007) Third-order nonlinear-optical parameters of gold nanoparticles in different matrices. J Lumin 127:181–185.

https://doi.org/10.1016/j.jlumin.2007.02.021

204. Ghosh B, Chakraborty P, Singh BP, Kundu T (2009) Enhanced nonlinear optical responses in metal-glass nanocomposites. Appl Surf Sci 256:389–394. https://doi.org/10.1016/j.apsusc.2009.05.093

205. Zhang Y, Jin Y, He M, et al (2018) Optical properties of bimetallic Au-Cu nanocrystals embedded in glass. Mater Res Bull 98:94–102. https://doi.org/10.1016/j.materresbull.2017.10.009

206. Yin Y, Alivisatos AP (2005) Colloidal nanocrystal synthesis and the organic-inorganic interface. Nature 437:664–670. https://doi.org/10.1038/nature04165

207. Wei J, Schaeffer N, Pileni M-P (2014) Ag nanocrystals: 1. Effect of ligands on plasmonic properties. J Phys Chem B 118:14070–14075. https://doi.org/10.1021/jp5050699

208. Zeng C, Chen Y, Kirschbaum K, et al (2015) Structural patterns at all scales in a nonmetallic chiral Au133(SR)52 nanoparticle. Surf Sci 1:1–6. https://doi.org/10.1126/sciadv.1500045

209. Zhu M, Aikens CM, Hollander FJ, et al (2008) Correlating the Crystal Structure of A Thiol-Protected Au25 Cluster and Optical Properties. J Am Chem Soc 130:5883–5885. https://doi.org/10.1021/ja801173r

210. Weissker H-C, Escobar HB, Thanthirige VD, et al (2014) Information on quantum states pervades the visible spectrum of the ubiquitous Au144(SR)60 gold nanocluster. Nat Commun 5:1–8. https://doi.org/10.1038/ncomms4785

211. Raschke G, Brogl S, Susha AS, et al (2004) Gold nanoshells improve single nanoparticle molecular sensors. Nano Lett 4:1853–1857. https://doi.org/10.1021/nl049038q

212. Kwak K, Thanthirige VD, Pyo K, et al (2017) Energy Gap Law for Exciton Dynamics in Gold Cluster Molecules. J Phys Chem Lett 8:4898–4905. https://doi.org/10.1021/acs.jpclett.7b01892

213. Kumara C, Dass A (2014) Au329(SR)84 Nanomolecules: Compositional Assignment of the 76.3 kDa Plasmonic Faradaurates. Anal Chem 86:4227–4232. https://doi.org/10.1021/ac403851s

214. Qian H, Zhu Y, Jin R (2012) Atomically precise gold nanocrystal molecules with surface plasmon resonance. PNAS 109:696–700. https://doi.org/10.1073/pnas.1115307109/

215. Vergara S, Santiago U, Kumara C, et al (2018) Synthesis, Mass Spectrometry, and Atomic Structural Analysis of Au∼2000(SR)∼290 Nanoparticles. J Phys Chem C 122:26733–26738. https://doi.org/10.1021/acs.jpcc.8b08531

216. Ahmadi TS, Logunov SL, El-Sayed MA (1996) Picosecond Dynamics of Colloidal Gold Nanoparticles. J Phys Chem 100:8053–8056. https://doi.org/10.1021/jp960484e

217. Hodak JH, Henglein A, Hartland G V. (2000) Electron-phonon coupling dynamics in very small (between 2 and 8 nm diameter) Au nanoparticles. J Chem Phys 112:5942–5947. https://doi.org/10.1063/1.481167

218. Link S, Furube A, Mohamed MB, et al (2002) Hot Electron Relaxation Dynamics of Gold Nanoparticles Embedded in MgSO4 Powder Compared To Solution : The Effect of the Surrounding Medium. J Phys Chem B 106:945–955. https://doi.org/10.1021/jp013311k

219. Nelet A, Crut A, Arbouet A, et al (2004) Acoustic vibrations of metal nanoparticles: High order radial mode detection. Appl Surf Sci 226:209–215. https://doi.org/10.1016/j.apsusc.2003.11.022

220. Elkabbash M, Rashed AR, Kucukoz B, et al (2017) Ultrafast transient optical loss dynamics in exciton–plasmon nano-assemblies. Nanoscale 9:6558–6566. https://doi.org/10.1039/c7nr01512g

221. Dell Fatti N, Tzortzakis S, Voisin C, et al (1999) Time resolved investigation of coherent acoustic mode oscillations in silver nanoparticles. Phys B Condens Matter 263–264:54–56. https://doi.org/10.1016/S0921-4526(98)01194-6

222. Hodak JH, Henglein A, Hartland G V. (2000) Coherent Excitation of Acoustic Breathing Modes in Bimetallic Core−Shell Nanoparticles. J Phys Chem B 104:5053–5055. https://doi.org/10.1021/jp000578v

223. Link S, El-sayed MA (1999) Spectral Properties and Relaxation Dynamics of Surface Plasmon Electronic Oscillations in Gold and Silver Nanodots and Nanorods. J Phys Chem

B 103:8410–8426. https://doi.org/10.1021/jp9917648

224. Sakthivel NA, Theivendran S, Ganeshraj V, et al (2017) Crystal Structure of Faradaurate-279: Au 279 (SPh - t Bu) 84 Plasmonic Nanocrystal Molecules. J Am Chem Soc 139:15450–15459. https://doi.org/10.1021/jacs.7b08651

225. Sakthivel NA, Dass A (2018) Aromatic Thiolate-Protected Series of Gold Nanomolecules and a Contrary Structural Trend in Size Evolution. Acc Chem Res 51:1774–1783. https://doi.org/10.1021/acs.accounts.8b00150

226. Kumara C, Zuo X, Ilavsky J, et al (2015) Atomic Structure of Au 329 (SR) 84 Faradaurate Plasmonic Nanomolecules. J Phys Chem C 119:11260–11266. https://doi.org/10.1021/jp512910a

227. Turkevich J, Stevenson PC, Hillier J (1951) A study of the nucleation and growth processes in the synthesis of colloidal gold. Discuss Faraday Soc 11:55–75. https://doi.org/10.1039/DF9511100055

228. Polyanskiy M Refractive index database https://refractiveindex.info

229. Jain PK, Qian W, El-Sayed MA (2006) Ultrafast Electron Relaxation Dynamics in Coupled Metal Nanoparticles in Aggregates. J Phys Chem B 110:136–142. https://doi.org/10.1021/jp055562p

230. Link S, El-Sayed MA (2003) Optical properties and ultrafast dynamics of metallic nanocrystals. Annu Rev Phys Chem 54:331–366. https://doi.org/10.1146/annurev.physchem.54.011002.103759

231. Bauer C, Abid J-P, Fermin D, Girault HH (2004) Ultrafast chemical interface scattering as an additional decay channel for nascent nonthermal electrons in small metal nanoparticles. J Chem Phys 120:9302–9315. https://doi.org/10.1063/1.1710856

232. Bauer C, Abid J-P, Girault HH (2006) Role of adsorbates on dynamics of hot-electron (type I and II) thermalization within gold nanoparticles. Comptes Rendus Chim 9:261–267. https://doi.org/10.1016/j.crci.2005.03.030

233. Bauer C, Abid J-P, Girault HH (2006) Hot Adsorbate-Induced Retardation of the Internal

Thermalization of Nonequilibrium Electrons in Adsorbate-Covered Metal Nanoparticles. J Phys Chem B 110:4519–4523. https://doi.org/10.1021/jp060179l

234. Kumar S, Sood AK (2016) Ultrafast Response of Plasmonic Nanostructures. arXiv:180200685 [cond-mat.mes-hall]. https://doi.org/10.1007/978-3-319-24606-2_6

235. Sun C-K, Vallée F, Acioli LH, et al (1994) Femtosecond-tunable measurement of electron thermalization in gold. Phys Rev B 50:15337–15348. https://doi.org/10.1103/PhysRevB.50.15337

236. Hodak JH, Martini I, Hartland G V. (1998) Spectroscopy and Dynamics of Nanometer-Sized Noble Metal Particles. J Phys Chem B 102:6958–6967. https://doi.org/10.1021/jp9809787

237. Rethfeld B, Kaiser A, Vicanek M, Simon G (2002) Ultrafast dynamics of nonequilibrium electrons in metals under femtosecond laser irradiation. Phys Rev B 65:1–11. https://doi.org/10.1103/PhysRevB.65.214303

238. Della Valle G, Conforti M, Longhi S, et al (2012) Real-time optical mapping of the dynamics of nonthermal electrons in thin gold films. Phys Rev B 86:1–6. https://doi.org/10.1103/PhysRevB.86.155139

239. Bilotsky ED, ; Tomchuk PM (1990) Electron-phonon interaction and hot electrons in small metal islands. Surf Sci 239:143–155. https://doi.org/10.1016/0039-6028(90)90626-J

240. Hodak JH, Henglein A, Hartland G V. (2000) Photophysics of Nanometer Sized Metal Particles: Electron−Phonon Coupling and Coherent Excitation of Breathing Vibrational Modes. J Phys Chem B 104:9954–9965. https://doi.org/10.1021/jp002256x

241. Voisin C, Christofilos D, Loukakos PA, et al (2004) Ultrafast electron-electron scattering and energy exchanges in noble-metal nanoparticles. Phys Rev B 69:1–13. https://doi.org/10.1103/PhysRevB.69.195416

242. Tang Y, Ouyang M (2007) Tailoring properties and functionalities of metal nanoparticles through crystallinity engineering. Nat Mater 6:754–759. https://doi.org/10.1038/nmat1982

243. Sokolov K, Follen M, Aaron J, et al (2003) Real-Time Vital Optical Imaging of Precancer

Using Anti-Epidermal Growth Factor Receptor Antibodies Conjugated to Gold Nanoparticles 1. Cancer Res 63:1999–2004

244. Haes AJ, Van Duyne RP (2002) A nanoscale optical biosensor: Sensitivity and selectivity of an approach based on the localized surface plasmon resonance spectroscopy of triangular silver nanoparticles. J Am Chem Soc 124:10596–10604. https://doi.org/10.1021/ja020393x

245. Stewart ME, Anderton CR, Thompson LB, et al (2008) Nanostructured plasmonic sensors. Chem Rev 108:494–521. https://doi.org/10.1021/cr068126n

246. Gómez-Hens A, Fernández-Romero JM, Aguilar-Caballos MP (2008) Nanostructures as analytical tools in bioassays. Trends Anal Chem 27:394–406. https://doi.org/10.1016/j.trac.2008.03.006

247. Sepúlveda B, Angelomé PC, Lechuga LM, Liz-Marzán LM (2009) LSPR-based nanobiosensors. Nano Today 4:244–251. https://doi.org/10.1016/j.nantod.2009.04.001

248. Dondapati SK, Sau TK, Hrelescu C, et al (2010) Label-free Biosensing Based on Single Gold Nanostars as Plasmonic Transducers. ACS Nano 4:6318–6322

249. Peng H-I, Miller BL (2011) Recent advancements in optical DNA biosensors: Exploiting the plasmonic effects of metal nanoparticles. Analyst 136:436–447. https://doi.org/10.1039/C0AN00636J

250. Zhang S, Bao K, Halas NJ, et al (2011) Substrate-induced Fano resonances of a plasmonic nanocube: A route to increased-sensitivity localized surface plasmon resonance sensors revealed. Nano Lett 11:1657–1663. https://doi.org/10.1021/nl200135r

251. Yanik AA, Cetin AE, Huang M, et al (2011) Seeing protein monolayers with naked eye through plasmonic Fano resonances. PNAS 108:11784–11789. https://doi.org/10.1073/pnas.1101910108

252. Sherry LJ, Chang S-H, Schatz GC, et al (2005) Localized Surface Plasmon Resonance Spectroscopy of Single Silver Nanocubes. Nano Lett 5:2034–2038. https://doi.org/10.1021/nl0515753

253. Fong KE, Yung LYL (2013) Localized surface plasmon resonance: A unique property of

plasmonic nanoparticles for nucleic acid detection. Nanoscale 5:12043–12071. https://doi.org/10.1039/c3nr02257a

254. Wei H, Hossein Abtahi SM, Vikesland PJ (2015) Plasmonic colorimetric and SERS sensors for environmental analysis. Environ Sci Nano 2:120–135. https://doi.org/10.1039/c4en00211c

255. Han X, Shokri Kojori H, Leblanc RM, Kim SJ (2018) Ultrasensitive Plasmonic Biosensors for Real-Time Parallel Detection of Alpha-L-Fucosidase and Cardiac-Troponin-I in Whole Human Blood. Anal Chem 90:7795–7799. https://doi.org/10.1021/acs.analchem.8b01816

256. Stranik O, McEvoy HM, McDonagh C, MacCraith BD (2005) Plasmonic enhancement of fluorescence for sensor applications. Sensors Actuators B Chem 107:148–153. https://doi.org/10.1016/j.snb.2004.08.032

257. R. Weissleder (2001) Http://Biotech.Nature.Com

258. Reinhard BM, Siu M, Agarwal H, et al (2005) Calibration of dynamic molecular rulers based on plasmon coupling between gold nanoparticles. Nano Lett 5:2246–2252. https://doi.org/10.1021/nl051592s

259. Joshi GK, Deitz-Mcelyea S, Johnson M, et al (2014) Highly specific plasmonic biosensors for ultrasensitive MicroRNA detection in plasma from pancreatic cancer patients. Nano Lett 14:6955–6963. https://doi.org/10.1021/nl503220s

260. Sriram M, Markhali BP, Nicovich PR, et al (2018) A rapid readout for many single plasmonic nanoparticles using dark-field microscopy and digital color analysis. Biosens Bioelectron 117:530–536. https://doi.org/10.1016/j.bios.2018.06.066

261. Kabashin A V., Evans P, Pastkovsky S, et al (2009) Plasmonic nanorod metamaterials for biosensing. Nat Mater 8:867–871. https://doi.org/10.1038/nmat2546

262. Nusz GJ, Curry AC, Marinakos SM, et al (2009) Rational Selection of Gold Nanorod Biosensors. ACS Nano 3:795–806. https://doi.org/10.1021/nn8006465

263. Säfsten P, Klakamp SL, Drake AW, et al (2006) Screening antibody-antigen interactions in parallel using Biacore A100. Anal Biochem 353:181–190. https://doi.org/10.1016/j.ab.

2006.01.041

264. Haes AJ, Duyne RP Van (2004) Preliminary studies and potential applications of localized surface plasmon resonance spectroscopy in medical diagnostics. Expert Rev Mol Diagn 4:527–537. https://doi.org/10.1586/14737159.4.4.527

265. Chen HC, Kou X, Yang Z, et al (2008) Shape- and Size-Dependent Refractive Index Sensitivity of Gold Nanoparticles. Langmuir 24:5233–5237. https://doi.org/Doi 10.1021/La800305j

266. Suh JY, Kim CH, Zhou W, et al (2012) Plasmonic bowtie nanolaser arrays. Nano Lett 12:5769–5774. https://doi.org/10.1021/nl303086r

267. Wang H, Brandl DW, Le F, et al (2006) Nanorice: A hybrid plasmonic nanostructure. Nano Lett 6:827–832. https://doi.org/10.1021/nl060209w

268. Ye Y, Chen TP, Liu Z, Yuan X (2018) Effect of Surface Scattering of Electrons on Ratios of Optical Absorption and Scattering to Extinction of Gold Nanoshell. Nanoscale Res Lett 13:1–11. https://doi.org/10.1186/s11671-018-2670-7

269. Galush WJ, Shelby SA, Mulvihill MJ, et al (2009) A nanocube plasmonic sensor for molecular binding on membrane surfaces. Nano Lett 9:2077–2082. https://doi.org/10.1021/nl900513k

270. Sun Y, Xia Y (2002) Increased Sensitivity of Surface Plasmon Resonance of Gold Nanoshells Compared to That of Gold Solid Colloids in Response to Environmental Changes. Anal Chem 74:5297–5305. https://doi.org/10.1021/ac0258352

271. Jain PK, El-sayed MA (2007) Surface plasmon resonance sensitivity of metal nanostructures: Physical basis and universal scaling in metal nanoshells. J Phys Chem C 111:17451–17454. https://doi.org/10.1021/jp0773177

272. Otte MA, Sepúlveda B, Ni W, et al (2010) Identification of the optimal spectral region for plasmonic and nanoplasmonic sensing. ACS Nano 4:349–357. https://doi.org/10.1021/nn901024e

273. Nehl CL, Liao H, Hafner JH (2006) Optical properties of star-shaped gold nanoparticles.

Nano Lett 6:683–688. https://doi.org/10.1021/nl052409y

274. Johnson PB, Christy RW (1972) Optical constants of the noble metals. Phys Rev B 6:4370–4379. https://doi.org/10.1103/PhysRevB.6.4370

275. Yurkin MA, Hoekstra AG (2007) The discrete dipole approximation: An overview and recent developments. J Quant Spectrosc Radiat Transf 106:558–589. https://doi.org/10.1016/j.jqsrt.2007.01.034

276. Yurkin MA, Hoekstra AG (2011) The discrete-dipole-approximation code ADDA: Capabilities and known limitations. J Quant Spectrosc Radiat Transf 112:2234–2247. https://doi.org/10.1016/j.jqsrt.2011.01.031

277. Fedrigo S, Harbich W, Buttet J (1993) Collective dipole oscillations in small silver clusters embedded in rare-gas matrices. Phys Rev B 47:706–715. https://doi.org/10.1103/physrevb.47.10706

278. Gaudry M, Lermé J, Cottancin E, et al (2001) Optical properties of (AuxAg1-x)n clusters embedded in alumina: Evolution with size and stoichiometry. Phys Rev B 64:1–7. https://doi.org/10.1103/PhysRevB.64.085407

279. Shi H, Zhang L, Cai W (2000) Composition modulation of optical absorption in AgxAu1-x alloy nanocrystals in situ formed within pores of mesoporous silica. J Appl Phys 87:1572–1574. https://doi.org/10.1063/1.372053

280. Belotelov VI, Carotenuto G, Nicolais L, et al (2006) Online monitoring of alloyed bimetallic nanoparticle formation by optical spectroscopy. J Appl Phys 99:1–9. https://doi.org/10.1063/1.2172722

281. Huang WC, Lue JT (1994) Quantum size effect on the optical properties of small metallic particles. Phys Rev B 49:17279–17289

282. Westcott SL, Jackson JB, Radloff C, Halas NJ (2002) Relative contributions to the plasmon line shape of metal nanoshells. Phys Rev B 66:1–5. https://doi.org/10.1103/PhysRevB.66.155431

283. Simmons J, Potter KS (2000) Optical Materials, 1st Editio. Academic Press, San Diego, CA

284. Liu P, Wang H, Li X, et al (2015) Localized Surface Plasmon Resonance of Cu Nanoparticles by Laser Ablation in RSC Advances Localized surface plasmon resonance of Cu nanoparticles by laser ablation in liquid media. RSC Adv 5:79738–79745. https://doi.org/10.1039/C5RA14933A

285. Santillán JMJ, Videla FA, Raap MBF van, et al (2012) Size dependent Cu dielectric function for plasmon spectroscopy: Characterization of colloidal suspension generated by fs laser ablation. J Appl Phys 112:1–8. https://doi.org/10.1063/1.4751328

286. Liu K, Song Y, Chen S (2015) Defective TiO2-supported Cu nanoparticles as efficient and stable electrocatalysts for oxygen reduction in alkaline media. Nanoscale 7:1224–1232. https://doi.org/10.1039/c4nr06128d

287. Zhu H, Zhang C, Yin Y (2005) Novel synthesis of copper nanoparticles: influence of the synthesis conditions on the. Nanotechnology 16:3079–3083. https://doi.org/10.1088/0957-4484/16/12/059

288. Rostovshchikovaa TN, Smirnova V V., Kozhevinb VM, et al (2005) New size effect in the catalysis by interacting copper nanoparticles. Appl Catal A Gen 296:70–79. https://doi.org/10.1016/j.apcata.2005.08.032

289. Kumara P, Mathpal MC, Swarta HC (2018) Multifunctional properties of plasmonic Cu nanoparticles embedded in a glass matrix and their thermodynamic behavior. J Alloys Compd 747:530–542. https://doi.org/https://doi.org/10.1016/j.jallcom.2018.03.038

290. Manikandan P, Manikandan D, et al (2014) Surface enhanced Raman scattering (SERS) of silver ions embedded nanocomposite glass. Spectrochim Acta Part Mol Biomol Spectrosc 124:203–207. https://doi.org/10.1016.j.saa.2014.01.033

291. Rajaramakrishna R, Saiyasombat C, Anavekar R V., Jain H (2014) Structure and nonlinear optical studies of Au nanoparticles embedded in lead lanthanum borate glass. J Non Cryst Solids 406:107–110. https://doi.org/10.1016/j.jnoncrysol.2014.09.052

292. Pereira RMS, Borges J, Smirnov G V., et al (2019) Surface Plasmon Resonance in a Metallic Nanoparticle Embedded in a Semiconductor Matrix: Exciton–Plasmon Coupling.

ACS Photonics 6:204–210. https://doi.org/10.1021/acsphotonics.8b01430

293. Nie WJ, Zhang YX, Yu HH, et al (2018) Plasmonic nanoparticles embedded in single crystals synthesized by gold ion implantation for enhanced optical nonlinearity and efficient Q-switched lasing. Nanoscale 10:4228–4236. https://doi.org/10.1039/c7nr07304f

294. Proença M, Borges J, Rodrigues MS, et al (2019) Nanocomposite thin films based on Au-Ag nanoparticles embedded in a CuO matrix for localized surface plasmon resonance sensing. Appl Surf Sci 484:152–168. https://doi.org/10.1016/j.apsusc.2019.04.085

295. Ren F, Xiao XH, Cai GX, et al (2009) Engineering embedded metal nanoparticles with ion beam technology. Appl Phys A 96:317–325. https://doi.org/10.1007/s00339-009-5205-3

296. Schaadt DM, Feng B, Yu ET (2005) Enhanced semiconductor optical absorption via surface plasmon excitation in metal nanoparticles. Appl Phys Lett 86:1–3. https://doi.org/10.1063/1.1855423

297. Derkacs D, Lim SH, Matheu P, et al (2006) Improved performance of amorphous silicon solar cells via scattering from surface plasmon polaritons in nearby metallic nanoparticles. Appl Phys Lett 89:1–3. https://doi.org/10.1063/1.2336629

298. Nakayama K, Tanabe K, Atwater HA (2008) Plasmonic nanoparticle enhanced light absorption in GaAs solar cells. Appl Phys Lett 93:121904. https://doi.org/10.1063/1.2988288

299. Ashcroft NW, Mermin ND (1976) Solid State Physics, 1st Editio. Cengage Learning

300. Li Y, Song L, Qiao Y (2015) Experimental and theoretical realization of enhanced light scattering spectroscopy of gold nanorods. Appl Phys Lett 106:1–4. https://doi.org/10.1063/1.4905889

301. Brioude A, Jiang XC, Pileni MP (2005) Optical Properties of Gold Nanorods: DDA Simulations Supported by Experiments. J Phys Chem B 109:13138–13142. https://doi.org/10.1021/jp0507288

Appendix A

A. MATLAB Script for Forming a Nanoparticle Using of Cubic Meshes. Four Different Shapes Have Been Provided in this m.file.

```
%%%%%%%%%%%%% Forming a 3D nanoparticle with cube meshes %%%%%%%%%%%%%%%%
clear all
clc
tic
%%%%%%%%%%%%%%%%%%%%%%%%%%%%%%%%%%%%%%%%%%%%%%%%%%%%%%%%%%%%%%%%%%%%%%%
% Nps_number=1 produces a Sphere with cubic mesh
% Nps_number=2 produces an Ellipsoid with cubic mesh
% Nps_number=3 produces a Rod, Made of a disk and two semi-sphere at ends
% Nps_number=4 produces a nanoshell, here I provided an example of a Rod Np
%%%%%%%%%%%%%%%%%%%%%%%%%%%%%%%%%%%%%%%%%%%%%%%%%%%%%%%%%%%%%%%%%%%%%%%
%%%%%%%%%% Initial parameters %%%%%%%%
r_eff=20;     % Effective radius of the Nps
Nps_number=2;  % Choosing the shape of NPs
d=1;         % size of each cube
dx=d;        % x-length of each cube
dy=d;        % y-length of each cube
dz=d;        % z-length of each cube
%%%%% Coordinate of the center of Np %%%%%
X0=0;
Y0=0;
Z0=0;
%%%%%%%%%%%%%%%%%%%%%%%%%%%%%%%%%%%%%%%%%%%%%%%%%%%%%%%%%%%%%%%%%%%%%%%
if Nps_number==1      % Nps is Sphere
   d_eff=2*r_eff;    % Effective diameter
   Lx=d_eff;
   Ly=d_eff;
   Lz=d_eff;
elseif Nps_number==2   % Nps is Ellipsoid
   ARyx=1;                  %Ratio of y-axis to to x-axis
   ARzx=2;                  %Ratio of z-axis to to x-axis
   %%%%% if a=b and a<c Nps is prolate (incident light in z-direction) %%%
   %%%%% if a=b and a>c Nps is oblate  (incident light in z-direction) %%%
```

```
  d_eff=2*r_eff;

  a=((1/(ARyx*ARzx))^(1/3))*r_eff;   % Semi- minor axis in x- direction
  b=ARyx*a;                  % Semi- minor axis in y- direction
  c=ARzx*a;                  % Semi- major axis in z- direction

  Lx=2*a;
  Ly=2*b;
  Lz=2*c;
elseif Nps_number==3  % Np is Rod with caps
  d_eff=2*r_eff;
  volume=4*pi/3*(r_eff^3);
  AR=2;       % Aspect Ratio: ratio of the long axis to short one
  r=(volume/(pi*(2*(AR-1)+4/3)))^(1/3); % Raduis of the Rod
  diameter=2*r;                % Diameter of the Rod
  higth=AR*diameter;             % Higth of the Rod
  Lx=diameter;
  Ly=diameter;
  Lz=higth;
else        %Np is nanoshell (Rod with caps)
  d_eff=2*r_eff;
  volume=4*pi/3*(r_eff^3);
  AR1=1;                % aspect ratio or ratio of b to a
  AR2=2;                % aspect ratio or ratio of c to a
  a=(volume/(AR1*AR2))^(1/3);    % First side of rectangular block
  b=AR1*a;                % Second side of rectangular block
  c=AR2*a;                % Third side of rectangular block
  Lx=a;
  Ly=b;
  Lz=c;
end
%%%%%%%%%%% Obtaining Coordinates of nanocubes or nanocells within the NPS %%%%%%%%%%
Max_x=Lx;
Max_y=Ly;
Max_z=Lz;
ix=-round(Max_x/(2*dx))-0.5:round(Max_x/(2*dx))+0.5;
iy=-round(Max_y/(2*dy))-0.5:round(Max_y/(2*dy))+0.5;
```

```
iz=-round(Max_z/(2*dz))-0.5:round(Max_z/(2*dz))+0.5;
[y,x,z]=meshgrid(iy,ix,iz);
Nx=length(ix);              % Number of the dipoles in the x-direction
Ny=length(iy);              % Number of the dipoles in the y-direction
Nz=length(iz);              % Number of the dipoles in the z-direction

N=Nx*Ny*Nz;                 % Total number of the dipoles
% Converting each component of the dipoles coordinates to a vector
X=(reshape(x,[N,1]))*dx;      % X-coordinates of the dipoles
Y=(reshape(y,[N,1]))*dy;      % Y-coordinates of the dipoles
Z=(reshape(z,[N,1]))*dz;      % Z-coordinates of the dipoles

r_block=[X Y Z];            % Position of the each dipoles inside Nps

%%%%%%%%%%%%%%%% Finding Dipoles inside the nanoparticle %%%%%%%%%%%%%%%%
if Nps_number==1    %Nps is a Sphere, vertically oriented
  Index_in=find(sqrt((X-X0).^2+(Y-Y0).^2+(Z-Z0).^2)<=(Lx/2-d/2));

elseif Nps_number==2  %Nps is an Ellipsoid, vertically oriented
  Index_in=find(sqrt((X-X0).^2/((Lx/2)^2)+(Y-Y0).^2/((Ly/2)^2)+(Z-Z0).^2/((Lz/2)^2))<=1);
elseif Nps_number==3  %Nps is Rod with caps, vertically oriented
  Index_in=find((sqrt((X-X0).^2+(Y-Y0).^2+(abs(Z-Z0)-Lz/2+Lx/2).^2)<=(Lx/2)...
    & abs(Z-Z0)>(Lz/2-Lx/2))|((sqrt((X-X0).^2+(Y-Y0).^2)<=(Lx/2))...
    & abs(Z-Z0)<=(Lz/2-Lx/2)));
else          %Nps is Rod-nanoshell with caps, vertically oriented
  % Drawing the cubes of a nanoshell, remove one quadratant of shape
  Lx_core=Lx-4*d;       % Diameter of the core region
  Ly_core=Ly-4*d;       % Diameter of the core region
  Lz_core=Lz-4*d;       % Hight of the core region

  % Finding dipoles inside the core region
  Index_core=find((sqrt((X-X0).^2+(Y-Y0).^2+(abs(Z-Z0)-Lz_core/2+Lx_core/2).^2)<=(Lx_core/2)...
    & abs(Z-Z0)>(Lz_core/2-Lx_core/2))|((sqrt((X-X0).^2+(Y-Y0).^2)<=(Lx_core/2))...
    & abs(Z-Z0)<=(Lz_core/2-Lx_core/2)));
  % Finding dipoles inside the whole particle
  Index_total=find((sqrt((X-X0).^2+(Y-Y0).^2+(abs(Z-Z0)-Lz/2+Lx/2).^2)<=(Lx/2)...
    & abs(Z-Z0)>(Lz/2-Lx/2))|((sqrt((X-X0).^2+(Y-Y0).^2)<=(Lx/2))...
    & abs(Z-Z0)<=(Lz/2-Lx/2)));
```

```
    % Finding dipoles inside the first quadrant of the core region
    Index_core_quad=find((X>=0 & Y>=0 & Z>=0 & (sqrt((X-X0).^2+(Y-Y0).^2+...
        (abs(Z-Z0)-Lz_core/2+Lx_core/2).^2)<=(Lx_core/2) ...
        & abs(Z-Z0)>(Lz_core/2-Lx_core/2)))| ...
        (X>=0 & Y>=0 & Z>=0 &(sqrt((X-X0).^2+(Y-Y0).^2)<=(Lx_core/2))...
        & abs(Z-Z0)<=(Lz_core/2-Lx_core/2)));
    % Finding dipoles inside the first quadrant of the whole Np
    Index_total_quad=find((X>=0 & Y>=0 & Z>=0 &(sqrt((X-X0).^2+(Y-Y0).^2+...
        (abs(Z-Z0)-Lz/2+Lx/2).^2)<=(Lx/2) & abs(Z-Z0)>(Lz/2-Lx/2)))| ...
        (X>=0 & Y>=0 & Z>=0 &(sqrt((X-X0).^2+(Y-Y0).^2)<=(Lx/2))& abs(Z-Z0)<=(Lz/2-Lx/2)));
    % Removing the contribution of the core region
    Multiply_core=zeros(N,1);
    Multiply_total=zeros(N,1);
    Multiply_core(Index_core,1)=Index_core;
    Multiply_core(Index_core_quad,1)=0;
    Multiply_total(Index_total,1)=Index_total;
    Multiply_total(Index_total_quad,1)=0;
    INDEX_Shell=Multiply_total-Multiply_core;
    Index_in=nonzeros(INDEX_Shell);
    Index_core=nonzeros(Multiply_core);
end
X_in=X(Index_in,1);
Y_in=Y(Index_in,1);
Z_in=Z(Index_in,1);
for i=1:length(X_in)
    % Obtaining coordinate of the corners of the each nanocube
    nodeCoordinates=[0+X_in(i), 0+Y_in(i), 0+Z_in(i); 0+X_in(i), 0+Y_in(i), d+Z_in(i);...
        d+X_in(i), 0+Y_in(i), d+Z_in(i); d+X_in(i), 0+Y_in(i), 0+Z_in(i);...
        0+X_in(i), d+Y_in(i), 0+Z_in(i); 0+X_in(i), d+Y_in(i), d+Z_in(i);...
        d+X_in(i), d+Y_in(i), d+Z_in(i); d+X_in(i), d+Y_in(i), 0+Z_in(i)];
    elementNodes = [1 4 3 2; 5 8 7 6; 1 2 6 5; 3 4 8 7; 2 3 7 6; 1 5 8 4];
    patch('Faces', elementNodes,'EdgeColor','g','FaceColor','y', 'Vertices', nodeCoordinates)
    light           % create a light
    lighting gouraud    % preferred method for lighting curved surfaces
    ii=i
    axis equal
    hold on
end
```

B. MATLAB Script for Calculating Scattering, Absorption and Extinction Efficiencies of Plasmonic NPs.

```
%HHHHHHHHHHHHHHHHHHHHHHHHHHHHHHHHHHHHHHHHHHHHHHHHHHHHHHHHHHHHHHHHHHHHHHHHHH%
% Calculating Cext, Cabs and Cscat using DDA
% Cext= Extinction cross section
% Cabs= Absorption cross section
% Cscat= Scattering cross section
% "GpuArray" will transfer data from CPU to GPU
% "gather" will transfer data from GPU to CPU
% if Nps_number=1,    Nps is spherical
% X if Nps_number=2,  Nps is ellipsoid, vertically oriented
% X if Nps_number=3,  Nps is Rod with caps, vertically oriented
% if Nps_number=4,    Nps is Rectangular block, vertically oriented
%MMMMMMMMMMMMMMMMMMMMMMMMMMMMMMMMMMMMMMMMMMMMMMMMMMMMMMMMMMMMMMMMMMMMMMMMM%
clear all
clc
tic
%%%%%%%%%%%%%%%%%%% Input Parameters %%%%%%%%%%%%%%%%%%%%%%%%
Nps_number=1;
nb=1.34;        % Refractive index of background medium
n_core=1;       % Refractive index of the matrix
r_eff=20;
d_eff=2*r_eff;
volume=4*pi/3*(r_eff^3);
d=0.5;              % size of the mesh
epsb=nb^2;          % Dielectric function of background medium
E0=[0 0 1];         % Incident electric field
K0=[0 1 0];         % unit vector in direction of wave vector

%GGGGGGGGGGGGGGGGGGGGGGGG Optical constants of Gold GGGGGGGGGGGGGGGGGGGGG%
% To calculate Cext, Cabs, Cscat of the other metals their corresponding
% data should be entered
hb_ev=6.58211951440*10^(-16);
Wp=8.9*1.5186*(10^15);          % plasma frequency of Au
L0=0.07/hb_ev;                  % Collision freguency of Au in bulk medium
Ap=0.5;                         % damping correction factor
Vf=1.4*(10^6);                  % Fermi Velocity
```

```
%%%%%%%%%%%%%%"loading Wavelength, and Refractive index of the metal" %%%%%%%%%%%%
% if initial data are save in an excell sheet it can load as below
Data=xlsread('Copy the address link of the initial data here\file name');

% if initial data are m.file can be loaded: ...
% Data=load('Copy the address link of the initial data here\file name');
Wavelength=Data(:,1);
Re_n=Data(:,2);                % Real part of the refractive index
Im_n=Data(:,3);                % Imaginary part of the refractive index
eps=(Re_n+1i*Im_n).^2;    % Dielectric function of the bulk metal

%%%%%%%%%%%%%%%% Obtaining Modified dielectric function %%%%%%%%%%%%%%%%%%
r_np=r_eff*(10^(-9));% radius of nanoparticle
W=2*pi*3*10^17./Wavelength;       % incident radiation frequency
k=2*pi./Wavelength*nb;           % wave vector of light in first layer
L=L0+Ap*Vf/r_np;                 % Modified damping frequency
eps_nps=eps+(Wp^2)./(W.^2+1i*L0.*W)-(Wp.^2)./(W.^2+1i*W.*L); % Modified dielectric function
ep_nps_eb=gpuArray(eps_nps./epsb);  % Ratio of metal-to-medium dielectric function
%NNNNNNNNNNNNNNNNNNNNNNNNNNNNNNNNNNNNNNNNNNNNNNNNNNNNNNNNNNNNNNNNNNNNNNNN%
% Finding dimension of the Rectangular block that NP is embedded inside it
[Lx,Ly,Lz]= Nps_parameters(r_eff,Nps_number);

% Finding coordinate of the dipoles inside the rectangular block
[Max_x,Max_y,Max_z,N,Nx,Ny,Nz,r_block,X,Y,Z]=Coordinates(d,Lx,Ly,Lz,d_inter,Structure);

% Finding index of the dipoles inside NPs and ingoring other elements
[Multiply_coeff]=INDEX_INSIDE_NP(X,Y,Z,N,Nps_number,Lx,Ly,Lz,Structure,d_inter);
INDEX_IN=gpuArray(reshape(Multiply_coeff,[Nx,Ny,Nz])); INDEX_INSIDE=reshape(INDEX_IN,[N,1]);

%Calculating RijRij-I3 and 3RijRij-I3 in interaction matrix A
[rjkrjk1_I,rjkrjk2_I,rjkrjk3_I,rjkrjk4_I,rjkrjk5_I,rjkrjk6_I,rjkrjk31_I,rjkrjk32_I,...
  rjkrjk33_I,rjkrjk34_I,rjkrjk35_I,rjkrjk36_I,RJK]=RijRij(r_block);

for J=1:length(Wavelength)
    %Obtaining inverse of polarizibilty of each nanocube at different Lambda
    eps_NP_eb=ep_nps_eb(J);
    kvec=gpuArray(k(J)*K0);
```

```
        [Inverse_Alpha]=Polarizability(kvec,eps_NP_eb,INDEX_IN,d,E0);

        % Calculating Incident electric filed components
        [E_x,E_y,E_z,E_vector]=Incident_Field(r_block,kvec,INDEX_INSIDE,Nx,Ny,Nz,E0);
        Exp_ikvec_rjk=exp(1i*norm(kvec)*RJK)./RJK;
        ikvec_rjk=(1i*norm(kvec)*RJK-1)./(RJK.^2);   % ikvec_rjk=(1i*norm(kvec)*rjk-1)/rjk^2

        % Calculating six tensor blocks:Axx, Axy, Axz, Ayy, Ayz, Azz
        [Axx,Axy,Axz,Ayy,Ayz,Azz]=Interaction_Matrix(kvec,Exp_ikvec_rjk,...
          ikvec_rjk, rjkrjk1_I,rjkrjk2_I,rjkrjk3_I,rjkrjk4_I,rjkrjk5_I,rjkrjk6_I,...
          rjkrjk31_I,rjkrjk32_I,rjkrjk33_I,rjkrjk34_I,rjkrjk35_I,rjkrjk36_I,Nx,Ny,Nz);
        % Calculating FFT of six tensor blocks of the interaction matrix
        [FFT_AXX,FFT_AXY,FFT_AXZ,FFT_AYY,FFT_AYZ,FFT_AZZ]=FFT_Interaction(Axx...
            ,Axy,Axz,Ayy,Ayz,Azz,Nx,Ny,Nz);
        %Applying Biconjugate gradient as an iterative method to obtainPx,Py,PZ
        [px,py,pz]=Biconjugate_Gradient(E_x,E_y,E_z,Nx,Ny,Nz,N,Inverse_Alpha,...
            INDEX_IN,E_vector,FFT_AXX,FFT_AXY,FFT_AXZ,FFT_AYY,FFT_AYZ,FFT_AZZ);
        clear FFT_AXX FFT_AXY FFT_AXZ FFT_AYY FFT_AYZ FFT_AZZ

        px=px.*INDEX_IN;
        py=py.*INDEX_IN;
        pz=pz.*INDEX_IN;
        PX_vector=reshape(px,[N,1]);
        PY_vector=reshape(py,[N,1]);
        PZ_vector=reshape(pz,[N,1]);
        Inv_Alpha=reshape(Inverse_Alpha,[N,1]);
        Inv_Alpha_vec=[Inv_Alpha;Inv_Alpha;Inv_Alpha];
        counting2=counting2+1

        P_vector=[PX_vector;PY_vector;PZ_vector];
        Cabs(J)=4*pi*norm(kvec)/sum(abs(E0.^2))*((imag(dot((conj(P_vector)), ...
          conj(P_vector.*Inv_Alpha_vec)))-2/3*norm(kvec)^3*(norm(P_vector).^2)));
        Cext(J)=4*pi*norm(kvec)/sum(abs(E0.^2))*imag(dot((E_vector),P_vector));
        Cscat(J)=Cext(J)-Cabs(J);
        clear PX_vector PY_vector PZ_vector P_vector px py pz a_CM_Nps anr_Nps ...
          aLDR_Nps  a_CM_Matrix anr_Matrix aLDR_Matrix Ex Ey Ez E_x E_y E_z ...
          E_vector Exp_ikvec_rjk ikvec_rjk Inverse_Alpha
end
```

```
toc;
C_ABS=gather(Cabs)/(pi*(r_eff^2));   % Transfering Data from GPU to CPU
C_EXT=gather(Cext)/(pi*(r_eff^2));   % Transfering Data from GPU to CPU
C_SCAT=gather(Cscat)/(pi*(r_eff^2)); % Transfering Data from GPU to CPU
plot(Wavelength,C_EXT,Wavelength,C_ABS,Wavelength,C_SCAT)
```

C. Calculating Electric Field Enhancement in Monomeric and Dimeric Structures Using 'E_field_Enhancement.m' File.

```
%HHHHHHHHHHHHHHHHHHHHHHHHHHHHHHHHHHHHHHHHHHHHHHHHHHHHHHHHHHHHHHHHHHHHHHHHHHHH%
% Calculating E-field enhancement in monomer and dimer structures
% "GpuArray" will transfer data from CPU to GPU
% "gather" will transfer data from GPU to CPU
% if Nps_number=1,   Nps is spherical
% if Nps_number=2,  Nps is ellipsoid, vertically oriented
% if Nps_number=3,  Nps is Rod with caps, vertically oriented
% if Nps_number=4,   Nps is Rectangular block, vertically oriented
%MMMMMMMMMMMMMMMMMMMMMMMMMMMMMMMMMMMMMMMMMMMMMMMMMMMMMMMMMMMMMMMMMMMMMMMMMMM%
clear all
clc
tic
%%%%%%%%%%%%%%%%%%%% Input Parameters %%%%%%%%%%%%%%%%%%%%%%%%
Nps_number=1;     % refer to the commends from line 5 to 8
Structure=2;         % Structure=1 will calculate E-field of monomer structure
%Structure=2;       % Structure=2 will calculate E-field of dimer structure
nb=1.34;              % Refractive index of background medium
n_core=1;             % Refractive index of the matrix
r_eff=20;
d=2;                  % size of the each nanocube
E0=[0 0 1];           % Incident electric field
K0=[0 1 0];           % unit vector in direction of wave vector

d_eff=2*r_eff;
d_inter=0.2*d_eff; % inter-particle distance in dimer structure
volume=4*pi/3*(r_eff^3);
epsb=nb^2;        % Dielectric function of background medium

%GGGGGGGGGGGGGGGGGGGGGGGG Optical constants of Gold GGGGGGGGGGGGGGGGGGGGG%
% To calculate Cext, Cabs, Cscat of the other metals their corresponding data should be entered
hb_ev=6.58211951440*10^(-16);
Wp=8.9*1.5186*(10^15);          % plasma frequency of Au
L0=0.07/hb_ev;                  % Collision freguency of Au in bulk medium
Ap=0.5;                         % damping correction factor
Vf=1.4*(10^6);                  % Fermi Velocit
```

```
% Lmax and corresponding refractive index of each
Wavelength=544;        % Insert LSPR wavelength and corresponding n
Re_n=0.4616;
Im_n=2.3929;
eps=(Re_n+1i*Im_n).^2;
Re_eps=real(eps);
Im_eps=imag(eps);

%%%%%%%%%%%%%% Obtaining Modified dielectric function %%%%%%%%%%%%%%%%%%
r_np=r_eff*(10^(-9));                % radius of nanoparticle
W=2*pi*3*10^17./Wavelength;          % incident radiation frequency
k=2*pi./Wavelength*nb;               % wave vector of light in first layer
L=L0+Ap*Vf/r_np;                     % Modified damping frequency
eps_nps=eps+(Wp^2)./(W.^2+1i*L0.*W)-(Wp.^2)./(W.^2+1i*W.*L); % Modified dielectric function
ep_nps_eb=gpuArray(eps_nps./epsb);  % Ratio of metal-to-medium dielectric function

% Finding dimension of the Rectangular block that NP is embedded inside it
[Lx,Ly,Lz]= Nps_parameters(r_eff,Nps_number);

% Finding coordinate of the dipoles inside the rectangular block
[Max_x,Max_y,Max_z,N,Nx,Ny,Nz,r_block,X,Y,Z]=Coordinates(d,Lx,Ly,Lz, d_inter, Structure);

%HH Finding index of the dipoles inside NPs and ingoring other elements HH%
[Multiply_coeff]=INDEX_INSIDE_NP(X,Y,Z,N,Nps_number,Lx,Ly,Lz,Structure,d_inter);
INDEX_IN=gpuArray(reshape(Multiply_coeff,[Nx,Ny,Nz]));
INDEX_INSIDE=reshape(INDEX_IN,[N,1]);

%Calculating RijRij-I3 and 3RijRij-I3 in interaction matrix A
[rjkrjk1_I,rjkrjk2_I,rjkrjk3_I,rjkrjk4_I,rjkrjk5_I,rjkrjk6_I,rjkrjk31_I,rjkrjk32_I,...
   rjkrjk33_I,rjkrjk34_I,rjkrjk35_I,rjkrjk36_I,RJK]=RijRij(r_block);

%Obtaining inverse of polarizibilty of each nanocube at different Lambda%
eps_NP_eb=ep_nps_eb;
kvec=k*K0;
[Inverse_Alpha]=Polarizability(kvec,eps_NP_eb,INDEX_IN,d,E0);

% Calculating Incident electric filed components
[E_x,E_y,E_z,E_vector]=Incident_Field(r_block,kvec,INDEX_INSIDE,Nx,Ny,Nz,E0);
```

```
% Calculating six tensor blocks: Axx, Axy, Axz, Ayy, Ayz, Azz
Exp_ikvec_rjk=exp(1i*norm(kvec)*RJK)./RJK;
ikvec_rjk=(1i*norm(kvec)*RJK-1)./(RJK.^2);      % ikvec_rjk=(1i*norm(kvec)*rjk-1)/rjk^2

[Axx,Axy,Axz,Ayy,Ayz,Azz]=Interaction_Matrix(kvec,Exp_ikvec_rjk,...
   ikvec_rjk, rjkrjk1_I,rjkrjk2_I,rjkrjk3_I,rjkrjk4_I,rjkrjk5_I,rjkrjk6_I,...
   rjkrjk31_I,rjkrjk32_I,rjkrjk33_I,rjkrjk34_I,rjkrjk35_I,rjkrjk36_I,Nx,Ny,Nz);

%Calculating FFT of six tensor blocks: Axx, Axy, Axz, Ayy, Ayz, Azz
[FFT_AXX,FFT_AXY,FFT_AXZ,FFT_AYY,FFT_AYZ,FFT_AZZ]=FFT_Interaction(Axx...
   ,Axy,Axz,Ayy,Ayz,Azz,Nx,Ny,Nz);

%Applying Biconjugate gradient as an iterative method to obtainPx,Py,PZ%
[px,py,pz]=Biconjugate_Gradient(E_x,E_y,E_z,Nx,Ny,Nz,N,Inverse_Alpha,...
   INDEX_IN,E_vector,FFT_AXX,FFT_AXY,FFT_AXZ,FFT_AYY,FFT_AYZ,FFT_AZZ);

clear FFT_AXX FFT_AXY FFT_AXZ FFT_AYY FFT_AYZ FFT_AZZ

px=px.*INDEX_IN;
py=py.*INDEX_IN;
pz=pz.*INDEX_IN;
PX_vector=reshape(px,[N,1]);
PY_vector=reshape(py,[N,1]);
PZ_vector=reshape(pz,[N,1]);
P_vector=[PX_vector;PY_vector;PZ_vector];
clear  a_CM_Nps anr_Nps aLDR_Nps  a_CM_Matrix anr_Matrix aLDR_Matrix Ex Ey Ez E_x E_y E_z ...
   E_vector Exp_ikvec_rjk ikvec_rjk Inverse_Alpha

%EEEEEEEEEEEEEEEEEEEEEEEEEEEEEEEEEEEEEEEEEEEEEEEEEEEEEEEEEEEEEEEEEEEEEEEEEEEE%
%%%%%%%% E-field of the structure can be calculated in any plane %%%%%%%%%
% For example I am calculating E-field in xz plane at y=0
% The electric field outside of the NPs has been calculated
dx=d;
dy=d;
dz=d;
X1=-round(Max_x/dx):round(Max_x/dx);
X_range=X1*dx;
Z1=-round(Max_z/dz):round(Max_z/dz);
```

```
Z_range=Z1*dz;
[X,Z]=meshgrid(X_range,Z_range);
SIZE=size(X);
N2=SIZE(1,1)*SIZE(1,2);   % Total number of nanocubes, inside NPs and outside region

xx=(reshape(X,[N2,1]));
yy=((0)*ones(N2,1));
zz=(reshape(Z,[N2,1]));
r_cube=[xx yy zz];              % Position of the each nanocubes inside and outside of the NPs boundary
r_cube=gpuArray(r_cube);

% Obtaining incident electric field at position of each dipole
kr=kvec(1)*r_cube(:,1)+kvec(2)*r_cube(:,2)+kvec(3)*r_cube(:,3);
expikr=exp(1i*kr);
Ex_incident=gpuArray(E0(1)*expikr);
Ey_incident=gpuArray(E0(2)*expikr);
Ez_incident=gpuArray(E0(3)*expikr);

r_blockGpu=gpuArray(r_block); % Position of each nanocubes inside NPs

% Calculating total E-field at each cubes
[Ex_total,Ey_total,Ez_total]=E_total(N2,r_blockGpu,r_cube,PX_vector,PY_vector,PZ_vector,xx,yy,zz,...
...Nps_number,Lx,Ly,Lz,d,kvec,d_inter,Structure,Ex_incident,Ey_incident,Ez_incident);

E_total=sqrt(Ex_total.*(Ex_total)+Ey_total.*(Ey_total)+Ez_total.*(Ez_total));
E_t=abs(reshape(E_total,[SIZE(1,1),SIZE(1,2)]));
I=E_t.^2;

% Transfering data from GPU to CPU
X=gather(X);
Z=gatehr(Z);
E_t=gather(E_t);
I=gather(I);

% Surface plot of the electric field
surf(X,Z,E_t,'EdgeColor','none','LineStyle','none','FaceLighting','phong');
axis equal
hold on
```

Appendix D

D. Discrete Dipole Approximation Formalism

D.1. Calculating Parameters of the NP.

```
% PPPPPPPPPPPPPPPPPPPPPPPPPPPPPPPPPPPPPPPPPPPPPPPPPPPPPPPPPPPPPPPPPPPPPPPPPPPPPPPPPPPPPP%
% Finding dimension of the Rectangular block that NP is embedded inside it
function [Lx,Ly,Lz]= Nps_parameters(r_eff,Nps_number)

if Nps_number==1      % Nps is Sphere
  d_eff=2*r_eff;    % Effective diameter
  Lx=d_eff;
  Ly=d_eff;
  Lz=d_eff;

elseif Nps_number==2   % Nps is Ellipsoid
  ARyx=1;                       %Ratio of y-axis to to x-axis
  ARzx=2;                       %Ratio of z-axis to to x-axis
  d_eff=2*r_eff;
  a=((1/(ARyx*ARzx))^(1/3))*r_eff;    % Semi- minor axis in x- direction
  b=ARyx*a;                      % Semi- minor axis in y- direction
  c=ARzx*a;                      % Semi- major axis in z- direction
  Lx=2*a;
  Ly=2*b;
  Lz=2*c;

elseif Nps_number==3  % Np is a rod with caps
  volume=4*pi/3*(r_eff^3);
  AR=2;       % Aspect Ratio: ratio of the long axis to short one
  r=(volume/(pi*(2*(AR-1)+4/3)))^(1/3); % Raduis of the Rod
  diameter=2*r;                   % Diameter of the Rod
  higth=AR*diameter;               % Higth of the Rod
  Lx=diameter;
  Ly=diameter;
  Lz=higth;

else        %Np is a rectangular block
  volume=4*pi/3*(r_eff^3);
  AR1=1;                    % aspect ratio or ratio of b to a
  AR2=2;                    % aspect ratio or ratio of c to a
```

```
    a=(volume/(AR1*AR2))^(1/3);    % First side of rectangular block
    b=AR1*a;                       % Second side of rectangular block
    c=AR2*a;                       % Third side of rectangular block
    Lx=a;
    Ly=b;
    Lz=c;
end
end
```

D.2. Obtaining Coordinates of the Dipoles.

```
%KKKKKKKKKKKKKKKKKKKKKKKKKKKKKKKKKKKKKKKKKKKKKKKKKKKKKKKKKKKKKKKKKKKKKKKKKKKKKKK%
function [Max_x,Max_y,Max_z,N,Nx,Ny,Nz,r_block,X,Y,Z]=Coordinates(d,Lx,Ly,Lz,...
                                    d_inter,Structure)
dx=d;
dy=d;
dz=d;

if Structure==1 % Monomeric structure
   Max_x=Lx;
   Max_y=Ly;
   Max_z=Lz;
else                % Dimeric Structure
   % For nanoparticles with head-tail orientation in z-direction
   Max_x=Lx;
   Max_y=Ly;
   Max_z=2*Lz+d_inter;
end
%%%%%%%% Obtaining Coordinates of nanocubs or nanocells within NPS %%%%%%%%
ix=-round(Max_x/(2*dx)):round(Max_x/(2*dx));
iy=-round(Max_y/(2*dy)):round(Max_y/(2*dy));
iz=-round(Max_z/(2*dz)):round(Max_z/(2*dz));
[y,x,z]=meshgrid(iy,ix,iz);
Nx=length(ix);              % Number of the dipoles in the x-direction
Ny=length(iy);              % Number of the dipoles in the y-direction
Nz=length(iz);              % Number of the dipoles in the z-direction

N=Nx*Ny*Nz;

X=gpuArray((reshape(x,[N,1]))*dx); % X-coordinates of the dipoles
Y=gpuArray((reshape(y,[N,1]))*dy); % Y-coordinates of the dipoles
Z=gpuArray((reshape(z,[N,1]))*dz); % Z-coordinates of the dipoles

r_block=[X Y Z];            % Position of the each dipoles inside rectangular block

end
```

D.3. Obtaining Index of the Nanocubes That Are Located Inside the NP.

```
%IIIIIIIIIIIIIIIIIIIIIIIIIIIIIIIIIIIIIIIIIIIIIIIIIIIIIIIIIIIIIIIIIIIIIIIIIIIIIIIIIIIIIIIIIIIIIIIIIIIIIIIIIIIIIIIIIIIIIIIIIIIIIIIIIIIIII%
function[Multiply_coeff]=INDEX_INSIDE_NP(X,Y,Z,N,Nps_number,Lx,Ly,Lz,Structure,d_inter)

if Structure==1 % Monomer structure
  X0=0; % d_inter is the distance from surface of first Np to surface of second one
  Y0=0;
  Z0=0;

  if Nps_number==1       % NPs are sphere
    Index_in=find((sqrt((X-X0).^2+(Y-Y0).^2+(Z-Z0).^2)<=(Lx/2)));  % Index of cubes inside NP

  elseif Nps_number==2 %NPs are ellipsoid, head-tail orientation in z-direction
    Index_in=find((sqrt((X-X0).^2/((Lx/2)^2)+(Y-Y0).^2/((Ly/2)^2)+...
      (Z-Z0).^2/((Lz/2)^2))<=1));                                     % Index of cubes inside NP



  elseif Nps_number==3    %NPs are Rod with caps, vertically oriented
    Index_in=find((sqrt((X-X0).^2+(Y-Y0).^2+(abs(Z-Z0)-Lz/2+Lx/2).^2)<=(Lx/2)...
      & abs(Z-Z0)>(Lz/2-Lx/2))|((sqrt((X-X0).^2+(Y-Y0).^2)<=(Lx/2))...
      &abs(Z-Z0)<=(Lz/2-Lx/2)));                                      % Index of cubes inside NP

  elseif Nps_number==4 %NPs are Rectangular block, vertically oriented
    % Index of cubes inside NP
    Index_in=find((abs(X-X0)<=Lx/2 & abs(Y-Y0)<=Ly/2 & abs(Z-Z0)<=Lz/2));
  end

else        % Dimer, structure=2
  X10=0; % d_inter is the distance from surface of first Np to surface of second one
  Y10=0;
  Z10=-(d_inter/2+Lz/2);
  X20=0;
  Y20=0;
  Z20=(d_inter/2+Lz/2);

  if Nps_number==1       % NPs are sphere
    % Index of cubes inside NP
    Index_in=find((sqrt((X-X10).^2+(Y-Y10).^2+(Z-Z10).^2)<=(Lx/2))|...
```

```
        (sqrt((X-X20).^2+(Y-Y20).^2+(Z-Z20).^2)<=(Lx/2)));

    elseif Nps_number==2    %NPs are ellipsoid and have head to tail orientation in z-direction
        % Index of cubes inside NP
        Index_in=find((sqrt((X-X10).^2/((Lx/2)^2)+(Y-Y10).^2/((Ly/2)^2)+...
            (Z-Z10).^2/((Lz/2)^2))<=1)|(sqrt((X-X20).^2/((Lx/2)^2)+...
            (Y-Y20).^2/((Ly/2)^2)+(Z-Z20).^2/((Lz/2)^2))<=1));

    elseif Nps_number==3    %NPs are Rod with caps, vertically oriented
        % Index of cubes inside NP
        Index_in=find((sqrt((X-X10).^2+(Y-Y10).^2+(abs(Z-Z10)-Lz/2+Lx/2).^2)...
            <=(Lx/2)& abs(Z-Z10)>(Lz/2-Lx/2))|...
            ((sqrt((X-X10).^2+(Y-Y10).^2)<=(Lx/2))&abs(Z-Z10)<=(Lz/2-Lx/2))|...
            (sqrt((X-X20).^2+(Y-Y20).^2+(abs(Z-Z20)-Lz/2+Lx/2).^2)<=(Lx/2)...
            & abs(Z-Z20)>(Lz/2-Lx/2))|(sqrt((X-X20).^2+(Y-Y20).^2)<=(Lx/2))...
            &abs(Z-Z20)<=(Lz/2-Lx/2)));

    elseif Nps_number==4 %NPs are Rectangular block, vertically oriented
        % Index of cubes inside NP
        Index_in=find((abs(X-X10)<=Lx/2 & abs(Y-Y10)<=Ly/2 & abs(Z-Z10)<=Lz/2)|...
            (abs(X-X20)<=Lx/2 & abs(Y-Y20)<=Ly/2 & abs(Z-Z20)<=Lz/2));

    end
end
Multiply_coeff=zeros(N,1);
% Considering dipoles inside the Np and ignoring contribution of the other terms
Multiply_coeff(Index_in,1)=1;
end
```

D.4. Obtaining Distance between Dipole i and Dipole j in Interaction Matrix A.

```
%RRRRRRRRRRRRRRRRRRRRRRRRRRRRRRRRRRRRRRRRRRRRRRRRRRRRRRRRRRRRRRRRRRRRRRRRRRRRRRR%
%Calculating RijRij-I3 and 3RijRij-I3 in interaction matrix A
function [rjkrjk1_I,rjkrjk2_I,rjkrjk3_I,rjkrjk4_I,rjkrjk5_I,rjkrjk6_I,rjkrjk31_I,...
   rjkrjk32_I,rjkrjk33_I,rjkrjk34_I,rjkrjk35_I,rjkrjk36_I,RJK]=RijRij(r_block)

rkj1=r_block(1,1)-r_block(:,1);
rkj2=r_block(1,2)-r_block(:,2);
rkj3=r_block(1,3)-r_block(:,3);

rk_to_rj=[rkj1  rkj2  rkj3];
rk_to_rj(1,:)=1;              % in order to scape from NAN Error
RJK=sqrt(rk_to_rj(:,1).^2+rk_to_rj(:,2).^2+rk_to_rj(:,3).^2);
rjkrjk=[rkj1./RJK  rkj2./RJK  rkj3./RJK];

rjkrjk1_I=rjkrjk(:,1).*rjkrjk(:,1)-1;
rjkrjk2_I=rjkrjk(:,1).*rjkrjk(:,2);
rjkrjk3_I=rjkrjk(:,1).*rjkrjk(:,3);
rjkrjk4_I=rjkrjk(:,2).*rjkrjk(:,2)-1;
rjkrjk5_I=rjkrjk(:,2).*rjkrjk(:,3);
rjkrjk6_I=rjkrjk(:,3).*rjkrjk(:,3)-1;

rjkrjk31_I=3*rjkrjk(:,1).*rjkrjk(:,1)-1;
rjkrjk32_I=3*rjkrjk(:,1).*rjkrjk(:,2);
rjkrjk33_I=3*rjkrjk(:,1).*rjkrjk(:,3);
rjkrjk34_I=3*rjkrjk(:,2).*rjkrjk(:,2)-1;
rjkrjk35_I=3*rjkrjk(:,2).*rjkrjk(:,3);
rjkrjk36_I=3*rjkrjk(:,3).*rjkrjk(:,3)-1;

rjkrjk1_I(1,1)=0;
rjkrjk2_I(1,1)=0;
rjkrjk3_I(1,1)=0;
rjkrjk4_I(1,1)=0;
rjkrjk5_I(1,1)=0;
rjkrjk6_I(1,1)=0;
rjkrjk31_I(1,1)=0;
rjkrjk32_I(1,1)=0;
```

```
rjkrjk33_I(1,1)=0;
rjkrjk34_I(1,1)=0;
rjkrjk35_I(1,1)=0;
rjkrjk36_I(1,1)=0;
end
```

D.5. ‘Polarizability.m’ File Will Calculate the Polarizability of each Nanocube Inside the NP.

```
%PPPPPPPPPPPPPPPPPPPPPPPPPPPPPPPPPPPPPPPPPPPPPPPPPPPPPPPPPPPPPPPPPPPPPPPPPPPPPPPP%
%Obtaining inverse of polarizibilty of each nanocube at different Lambda%
function [Inverse_Alpha]=Polarizability(kvec,eps_NP_eb,INDEX_IN,d,E0)
k0 = 2*pi;
b1 = -1.891531;
b2 = 0.1648469;
b3 = -1.7700004;
dcube = d^3;
a_hat = kvec/norm(kvec);
e_hat = E0/norm(E0);
S = 0;

for j = 1:3
  S = S + (a_hat(j)*e_hat(j))^2;
end

a_CM =3*dcube/(4*pi)*(eps_NP_eb - 1)./(eps_NP_eb + 2); % Clausius-Mossotti
anr=a_CM./(1 + (a_CM/dcube).*(b1+eps_NP_eb*b2+eps_NP_eb*b3*S)*((norm(kvec)*d)^2));
aLDR=gpuArray(anr./(1-2/3*1i*(anr/dcube)*((norm(kvec)*d)^3)));
Inverse_Alpha=1/aLDR*INDEX_IN;
end
```

D.6. Calculating Incident Electric Field at the Position of each Dipole.

```
%EEEEEEEEEEEEEEEEEEEEEEEEEEEEEEEEEEEEEEEEEEEEEEEEEEEEEEEEEEEEEEEEEEEEEEEEEEEEEEEEEE%
% Calculating Incident electric filed components
function [E_x,E_y,E_z,E_vector]=Incident_Field(r_block,kvec,INDEX_INSIDE,Nx,Ny,Nz,E0)
kr=kvec(1)*r_block(:,1)+kvec(2)*r_block(:,2)+kvec(3)*r_block(:,3);
expikr=exp(1i*kr);
Ex=gpuArray(E0(1)*expikr).*INDEX_INSIDE;
Ey=gpuArray(E0(2)*expikr).*INDEX_INSIDE;
Ez=gpuArray(E0(3)*expikr).*INDEX_INSIDE;

E_x=reshape(Ex,[Nx,Ny,Nz]);
E_y=reshape(Ey,[Nx,Ny,Nz]);
E_z=reshape(Ez,[Nx,Ny,Nz]);
E_vector=[Ex;Ey;Ez];
end
```

D.7. Computing Six Tensor Blocks of the Interaction matrix.

```
%MMMMMMMMMMMMMMMMMMMMMMMMMMMMMMMMMMMMMMMMMMMMMMMMMMMMMMMMMMMMMMMMMMMMMMM%
% Calculating six tensor blocks: Axx, Axy, Axz, Ayy, Ayz and Azz
function [Axx,Axy,Axz,Ayy,Ayz,Azz]=Interaction_Matrix(kvec,Exp_ikvec_rjk,ikvec_rjk, rjkrjk1_I,rjkrjk2_I,...
rjkrjk3_I,rjkrjk4_I,rjkrjk5_I,rjkrjk6_I, rjkrjk31_I,rjkrjk32_I,rjkrjk33_I,rjkrjk34_I,rjkrjk35_I,rjkrjk36_I,Nx,Ny,Nz)

A1=gpuArray(Exp_ikvec_rjk.*((norm(kvec)^2)*rjkrjk1_I+ ikvec_rjk.*rjkrjk31_I));
Axx=reshape(A1,[Nx,Ny,Nz]);
Axx(1,1,1)=0;
clear A1
A2=gpuArray(Exp_ikvec_rjk.*((norm(kvec)^2)*rjkrjk2_I+ ikvec_rjk.*rjkrjk32_I));
Axy=reshape(A2,[Nx,Ny,Nz]);
Axy(1,1,1)=0;
clear A2
A3=gpuArray(Exp_ikvec_rjk.*((norm(kvec)^2)*rjkrjk3_I+ ikvec_rjk.*rjkrjk33_I));
Axz=reshape(A3,[Nx,Ny,Nz]);
Axz(1,1,1)=0;
clear A3
A4=gpuArray(Exp_ikvec_rjk.*((norm(kvec)^2)*rjkrjk4_I+ ikvec_rjk.*rjkrjk34_I));
Ayy=reshape(A4,[Nx,Ny,Nz]);
Ayy(1,1,1)=0;
clear A4
A5=gpuArray(Exp_ikvec_rjk.*((norm(kvec)^2)*rjkrjk5_I+ ikvec_rjk.*rjkrjk35_I));
Ayz=reshape(A5,[Nx,Ny,Nz]);
Ayz(1,1,1)=0;
clear A5
A6=gpuArray(Exp_ikvec_rjk.*((norm(kvec)^2)*rjkrjk6_I+ ikvec_rjk.*rjkrjk36_I));
Azz=reshape(A6,[Nx,Ny,Nz]);
Azz(1,1,1)=0;
clear A6  Exp_ikvec_rjk
end
```

D.8. Calculating FFT of the Six Tensor Blocks of the Interaction Matrix.

```
%AAAAAAAAAAAAAAAAAAAAAAAAAAAAAAAAAAAAAAAAAAAAAAAAAAAAA%
function [FFT_AXX,FFT_AXY,FFT_AXZ,FFT_AYY,FFT_AYZ,FFT_AZZ]=FFT_Interaction(Axx...
  ,Axy,Axz,Ayy,Ayz,Azz,Nx,Ny,Nz)
AXX=gpuArray(zeros(2*Nx-1,2*Ny-1,2*Nz-1));
AXY=gpuArray(zeros(2*Nx-1,2*Ny-1,2*Nz-1));
AXZ=gpuArray(zeros(2*Nx-1,2*Ny-1,2*Nz-1));
AYY=gpuArray(zeros(2*Nx-1,2*Ny-1,2*Nz-1));
AYZ=gpuArray(zeros(2*Nx-1,2*Ny-1,2*Nz-1));
AZZ=gpuArray(zeros(2*Nx-1,2*Ny-1,2*Nz-1));

AXX(1:Nx,1:Ny,1:Nz)=Axx;
AXY(1:Nx,1:Ny,1:Nz)=Axy;
AXZ(1:Nx,1:Ny,1:Nz)=Axz;
AYY(1:Nx,1:Ny,1:Nz)=Ayy;
AYZ(1:Nx,1:Ny,1:Nz)=Ayz;
AZZ(1:Nx,1:Ny,1:Nz)=Azz;
% Calculating FFT of 6 tensor blocks of the interaction matrix in x-direction%%
%%%%% X-DFT
AXX(Nx+1:2*Nx-1,1:Ny,1:Nz)=Axx(Nx:-1:2,1:Ny,1:Nz);
clear Axx
AXY(Nx+1:2*Nx-1,1:Ny,1:Nz)=-Axy(Nx:-1:2,1:Ny,1:Nz);
clear Axy
AXZ(Nx+1:2*Nx-1,1:Ny,1:Nz)=-Axz(Nx:-1:2,1:Ny,1:Nz);
clear Axz
AYY(Nx+1:2*Nx-1,1:Ny,1:Nz)=Ayy(Nx:-1:2,1:Ny,1:Nz);
clear Ayy
AYZ(Nx+1:2*Nx-1,1:Ny,1:Nz)=Ayz(Nx:-1:2,1:Ny,1:Nz);
clear Ayz
AZZ(Nx+1:2*Nx-1,1:Ny,1:Nz)=Azz(Nx:-1:2,1:Ny,1:Nz);
clear Azz
AXX(:,1:Ny,1:Nz)=fft(AXX(:,1:Ny,1:Nz));
AXY(:,1:Ny,1:Nz)=fft(AXY(:,1:Ny,1:Nz));
AXZ(:,1:Ny,1:Nz)=fft(AXZ(:,1:Ny,1:Nz));
AYY(:,1:Ny,1:Nz)=fft(AYY(:,1:Ny,1:Nz));
AYZ(:,1:Ny,1:Nz)=fft(AYZ(:,1:Ny,1:Nz));
AZZ(:,1:Ny,1:Nz)=fft(AZZ(:,1:Ny,1:Nz));
```

```
% Calculating FFT of 6 tensor blocks of the interaction matrix in y-direction%%
%%%%% Y- DFT
AXX(:,Ny+1:2*Ny-1,1:Nz)=AXX(:,Ny:-1:2,1:Nz);

AXY(:,Ny+1:2*Ny-1,1:Nz)=-AXY(:,Ny:-1:2,1:Nz);
AXZ(:,Ny+1:2*Ny-1,1:Nz)=AXZ(:,Ny:-1:2,1:Nz);
AYY(:,Ny+1:2*Ny-1,1:Nz)=AYY(:,Ny:-1:2,1:Nz);
AYZ(:,Ny+1:2*Ny-1,1:Nz)=-AYZ(:,Ny:-1:2,1:Nz);
AZZ(:,Ny+1:2*Ny-1,1:Nz)=AZZ(:,Ny:-1:2,1:Nz);

AXX=fft(AXX(:,:,1:Nz),[],2); % Calculating FFT in y-direction
AXY=fft(AXY(:,:,1:Nz),[],2); % Calculating FFT in y-direction
AXZ=fft(AXZ(:,:,1:Nz),[],2); % Calculating FFT in y-direction
AYY=fft(AYY(:,:,1:Nz),[],2); % Calculating FFT in y-direction
AYZ=fft(AYZ(:,:,1:Nz),[],2); % Calculating FFT in y-direction
AZZ=fft(AZZ(:,:,1:Nz),[],2); % Calculating FFT in y-direction
% Calculating FFT of 6 tensor blocks of the interaction matrix in z-direction%
%%%%%  Z- DFT
AXX(:,:,Nz+1:2*Nz-1)=AXX(:,:,Nz:-1:2);
AXY(:,:,Nz+1:2*Nz-1)=AXY(:,:,Nz:-1:2);
AXZ(:,:,Nz+1:2*Nz-1)=-AXZ(:,:,Nz:-1:2);
AYY(:,:,Nz+1:2*Nz-1)=AYY(:,:,Nz:-1:2);
AYZ(:,:,Nz+1:2*Nz-1)=-AYZ(:,:,Nz:-1:2);
AZZ(:,:,Nz+1:2*Nz-1)=AZZ(:,:,Nz:-1:2);

FFT_AXX=fft(AXX,[],3); % Calculating FFT in z-direction
clear AXX
FFT_AXY=fft(AXY,[],3); % Calculating FFT in z-direction
clear AXY
FFT_AXZ=fft(AXZ,[],3); % Calculating FFT in z-direction
clear AXZ
FFT_AYY=fft(AYY,[],3); % Calculating FFT in z-direction
clear AYY
FFT_AYZ=fft(AYZ,[],3); % Calculating FFT in z-direction
clear AYZ
FFT_AZZ=fft(AZZ,[],3); % Calculating FFT in z-direction
clear AZZ
end
```

D.9. Iterative Method (BCG) to Compute Matrix-Vector Multiplication.

```
%IIIIIIIIIIIIIIIIIIIIIIIIIIIIIIIIIIIIIIIIIIIIIIIIIIIIIIIIIIIIIIIIIIIIIIIIIIIIIIIIIIIIIIIIIIIIIIIIIIIIIIIIIIIIIIIIIIIIIIIIIIIIIIII%
%Applying Biconjugate gradient as an iterative method to obtainPx,Py,PZ%
function [px,py,pz]=Biconjugate_Gradient(E_x,E_y,E_z,Nx,Ny,Nz,N,Inverse_Alpha,...
  INDEX_IN,E_vector,FFT_AXX,FFT_AXY,FFT_AXZ,FFT_AYY,FFT_AYZ,FFT_AZZ)
% Initial amounts of the PX, PY and PZ %
px=0;
py=0;
pz=0;
Apkx=0;
Apky=0;
Apkz=0;
rkx=(E_x-Apkx);
rky=(E_y-Apky);
rkz=(E_z-Apkz);
%%%%%%%%%%%% qk=rk;
qkx=rkx;
qky=rky;
qkz=rkz;
%%%%%%%%%%% qk_bar=conj(qk);
Error=1;
counting=0;
%CCCCCCCCCCCCCCCC Applying complex conjugate gradient CCCCCCCCCCCCCC%
while Error>0.002
  %%%%% Performing inverse FFT to obtain matrix-vector multiplication%%%%
  [Aqkx,Aqky,Aqkz]=Inverse_FFT(qkx,qky,qkz,Nx,Ny,Nz,INDEX_IN,Inverse_Alpha,...
       FFT_AXX,FFT_AXY,FFT_AXZ,FFT_AYY,FFT_AYZ,FFT_AZZ);

  %%%%%%%%%%%%%% alphak=(rk')*rk/(qk'*Aqk)
  rkx_vector=reshape(rkx,[N,1]);
  rky_vector=reshape(rky,[N,1]);
  rkz_vector=reshape(rkz,[N,1]);

  Aqkx_vector=reshape(Aqkx,[N,1]);
  Aqky_vector=reshape(Aqky,[N,1]);
  Aqkz_vector=reshape(Aqkz,[N,1]);
```

```
qkx_vector=reshape(qkx,[N,1]);
qky_vector=reshape(qky,[N,1]);
qkz_vector=reshape(qkz,[N,1]);

alphak=(transpose(rkx_vector)*rkx_vector+transpose(rky_vector)*rky_vector...
   +transpose(rkz_vector)*rkz_vector)/(transpose(qkx_vector)*Aqkx_vector...
   +transpose(qky_vector)*Aqky_vector+transpose(qkz_vector)*Aqkz_vector);

clear Aqkx_vector Aqky_vector Aqkz_vector

% Pk=Pk+alphak*qk
rk0x=rkx;
clear rkx
rk0y=rky;
clear rky
rk0z=rkz;
clear rkz

rk0x_vector=rkx_vector;
clear rkx_vector
rk0y_vector=rky_vector;
clear rky_vector
rk0z_vector=rkz_vector;
clear rkz_vector

rkx=rk0x-alphak*Aqkx;
clear rk0x Aqkx
rky=rk0y-alphak*Aqky;
clear rk0y Aqky
rkz=rk0z-alphak*Aqkz;
clear rk0z Aqkz

rkx_vector=reshape(rkx,[N,1]);
rky_vector=reshape(rky,[N,1]);
rkz_vector=reshape(rkz,[N,1]);

px=(px+alphak*qkx).*INDEX_IN;
py=(py+alphak*qky).*INDEX_IN;
```

```
    pz=(pz+alphak*qkz).*INDEX_IN;

    rk_vector=[rkx_vector;rky_vector;rkz_vector];
    Error=norm(rk_vector)/norm(E_vector);
    clear rk_vector

    % betak=rk_bar'*rk/(rk0_bar'*rk0)
    betak=(transpose(rkx_vector)*rkx_vector+transpose(rky_vector)*rky_vector...
      +transpose(rkz_vector)*rkz_vector)/(transpose(rk0x_vector)*rk0x_vector...
      +transpose(rk0y_vector)*rk0y_vector+transpose(rk0z_vector)*rk0z_vector);
    clear rkx_vector rky_vector rkz_vector rk0x_vector rk0y_vector rk0z_vector

    % qk=rk+betak*qk;
    % qk_bar=rk_bar+conj(betak)*qk_bar;
    qkx=(rkx+betak*qkx).*INDEX_IN;
    qky=(rky+betak*qky).*INDEX_IN;
    qkz=(rkz+betak*qkz).*INDEX_IN;

    counting=counting+1;
end
end
```

D.10. Computing Inverse FFT to Obtain Matrix-Vector Multiplication Result.

```
%FFFFFFFFFFFFFFFFFFFFFFFFFFFFFFFFFFFFFFFFFFFFFFFFFFFFFFFFFFFFFFFFFFFFFFFFFFFF%
%%%%% Performing inverse FFT to obtain matrix-vector multiplication%%%%
function [Aqkx,Aqky,Aqkz]=Inverse_FFT(qkx,qky,qkz,Nx,Ny,Nz,INDEX_IN,Inverse_Alpha,...
         FFT_AXX,FFT_AXY,FFT_AXZ,FFT_AYY,FFT_AYZ,FFT_AZZ)
%Aqk=A*qk;
% Calculating FFT in y-direction for px (qx), py (qy), and pz (qz)
FFT_qkx_Y=fft(qkx,2*Ny-1,2);
FFT_qky_Y=fft(qky,2*Ny-1,2); % Calculating FFT in y direction
FFT_qkz_Y=fft(qkz,2*Ny-1,2); % Calculating FFT in y direction

% Calculating FFT in x-direction for px (qx), py (qy), and pz (qz)
FFT_qkx_x=fft(FFT_qkx_Y,2*Nx-1,1);
clear FFT_qkx_Y
FFT_qky_x=fft(FFT_qky_Y,2*Nx-1,1);
clear FFT_qky_Y
FFT_qkz_x=fft(FFT_qkz_Y,2*Nx-1,1);
clear FFT_qkz_Y

% Computing FFT in z-direction for px (qx), py (qy), and pz (qz)
FFT_qkx_z=fft(FFT_qkx_x,2*Nz-1,3);% Calculating FFT in Z direction
clear FFT_qkx_x
FFT_qky_z=fft(FFT_qky_x,2*Nz-1,3);% Calculating FFT in Z direction
clear FFT_qky_x
FFT_qkz_z=fft(FFT_qkz_x,2*Nz-1,3);% Calculating FFT in Z direction
clear FFT_qkz_x

% Performing matrix-vector elementwise multiplication in Fourier domain%
FFT_APX=FFT_AXX.*FFT_qkx_z+FFT_AXY.*FFT_qky_z+FFT_AXZ.*FFT_qkz_z;
FFT_APY=FFT_AXY.*FFT_qkx_z+FFT_AYY.*FFT_qky_z+FFT_AYZ.*FFT_qkz_z;
FFT_APZ=FFT_AXZ.*FFT_qkx_z+FFT_AYZ.*FFT_qky_z+FFT_AZZ.*FFT_qkz_z;
clear FFT_qkx_z FFT_qky_z FFT_qkz_z
% Performing ifft in z-direction %
IFFT_APX_Z=ifft(FFT_APX,[],3);% Calculating IFFT in Z direction
clear FFT_APX
IFFT_APY_Z=ifft(FFT_APY,[],3);% Calculating IFFT in Z direction
clear FFT_APY
```

```
IFFT_APZ_Z=ifft(FFT_APZ,[],3);% Calculating IFFT in Z direction
clear FFT_APZ

% Performing ifft in x-direction %
IFFT_APX_X=ifft(IFFT_APX_Z(1:2*Nx-1,1:2*Ny-1,1:Nz));
clear IFFT_APX_Z
IFFT_APY_X=ifft(IFFT_APY_Z(1:2*Nx-1,1:2*Ny-1,1:Nz));
clear IFFT_APY_Z
IFFT_APZ_X=ifft(IFFT_APZ_Z(1:2*Nx-1,1:2*Ny-1,1:Nz));
clear IFFT_APZ_Z
% Performing ifft in y-direction %
IFFT_APX=ifft(IFFT_APX_X(1:Nx,1:2*Ny-1,1:Nz),[],2);
clear IFFT_APX_X

IFFT_APY=ifft(IFFT_APY_X(1:Nx,1:2*Ny-1,1:Nz),[],2);
clear IFFT_APY_X
IFFT_APZ=ifft(IFFT_APZ_X(1:Nx,1:2*Ny-1,1:Nz),[],2);
clear IFFT_APZ_X

Aqkx=IFFT_APX(1:Nx,1:Ny,1:Nz).*INDEX_IN+Inverse_Alpha.*qkx.*INDEX_IN;
clear IFFT_APX
Aqky=IFFT_APY(1:Nx,1:Ny,1:Nz).*INDEX_IN+Inverse_Alpha.*qky.*INDEX_IN;
clear IFFT_APY
Aqkz=IFFT_APZ(1:Nx,1:Ny,1:Nz).*INDEX_IN+Inverse_Alpha.*qkz.*INDEX_IN;
clear IFFT_APZ

end
```

D.11. E_total.m File to Calculate the Total Electric Field.

```
%EEEEEEEEEEEEEEEEEEEEEEEEEEEEEEEEEEEEEEEEEEE%
%Finding total E_field at each nanocubes
function [Ex_total,Ey_total,Ez_total]=E_total(N2,r_blockGpu,r_cube,PX_vector,...
  PY_vector,PZ_vector,xx,yy,zz,Nps_number,Lx,Ly,Lz,d,kvec,d_inter,Structure,...
  Ex_incident,Ey_incident,Ez_incident)
for m=1:N2
  rij=r_cube(m,:)-r_blockGpu;
  %    Nan_Zero_rij=find(rij(:,1)~=0 | rij(:,2)~=0 | rij(:,3)~=0);
  Nan_Zero_rij=find(sqrt(rij(:,1).^2+rij(:,2).^2+rij(:,3).^2)>=(2*d));
  if length(Nan_Zero_rij)<length(rij)
    Zero_rij=find(sqrt(rij(:,1).^2+rij(:,2).^2+rij(:,3).^2)<(2*d));  % finding index of rij=0
    rij(Zero_rij,:)=1;                                                % in order to evade NAN error
  end

  r_norm=sqrt(rij(:,1).^2+rij(:,2).^2+rij(:,3).^2);
  r_hat=rij./r_norm;                      % Unit vector in the direction of the r

  rhat1_I=r_hat(:,1).*r_hat(:,1)-1;
  rhat2_I=r_hat(:,1).*r_hat(:,2);
  rhat3_I=r_hat(:,1).*r_hat(:,3);
  rhat4_I=r_hat(:,2).*r_hat(:,2)-1;
  rhat5_I=r_hat(:,2).*r_hat(:,3);
  rhat6_I=r_hat(:,3).*r_hat(:,3)-1;

  rhat31_I=3*r_hat(:,1).*r_hat(:,1)-1;
  rhat32_I=3*r_hat(:,1).*r_hat(:,2);
  rhat33_I=3*r_hat(:,1).*r_hat(:,3);
  rhat34_I=3*r_hat(:,2).*r_hat(:,2)-1;
  rhat35_I=3*r_hat(:,2).*r_hat(:,3);
  rhat36_I=3*r_hat(:,3).*r_hat(:,3)-1;

  Exp_ikvec_r=exp(1i*norm(kvec)*r_norm)./r_norm;
  ikvec_rjk=(1i*norm(kvec)*r_norm-1)./(r_norm.^2);  % ikvec_rjk=(1i*norm(kvec)*rjk-1)/rjk^2
  Axx=Exp_ikvec_r.*((norm(kvec)^2)*rhat1_I+ ikvec_rjk.*rhat31_I);
  Axy=Exp_ikvec_r.*((norm(kvec)^2)*rhat2_I+ ikvec_rjk.*rhat32_I);
  Axz=Exp_ikvec_r.*((norm(kvec)^2)*rhat3_I+ ikvec_rjk.*rhat33_I);
```

```
  Ayy=Exp_ikvec_r.*((norm(kvec)^2)*rhat4_I+ ikvec_rjk.*rhat34_I);
  Ayz=Exp_ikvec_r.*((norm(kvec)^2)*rhat5_I+ ikvec_rjk.*rhat35_I);
  Azz=Exp_ikvec_r.*((norm(kvec)^2)*rhat6_I+ ikvec_rjk.*rhat36_I);
  Ex_sc=Axx.*PX_vector+Axy.*PY_vector+Axz.*PZ_vector;



  Ey_sc=Axy.*PX_vector+Ayy.*PY_vector+Ayz.*PZ_vector;
  Ez_sc=Axz.*PX_vector+Ayz.*PY_vector+Azz.*PZ_vector;

  clear Axx Axy Axz Ayy Ayz Azz rhat1_I rhat2_I rhat3_I rhat4_I rhat5_I rhat6_I ...
    rhat31_I rhat32_I rhat33_I rhat34_I rhat35_I rhat36_I

  if length(Nan_Zero_rij)<length(rij)
     Ex_sc(Zero_rij)=0;
     Ey_sc(Zero_rij)=0;
     Ez_sc(Zero_rij)=0;
  end
  Ex_scat(m,1)=sum(Ex_sc);
  Ey_scat(m,1)=sum(Ey_sc);
  Ez_scat(m,1)=sum(Ez_sc);
  clear Ex_sc Ey_sc Ez_sc
end
toc

% excluding the contribuation of the dipoles inside the NPs
[Outside_Index]=Excluding_NPs(xx,yy,zz,N2,Nps_number,Lx,Ly,Lz,d_inter,Structure);
Ex_total=(Ex_incident+Ex_scat).*Outside_Index;
Ey_total=(Ey_incident+Ey_scat).*Outside_Index;
Ez_total=(Ez_incident+Ez_scat).*Outside_Index;
end
```

D.12 Excluding Contribution of the Nanocubes Which Are Located Outside the Nanoparticle(s) using Excluding_NPs.m file.

```
%DDDDDDDDDDDDDDDDDDDDDDDDDDDDDDDDDDDDDDDDDDDDDDDDDDDDDDDDDDDDDDDDDDDDDDD%
% Finding index of the dipoles outside of the NPs and excluding inside NPs
Function [Outside_Index]=Excluding_NPs(xx,yy,zz,N2,Nps_number,Lx,Ly,Lz,d_inter,Structure)

if Structure==1 % Monomer structure
  X0=0; % d_inter is the distance from surface of first Np to surface of second one
  Y0=0;
  Z0=0;

  if Nps_number==1      % NPs are sphere
    % Index of cubes inside NP
    Index_in=find((sqrt((xx-X0).^2+(yy-Y0).^2+(zz-Z0).^2)<=(Lx/2)));

  elseif Nps_number==2 %NPs are ellipsoid, head-tail orientation in z-direction
    % Index of cubes inside NP
    Index_in=find((sqrt((xx-X0).^2/((Lx/2)^2)+(yy-Y0).^2/((Ly/2)^2)+...
      (zz-Z0).^2/((Lz/2)^2))<=1));
  elseif Nps_number==3    %NPs are Rod with caps, vertically oriented
    % Index of cubes inside NP
    Index_in=find((sqrt((xx-X0).^2+(yy-Y0).^2+(abs(zz-Z0)-
      Lz/2+Lx/2).^2)<=(Lx/2)...
      & abs(zz-Z0)>(Lz/2-Lx/2))|((sqrt((xx-X0).^2+(yy-Y0).^2)<=(Lx/2))...
      &abs(zz-Z0)<=(Lz/2-Lx/2)));

  elseif Nps_number==4 %NPs are Rectangular block, vertically oriented
    % Index of cubes inside NP
    Index_in=find((abs(xx-X0)<=Lx/2 & abs(yy-Y0)<=Ly/2 & abs(zz-Z0)<=Lz/2));
  end

else % Dimer, structure=2
  X10=0; % d_inter is the distance from surface of first Np to surface of second one
  Y10=0;
  Z10=-(d_inter/2+Lz/2);
  X20=0;
  Y20=0;
  Z20=(d_inter/2+Lz/2);
```

```
  if Nps_number==1       % NPs are sphere
    % Index of cubes inside NP
    Index_in=find((sqrt((xx-X10).^2+(yy-Y10).^2+(zz-Z10).^2)<=(Lx/2))|...
      (sqrt((xx-X20).^2+(yy-Y20).^2+(zz-Z20).^2)<=(Lx/2)));

  elseif Nps_number==2 %NPs are ellipsoid, head-tail orientation in z-direction
    % Index of cubes inside NP
    Index_in=find((sqrt((xx-X10).^2/((Lx/2)^2)+(yy-Y10).^2/((Ly/2)^2)+...
      (zz-Z10).^2/((Lz/2)^2))<=1)|(sqrt((xx-X20).^2/((Lx/2)^2)+...
      (yy-Y20).^2/((Ly/2)^2)+(zz-Z20).^2/((Lz/2)^2))<=1));

  elseif Nps_number==3    %NPs are Rod with caps, vertically oriented
    % Index of cubes inside NP
    Index_in=find((sqrt((xx-X10).^2+(yy-Y10).^2+(abs(zz-Z10)-
       Lz/2+Lx/2).^2)<=(Lx/2)...
      & abs(zz-Z10)>(Lz/2-Lx/2))|((sqrt((xx-X10).^2+(yy-Y10).^2)<=(Lx/2))...
      &abs(zz-Z10)<=(Lz/2-Lx/2))|...
      (sqrt((xx-X20).^2+(yy-Y20).^2+(abs(zz-Z20)-Lz/2+Lx/2).^2)<=(Lx/2)...
      & abs(zz-Z20)>(Lz/2-Lx/2))|((sqrt((xx-X20).^2+(yy-Y20).^2)<=(Lx/2))...
      &abs(zz-Z20)<=(Lz/2-Lx/2)));

  elseif Nps_number==4 %NPs are Rectangular block, vertically oriented
    % Index of cubes inside NP
    Index_in=find((abs(xx-X10)<=Lx/2 & abs(yy-Y10)<=Ly/2 & abs(zz-Z10)<=Lz/2)|...
      (abs(xx-X20)<=Lx/2 & abs(yy-Y20)<=Ly/2 & abs(zz-Z20)<=Lz/2));
  end
end
Multiply_Nps=zeros(N2,1);
Multiply_Nps(Index_in,1)=1;

Mult=ones(N2,1);
Outside_Index=Mult-Multiply_Nps;
clear Multiply_Nps Index_in Multiply_coeff
end
```